



JOHANNES GUTENBERG
UNIVERSITÄT MAINZ

**Synthesis, evaluation and structural analysis of new ligands
for the integrin alpha v beta 6 for PET imaging of liver fibrosis**

Dissertation

Zur Erlangung des Grades

„Doktor der Naturwissenschaften“

Im Promotionsfach Chemie

Am Fachbereich Chemie, Pharmazie und Geowissenschaften

Der Johannes Gutenberg-Universität Mainz

Berit Kühle

Geboren am 28.02.1987 in Soest

Mainz, 2014

Max Planck **Graduate Center** 
mit der Johannes Gutenberg-Universität Mainz

Dekan: Prof. Dr. Xxxxxx Xxxx

1. Berichtstatter: Prof. Dr. Xxxxxx X. Xxxx
2. Berichtstatter: Prof. Dr. Dr. Xxxxxx Xxxxxxxx

Meiner Familie

*Falls Gott die Welt geschaffen hat, war seine Hauptsorge sicher nicht,
sie so zu machen, dass wir sie verstehen können.*

Albert Einstein

Zusammenfassung

Leberfibrose ist eine relativ häufige Erkrankung, die in vielen Fällen zu einer Notwendigkeit der Lebertransplantation führt. Dies liegt im Fehlen von anti-fibrotischen Medikamenten begründet – die klassische Behandlung erfolgt daher kausativ. Häufig ist die Bekämpfung der zugrunde liegenden Hepatitis B/C, einer nicht-alkoholischen Steatohepatitis, oder von Alkoholmissbrauch aber nicht ausreichend um das Fortschreiten der Erkrankung zu verhindern. Außerdem, ist der momentane diagnostische ‚gold standard‘ einer Leberbiopsie ebenfalls problembehaftet. Da die Probe nur 1/50.000 des Gesamtorgans repräsentiert, können leicht falsch-positive oder falsch-negative Ergebnisse erhalten werden. Insbesondere für mittlere Schweregrade ist die differenzierte Diagnose schwierig. Daher wird der Einsatz der Positronen-Emissions-Tomographie (PET) für vielversprechend gehalten, falls eine geeignete Tracer-Substanz gegeben ist.

Die Entwicklung solch einer Substanz war das Ziel dieser Arbeit. Das Integrin $\alpha_v\beta_6$ wurde als Target Struktur gewählt, da es direkt in die fibrogenetischen Prozesse involviert ist und zudem innerhalb der Leber abgesehen von den Cholangiozyten von keinen weiteren Zellen exprimiert wird. Dazu wurde der für nanomolare Affinität bekannte Ligand EMD527040 synthetisiert und zwei Derivate konnten davon als Markierungsvorläufer für die Radiomarkierung mit ^{68}Ga hergestellt werden. Für beide Substanzen wurden geeignete Markierungsprotokolle entwickelt mit denen radiochemische Ausbeuten von über 95 % erzielt werden können.

Stabilitätsstudien über zwei Stunden, sowie die Bestimmung der Lipophilie wurden erfolgreich durchgeführt. In in vitro Studien konnte hingegen weder auf $\alpha_v\beta_6$ -tragenden Zellen, noch am immobilisierten Integrin selbst eine Affinität nachgewiesen werden. Dies wurde in Biodistributionen und PET-Aufnahmen bestätigt – zwischen fibrotischen und gesunden Mäusen konnte kein signifikanter Unterschied beobachtet werden. Allerdings wurden verschiedene Stoffwechselwege beobachtet: Um eine Verstoffwechslung über die hepato-biliären Systeme zu verhindern, sollte daher der logD Wert für zukünftige Substanzen unter -0,19 liegen.

Diese unerwarteten Resultate wurden mittels einer theoretischen Studie untersucht. Ein homologes Model des $\alpha_v\beta_6$ wurde anhand der für $\alpha_v\beta_3$ bekannten Kristallstruktur konstruiert. Außerdem wurden die elektronischen sowie elektrostatischen Eigenschaften literaturbekannter Liganden (teils an derselben Position derivatisiert) untersucht und an das $\alpha_v\beta_6$ Model gedockt. Hieraus konnte eine Hypothese abgeleitet werden, die die gefunden Unterschiede erklärt und einen Vorschlag für vielversprechendere Substanzen erlaubt.

Abstract

Liver fibrosis is a very frequent disease and often leads to the necessity of transplantation for the patient. This is due to the lack of any anti-fibrotic drugs – therefore, the typical treatment is purely causative. But the treatment of an underlying hepatitis B/C, non-alcoholic-steato hepatitis or alcohol abuse are not always sufficient in order to halt the diseases progression. Furthermore, the current diagnostic ‘gold standard’ of a biopsy is not ideal – the sample represents only a 1/50.000 of the whole organ, which can cause false-positive as well as false-negative results. Especially for intermediate stages, it is difficult to obtain information allowing conclusions about treatment efficiency. For that reason, the positron emission tomography (PET) is thought to be a promising technique, which could overcome the current diagnostic pitfalls, if a suitable tracer substance was given.

The development of such a substance was the aim of this work. The integrin $\alpha_v\beta_6$ was chosen as the target structure, as it is directly involved in the fibrogenetic pathway and furthermore in the liver it is solely expressed by cholangiocytes. The high affinity ligand EMD527040 was therefore synthesized and two derivatives thereof were produced – to be used as labelling precursors for ^{68}Ga , an easily available PET nuclide. For both substances, convenient labelling procedures were developed, yielding radiochemical yields of >95 %.

Stability studies over two hours as well as the determination of their lipophilicity have successfully be performed. The in vitro studies on $\alpha_v\beta_6$ bearing cells though, did not show any retention on the receptor. Also tests on the isolated and immobilized integrin could not show a binding. This was supported from the biodistribution studies and PET images of both tracer substances – no significant difference between healthy and fibrotic mice was observed. Nevertheless, the more lipophilic substance was apparently metabolized via hepato biliary pathways while the more hydrophilic one was cleared via the kidneys. The logD value for further derivatives should therefore be below -0.19.

As these results were unexpected, a computational study was initiated – a homology model of $\alpha_v\beta_6$ was derived from a template crystal structure of $\alpha_v\beta_3$. Furthermore, the electronic as well as electrostatic characteristics of literature known ligands (partially derivatized at the same position) were investigated and also docked to the homology model. A hypothesis could be derived which explains why our ligands did unexpectedly not bind to the target integrin and allowed the proposal of more promising structures.

CONTENTS

I.	INTRODUCTION	1
I.I	LIVER FIBROSIS	2
I.I.I	MOLECULAR MECHANISMS	4
I.I.II	CURRENT DIAGNOSTIC METHODS – ADVANTAGES AND PITFALLS	6
I.II	NUCLEAR MEDICINE	9
I.II.I	POSITRON EMISSION TOMOGRAPHY	10
I.II.II	SINGLE PHOTON EMISSION COMPUTED TOMOGRAPHY	14
I.II.III	NUCLEAR ASPECTS FOR PET- AND SPECT-AGENTS	15
I.II.IV	ORGANO-CHEMICAL AND BIOLOGICAL ASPECTS FOR PET- AND SPECT-AGENTS	18
I.III	TARGETED RECEPTORS	21
I.III.I	INTEGRINS	21
I.III.II	PROTEASES	23
I.III.III	AFFINITY ASSAYS	25
I.IV	MOLECULAR MODELLING	28
I.IV.I	AB INITIO AND SEMI-EMPIRICAL METHODS	29
I.IV.II	MOLECULAR MECHANICS	30
I.IV.III	MOLECULAR DYNAMICS	31
I.IV.IV	HOMOLOGY MODELLING	33
II.	AIMS AND SCOPE	37
III.	RESULTS AND DISCUSSION	40
III.I	ORGANIC SYNTHESSES	40
III.I.I	SYNTHESIS OF EMD527040	41
III.I.II	SYNTHESIS OF LABELLING PRECURSORS	44
III.I.III	DERIVATIZATION OF TALABOSTAT	48
III.II	RADIOLABELLING	49
III.III	AFFINITY ASSAYS	53
III.III.I	CELL ASSAYS	54
III.III.II	ELISA ASSAYS	59
III.III.III	QUARTZ CRYSTAL MICROBALANCE	70

III.III.IV CONCLUSION – <i>IN VITRO</i> EXPERIMENTS	71
III.IV ANIMAL STUDIES	73
III.IV.I BK23 – ETHYL SPACER	74
III.IV.II BK39 – OLIGO-ETHYLENE-GLYCOL-SPACER	78
III.IV.III SUMMARY	82
III.V COMPUTATIONAL STUDIES	83
III.V.I SMALL MOLECULES / LIGANDS	83
III.V.II GENERATION OF RECEPTOR MODEL FOR A_vB_6	98
III.V.III DOCKING EXPERIMENTS	105
IV. CONCLUSIONS AND OUTLOOK	111
V. EXPERIMENTAL	114
V.I ORGANIC SYNTHESIS	114
V.I.I SYNTHESIS OF EMD 527040	115
V.I.II SYNTHESIS OF LABELLING PRECURSORS	122
V.II RADIOCHEMISTRY	128
V.II.I LABELLING PROCEDURE	128
V.II.II KINETIC STUDIES	128
V.II.III STABILITY STUDIES	129
V.II.IV LOG D	129
V.III CELL ASSAYS	130
V.III.I AFFINITY	130
V.III.II UPTAKE	130
V.III.III CHALLENGE	131
V.IV ELISA – PROTOCOLS	132
V.IV.I ALPHA_v – SANDWICH-ASSAY	132
V.IV.II ANTI- A_vB_6 -BASED ASSAY	132
V.IV.III FIBRONECTIN BIOTINYLATION	133
V.IV.IV FIBRONECTIN-BASED ASSAY	134
V.IV.V RADIOASSAY ON A_vB_6 –COATED ELISA PLATES	134
V.IV.VI GENERAL PROCEDURE – LAP ASSAY	135
V.V QUARTZ CRYSTAL MICROBALANCE	136
V.VI ANIMAL STUDIES	137

V.VII COMPUTATIONAL METHODS	138
V.VII.I OBTAINING LIGAND STRUCTURES	138
V.VII.II LIGAND CHARACTERISTICS – ORBITALS AND ELECTROSTATIC POTENTIAL	138
V.VIII HOMOLGY MODELLING	139
V.VIII.I PRODUCTION OF AVB6 – MODEL WITH SWISS-MODEL	139
V.VIII.II PRODUCTION OF A_vB₆–MODEL WITH MODELLER	139
V.VIII.III PROTEIN-MODEL REFINEMENT	139
V.IX DOCKING STUDIES	140
VI. LITERATURE	141
VII. LIST OF ABBREVIATIONS	148
VIII. LIST OF FIGURES	151
IX. LIST OF TABLES	157
X. DANKSAGUNG / ACKNOWLEDGEMENTS	158
XI. EIDESSTATTLICHE ERKLÄRUNG	160
XII. CURRICULUM VITAE	161

I. Introduction

The liver is one of the most complex organs in the human body as it fulfils a central function in metabolism. Any dysfunction can therefore be extremely crucial for the affected individual. According to the *German Organ Transplantation Foundation (DSO)* it is the second-most transplanted organ, only outnumbered by the kidneys.¹

In Germany, 1097 livers could be transplanted in 2012, which unfortunately were only about two thirds of the 1689 newly registered patients in need of a donor liver. The three main indications for a liver transplantation are alcoholic liver disease (28.9%), liver fibrosis and cirrhosis (26.2%) and malignancies in liver and intrahepatic bile ducts (17.4%).¹ But even for a patient receiving a liver, the 5-year-function-rate is only stated to be 53.8% in average.

Changing to a world-wide view, in 2004, the World Health Organization (WHO) stated 12.9 deaths per 100.000 population which are due to liver cirrhosis in Germany. This is only a medium value compared to regions in Asia, North Africa and Latin America showing values of 54.3 (Afghanistan), 26.3 (Russia), 50 (Sudan) or 30 (Peru).²

These figures show very clearly the urgent need for further research in Hepatology. The lack of any specifically anti-fibrotic drug³ enhances the importance of investigation within fibrotic events even further.

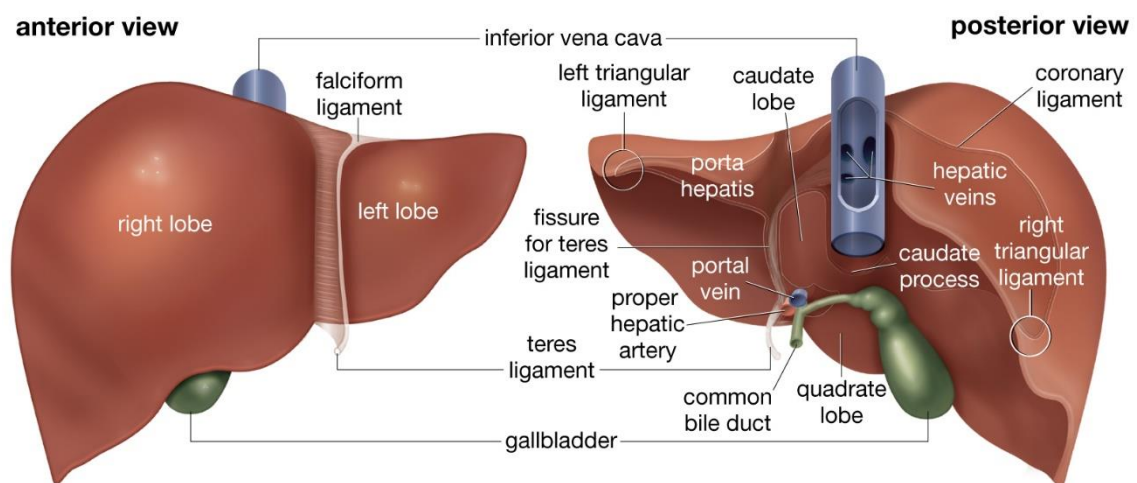
As will be outlined below, the diagnostic techniques in nuclear medicine are expected to carry the potential of significantly improving the diagnostic methods for liver fibrosis, if a suitable tracer substance was given. In the long-term perspective, this could hopefully lead to the development of anti-fibrotic drugs and therefore a significant decrease in the need for donor organs as well as liver disease-related death rates.

In the following chapters, this work will therefore focus on the (bio)chemical, nuclear and technical aspects that need to be considered in order to successfully combine them for the benefit of the patient.

I.1 Liver fibrosis

Fibrosis itself is simply defined as an “increase of connective tissue”.⁴ This is not necessarily a pathological phenomenon, as it is an essential requirement for successful wound healing and scar formation. Only when this process exceeds the given requirements, it becomes a clinical concern in itself. If it leads to a transformation of tissue including its rigidification and abolition of its inherent structure, a cirrhosis is present.⁴

The liver structure is essential for its function. Macroscopically the liver is partitioned into four lobes, namely *Lobus dexter*, *sinister*, *caudatus* and *quadratus*. The blood supply is conducted mainly via the portal vein (75-80%), whereas the hepatic artery plays only a minor role. The so-called liver sinusoids are capillaries collecting and draining the blood into the inferior vena cava. The portal vein blood is enriched with carbohydrates, proteins, fatty acids as well as substances from spleen and pancreas, which have been absorbed in areas of stomach, small and large intestine. In the liver they will be processed further.⁵



© 2010 Encyclopædia Britannica, Inc.

Figure 1: Macroscopic structure of the human liver.⁶

The classical approach to describe the microscopic liver structure uses the term of *liver lobules*. In tissue sections of the liver they appear roughly hexagonal with a diameter of 1-2 mm.⁵ Liver lobules are characterized by central veins in their middle, surrounded by radially distributed hepatic cells. They are separated by small amounts of connective tissue, which accumulates in positions where several lobules meet. In these *periportal fields* the branches of portal vein, hepatic artery and hepatic bile ducts can be found.⁵ Liver sinusoids are bounded by highly fenestrated walls, made up by endothelial cells as well as hepatic stellate cells (HSC; named as

well Ito-cells, lipocytes or perisinusoidal cells)⁷. The liver sinusoid's walls are separated from hepatic cells by the *Disse space*.⁵ Details of the microscopic structure can be seen below in Figure 2.

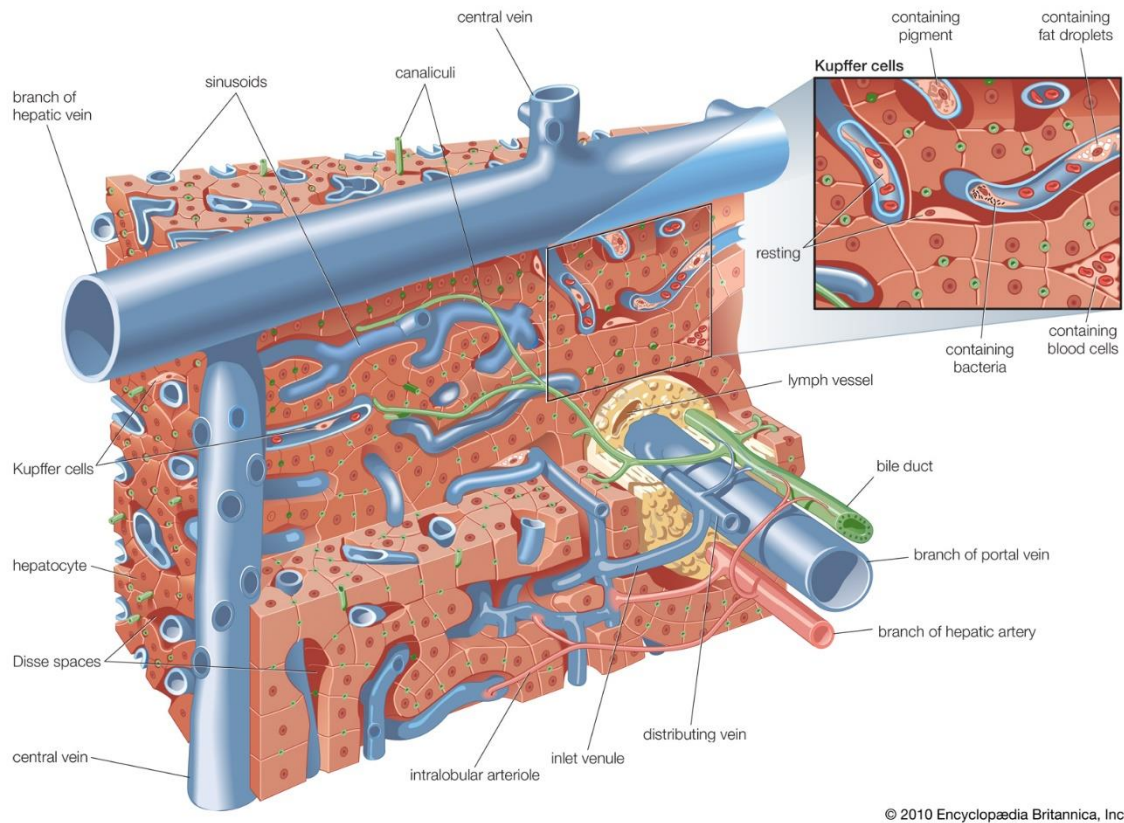


Figure 2: Microscopic structure of the human liver, detailing some liver sinusoids.⁸

A newer term than the *liver lobule* is the *liver azinus*. In the former case the definition is based on the central vein, whereas the latter term defines the liver parenchyma surrounding a periportal field in its centre.⁵

In the case of liver fibrosis, an excessive deposition of extracellular matrix (ECM) is observed.⁹ The larger the extent of deposition, the more hindered will be the permeation of blood from periportal fields towards the sinusoids. This increasing blockage (especially affecting the Disse space) leads to a worsening of physiological functions during the course of the disease, finally up to liver failure. The liver is able to compensate fibrotic events to quite a large extent, which is why patients can stay asymptomatic for many years.¹⁰ When these capacities are no longer sufficient, complications like variceal bleeding, ascites or hepatic encephalopathy can occur.¹⁰ Portal hypertension is another phenomenon induced by the blockage of the tissue. Additional bacterial infections are also common, just as the risk for renal failure and the development of hepatic carcinoma rises.⁹

As mentioned before, there is no drug available targeting directly the fibrogenetic process itself. Therefore, therapy options remain symptomatic on the one hand and causative on the other hand. Main reasons for the development of liver fibrosis are alcohol abuse, chronic forms of Hepatitis (i.e. B and C) and non-alcoholic-steato-hepatitis (NASH). Also drugs and autoimmune attacks can serve as initiator.¹¹ The removal of the underlying cause is consequently the most important “therapy” option today. Depending on the individual case this can be alcohol withdrawal, administration of anti-viral drugs or a diet and exercise.⁹

As this is not always very effective, for many patients the liver transplantation remains the last option.⁷ Its limited availability and severe invasiveness are obvious reasons for the necessity of the development of anti-fibrotic drugs.

I.I.I Molecular mechanisms

Trying to find a target, allowing us to intervene in the fibrotic process, one first needs to understand the underlying mechanisms in more detail. Generally, the common final path is the excessive production and deposition of ECM, but this can be triggered in different ways – depending on the underlying cause of the disease.

The fibrous material consists of a variety of different proteins, though collagen is by far the most prominent. Apart from collagen type I, III and IV also fibronectin, elastin, laminin, hyaluronan, undulin and proteoglycans can be found.⁷ They are not only increasingly synthesized but also degraded to a lesser extent. Their degradation is usually executed by Matrix-Metallo-Proteases (MMPs), which find themselves to be further inhibited by specific tissue inhibitors of metalloproteinases (TIMPs).⁷

Hepatic stellate cells are the most important cell type within the excessive production of ECM. They make up about 15% of total liver cells and are mostly a storage site of retinoids in their quiescent state. Only upon activation they become proliferative, fibrogenic and contractile myofibroblasts.¹¹ These activated HSCs produce vast amounts of ECM. Their activation is induced by several factors. Reactive Oxygen Intermediates (ROI) are produced by injured hepatocytes and Kupffer cells (liver resident macrophages) and stimulate HSC's activation. Also endothelial cells play a role by activating the latent form of transforming growth factor- β 1 (TGF- β 1).¹¹ Typical features of the activated HSC phenotype are proliferation, contractility,

fibrogenesis, matrix degradation, chemotaxis, retinoid loss, cytokine release and white blood cell attraction.¹¹ Due to autocrine signalling these features become permanent.

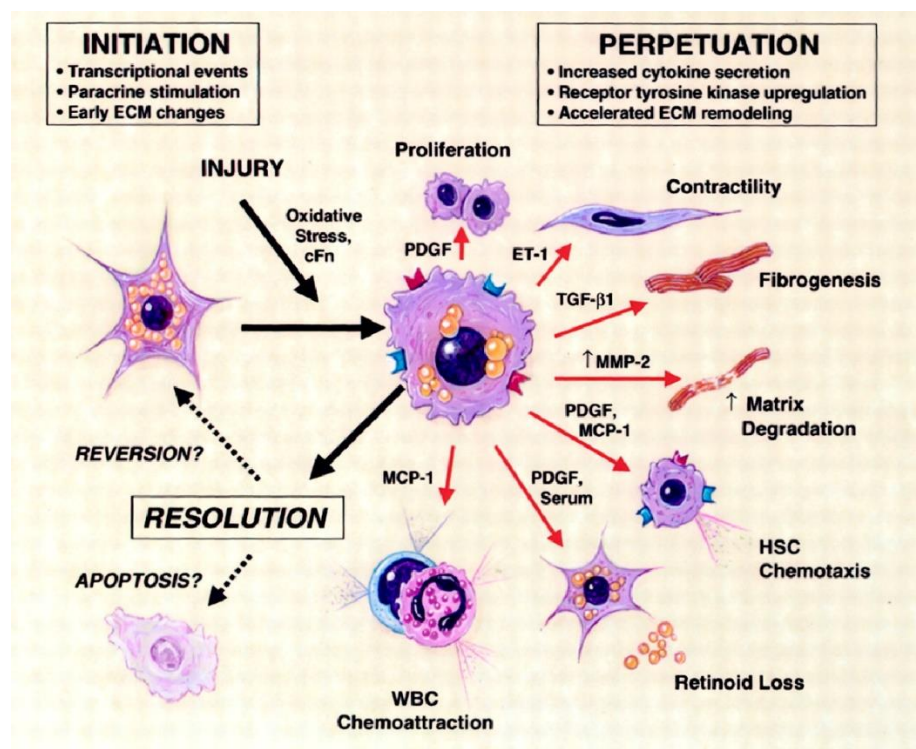


Figure 3: Activated hepatic stellate cells and their role in fibrogenesis. Whether they reverse into a quiescent state or undergo apoptosis upon resolution of liver injury remains unsure.¹¹

Figure 3 shows the different substances involved in the expression of those phenotypic features. Platelet-derived Growth Factor (PDGF) induces proliferation of activated HSCs as well as it attracts other activated (not quiescent) HSCs via chemotactic means. Contractility is enhanced by endothelin-1 (ET-1) which also promotes proliferation. The increased contractility is one of the main mechanisms leading to portal resistance.¹¹

The most dominant stimulus for ECM production is TGF-β1. It is secreted by HSCs themselves but also by Kupffer-cells and platelets. Hepatic stellate cells carry different forms of the TGF-β1 Receptors and are increasingly sensitive to their ligand upon activation.¹⁰ Intracellular signalling via SMAD pathways induce the production of ECM. The latent form of TGF-β1 can be activated via several ways, including plasmin, reactive oxygen species and the integrin $\alpha_v\beta_6$.¹²

Activated stellated cells also excrete MMP-2 which is able to degrade the normal subendothelial ECM. Its replacement by fibril collagen enhances the course of disease even further.¹¹

However, quiescent hepatic stellate cells are not the only source for activated myofibroblasts. As can be seen in Figure 4, also portal or vascular fibroblasts can undergo activation, as well as

endothelial-mesenchymal-transition (EMT) can occur to hepatocytes and cholangiocytes (namely the epithelial cells of the bile ducts). Also circulating fibrocytes can be recruited.

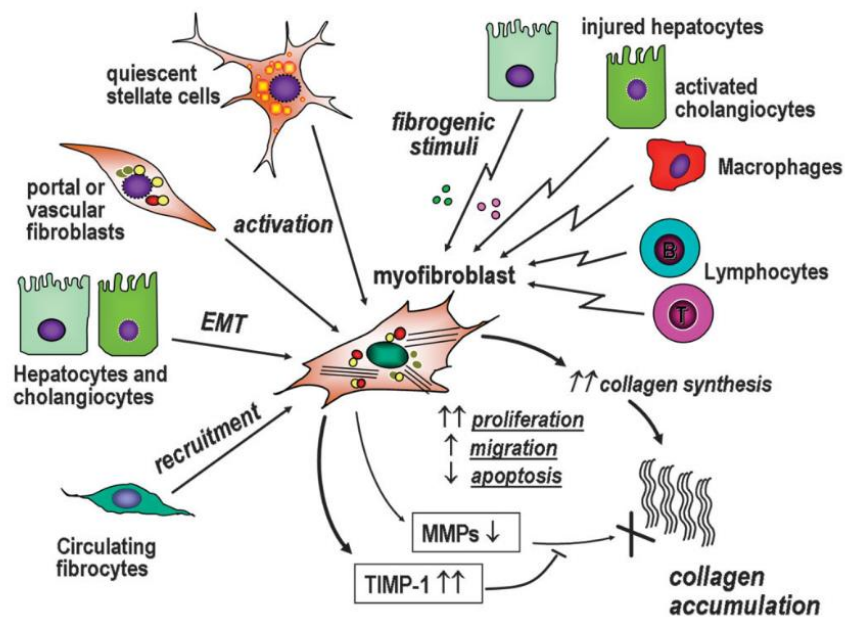


Figure 4: Different cell types with the capability of converting into activated myofibroblasts. It is shown as well how they contribute to the establishment of fibrosis.¹³

Furthermore, the immune system plays a role as well. If hepatocytes are injured and eventually undergo apoptosis, white blood cells are being recruited. As activated myofibroblasts excrete adhesion molecules and inflammatory chemokines, whereas lymphocytes induce collagen production in activated HSCs, a vicious circle can easily be established.⁷

I.1.II Current diagnostic methods – advantages and pitfalls

For such a complex disease, the development of diagnostic methods is obviously challenging. Those available at the moment can be divided into three groups: Non-invasive methods are Serum-Tests as well as the investigation on the livers' stiffness, whereas the histological examination of a liver sample requires an invasive biopsy.

Serum-Tests generally bear the problem, that the blood does not present one single marker being specific for liver fibrosis.¹⁴ For the so-called 'direct markers' blood levels of ECM components like hyaluronate, laminin, YKL-40 and procollagen III N-peptide or type IV collagen are examined.¹⁵ Also collagenases, MMPs and TIMPs can be used as markers.¹⁵ Their drawback

is that they may be altered due to liver fibrosis, but the change may just as well be related to other diseases/organs. Therefore, they have to be interpreted very carefully.

Indirect markers use parameters of routine blood tests like platelet count and the ratio of aspartate aminotransferase to alanine aminotransferase (AST/ALT), revealing malfunction of the liver.¹⁵

Algorithms, combining direct and indirect markers, have been developed in order to classify the extent of fibrosis. As only one example FibroTest[®] is a commercially available test that combines six serum parameters with age and sex of the patient. Alpha-2-macroglobulin, Haptoglobin, Apolipoprotein A1, Gamma-Glutamyl-transpeptidase (GGT), total bilirubin and ALT are the measured values¹⁶ – clearly not solely specific for liver fibrosis, but gaining in terms of predictive value due to their combination. For example, false positive results can be obtained in patients with Gilbert's syndrome or haemolysis for their hyperbilirubinaemia.¹⁵

The livers' stiffness is a physical attribute which changes with progression of the disease. The two elastographic methods use either ultrasound (US) or magnetic resonance imaging (MRI) to measure any rigidification. A low-frequency (50 Hz) elastic shear wave is sent through the liver while its velocity is being measured.¹⁵ This is directly proportional to the stiffness, or elastic modulus E : $E = 3\rho v^2$ Here, the tissue density is assumed to be constant.¹⁵ The wave propagates faster, the denser the tissue – yielding higher values for severer stages of fibrosis.¹⁵

Transient elastography (TE) has proven to be very successful in the diagnosis of cirrhosis, whereas lower fibrotic stages remain difficult to differentiate.¹⁵ Additionally – stiffness can be present due to other reasons than fibrosis, e.g. acute hepatitis, extra-hepatic cholestasis and liver congestion.¹⁷ For some patients it may even be impossible to obtain a result. Obesity can be a problem, but also narrow intercostal spaces and patients that have developed ascites.^{15,17}

The common huge advantage of the methods described so far, is their simplicity and therefore availability for patients. From the methodological point of view, they are well-validated and highly reproducible. Nevertheless, due to the aforementioned drawbacks, the 'gold standard'¹⁸ in liver fibrosis diagnostics remains the liver biopsy.

Liver biopsies can be performed in three different techniques – laparoscopic, transjugular and percutaneous, of which the latter is the most widely used.¹⁹ After Menghini's description²⁰ of his technique in 1958 it became a widely used diagnostic method. A tissue sample is taken with a

needle (of either ‘cutting’ or ‘suction’ type) and subsequently investigated histologically. The results are assessed according to a scoring system – a prominent one is the METAVIR system. Within this scheme, the disease is classified in 5 groups, numbered from 0 to 4:²¹

Table 1: The METAVIR score scheme with the respective histological characteristics.²¹

<i>METAVIR Score</i>	<i>Histological characteristic</i>
0	No fibrosis
1	Stellate enlargement of portal tract but without septa formation
2	Enlargement of portal tract with rare septa formation
3	Numerous septa without cirrhosis
4	Cirrhosis

But even though the histological evaluation of a tissue sample allows a clear view on the proceedings in the organ, the method bears some problems as well. First of all, as an invasive method it is unpleasant and eventually painful for the patient. Furthermore, complications such as bleeding may arise, requiring intensive care of the patient.¹⁹

Also, the sample is scored by humans, which always includes an inter- and intra-observer variability.^{17,21} And finally it is relatively small – only 1 – 3 cm in length and 1.2 – 2 mm in diameter,¹⁹ which represents only about 1/50.000 of the whole organ. The sampling error can therefore be of significant size, as shown below in Table 2:

Table 2: Occurrence of 1 stage difference in the METAVIR scheme, which is due to sampling error. PBC = Primary biliary cirrhosis.

<i>Diagnosis</i>	<i>Occurrence of 1 stage difference</i>	<i>Reference</i>
<i>HCV</i>	33.1%	Regev et al. ²²
<i>NASH</i>	> 40%	Ratziu et al. ²³
<i>PBC</i>	> 60%	Garrido et al. ²⁴

This shows that the ideal diagnostic tool would therefore be one, which is capable of assessing the whole organ. Furthermore, it should be quantitative and of high specificity as well as sensitivity. Nuclear medicine provides imaging technologies which theoretically could fulfil all

these criteria – if a suitable tracer was given. An introduction into those techniques will be given in the next chapter.

I.II Nuclear Medicine

Nuclear medicine is a medical branch engaging in the therapeutic and diagnostic application, i.e. participating in the metabolism, of radionuclides and radiolabelled compounds.⁴

The different properties of several radioactive decay types are applied for various means. The destructive potency of radiation can be used for therapeutic effects – mostly in oncological applications. On the other hand, the high sensitivity of radiation detection methods is a powerful tool for the detection of very small substance amounts. This is of use in *in vitro* tests, e.g. in Radio Immuno Assays (RIA)²⁵ as well as for *in vivo* applications in the clinical environment.

For therapeutic means, nuclear medicine solely focuses on endoradiotherapeutic approaches whereas external radiation therapies belong to the field of radiology. The principle comprises the intravenous application of a radioactive drug, which reaches its target tissue as specifically as possible. The energy set free by the radioactive decay is deposited in the malign tissue, which leads to ionisation processes (radicals, peroxides etc.) damaging the cells and hopefully to cell death and shrinkage of the tumour.²⁶ Local application of the radioactive drug is also possible (radiation synovectomy)²⁷ and applied mostly for inflammatory indications, i.e. rheumatoid arthritis.

The diagnostic usage of radioactivity is based on the so-called tracer principle. This was first applied by the Hungarian chemist György de Hevesy, who was credited with the Nobel prize in 1943 “for his work on the use of isotopes as tracers in the study of chemical processes”.²⁸ The principle states that, by the application of extremely dilute radioactive isotopes, the behaviour of a system can be observed, simply by detection of this isotope. The concentration is meant to be low enough, to make the assumption that its addition does not change the system but allows a mere observation of the system ‘as is’. De Hevesy used this e.g. for investigations on the absorption and translocation of lead by plants.²⁹

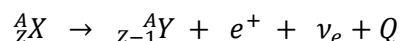
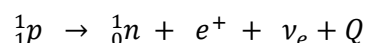
Nowadays, this principle is used in the diagnostic methods named Positron Emission Tomography (PET) and Single Photon Emission Computed Tomography (SPECT). Depending on the substance used, these techniques allow to obtain a wide array of functional (as opposed to

morphological) information. Also, they are non-invasive, which makes them ideal for a use in oncology, neurology or cardiology – their most frequent fields of use.³⁰

I.II.I Positron Emission Tomography

After radioactivity was discovered by Henri Becquerel in 1896,³¹ it was studied extensively. Not only the different decay types became known, but it found many applications, also in medicine, quite rapidly.

The principle of Positron Emission Tomography is based on the beta plus decay type. Herein, a stabilization of proton-rich nuclei takes place by emission of a positron (e^+ , β^+) and an electron neutrino (ν_e):³²



with p = proton, n = neutron, e^+ = positron, ν_e = electron neutrino, X = mother nuclide, Y = daughter nuclide, A = mass number, Z = atomic number, Q = energy released.

The atomic number is reduced by one in this process, whereas the mass number remains unchanged. The positron is the antiparticle of the electron – therefore, it bears a single positive charge, a spin of $\frac{1}{2} \hbar$ and the same mass as the electron. Being stable in vacuum, it lasts only about $10^{-10} - 10^{-7}$ s in condensed matter.³³ The electron neutrino initially was not part of the picture. Its existence was postulated by Pauli only in 1930, since the continuous beta-spectrum as well as spin discrepancies could not be explained without it. The experimental confirmation lasted until 1955 by Reines and Cowan. It bears only negligible mass, no charge and spin $\frac{1}{2} \hbar$.³⁴ Both, positron and electron neutrino share the kinetic energy which is set free in the decay process.

If the positron travels through matter, it slows down by elastic and inelastic collisions. A Positronium is formed upon the encounter of an electron – a situation which can be compared to the one in an Hydrogen atom, since the negatively charged electron orbits around the positively charged positron.³³ Two different states are possible, namely *ortho*- and *para*-Positronium. They differ in parity, as the spins can be coupled parallel as well as anti-parallel. In both cases, an annihilation into gamma-quants takes place. The sum of their energies always equals 1.022 MeV as this represents the rest mass of electron and positron according to $E = mc^2$.

The difference is, that the *para*-Positronium decays into two gamma-quants, emitted in an angle of nearly 180° and an exact energy of 511 keV each, whereas the *ortho*-Positronium decays into an odd number of gamma-quants with varying angles and energies.³³ Both annihilation modes are depicted in Figure 5.

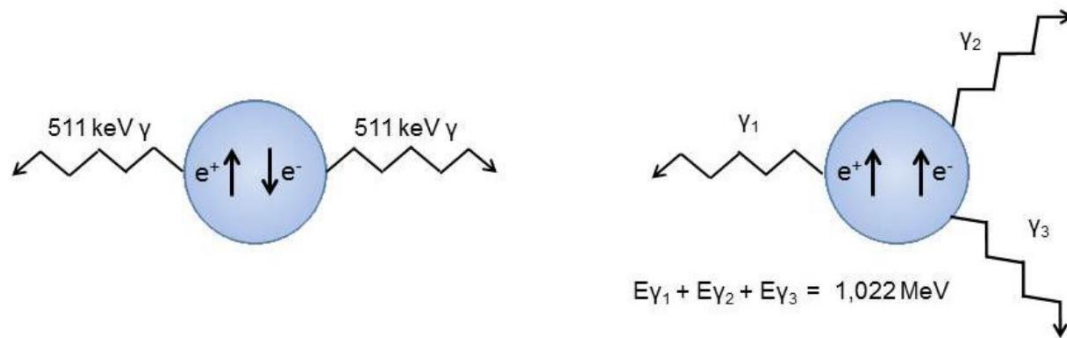


Figure 5: Decay of the Positronium into 2 vs. 3 gamma-quants. Left: *para*, Right: *ortho*.³³

Even though the *ortho*-form of the Positronium is formed initially at about 75%, in condensed matter, it converts into the *para*-form to a very large extent. Finally almost 99% of Positroniums emitted can be used for the coincidence-detection in PET, which relies on the 180° angle and is the base for a very high sensitivity.³³

For the examination of a patient the tomograph is equipped with scintillation detectors in a circular fashion. Only events registered in the same small time frame (few nanoseconds) by opposed detectors are accounted as true. For image reconstruction the site of annihilation is set on the 'line of response' (LOR) between those two detectors. As this is not equal to the decay site, the PET technique exhibits an inherent site uncertainty. Its degree depends on the used nuclide and its beta-energy.³⁵

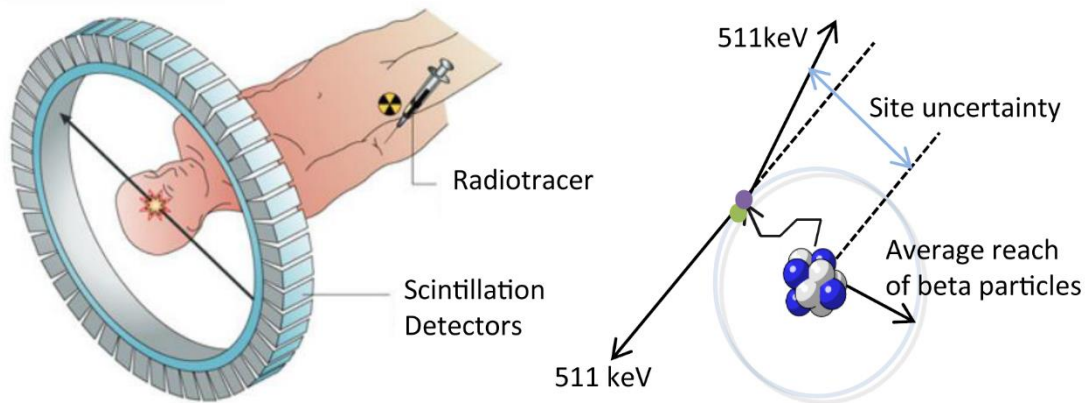


Figure 6: Principle of PET examination (left)³⁶ and site uncertainty (right).

As the obtained image is utterly dependent on the applied radiotracer, the image is highly functional – being the greatest advantage of PET and a drawback simultaneously. The anatomical interpretation can be rather difficult without any morphological information. Therefore, the development of combined techniques like PET/CT and PET/MRI has meant a substantial progress in the field.^{35,37}

The most frequently used PET-Tracer to date is the glucose analogue [^{18}F]FDG (2- ^{18}F fluoro-2-desoxy-*D*-glucose). The high energy consumption of tumour tissue leads to the accumulation of [^{18}F]FDG.³⁸ Below, in Figure 7, an example is shown – comparing the two different tracers [^{18}F]FDOPA and [^{68}Ga]DOTA-TATE in the same patient. It clearly depicts the importance of choosing the best tracer for the visualization of a certain biochemical process. While the primary tumour can be seen in the [^{18}F]FDOPA image (a and c) and the CT image (d), the vast amount of liver metastases is only shown by [^{68}Ga]DOTA-TATE (b and e). Primary tumour and metastases obviously display an altered biology – eventually requiring different therapies – which would not have been detected otherwise.³⁹

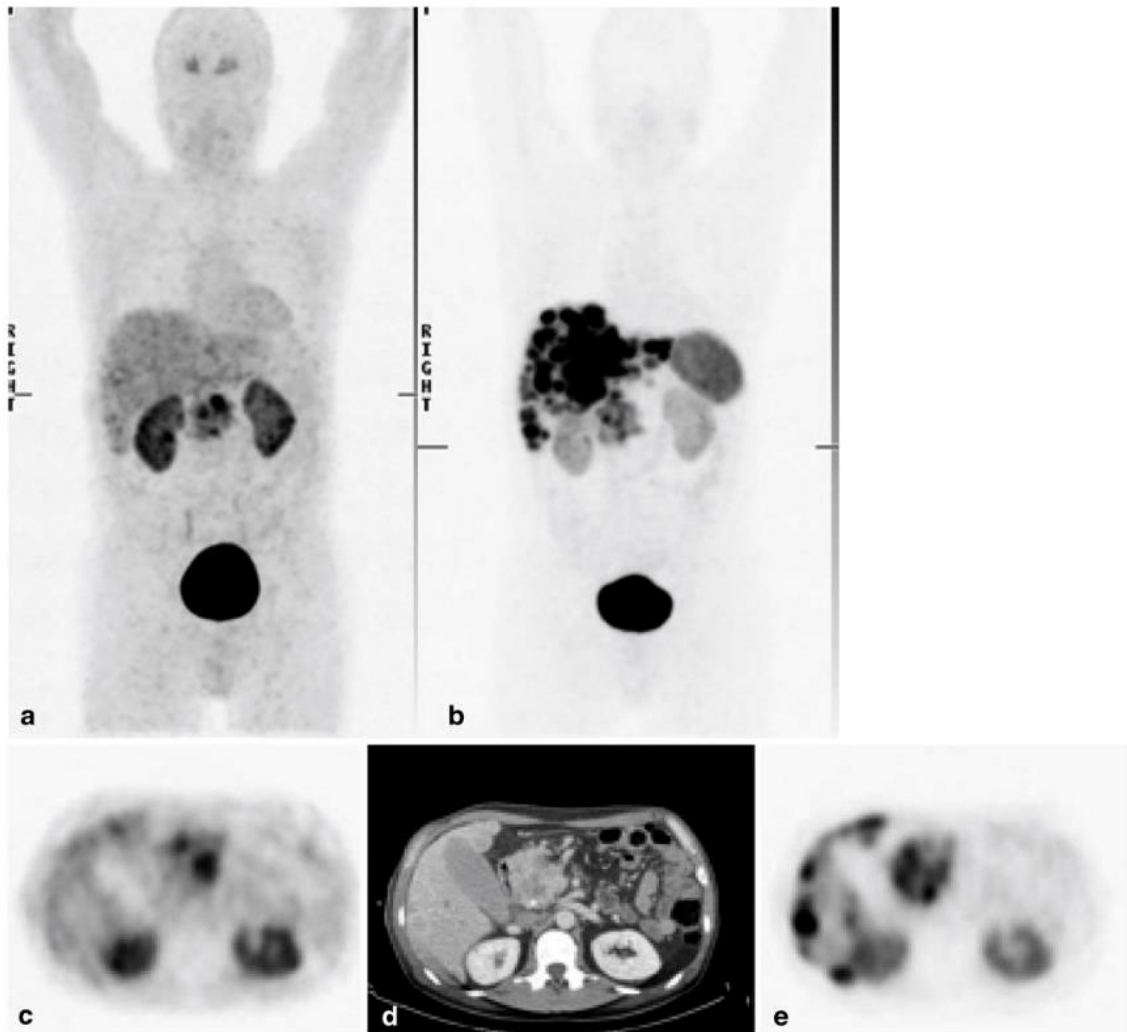


Figure 7: PET image examples. The primary pancreas tumour of the patient is well delineated on the CT image (d) and shows inhomogeneous increased uptake of both $[^{18}\text{F}]\text{-DOPA}$ (a,c SUVmax 3.9) and $[^{68}\text{Ga}]\text{-DOTA-TATE}$ (b,e SUVmax 7.2) while the hepatic metastases were visualized only by $[^{68}\text{Ga}]\text{-DOTA-TATE}$ PET but not by $[^{18}\text{F}]\text{-DOPA}$ PET indicating a different tumour biology of the primary tumour and the metastases.³⁹

I.II.II Single Photon Emission Computed Tomography

On a first glance, the SPECT technique appears to be rather similar to PET – but as it is based on a different nuclear process, some technical changes are required.

As the name states, for this technique nuclides are used which emit only a single photon – unlike the positron-emitters resulting in two photons. The underlying nuclear process is the gamma-decay. It may rather be termed gamma conversion, as the nuclide is not changed in its nucleon composition, but an excited state relaxes into a lower or the ground state, emitting its energy. In principle an excited nucleus has several options for relaxation, including the emission of a single gamma-quant, inner conversion as well as pair production. For pair production the energy difference between excited and ground state needs to be at least the rest mass of the two produced particles which are emitted – i.e. 1.022 MeV as the sum of positron and electron. It is observed relatively seldom. In inner conversion the excess energy is transferred from the nucleus to a shell electron, frequently from the K-shell, which is emitted from the atom and therefore leaves the atom positively charged and initialises further secondary processes such as Auger electron emission.³² The process used for SPECT is the direct emission of a gamma-quant from the nucleus which can be detected by similar scintillation detectors as in PET.

Such an excited state is typically obtained by a preceding α - or β -decay. In most cases the subsequent γ -decay occurs that fast, that it is typically assigned to the mother nuclide. For half-lives > 0.1 s the excited state nuclei are termed meta-stable. In contrast to β -decay processes, the gamma-quant carries the whole decay energy, leading to monoenergetic spectra.³² In SPECT, this allows the simultaneous application of two different tracers, if they are labelled with sufficiently differing nuclides – as they can be discriminated according to their specific energy.⁴⁰ This is obviously not possible in PET measurements where the detected radiation always has the same energy of 511 keV, regardless of the utilized isotope. Typical energies for SPECT nuclides are between 30 and 300 keV.⁴⁰

Compared to PET, in SPECT the site of decay is detected rather than the site of annihilation – giving SPECT a theoretical advantage over PET in terms of site uncertainty. But this advantage remains theoretical, as it is over-compensated by another effect. Due to the fact that only single photons per decay are emitted, a ‘line of response’ cannot be drawn. Therefore, the direction of the detected photons has to be determined in a different way. The use of lead collimators allows the detection of photons coming from a certain angle – all others are being absorbed.⁴¹

The principle can be seen below in Figure 8. It allows the reconstruction of three dimensional images on the one hand, but also the sensitivity and feasibility of quantification are severely reduced on the other hand. The overall site uncertainty remains larger than for PET as well.

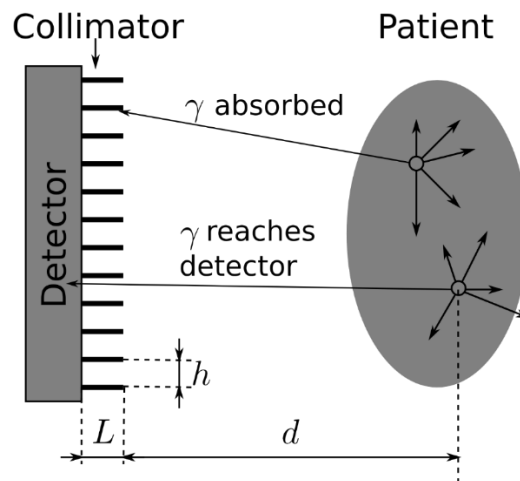


Figure 8: Principle of SPECT Detectors. The Collimator only allows entry of gamma rays from a distinct direction.⁴²

Besides the aforementioned drawbacks, SPECT is a very common technique in nuclear medicine – mainly due to the simple availability of tracers. ^{99m}Tc remains the most widely used nuclide in nuclear medicine as a whole, not only for SPECT.

I.II.III Nuclear Aspects for PET- and SPECT-agents

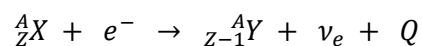
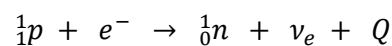
Radiopharmaceutical tracer substances can be divided into two groups: isotopic tracers resemble the exact ligand structure, as an element which is available as PET- or SPECT-isotope is part of the original structure. The second group are analogous tracers – in their cases an alteration of the structure was inevitable in order to introduce the radionuclide.

The isotopes' half-life is obviously a crucial point – if it is too short, chemical modifications are no longer possible after their production. If it is too long, the dose exposure becomes unjustifiable for the patient. The physical half-life of the nuclide should also match the half-life of the biological process. Another important feature is the nuclides' production routes – whether they are produced in a reactor, a cyclotron or are obtained from a radionuclide-generator enhances the availability dramatically (in this order). In Table 3, a choice of typical radionuclides used in nuclear medicine is shown:

Table 3: A choice of typical nuclides for PET and SPECT.^{35,43,44,45,46,47}

Nuclide	$T_{1/2}$	β^+ branching / emission yield [%]	Decay energy	PET / SPECT	Production route
^{15}O	2.03 min	> 99	1.70 MeV	PET	Cyclotron
^{13}N	9.96 min	> 99	1.19 MeV	PET	Cyclotron
^{11}C	20.37 min	> 99	0.96 MeV	PET	Cyclotron
^{68}Ga	67.71 min	89	1.92 MeV	PET	Generator
^{18}F	109.7 min	96.6	0.63 MeV	PET	Cyclotron
$^{99\text{m}}\text{Tc}$	6.006 h	87.2	140.5 keV	SPECT	Generator
^{123}I	13.2 h	83.3	159.0 keV	SPECT	Cyclotron
^{111}In	2.807 d	90.24	171.3 keV	SPECT	Cyclotron
^{201}Tl	3.046 d	94.0	245.4 keV	SPECT	Cyclotron
		26.9	68.9 keV		
		46.0	70.82 keV		
^{67}Ga	3.261 d	20.4	184.6 keV	SPECT	Cyclotron
^{131}I	8.04 d	81.2	364.5 keV	SPECT	Reactor

In the case of PET-nuclides, it is important to consider another point: the branching rate of β^+ -decay versus *electron capture* (EC), its competitive process. The EC does not result in the emission of two 511 keV gamma-quants and is therefore lost for the imaging process.



with p = proton, n = neutron, e^- = electron, ν_e = electron neutrino, X = mother nuclide, Y = daughter nuclide, A = mass number, Z = atomic number, Q = energy released.

It results in the same conversion of a certain nuclide A_ZX into ${}^A_{Z-1}Y$ as it does in β^+ -decay, but the process is a different one. The proton of the nucleus does not decay into a neutron under emission of a positron and an electron neutrino, but instead the nuclei captures an electron from the orbital electrons (generally from the K-shell), emitting only the electron neutrino. In

the case of β^+ -decay, the mass difference between the proton on the one hand and the sum of neutron and positron on the other hand (the latter being heavier) has to be brought up by the energy gained in the conversion. If the reaction energy is less than 1.022 MeV, electron capture remains therefore the only decay option for such nuclei.³² For PET imaging nuclides with a low occurrence of electron capture are therefore preferred.

The widespread use of ^{99m}Tc is based on its simple (commercial) availability via a radionuclide-generator. Also the PET-nuclide ^{68}Ga is obtained in this fashion. Practically, the mother nuclide is fixed on solid phase (column) where it decays into its daughter. The careful choice of a suitable solvent system allows the elution of the daughter nuclide, while the mother remains on the column. While the isotopes along one decay chain typically become more and more stable, building such a generator is only possible in exceptional cases. If the mother nuclide shows a remarkably longer half-life than the daughter, it is possible to 'milk' the generator repetitively in order to obtain the desired daughter nuclide purely.⁴³

These generators are based on the radioactive equilibrium. The production rate of the daughter nuclide (decaying itself) is the following:

$$\frac{dN_2}{dt} = -\frac{dN_1}{dt} - \lambda_2 N_2 = \lambda_1 N_1 - \lambda_2 N_2$$

with the indices 1 and 2 referring to mother (1) and daughter (2) nuclide. N = particle number, λ = decay rate, t = time.

The first part of the equation represents the formation of the daughter, expressed by the decay rate of the mother, while the second part represents the daughters' own decay.³²

Introduction of the decay law $N_1 = N_1^0 e^{-\lambda_1 t}$ for the mother nuclide and subsequent solution of the linear differential equation yields the following correlation for the daughters particle number, depending on time and starting material of mother and daughter at t = 0 (N_1^0 and N_2^0):³²

$$N_2 = \frac{\lambda_1}{\lambda_2 - \lambda_1} N_1^0 (e^{-\lambda_1 t} - e^{-\lambda_2 t}) + N_2^0 e^{-\lambda_2 t}$$

For the radionuclide-generator the second summand can be neglected, as there is no daughter nuclide after separation by means of elution at t = 0. If $e^{-\lambda_1 t}$ is further excluded, the equation can be shortened to³²

$$N_2 = \frac{\lambda_1}{\lambda_2 - \lambda_1} N_1 (1 - e^{-(\lambda_2 - \lambda_1)t})$$

Typically, after about ten half-lives of the daughter the radioactive equilibrium is reached, where the ratio of N_1 to N_2 is stable. This is when the exponential function becomes negligible. It is of note, that the radioactive equilibrium is not an equilibrium in the typical chemical view, where reaction paths are reversible. The radioactive equilibrium is a 'one-way' equilibrium and comparable to a steady state, yielding a constant ratio of mother and daughter, but the daughter is never transformed back into the mother.³²

Two different types of radioactive equilibria are differentiated: the transient and the secular equilibrium. They differ in the ratios displayed by the decay constants of mother and daughter. If the mother's half-live is very long compared to the daughters', the mother's decay can be ignored. Hence, the mother's concentration/particle number can be presumed to be constant. In this case, a secular equilibrium is present.³² The $^{68}\text{Ge}/^{68}\text{Ga}$ -generator used in this work is an example for such a secular equilibrium. In contrast, the $^{99}\text{Mo}/^{99\text{m}}\text{Tc}$ -generator displays a transient equilibrium, where the mother's half-live cannot be ignored anymore.

If the above function (without the exponential function) is further transformed into a correlation for activities rather than particle numbers, the following is true:³²

$$\frac{A_1}{A_2} = 1 - \frac{\lambda_1}{\lambda_2}$$

This explains that in a secular equilibrium (where the ratio of λ_1 and λ_2 tends to 0), the activities of mother and daughter are equal, whereas in a transient equilibrium, the daughter's activity level reaches higher values than the mother. This is of importance for radionuclide-generators as it determines their shelf-live and is an economical factor for research as well as patient care. The $^{99}\text{Mo}/^{99\text{m}}\text{Tc}$ -generator has to be replaced once a week, whereas a $^{68}\text{Ge}/^{68}\text{Ga}$ -generator can be used for about one year.

I.II.IV Organo-chemical and biological aspects for PET- and SPECT-agents

The task for the synthetic chemist is to combine biologically relevant structures with appropriate radionuclides (see Table 3). Due to their very short half-lives only very fast and basic chemistry is possible with ^{15}O and ^{13}N . Covalent bonds can be formed by ^{11}C and ^{18}F and the iodine isotopes

with organic molecules, which allows a variety of reaction types. The most prominent radiosynthesis is the one for [^{18}F]FDG. [^{18}F]fluoride attacks *mannose* triflate nucleophilically and as it undergoes a Walden inversion, the ^{18}F -*glucose* derivative only needs to be deprotected subsequently. The careful avoidance of water and addition of a crown ether as phase transfer catalyst are important, as both improves the nucleophilicity of [^{18}F]fluoride enormously.

On the other hand, many elements that show physically interesting characteristics for imaging purposes, are radiometals. Under physiological conditions any metal-organic species are typically not stable, even if it may be possible to produce them in the first place. Therefore, the usage of chelates is the method of choice for the connection of radiometals with biologically relevant structures.

^{68}Ga forms hydrated $^{68}\text{Ga}^{3+}$ ions in aqueous media at an acidic pH. At a macroscopic scale, with rising pH, first the insoluble $\text{Ga}(\text{OH})_3$ is formed and in basic pH it changes to the gallate $[\text{Ga}(\text{OH})_4]^-$. Nevertheless, the low amounts which are used in radiochemistry, do not allow the observation of a precipitation. But still, a kinetic hindrance of complex formation takes place, which is why labelling procedures are typically conducted at pH 3-4. As a trivalent cation Ga has the electron configuration $[\text{Ar}]3d^{10}$. With the radius in hexadentate coordination of 62 pm, it is classified as a hard acid according to the HSAB concept. Therefore, it requires hard counterparts in its ligands like O or N atoms as donors. Typical donors are carboxylic acids, phenols or amines.⁴⁸

Two well established chelates are DOTA (1,4,7,10-tetra-acetic acid – 1,4,7,10-tetra-aza-cyclo-dodecane) and NOTA (1,4,7-tri-acetic acid – 1,4,7-tri-aza-cyclo-nonane). While NOTA forms the thermodynamically more stable complex (the radius fits better for ^{68}Ga), it needs a branching in its carbon backbone for a connection with any targeting vector (TV) – the N_3O_3 system only contains the exact 6 coordination sites being necessary for complexation and no further functional group. The most prominent branched derivative of NOTA is NODAGA – to be seen in Figure 9. On the other hand, DOTA is an N_4O_4 system – therefore, two of the carboxy functions can be used for derivatization. Another advantage of DOTA is that it allows for complexation of larger cations like ^{90}Y or ^{177}Lu . These radionuclides can be used for therapeutic purposes in oncology – hence allowing a ‘*theranostic*’ approach.⁴⁴

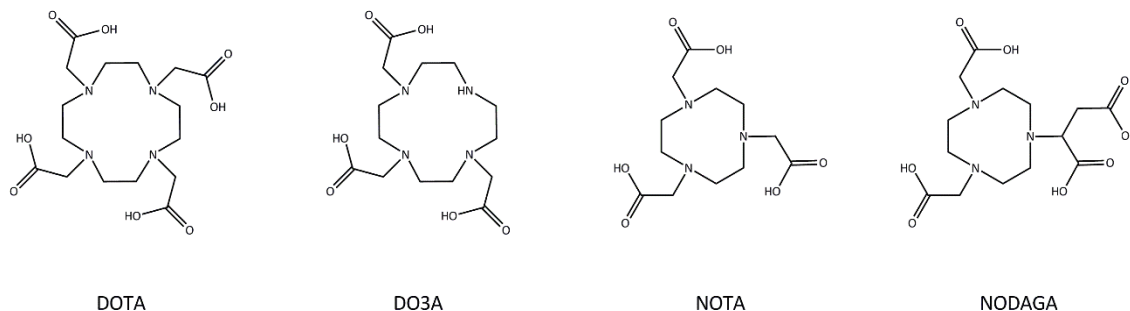


Figure 9: Chemical structures of the chelates DOTA, NOTA and derivatives thereof.

^{99m}Tc can occur in all oxidation states from $-III$ to $+VII$, which makes its complex chemistry more diverse than that of Ga.⁴⁹ From the generator it is obtained as $^{99m}\text{TcO}_4^-$ in saline, which is $+VII$, but many complexes are formed in the oxidation state $+V$. This requires a reduction step prior to the actual complexation. Also several different coordination numbers are possible, ranging from four to seven. As Tc is a softer acid than Ga, other elements have been used as ligands as well: O, N, S and P.⁵⁰ A couple of frequently used chelates are shown in Figure 10.

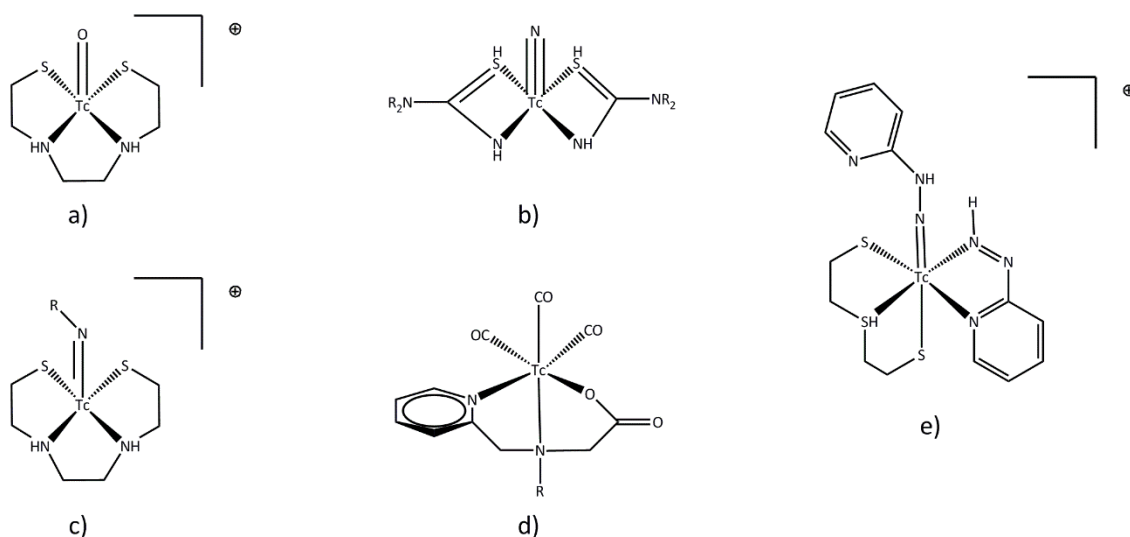


Figure 10: Structures of typical Tc-chelates. A) Tc(V)oxo; b) Tc(V)-nitrido; c) Tc(V)imido; d) Tc(I)tricarbonyl; e) Tc(V)hydrazido.⁵⁰

Once a radiotracer is injected into a patient, its pharmacokinetic behaviour is very important for the quality of the image. For the ideal image, 100 % of the injected activity had to accumulate in the tissue of interest, while the background signal in surrounding tissue would be zero. But of course, the principles of ADME (absorption, distribution, metabolism, excretion) apply to radiotracers just as well as to any other xenobiotic.⁵¹ Excretion of any unbound tracer can either follow the renal or the hepato-biliary pathway. In renal excretion, the compound is filtrated in the renal glomeruli from blood into urine and is thus eliminated from the body. Typically, this is the pathway for small and hydrophilic molecules. In hepatobiliary excretion, the xenobiotic is

taken up by hepatocytes and undergoes biotransformation. In phase I reactions, only oxidative, reductive, hydrolytic and decarboxylating reactions take place.⁵¹ In phase II the compounds are usually conjugated to endogenous hydrophilic substances like glycine, sulphuric acid, glutathione or glucuronic acid.⁵¹ Both phases commonly aim at a hydrophilization of the drug in order to facilitate its excretion. The transformed drug is excreted into bile and therefore secreted to the intestines. From here it can be reabsorbed to the blood or eliminated via faeces.⁵²

The crucial characteristic of a drug, determining its metabolic fate is the lipophilicity. The more lipophilic, the higher the chances for a hepatobiliary excretion. Molecular weight can also influence this, as larger molecules have a tendency towards hepatobiliary excretion.⁵²

With regard to this project – aiming at the obtainment of a highly specific signal in the liver – a high hydrophilicity of the designed drugs is of great importance, as the unspecific background needs to be as low as possible.

I.III Targeted Receptors

In this chapter it will be discussed, which receptors were chosen as targets for the development of a radiotracer, suitable for the imaging of liver fibrosis and fibrogenesis. The integrin $\alpha\beta6$ and the fibroblast activating protein were identified as interesting candidates. Their connection to molecular processes within fibrosis fibrogenesis will be discussed in the following.

I.III.I Integrins

Integrins form a receptor family that connects the ECM with intracellular cytoskeleton components. They are made up of two non-covalently linked hetero-dimers. In vertebrates, 18 different α -subunits and 8 β -subunits are known.⁵³ But they do not form all theoretically possible combinations – only 24 distinct variations are expressed.⁵⁴ The specific combination has an impact on ligand binding, tissue distribution and therefore also their role in certain (patho)physiological processes.

On a molecular base, they usually consist of roughly 1000 amino acids for the α -subunits and about 700 residues for β -subunits. The subunits share homology within themselves, but there is no homology between α - and β -chains.⁵³ The possible combinations can be seen in Figure 11, divided into the four different ligand classes. The most prominent ones, are those recognising the RGD motif (Arginine-Glycine-Aspartic Acid).

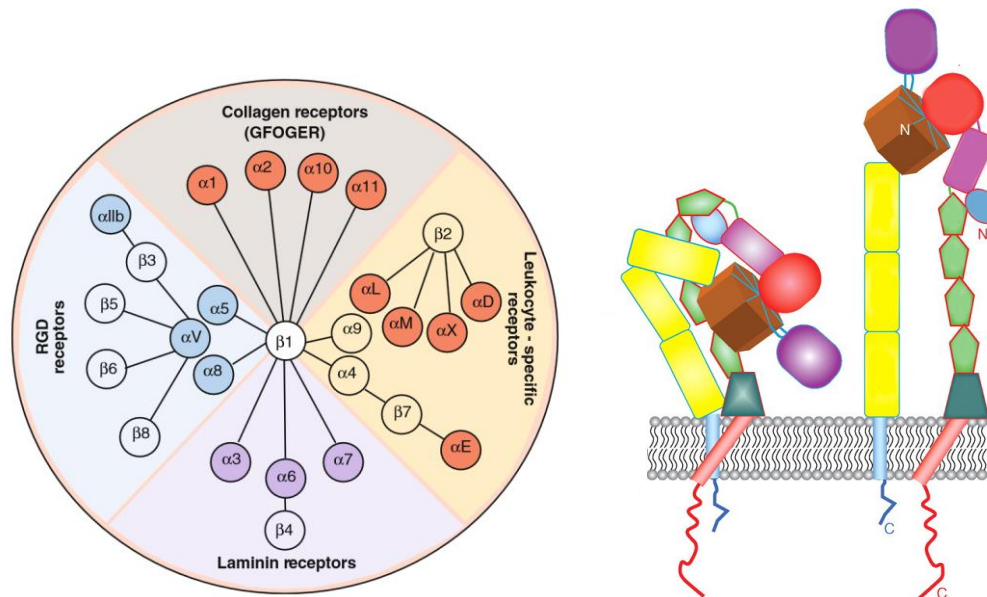


Figure 11: Left: Combinations of α - and β -chains, sorted by ligand specificity.⁵³ Right: Bent (rather inactive) and upright (presumably active) conformation of integrins.⁵⁴

Integrins are involved in bidirectional signalling processes across the membranes: ‘outside-in’ as well as ‘inside-out’. By ‘outside-in’ signalling, processes like gene expression, cell cycle and cytoskeletal reorganisation are affected.⁵⁵ In ‘inside-out’ signalling, integrins become activated into a form that binds its ligands easier.⁵⁵ Structurally, the largest part of both chains lies extracellular, whereas only a small portion remains intracellular. This short tail does not display any enzymatic activity but is prone to dynamic phosphorylation which directs assembly of downstream effectors like serine/threonine-protein-kinases, tyrosine-kinases, adaptor proteins and stress fiber proteins.⁵⁵ The extracellular part shows different activity states: While the bent form is usually observed in crystal structures, some electron microscopy data suggests an upright conformation with functional relevance.⁵⁴

Due to their diversity, integrins are targeted for quite a number of different indications. Thrombosis, multiple sclerosis, cancer, stroke, ischemia, dry eye, conjunctivitis, immunosuppression, Crohn’s disease, inflammatory bowel disease and ulcerative colitis – to name only those with approved and phase III drugs.⁵⁶ It is therefore necessary to discuss with more detail the specific integrin chosen for this project.

I.III.I.I Integrin $\alpha_v\beta_6$

The integrin $\alpha_v\beta_6$ is very rarely expressed. In healthy adult tissue the expression rate is low to undetectable.⁵⁷ Generally, it becomes up regulated in processes of tissue remodelling. Therefore, it can be found during embryogenesis, tumorigenesis as well as in wound healing processes.⁵⁸ Unsurprisingly, it is highly up regulated (up to 90fold) in fibrotic processes, as this represents excessive wound healing.⁵⁸ In a fibrotic liver, it is solely expressed by activated cholangiocytes – namely the epithelial cells of the bile ducts.⁵⁸

$\alpha_v\beta_6$ binds to the RGD motif in ECM components like fibronectin, tenascin-C and vitronectin. But it also binds the latency-associated-peptide (LAP) of TGF- β 1 and TGF- β 3. Furthermore, the foot-and-mouth-disease virus (FMDV) and the coxsackie virus 9 (CAV-9) are known ligands to $\alpha_v\beta_6$.⁵⁹

The molecular connection to fibrogenesis can be explained via the binding and activation of LAP of TGF- β 1. When TGF- β 1 is released from its complex with LAP, it can trigger surrounding myofibroblasts to continue producing ECM. Cholangiocytes and myofibroblasts additionally find themselves in a positive feedback loop of growth factors and cytokines, which results in an ever-continuing progression of fibrosis.¹³ This is what makes $\alpha_v\beta_6$ a very interesting target for liver fibrosis imaging.

I.III.II Proteases

Proteases are a much larger protein family than integrins. While there are only 24 subtypes for the integrins, there are over 700 human proteases.⁶⁰ They all have in common the catalysis of the same reaction: i.e. the hydrolysis of peptidic bonds.⁶¹ This is necessary in order to break down proteins into their parts – the amino acids. But they do not only have such degradation tasks – the cleavage of signal peptides very often leads to an activation or other hydrolytic reactions are needed to allow post-translational modifications.

The sheer amount of different proteases already shows, that their structures, tasks and occurrence are very diverse. The MEROPS database started to classify proteases into clans and families in 1996.⁶² The clans are sorted according to their catalytic mechanism – there are aspartic-, cysteine-, glutamic- and metallo-peptidases as well as asparagine-, serine- and threonine-peptidases. Additionally there are clans of mixed catalytic type (cysteine, serine and

threonine) and a couple of unclassifiable individuals.⁶³ Families within the clans are sorted for homologies.

One of the largest clan in humans are the serine-proteases. They make up about one third of all peptidases.⁶⁴ The clan is named after the nucleophilic residue which attacks the carbonyl within the peptide. Very often, the catalytic serine finds itself in the 'catalytic triad' of Asp-His-Ser.⁶¹ This combination enhances the nucleophilicity of the serine and therefore supports the reaction. It was found for the first time by David Blow in the structure of chymotrypsin.^{61,64,65}

The following chapter will discuss in further detail the Fibroblast Activating Protein – a serine protease.

I.III.II.I Fibroblast Activating Protein

The Fibroblast Activating Protein (FAP) is also called seprase, which stands for *surface expressed protease*. This implies the most frequent expression site – it is a membrane protein. But also the soluble antiplasmin cleaving-enzyme (APCE) has been identified as an isoform of FAP.⁶⁶ They share the ability to cleave post-proline peptidic bonds, which is rare among proteases. Due to their circular fashion, proline residues require highly specialized enzymes in order to cleave them. In many cases terminal proline residues even seem to prevent protein degradation.⁶⁷

Similar to the integrins FAP is also a dimer – but in this case it is a homodimer instead of a heterodimer. The crystal structure has been resolved⁶⁸ and shows a large extracellular portion. The membrane-spanning and intracellular parts are very small. Figure 12 shows the dimeric extracellular part of FAP. Interestingly, the monomeric form does not show any catalytic activity, even though the catalytic centres do not interact with the other dimer.⁶⁷

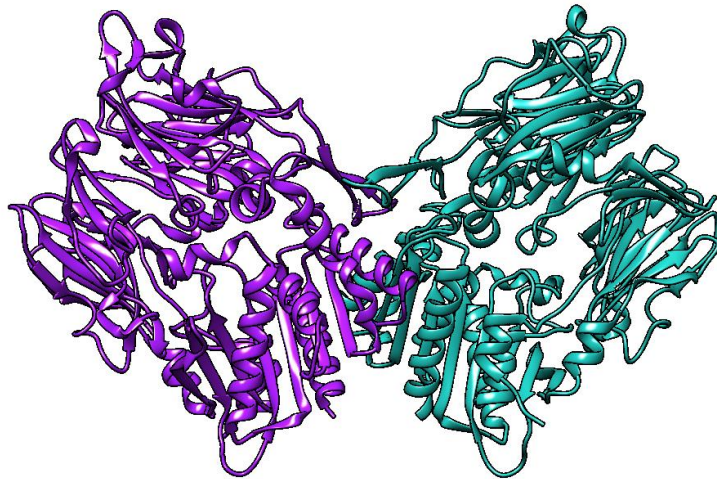


Figure 12: Structure of the extracellular part of FAP. PDB entry 1Z68.⁶⁸

Similar to $\alpha_v\beta_6$, seprase is not expressed in normal adult tissue. It can be found in fetal mesenchymal tissues, and a number of cancer types. Those include colorectal, breast, ovarian, bladder, and lung carcinomas. But also in wound healing processes and scar formation it is expressed.⁶⁷ Furthermore, FAP has been found in idiopathic pulmonary fibrosis,⁶⁹ as well as liver fibrosis. In this case it is expressed by hepatic stellate cells⁷⁰ – being the ones that produce the excessive ECM.

Which role FAP plays in fibrotic processes is not quite clear. Among its ligands are gelatine and thermally degraded collagen type I and IV. It has been concluded that seprase needs to work together with other peptidases in order to break down ECM.⁶⁷

Obviously, in fibrotic patients this does not happen with sufficient efficiency. But its specific expression in pathological conditions makes it an ideal target for imaging approaches.

I.III.III Affinity Assays

When a ligand is designed for a certain receptor, it is necessary to investigate their interactions with each other. According to the law of mass action, the receptor [R] and the ligand [L] react to a receptor-ligand complex [RL].⁷¹



When an equilibrium state is reached, the equilibrium constant K is the ratio of k_{on} (rate constant of the association) and k_{off} (rate constant of the dissociation):⁷¹

$$K = \frac{k_{on}}{k_{off}} = \frac{[RL]}{[R] * [L]}$$

The wider used parameter to express the affinity of a ligand to a receptor is the equilibrium constant for the dissociation reaction, K_d .⁷¹

$$K_d = \frac{k_{off}}{k_{on}} = \frac{[R] * [L]}{[RL]}$$

If $[RL]$ is measured for varying concentrations of $[L]_{total}$ and stable concentrations of $[R]_{total}$, the binding curve will approach a maximum value – which cannot be exceeded by higher ligand concentrations. This represents the total number of available receptors, i.e. the sum of $[R] + [RL]$. K_d can also be obtained from such a curve – when 50% of the receptor are occupied $[R]$ equals $[RL]$. In this case K_d is equal to $[L]$ and it can be read out easily from the plotted data (cf. Figure 13).⁷²

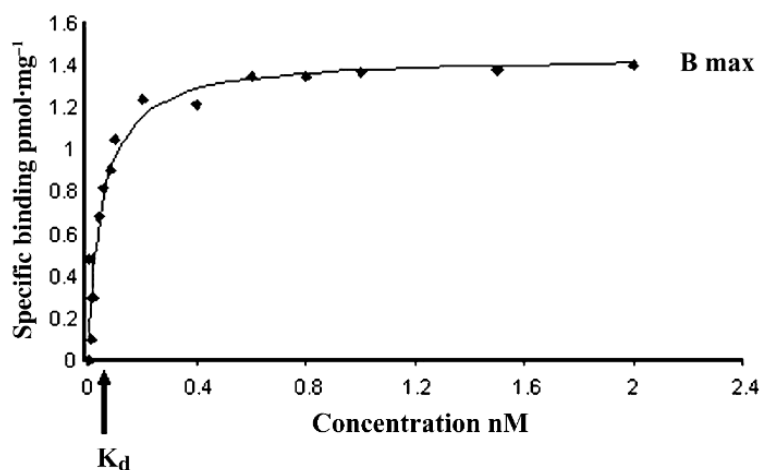


Figure 13: Typical curve of a ligand binding assay. The ligand concentration at the 50% value of B_{max} is equivalent to the K_d value.⁷²

While K_d is a thermodynamically constant value for a given Receptor/Ligand pair, there is another value which is widely used for indicating affinities. Sometimes it is easier to investigate the potential of a substance to inhibit a second ligand in its binding with the receptor. In these competitive assays the so-called IC_{50} values are obtained – which represent the concentration of an inhibitor necessary in order to inhibit 50 % of the other ligands binding. Therefore, the ligand's concentration is kept stable, while the inhibitors concentrations are varied over a wide range. Obviously, IC_{50} values are difficult to compare among each other – as they depend on the used ligand as well as on its concentration. Cheng and Prusoff have presented an equation in 1973, which puts IC_{50} and K_i in a relationship:⁷³

$$K_i = \frac{IC_{50}}{1 + \frac{[L]}{K_d}}$$

In this notation K_i represents the K_d value of the inhibitor, while the ligand concentration $[L]$ and K_d belong to the known ligand.

To detect the different concentrations of reaction partners a variety of techniques can be used. The use of radioligands is relatively straightforward, but also gel electrophoresis, ELISA or immunoblots can be used for this purpose. If the components have interesting fluorescence/UV features, also direct optical measurements can be carried out.⁷¹

With respect to this work, the principle of ELISA (Enzyme Linked Immuno Sorbent Assay) measurements will be outlined.

In general, ELISAs are based on immunological reactions. An antibody linked with an enzyme is always the last step in order to detect the compound of interest. The detection is carried out photometrically – the enzyme converts its substrate into a product, which can be measured at a certain wavelength.⁷⁴ The extinction ϵ_λ correlates with the concentration c of the substance according to the Lambert-Beer law:

$$E_\lambda = \lg\left(\frac{I_0}{I_1}\right) = \epsilon_\lambda * c * d$$

The thickness d of the system and the extinction coefficient ϵ_λ are easily kept constant, which leaves the extinction only dependent on the concentration c .

But before this is actually measured, a (couple of) immunological reaction(s) have to take place. The solid phase (96 well plates are widely used) is always coated with either an antigen or antibody, which can subsequently react with a compound in the tested fluid. After a certain incubation time, the fluid is washed off and the next antibody can be added.⁷⁵

Three different types of ELISAs are distinguished: The direct, the indirect and the sandwich ELISA. In the direct ELISA an antigen is coated to the wells, and in the next step its antibody is added in an enzyme-labelled version. Additionally, the fluid to be tested is added – if it contains the antigen, less antibody will bind than in the reference sample.⁷⁵

The indirect ELISA uses more steps, it is useful to detect antibodies in sample fluids. Also an antigen is coated to the wells. If the sample contains the antibody it will bind to the well.

Subsequently, the detection antibody is added which recognizes the sample antibody and carries the enzyme relevant for detection.⁷⁵

The third type is the so-called sandwich ELISA – in this case, an antibody is coated to the surface and the sample antigen will bind to this. Then again an antibody is added – which causes the ‘sandwich’ image – either carrying an enzyme already, or a secondary antibody is needed on top.⁷⁵

ELISA assays are well established in clinical routine and available as commercial kit systems. Nevertheless, it may be necessary to develop one’s own system.

I.IV Molecular Modelling

Computer simulations are nowadays able to give important insight into scientific problems, difficult to understand. With molecular modelling methods, tools for the prediction of characteristics and behaviour of the studied molecules are at hand. Important insight can be gained for example in structural, surface and thermodynamical properties. Also the interaction of different molecules can be investigated and predicted. In the biochemical environment, the investigation of protein folding, enzyme catalysis or conformational changes can lead to important understandings.

Generally, molecular characteristics and behaviour rely on the Schrödinger equation:⁷⁶

$$\hat{H}\Psi = E\Psi$$

With \hat{H} being the Hamiltonian operator, Ψ the wave function and E the particle’s energy. This is valid for a steady state, whereas the time-dependent version of the Schrödinger equation is as follows:⁷⁶

$$\hat{H}\Psi = i\hbar \frac{\partial \Psi}{\partial t}$$

A precise solution of this equation is only possible for very small systems like the hydrogen atom.⁷⁶ For any larger system it is necessary to include approximations. With regard to this, one can differentiate between *ab initio*, semi-empirical and empirical methods.

I.IV.1 *Ab initio* and semi-empirical methods

Ab initio methods are the most exact quantum mechanical methods available but require high computational efforts. They do not rely on any experimental input data, but are purely mathematic. Their major drawback is the enormous computational demand, which limits it to relatively small systems.⁷⁷

An approximation which underlies these methods as well as all the following, is the Born-Oppenheimer approximation.⁷⁸ It states that nuclei and electrons can be considered separately from each other. This is based on their large mass difference – therefore electrons move significantly faster than nuclei and relax into the ground state under nuclear motion. Consequently, the time-independent Schrödinger equation can be solved solely for the electrons, before the thus obtained energy is used to calculate the nucleus' motion.⁷⁷

As a way to describe the molecular orbital wavefunctions, the Slater determinant is used. It introduces the principles of anti-symmetry (electrons are indistinguishable) and Pauli (no two electrons can have the same quantum numbers) to the calculation. The wavefunction gets the form:

$$\Psi_{mol} = \frac{1}{\sqrt{N!}} \begin{vmatrix} \chi_1(1) & \chi_2(1) & \cdots & \chi_N(1) \\ \chi_1(2) & \chi_2(2) & \cdots & \chi_N(2) \\ \vdots & \vdots & \ddots & \vdots \\ \chi_1(N) & \chi_2(N) & \cdots & \chi_N(N) \end{vmatrix}$$

By use of the Hartree-Fock theory the best wavefunction can be found. It assumes that the better the wavefunction, the lower the energy will be. Therefore, the condition $\delta E = 0$ is introduced for the iterative approach. The Hamiltonian in Hartree-Fock theory contains terms for interactions with the cores, of coulombic nature and for exchange.⁷⁷ For the coulombic term it is of note, that the electron is seen as moving in an average potential of the other electrons, but there is no direct correlation. This is the main weakness of the theory which has been addressed in later developments.⁷⁷

Another important point in *ab initio* calculations is the choice of the basis sets. The functions used to describe the orbitals are Gaussian functions of the general form $x^a y^b z^c \exp(-\alpha r^2)$, which eases the computation significantly, as two Gaussian functions can be easily expressed as one Gaussian function.⁷⁷ It is generally presumed that at least three Gaussian functions are necessary to describe one orbital. The STO-3G basis set is therefore the minimal one, but more

sophisticated sets have been developed – polarizable functions, for example, are able to introduce effects of neighbouring atoms.⁷⁷

The semi-empirical methods differ from *ab initio* methods insofar, as they are not solely based on mathematics. They contain parameters either derived from *ab initio* calculations or from experimental data. In order to minimize computational demand, semi-empirical methods explicitly consider only valence electrons and leave out the inner shells.⁷⁷ This follows the assumption that only valence electrons are of importance for the chemical behaviour/reactions of the studied compounds. While the first methods were based on parameters from *ab initio* calculations (of moderate quality), the first method containing experimental data was MINDO/3.⁷⁹ This was followed by MNDO,⁸⁰ which contained parameters for more elements, but transition metals were not yet included as the basis set only contained functions for s- and p-orbitals. Another advancement was the introduction of monatomic parameters instead of diatomic ones. Nevertheless, MNDO carried the problem that it overestimated repulsion for atoms which were separated by the sum of their vdW (van der Waals) radii.⁷⁷ This repulsion problem was overcome by the introduction of the Austin Model 1 (AM1).⁸¹ The next parameterization for MNDO was released with the PM3 method – and since then the nomenclature was kept as today the latest version is PM7. Transition metals are now included in the method and PM7 was explicitly improved for non-covalent bonds.⁸²

The success of these methods lies mainly in its simple availability via programs like MOPAC, which is available free of charge for academic purposes.⁸³

I.IV.II Molecular Mechanics

In the next step of simplifications, the quantum theoretical calculations are abolished altogether. Molecular Mechanics are a solely empiric method, which neglects electronic effects.⁷⁷ This is only possible due to the already mentioned Born-Oppenheimer approximation.

Instead, the method works with force fields – they contain empirical information about bonds, angles, torsions and non-bonded interactions (electrostatic as well as vdW) which sum up to the potential energy.⁷⁷ Important in the development of such a force field is its transferability. Parameters like bond lengths are derived from a set of experimentally known structures – but

they will be used in order to predict different compounds. In many examples it is possible to obtain very good results – even for macromolecules, if the parameterization was carried out on small molecules. But one has to bear in mind that the prediction of a certain property may fail if it was not included in the parameterization process. The choice of the correct force field is therefore crucial for the outcome of one's study.⁷⁷

Force fields normally differentiate for different 'atom types'. In the case of carbon, for example, different data for sp²- or sp³-hybridized atoms is stored in a force field and subsequently they will be treated differently. Examples for frequently used force fields are MM2/MM3/MM4^{84,85,86} for small molecules and AMBER⁸⁷ for proteins and nucleic acids. A force field containing the whole periodic table is the universal force field UFF.⁸⁸

I.IV.III Molecular Dynamics

In Molecular Dynamics on the other hand, a whole new dimension is introduced into the calculations. Still, force fields are used for the description of atom types, bonds, angles, torsions and non-bonded terms. But the application of Newton's law of motion to the studied system requires the incorporation of time.⁸⁹

$$F = m * a$$

Within Newton's equation this is realized in the term of acceleration a with the unit m*s⁻². As a result, a trajectory of the moving molecules is obtained. Each set of coordinates is dependent on its predecessors, they are connected via time.⁷⁷ In comparison to Molecular Mechanics, the focus shifts from a rather static energy minimization towards the motion of molecules – may that be solvent or other molecules of interest.

To obtain such trajectories, finite difference methods are used: the problem is split into very small time steps (femto-seconds) for which constant forces are assumed. Initial input therefore has to contain information about conformation and velocity (temperature) of the system.⁷⁷

To subsequently calculate the trajectory algorithms are used which all share one characteristic: They are based on Taylor series for position and dynamic properties like velocity and acceleration:

$$\mathbf{r}(t + \delta t) = \mathbf{r}(t) + \delta t \mathbf{v}(t) + \frac{1}{2} \delta t^2 \mathbf{a}(t) + \frac{1}{6} \delta t^3 \mathbf{b}(t) + \frac{1}{24} \delta t^4 \mathbf{c}(t) + \dots$$

$$\mathbf{v}(t + \delta t) = \mathbf{v}(t) + \delta t \mathbf{a}(t) + \frac{1}{2} \delta t^2 \mathbf{b}(t) + \frac{1}{6} \delta t^3 \mathbf{c}(t) + \dots$$

$$\mathbf{a}(t + \delta t) = \mathbf{a}(t) + \delta t \mathbf{b}(t) + \frac{1}{2} \delta t^2 \mathbf{c}(t) + \dots$$

$$\mathbf{b}(t + \delta t) = \mathbf{b}(t) + \delta t \mathbf{c}(t) + \dots$$

In this case, \mathbf{v} (velocity) is the first derivative of the position \mathbf{r} , \mathbf{a} the second derivative (acceleration), \mathbf{b} the third derivative, and so on.

Again, in most molecular dynamics simulation some important approximations are made. Those are periodic boundary conditions, non-bonded cut-offs and the Particle Mesh Ewald method for electrostatic interactions.⁷⁷ For simulations in explicit solvent periodic boundary conditions are especially useful. Instead of using a large bulk of solvent, the system is placed in a cell which is infinitely mirrored in all Cartesian directions. Therefore, a much smaller system can be computed while the molecules experience forces as if in a larger bulk system. Molecules leaving the cell are replaced by the same molecule entering at the opposite side of the cell.⁷⁷

Cut-offs can be set for non-bonded interactions, which are computationally very demanding. Each added atom multiplies the computational demand, as it interacts theoretically with every already existing atom in a non-bonded fashion. But according to the Lennard-Jones potential, these effects become negligible with increasing distance:⁷⁷

$$V = 4\varepsilon \left\{ \left(\frac{\sigma}{r} \right)^{12} - \left(\frac{\sigma}{r} \right)^6 \right\}$$

With the introduction of a cut-off value, interactions for longer distances can simply be set to zero and not included into the calculations. The value should not exceed half of the periodic cell to make sure, no atom 'sees' any other atom double. A typical value for the cut-off is 10 Å.⁷⁷

Electrostatic forces, decaying only as r^{-1} have to be treated differently. By use of the Ewald summation, those forces can be separated into short range and long range forces. As both terms converge, they can be truncated and thus result in shorter calculation times.^{90,77}

I.IV.IV Homology Modelling

When no crystal structure of a protein/receptor of interest is available, but only its sequence – homology modelling is an option to obtain a fairly realistic model in the meantime. The model is then built upon a given X-ray structure of a homologous protein. In order to obtain a good model the sequence homology between target and template sequence should range at least between 40 – 50 %.⁹¹ The search for an appropriate template structure for one's purpose as well as the exact sequence alignment are crucial for the quality of the resulting model.

I.IV.IV.I Sequence Alignment

An alignment of two or more sequences (DNA, RNA or Proteins) is the assigning of matching amino acids or bases while their orders remain unchanged. The occurrence of gaps and insertions is intentionally allowed.

Already simple examples⁹¹ like the sequences *gctgaacg* and *ctataatc* allow the formation of several different alignments:

```

— — — — — g c t g a a c g      g c t g a a c g      g c t g a — a — — c g
c t a t a a t c — — — — —      c t a t a a t c      — — c t — a t a a t c

```

```

g c t g — a a — c g
— c t a t a a t c —

```

The upper left alignment does not convey any information about similarity, the upper middle alignment does not contain any gaps, which the upper right one does. The most useful alignment in this case would probably be the lower one. This example shows quite simply, that for longer systems it is essential to establish a system how to decide which alignment is the best one possible.

First of all it is presumed, that for the alignment of two sequences it is possible to convert one into the other by a stepwise application of one of three operations: substitution, insertion or deletion. It is usually possible to follow different paths in order to get to the same result – which

represents the different alignment possibilities. Each operation is assigned with a certain score – later allowing to differentiate which path was found to be the best one.

The scoring scheme acknowledges the fact that certain substitutions occur more frequently than others. The first scoring schemes classified the amino acids according to their physico-chemical properties and assigned higher scores to residues out of the same class. This was followed by the first investigation on statistical frequencies of substitutions in known protein sequences. The PAM matrices by M.O. Dayhoff were used for scoring since the 1970s.⁹² Later, in 1992, the BLOSUM matrices were developed⁹³ – as they are based on a larger sequence database, they soon replaced the PAM matrices.

A last thing to be integrated in the score is the insertion/deletion of a residue. The ‘gap penalty’ for a newly inserted gap is usually set higher than that one for the prolongation of an existing gap.

An algorithm to find the actual best alignment has been developed by Needleman and Wunsch⁹⁴, which’s details go beyond the scope of this introduction. In short, it uses the so-called *dynamic programming*, which produces a matrix with one sequence in the first row and the other in the first column. Scores for each operation are assigned within the matrix – by means of tracing back only the highest scores, the optimal alignment can be found.⁹¹ With this procedure a global optimum is found – but there may result several different alignments with the same score. The biological signification has to be assessed by the scientist.

For the comparison of only two sequences this is a very good manner to produce an alignment of high quality. If a sequence database is to be searched for similar proteins/genes, this approach consumes far too much computation capacity. Therefore, a simpler approximation is used. Typically a small integer k is chosen and all sections of k -residues in the target sequence are searched within the whole database. Sequences in which several k -sections are found are of interest and applied to a simplified algorithm which results in actual alignments. This procedure is very successful in finding closely related sequences – whereas it frequently fails to find rather distant relationships.⁹¹

I.IV.IV.II Constructing the Model

Once the alignment is set, one can approach the task of obtaining the actual model. In general, the first step is to obtain the coordinates of a backbone chain. The C α – atoms can be copied relatively easy from the template structure for those residues which are well aligned.⁷⁷ But they can also be obtained by the method of spatial restraints. The template is used to construct geometric distance restraints, from which in turn, a backbone chain can be calculated.⁷⁷

Insertions and deletions are treated subsequently. They can either be modelled *ab initio* or by searching the databases for similar sequence blocks – if successful combinations are found, the loops can be modelled in a similar fashion as the first step.⁷⁷ The loop conformations should have low internal energies and should not interact unfavourably with another part of the protein. Parameters for the database search are chain length, the similar spatial distance of first and last amino acid and eventually a homology test.⁹⁵ When the loops are constructed without database support, a way to minimize computational time is to start from both ends – and only put together the fragments in the middle.⁹⁵

In a last phase, the side chains are added to the model. Again, they can be copied easily for identical amino acids, while they have to be predicted for differing residues.⁷⁷ From the examination of X-ray structures, it is known that certain amino acids prefer certain conformations of their side chains (rotamers).⁹⁵ Such preferences are again linked to typical backbone conformations, which makes it possible to assign probable side chain conformations. The best combination is found by scoring according to an energy function. In any way – the backbone conformation is kept fixed during this step.⁷⁷

I.IV.IV.III Refinement

A problem during this process is obvious: the correct backbone conformation is necessary to predict the correct rotamers. On the other hand, the side chains affect the backbone conformation, but those two components are not modelled at the same time. Therefore, many initial structures are of a relatively high energy.⁷⁷ It is necessary to minimize it, but unfortunately the classical force fields are not of enough accuracy for such large systems – the energy minimization process can introduce more mistakes than it solves.⁹⁵

There are a few ways around this problem – one option is to use quantum force fields. The usage of quantum chemistry introduces large computational time demands, especially molecules as big as proteins. Another option is the use of self-parameterizing force fields.⁹⁵ This results in much better minimizations but is equally computationally demanding, as it is an iterative process of parameter change – minimization – check if improvement was made – parameter change etc. A rather straightforward approach is to run a molecular dynamics simulation of the model. The idea behind this is, that the protein folding process is mimicked and it will find its true structure during the simulation.⁹⁵

In any way, the results always have to be checked carefully before any further work is performed with the final model.

II. Aims and Scope

The aim of the project was to develop a radiotracer, which could potentially be used as an indicator of liver fibrosis progression / liver fibrogenesis. For this purpose, it is necessary to identify a target structure in the body, related to the pathological process. As described before, the integrin $\alpha_v\beta_6$ as well as the protease Fibroblast Activating Protein (FAP) represent promising candidates. The main focus of this work lies on the integrin $\alpha_v\beta_6$, while the research for targeting the FAP has just been started.

With identified target structures, next it is necessary to find a motive which is known for good binding characteristics to the respective receptors.

In the case of $\alpha_v\beta_6$, the ligand EMD527040 was identified as such.^{96,97} Its structure is shown in Figure 14, and it is known for high affinity (6 nM) and high selectivity over other integrins (9500 nM for $\alpha_v\beta_3$ and >10.000 for $\alpha_v\beta_5$).⁹⁸

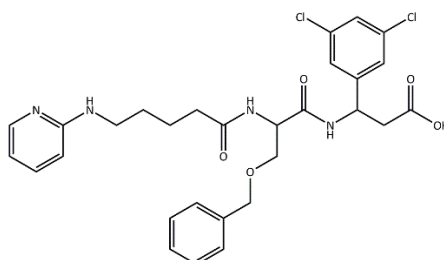


Figure 14: Structure of EMD527040, a highly specific and selective ligand of $\alpha_v\beta_6$.

It has shown antifibrotic potential – in bile duct ligated rats as well as Mdr/-2- knock out mice, the increased collagen deposition could be lowered by 40 – 50 % through doses of 20 mg/kg/day and 60 mg/kg/day over 4 weeks. Furthermore, fibrogenic genes were down- and fibrolytic genes were up-regulated.⁹⁸

First attempts have been made to use this compounds as radiotracers. EMD527040 was derivatized via a hexyl spacer and mounted on an adamantane backbone as mono-, di- and trimer by Schuppan et al.⁹⁹ Those structures can be seen in Figure 15. Being precursors for labelling with ^{99m}Tc , herein they are named **TC1**, **TC2** and **TC3**.

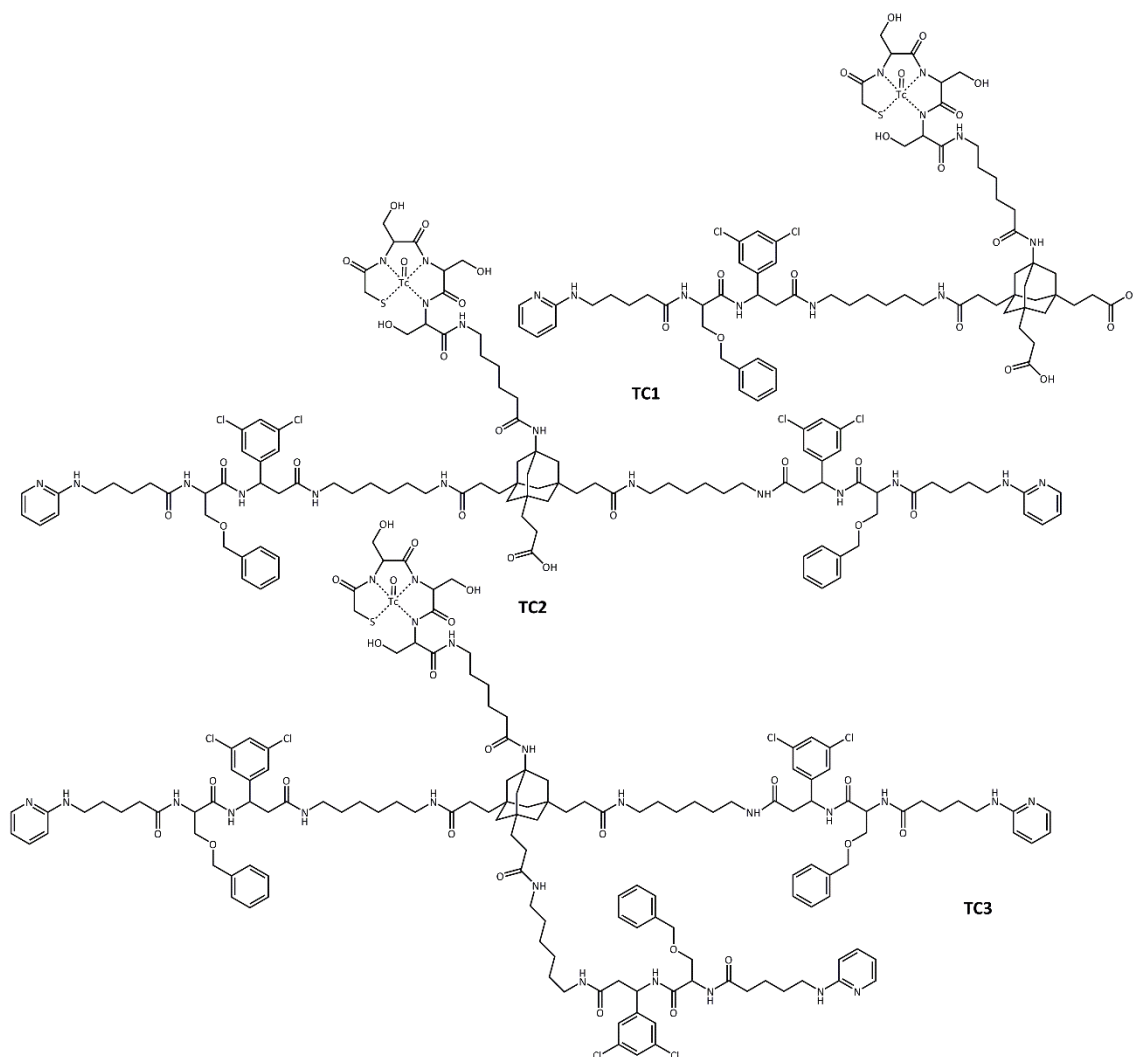


Figure 15: Structures of TC1, TC2 and TC3 - ^{99m}Tc -labelled mono-, di- and trimers of EMD527040.⁹⁹

The results obtained from these ligands were quite promising. The compounds showed affinities ranging between 10.7 nM and 2.5 nM for the monomer and the trimer, respectively. For experiments in healthy and *Mdr/-2*- knockout mice, a signal/noise ratio of >2 was observed for the trimer. This was interpreted as proof of concept, that liver fibrogenesis imaging via $\alpha_v\beta_6$ is feasible, but the compounds' *in vivo* behaviour still needs improvement. One hypothesis explaining the low signal/noise ratio could be the high lipophilicity of the compound – the adamantane backbone combined with the hexyl spacers, induces quite a large lipophilic moiety. This would be prone to unspecific retention in the liver.

Therefore, the scope of this project was the development of more hydrophilic radiotracers, based on EMD527040. Furthermore, the advantages of PET (mainly the option of exact quantification and high spatial resolution) over SPECT were meant to be used, which is why the use of the positron emitting radionuclide ^{68}Ga was planned. Its commonly used chelators like

DOTA and NOTA display a much higher hydrophilicity and could in this way address the issue of lipophilicity 'in situ'.

Another aim of this work was the establishment/development of affinity assays for our compounds. The use of HT-29 and 603B cells is being investigated as well as the purified and immobilized integrin $\alpha_v\beta_6$.

The use of the ELISA method for a non-radioactive analytical method will be tested on the basis of endogenous ligands. For this purpose, fibronectin was used in its biotinylated form. Also, the latency associated peptide of TGF- β 1 was used with an appropriate antibody pair. The feasibility of these methods was investigated.

Furthermore, during the accomplishment of this work, the question about the nature of the binding mode of EMD527040 to the integrin $\alpha_v\beta_6$ arose. Since no crystal structure of the receptor (integrin) is available, but only for the homologous integrin $\alpha_v\beta_3$, the methods of homology modelling were meant to be applied. Once a successful model is obtained, it was intended to be used for investigations on the question which structural feature of a compound actually make it a good binder for $\alpha_v\beta_6$. The use of molecular docking software will be used for this purpose.

As mentioned before, also the fibroblast activating protein (FAP) displays a good candidate as a target structure for molecular imaging of liver fibrosis. Talabostat is a well-known drug, binding to this receptor with high affinity (11 nM).¹⁰⁰ Its derivatization with a $^{68}\text{Ga}^{3+}$ chelating structure was also intended.

III. Results and Discussion

In this chapter, the obtained experimental results will be presented and discussed. First of all, the organic syntheses are presented, followed by a chapter about the radiolabelling of the obtained precursors. Furthermore, the results of in vitro assays on cells and isolated integrins will be shown, before the animal tests are displayed. Finally, a chapter addressing the question of the binding mode of the integrin $\alpha_v\beta_6$ via theoretical/computational methods will complete the results of this thesis.

III.1 Organic Syntheses

In the first place, the ligand EMD527040 had to be synthesized. For this task, we chose a route which abuts on the methods of Goodman and Sulyok.^{101,102} It is outlined below in Figure 16.

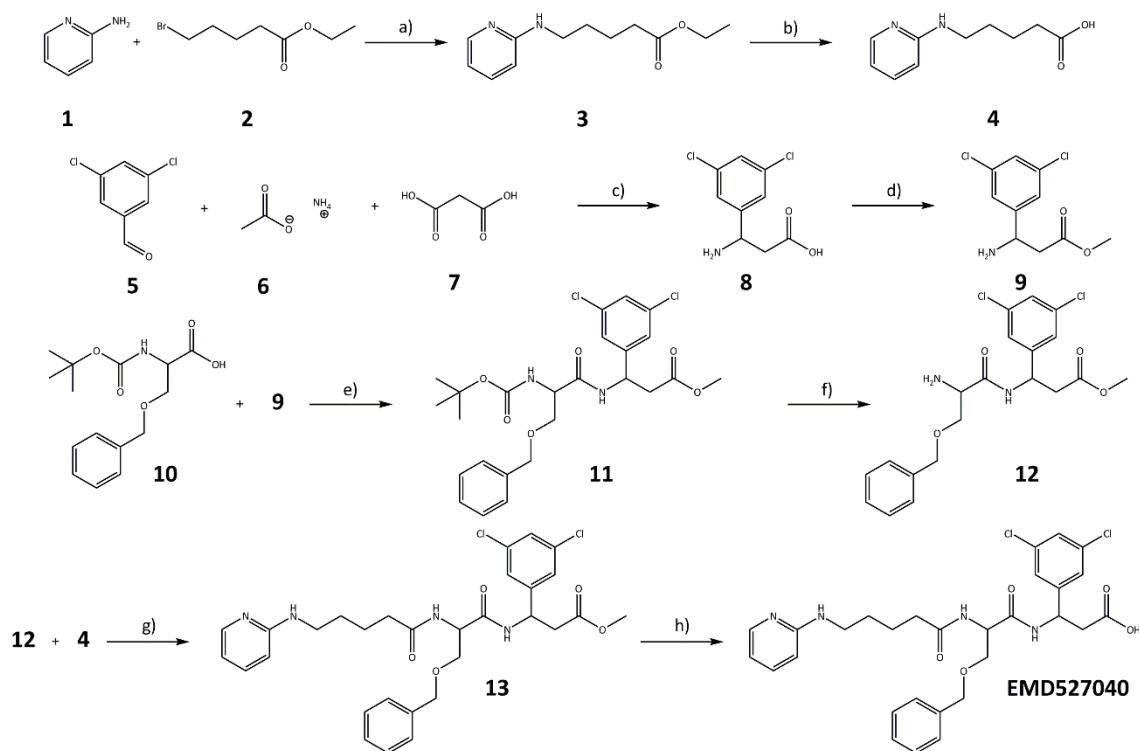


Figure 16: Proposed synthesis route to EMD527040. Based on methods of Goodman and Sulyok.^{101,102}

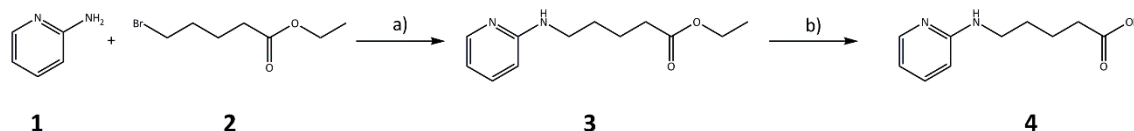


Figure 18: a) Na_2CO_3 , 130°C , overnight (27 %); b) dioxane, HCl (1N), 105°C , reflux, overnight (quantitative).

Conducting the reaction in solution has been tested, but was not successful. As solvents were used dimethylformamide with sodium carbonate as well as sodium hydride as base, which did not result in any product. The highest yield obtained in solution were 9 % in tetrahydrofuran with 1.1 equivalent sodium hydride according to Patriciu et al.¹⁰³ Their high yields between 70 % and 83 % could not be reproduced. Therefore, the bulk reaction was preferred – since the educts are of low cost, the moderate yields could easily be compensated by higher scales.

The saponification of ester **3** was subsequently performed. A mixture of hydrogen chloride in dioxane (1N) was heated to reflux overnight. In this case a quantitative yield was obtained. It could be purified with a number of extraction steps - the use of non-aqueous hydrogen chloride in dioxane instead of an aqueous acid might have facilitated this. This was not further tested since the resulting yield of more than 2 grams were enough for the following steps.

In order to build the second building block of EMD527040, 3,5-dichloro benzaldehyde was reacted with malonic acid and ammonium acetate. Both, the aldehyde as well as the malonic acid were soluble in methanol, but upon addition of ammonium acetate a white precipitate was observed. This dissolved while the reaction mixture was heated to reflux. The next morning, a new white precipitate could be observed which remained throughout the day of stirring at room temperature. This precipitate was filtered off the solution and identified as the desired product. Between 53 % and 64 % yield could be obtained.

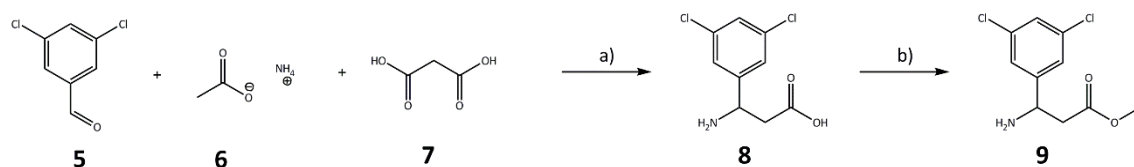


Figure 19: a) MeOH , reflux \rightarrow rt (53 – 64 %); b) MeOH , SOCl_2 , DMF , -78°C \rightarrow rt (56-84%).

The second step displayed in Figure 19 is the protection of the β amino acid **8** as methyl ester. For that purpose, 0.15 equivalents of DMF were added to the solvent and cooled down to -78°C before addition of thionyl chloride. After ten minutes, compound **8** was added and the mixture was allowed to stir at room temperature. The next day the solvent was reduced in vacuum. By

precipitation in cold diethyl ether, the product could be obtained in satisfying yields of 56 % – 84 %.

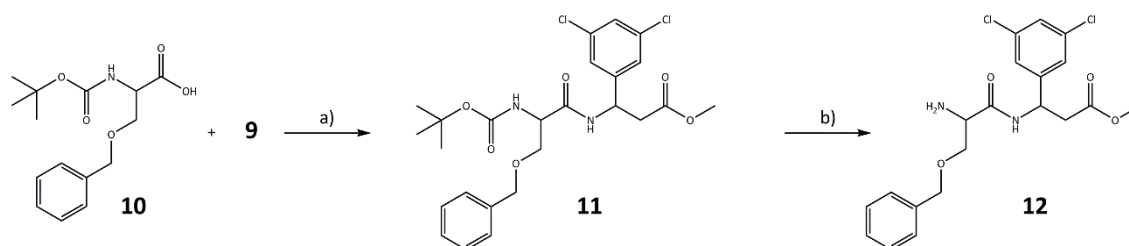


Figure 20: a) DIPEA, HOBT, EDCI*HCl, DMF, 18-25 h, rt (64 – 77 %); b) HCl in dioxane (4M), rt, 20 h, (97 %).

The coupling displayed in Figure 20 of compound **9** with the N-boc O-benzyl protected serine **10** could successfully be performed with EDCI*HCl and HOBT as coupling agents. It is of note that the use of the free base of EDC instead of the hydrochloride did not result in any conversion at all. Furthermore, the mixture was poured into ice water after finishing – at this point the product never precipitated properly but rather formed a viscous second phase. Therefore, it had to be separated by decanting – possibly a point at which significant losses in yield are most likely.

For further workup, recrystallization from warm diethyl ether has proven more effective than column chromatography – since recovery was bad in the latter case. If necessary, the product was doubly recrystallized.

The removal of the boc group was performed with HCl in dioxane (4N). After twenty hours, a yield of 97 % could be obtained while shorter times (4 hours) did only yield 63 %. The high yield made a further workup apart from solvent removal obsolete.

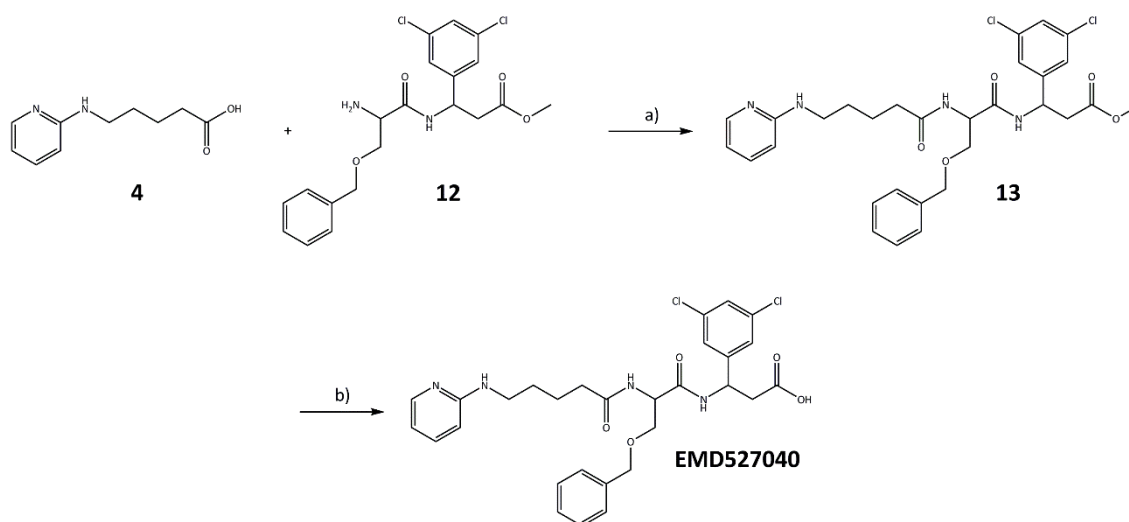


Figure 21: DIPEA, HOBT, EDCI*HCl, DMF, overnight, rt (63%); b) NaOH, pH 11, 4 days (97%).

The last coupling was performed under the same conditions as before (EDC·HCl, HOBT and DIPEA in DMF overnight at room temperature). In this case the reaction was taken up in dichloromethane and extracted with KHSO₄, NaHSO₄ and HCl – that way the product was obtained in the organic phase. Similar yields as before (63 %) were obtained.

The last step, the saponification of the methyl ester which was introduced in step d) of Figure 16, took four days of reaction time but was nearly quantitative in result.

In conclusion, the $\alpha_v\beta_6$ antagonist EMD527040 could be synthesized with an overall yield of 24 % (based on the branch starting from 3,5-dichloro benzaldehyde).

III.1.II Synthesis of labelling precursors

In this chapter, the synthesis of the two labelling precursors **BK23** and **BK39** will be described. It is based on peptide coupling, which was successfully performed in a laboratory microwave in this case. The strategy for protection groups was chosen in an orthogonal fashion – tert-butyl esters being acid labile, and the Cbz group, which can be cleaved by hydrogenation.

III.1.II.1 Synthesis of BK23

As depicted in Figure 22, EMD527040 was coupled to the commercially available chelator DO3AtBu-N-(2-aminoethyl)ethanamide **14**. In this case, the coupling was not performed with EDC·HCl, but instead the coupling reagent COMU was used. This is reported as highly efficient as the morpholino group enhances solubility and the Oxyma group represents a better leaving group within the class of known immonium/uranium salts as peptide coupling agents. Furthermore it is easy to use, since a colour shift from pink to yellow shall be observed during the course of the reaction.¹⁰⁴

Also, the reaction was performed in a laboratory microwave – ten seconds at 55 W were repeated in total twenty times. Between every step, the reaction mixture was cooled down to room temperature in an ice bath. Nevertheless, a yield of 60 % is comparable to the results which were earlier obtained with EDC·HCl. An increase could not be found.

Also, the colour shift was not as strong as reported – an assessment whether the reaction had finished or not was not possible for this reaction. Possibly, this could be due to the small scale of our reaction – maybe this effect can be seen well in larger scale.

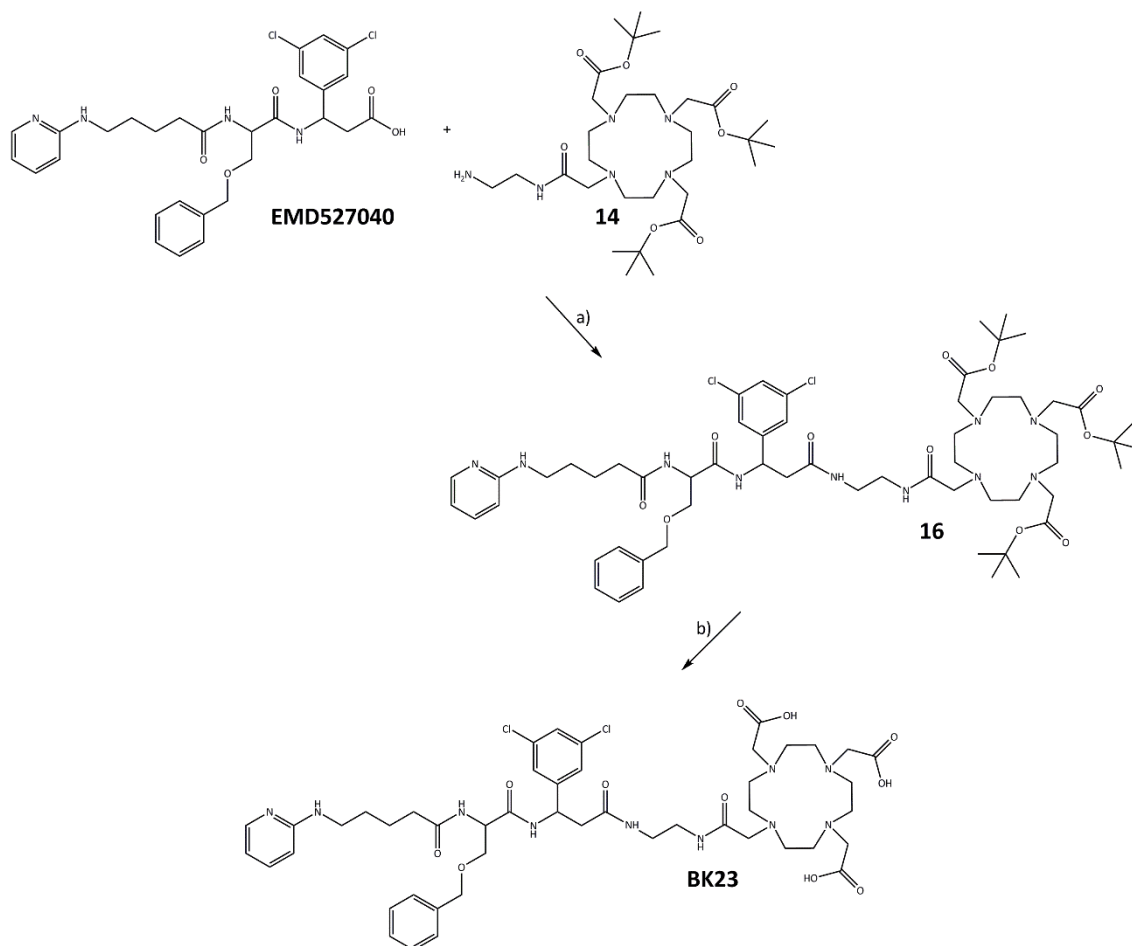


Figure 22: a) DMF, COMU, TMP, 20 x 10 s microwave 55W, (60%); b) DCM/TFA (1/1), 36 h, rt (33% after HPLC purification).

The final step in order to obtain the first labelling precursor was the deprotection of tert-butyl esters for liberation of the carboxy functions which will later be relevant for the complexation of $^{68}\text{Ga}^{3+}$. This was performed at room temperature in a 1/1 mixture of dichloromethane and trifluoro acetic acid. After 1.5 days the reaction was stopped by evaporation of the solvents. It was necessary to purify the final compound via HPLC – a large loss of mass was due to the necessity of performing this step twice before a pure product was obtained. Eventually this could be avoided by further optimization of the HPLC method.

In total, the labelling precursor **BK23** was successfully synthesized in an overall yield of 20 %.

III.1.11.11 Synthesis of BK39

A similar approach was used for the synthesis of **BK39** – an EMD527040 derivative with a longer spacer in between the targeting vector and the chelating moiety. The tetra ethylene glycol chain was chosen in order to increase the hydrophilicity of the molecule.

The same coupling method as before was used in the first step. Together with COMU and TMP a yield of 48 % could be achieved after column chromatography with the above described microwave procedure.

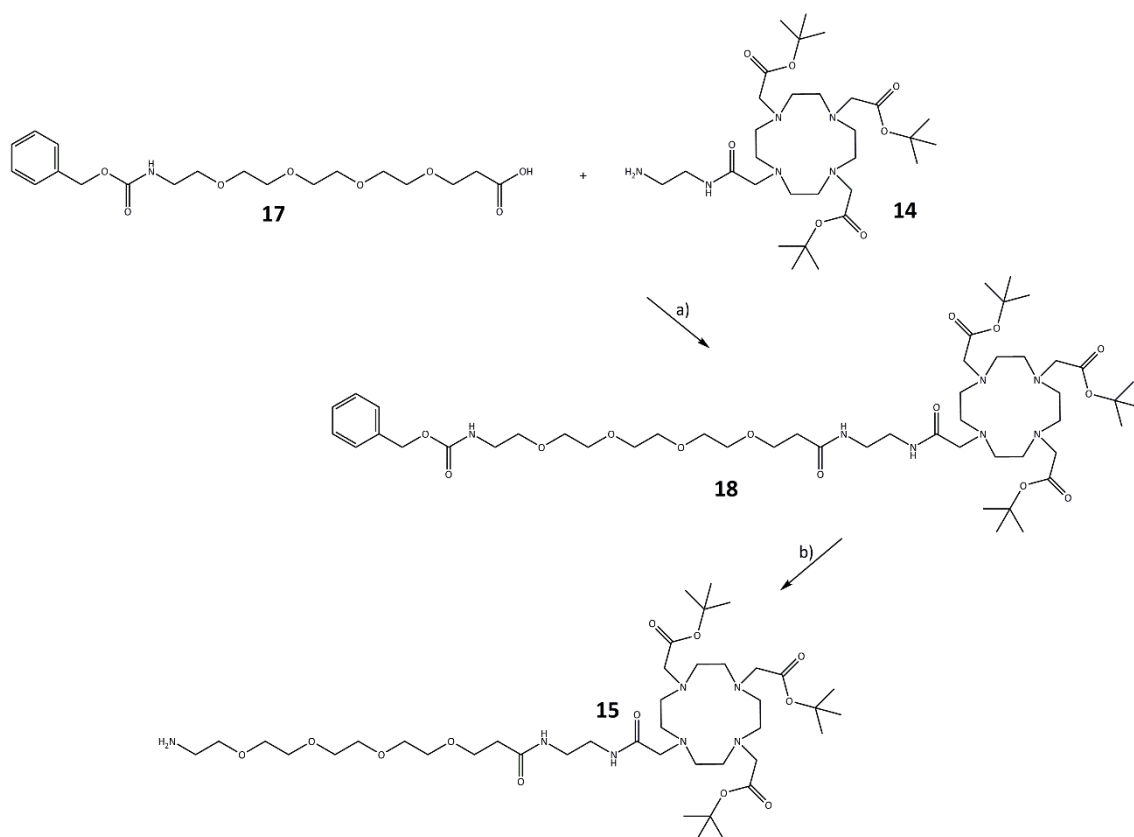


Figure 23: a) DMF, COMU, TMP, 20 x 10 s microwave 55W, (48 %); b) MeOH/TEA (3/1), Pd/C (10%), H₂, rt, 10 h (40%).

The deprotection of the amine group was achieved by hydrogenation. As good experiences had previously been made with a 3/1 mixture of methanol/triethylamine, this solvent was chosen again.¹⁰⁵ In this case, after ten hours and subsequent workup by column chromatography, 40 % yield were obtained.

With these reactions, a modified chelator was obtained which could be coupled to the targeting vector EMD527040.

For this purpose, again, the COMU based coupling method in the microwave was applied. This procedure yielded 45 % of the desired product **19** after column chromatography and lies therefore in the same range as the aforementioned coupling reactions.

The last step was similar to the deprotection step in the synthesis of **BK23**. In order to allow the chelator for complexation with $^{68}\text{Ga}^{3+}$, the tert-butyl esters need to be hydrolysed. This deprotection was achieved by stirring at room temperature overnight in dichloromethane/trifluoro acetic acid (3/1). The yield of 60 % is about double as high as in the case of **BK23**, but this is due to an improved HPLC purification, which was successful already after a single run.

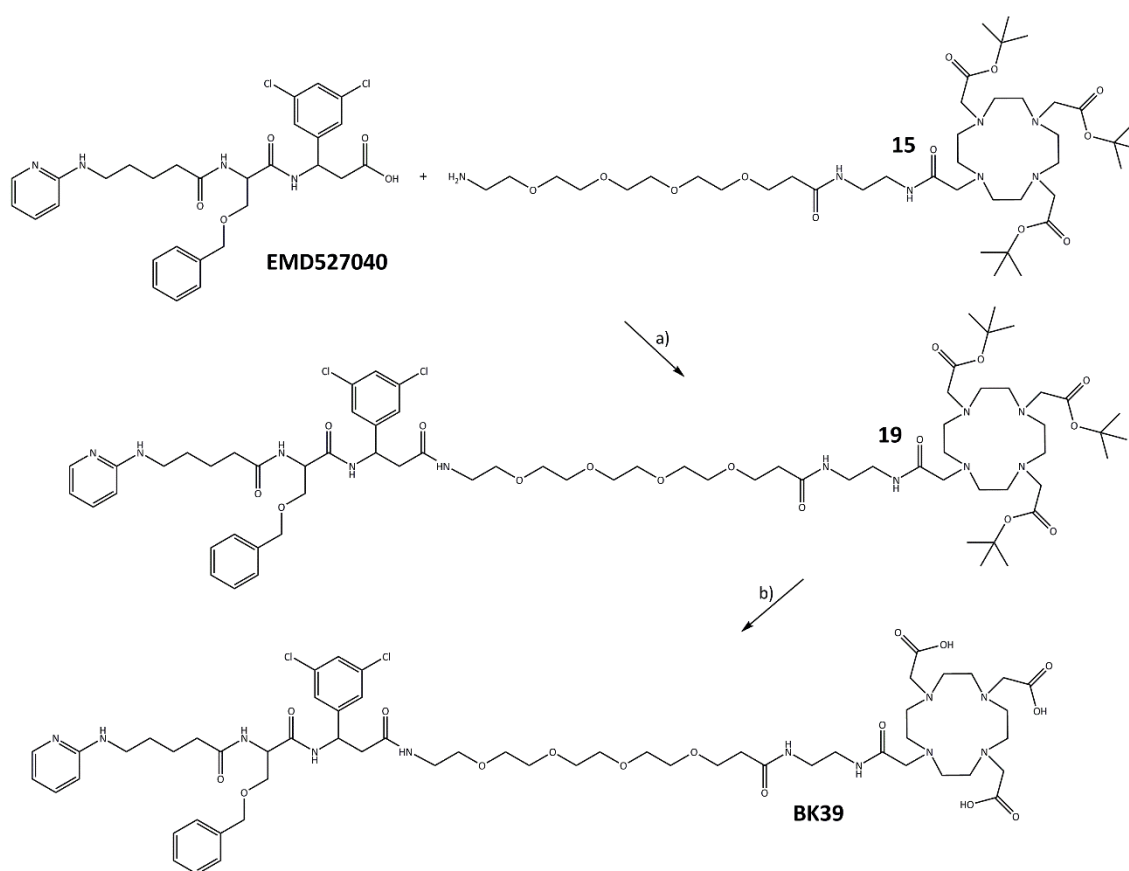


Figure 24: a) DMF, COMU, TMP, 20 x 10 s microwave 55W, (45 %); b) DCM/TFA (3/1), overnight, rt (60 % after HPLC purification).

In conclusion, **BK39** – an EMD527040 derivative with a longer spacer – has successfully been synthesized in an overall yield of 5 % over four steps.

In the next chapters, the evaluation of the new precursors (**BK23** and **BK39**) for radiolabelling with $^{68}\text{Ga}^{3+}$, subsequent cell tests as well as animal experiments will be described.

III.I.III Derivatization of Talabostat

For the derivatization of talabostat (**20**), the NODAGA-based isothiocyanate **21** was chosen for a straight forward coupling approach with the primary amino group of talabostat. It was performed in two different solvents, equimolar amounts were used in both cases and the reactions were stirred at room temperature. In methanol, the chelate **21** became methylated, according to mass spectrometry. The mass difference of 14 suggests the building of methyl esters rather than MeOH adducts (those would have to be 32). This is not desired, since the methylation of the carboxy groups would hinder the complexation of $^{68}\text{Ga}^{3+}$. This approach was therefore not followed any further.

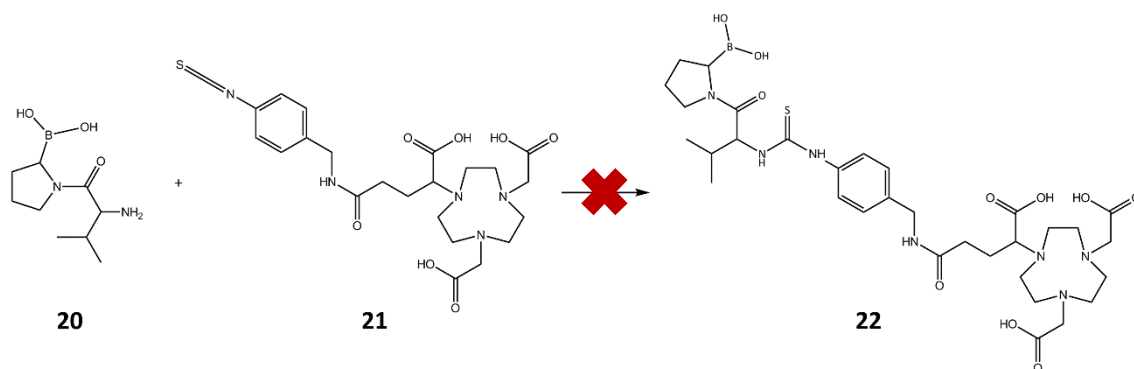


Figure 25: Intended reaction for talabostat derivatization.

The approach in DMF did not show any change at all, initially. It has to be mentioned that both substances were supplied as hydrochloric salts, which leaves the amino group inactive. Therefore, after 24 h, 0.1 equivalents of K_2CO_3 were added to the mixture. Again, no change could be detected. Since this was attributed to the hydrochloric salts, the amount of K_2CO_3 was further increased to 1.0 equivalent.

Within 4 hours, an undesired side reaction was observed. By mass spectrometry peaks of 393 and 197 were detected as the main contents of the reaction mixture. Those can be assigned to the mono-cyclization product **23** or the single and double protonated dimer of talabostat **24** (cf. Figure 26). Therefore, the desired product could not be obtained.

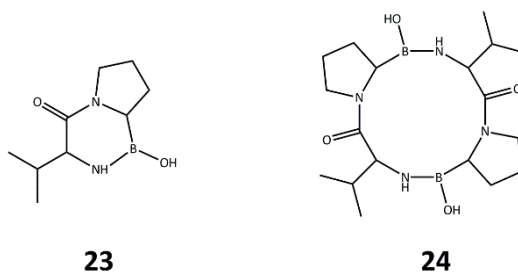


Figure 26: Possible cyclisation products during the course of talabostat coupling.

The conclusion in this case needs to be that a protection group for the boronic acid would have been necessary in order to successfully accomplish this reaction.

III.II Radiolabelling

The radiolabelling of the two successfully synthesized precursors **BK23** and **BK39** was performed under typical conditions for DOTA derivatives. ^{68}Ga was obtained from a $^{68}\text{Ge}/^{68}\text{Ga}$ generator, from which it was eluted with 0.1 M HCl directly to a post-processing system for purification. The cation exchange resin based system by Zhernosekov et al. was used in all cases.⁴³ This yields the pure $^{68}\text{Ga}^{3+}$ in 400 μL of so called N2 solution (97.6 % acetone / 0.05 M HCl).

In first trials with **BK23**, the reaction was performed in HEPES buffer (0.13 M). To 400 μL of the buffer, between 10 and 40 μL of the precursor stock solution (1 mg/mL) were added, before the generator eluate (400 μL) was added. By this way a pH of 3.4 is reached. This mixture was heated to 95 $^{\circ}\text{C}$ for 10 minutes. As Figure 27 shows below, high yields could be achieved with only 20 nmol. In the case of **BK39**, even 10 nmol precursor yielded 95 % RCY (radiochemical yield), although it shows slower kinetics. This is also the case for **BK23**, but the RCY did not surpass 70 % after ten minutes. If this could have been improved by longer reaction times was not investigated.

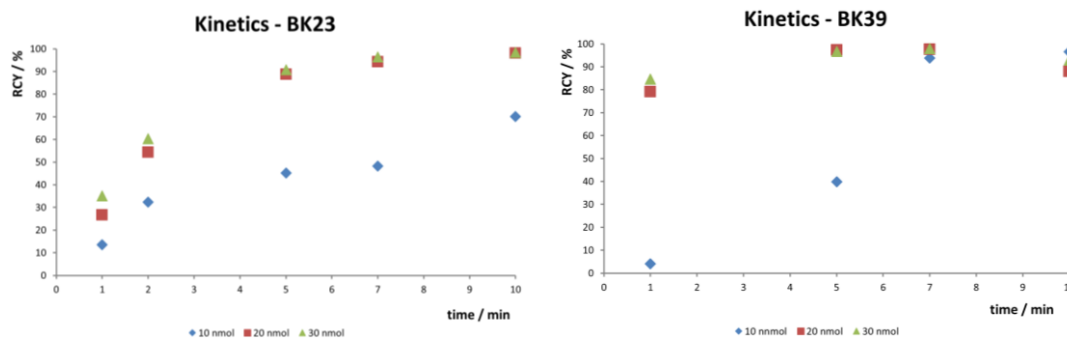


Figure 27: Kinetic studies for radio labelling of BK23 and BK39 with 10, 20 and 30 nmol precursor, respectively (blue, red, green). RCY determined by radio-TLC.

Since the curves for 20 nmol precursor and 30 nmol precursor showed practically the same slope, 20 nmol were preferred for the purpose of higher specific activities.

Subsequently, a method for the purification from remaining free $^{68}\text{Ga}^{3+}$ was developed. 1 mL of water was added to the reaction mixture and passed through a pre-conditioned (2 mL of ethanol followed by 2 mL of water) Strata-X cartridge (C-18 phase). The fixed radiotracer was washed with water in order to remove the free $^{68}\text{Ga}^{3+}$ before the desired compound was eluted with 0.5 mL of ethanol. After evaporation of the ethanol, the radiotracer could be taken up in the desired physiological solution.

A typical activity balance can be seen in Table 4. About 15 % of the activity remained in the syringe used for application of the reaction mixture to the cartridge. Other differences can be explained by the decay during the procedure. In total, around 50 % of the starting activity was recovered as the desired product – readily formulated for further applications.

Table 4: Activity balance for BK23 purification via Strata-X cartridge. Non decay-corrected values.

	Starting Activity	Fixation on cartridge	Washing step with H_2O	Elution with EtOH	Activity after evaporation
	58.03 MBq				29.92 MBq
Activity on cartridge		47.86 MBq	45.40 MBq	3.02 MBq	
Activity breakthrough		1.55 MBq	0.47 MBq	41.15 MBq	

However, such a ratio could only be obtained for small starting activities. Problems were encountered upon up-scaling the reaction. For instance, with a generator eluate of 623 MBq,

only 50.5 MBq formulated product were obtained. This correlated with low radiochemical yields, dropping down to 14 %.

A couple of ways were tried to overcome this problem. First of all, higher volumes were used. With 1.5 mL HEPES buffer and 1.5 mL N2 generator eluate, the yields rose to 29 %. By this way 70 MBq could be produced from 600 MBq starting activity. This is an improvement compared to 50 MBq but not yet compelling.

The addition of ascorbic acid (3 mg, added to a mixture with 3 mL volume) left the results unchanged.

Only by the addition of ethanol, the problem could be overcome. Returning to the 400 μ L HEPES buffer and 400 μ L N2 generator eluate, 200 μ L of ethanol were added. By this change, the reaction recovered back to RCY of over 90 %. In the first purification trials, nevertheless, the product could not be recovered to great extents, but instead the product was eluted with 1 mL water. This was ascribed to the high extent of organic solvent in the mixture, which was passed over the cartridge – resulting in a less effective adsorption of the tracer to the surface. Indeed, by changing the volume of water, which was used for dilution of the original reaction mixture, this problem was circumvented. By taking the reaction up in 7 mL water, 140 MBq could be obtained out of 513 MBq, while 8 mL allowed a recovery of the initial 50 % we observed for smaller activities (282 MBq from 529 MBq).

Hence, the final ‘standard protocol’ was established as heating 400 μ L of HEPES buffer, 400 μ L N2 generator eluate and 200 μ L ethanol together with 20 nmol precursor for 10 minutes at 95 °C in an open vessel. For purification, this mixture was taken up in 8 mL water before passage over a Strata-X cartridge. The cartridge was washed with 1 mL water and subsequently eluted with 0.5 mL ethanol, which was evaporated.

These observations and optimizations were made using **BK23** – for **BK39** the ‘standard protocol’ was immediately applied, resulting in the same satisfying yields.

After the successful establishment of labelling protocols, the stability as well as the lipophilicity of the two compounds were investigated. Figure 28 shows the results of the stability study. Both compounds show high stabilities of above 90 % for at least two hours. The media used, were PBS, PBS with added transferrin, saline (0.9 %), cell media and human serum.

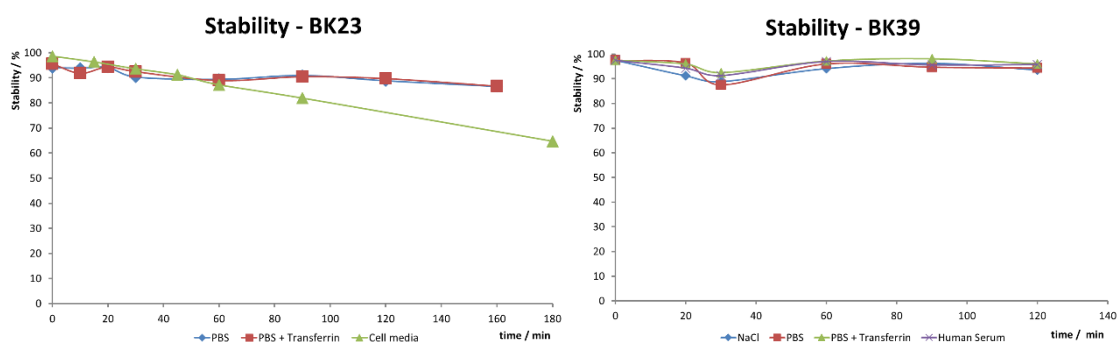


Figure 28: Stability investigation on the ^{68}Ga -labelled tracers BK23 and BK39. Determined by radioTLC.

The lipophilicity was investigated according to the 'shake-flask method'. The partition coefficient between PBS buffer and 1-octanol was investigated by determination of the activity contained in both phases.

The results met our expectations: For **BK23** a value of -0.19 ± 0.3 was determined, while for **BK39** a value of -0.27 ± 0.16 was identified.

Negative logD values indicate a higher solubility in the aqueous phase than in the organic phase. This was expected, since the DOTA-core is a quite polar moiety. This polar block is part of both compounds, as well as the EMD527040 moiety. The difference lies in the spacer – which is indeed more polar for the tetra ethylene glycole spacer of **BK39**.

It is thought that the polarity of the compounds has an impact on their behaviour *in vivo*. This is further discussed in chapter III.IV, where the results of the animal studies are presented and discussed.

III.III Affinity Assays

After the successful synthesis and establishment of a radiolabelling protocol, the affinity of the compounds was meant to be investigated. In the first place, cell assays were performed with limited success. Subsequently, the usage of the immobilized integrin was tested. The radioligands were used as well as the possibility to develop a non-radioactive ELISA assay was exploited. Finally, the Quartz Crystal Microbalance (QCM) method, was tested for its applicability in order to gain insights into the binding characteristics of $\alpha_v\beta_6$ and EMD527040-based ligands.

In short, the QCM method is based on the inverse piezoelectric effect. The piezoelectric effect is known for the creation of electrical charges upon deformation of a crystal along a given axis. Inversely, a quartz crystal resonates in a certain frequency, if an electric current is applied.¹⁰⁶ According to the Sauerbrey model, the resonance frequency is dependent on the mass of the crystal:¹⁰⁷

$$\Delta f = C_f * f_0^2 * \Delta m/A$$

Herein Δf represents the frequency change, C_f the Sauerbrey constant representing the QCM/mass sensitivity, f_0 the eigenfrequency of the crystal, Δm the mass difference and A the area of the crystal.

Mass changes in the sub-nanogram range can therefore be detected by this method. Below in Figure 29 an example of a typical experimental setup can be seen.

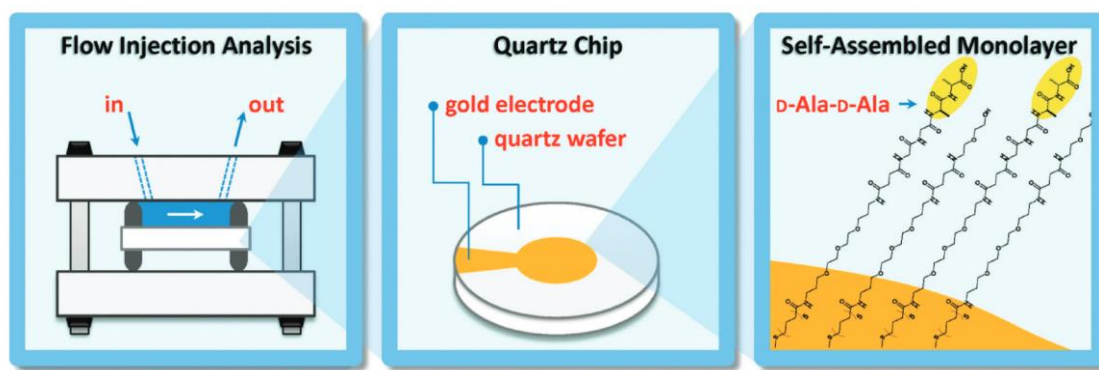


Figure 29: Typical experimental setup of QCM measurements.¹⁰⁶

The quartz crystals are typically metal coated which can be further functionalized. Cheng et al. have published an extensive review about functionalization methods.¹⁰⁶

The application potential for QCM is broad – depending on how the surface has been modified, biological interactions like ligand/receptor can be studied as well as for example the temperature- and pH-dependent behaviour of responsive polymer structures if they are coated to the surface.^{108–110}

III.III.I Cell Assays

In order to investigate the affinity of **BK23** and **BK39**, cell tests were performed with three different cell lines. HT-29 and 603 B were used as $\alpha_v\beta_6$ – positive cell lines, the former being a human colon carcinoma cell, the latter originating from murine cholangiocytes. As a negative control, Huh-7 cells were used – those are human hepato-carcinoma cells.

The cells were seeded into single-breakable high-binding ELISA plates and grown to a confluence of 50 % or 100 % over night.

In total, four different assay types were performed – all of them for **BK39**, only two of them for **BK23**. The incubation time was examined with **BK39** and also the challenge experiment with constant radiotracer concentration and varying blocking concentrations of EMD527040 was only performed for this compound. Uptake experiments and affinity assays with increasing tracer concentration were performed for both, **BK23** as well as **BK39**.

For each assay, both radiotracers were freshly produced according to the optimized procedure described in Chapters III.II and V.II.I.

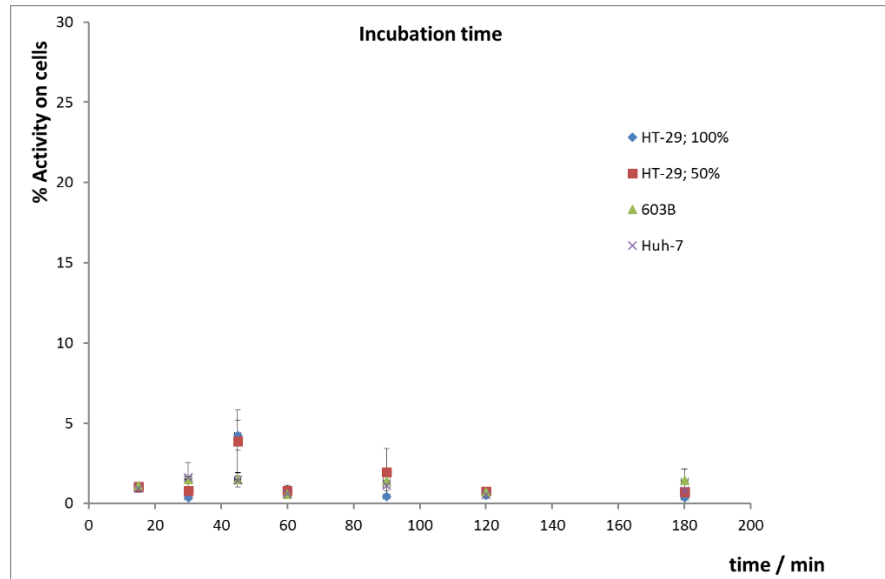


Figure 30: Incubation of $\alpha v\beta 6$ positive (HT-29 and 603B) and negative (Huh-7) cells with BK39.

As shown in Figure 30, incubation of the tracer **BK39** did not show very high retention on the investigated cells over a period of three hours. Nevertheless, at 45 minutes a slight peak in the curve could be observed, reaching up to 5 %. Therefore, the following experiments were performed with an incubation time of 45 minutes. Also due to the half-life of ^{68}Ga (67 minutes) an incubation time of less than one hour is favourable.

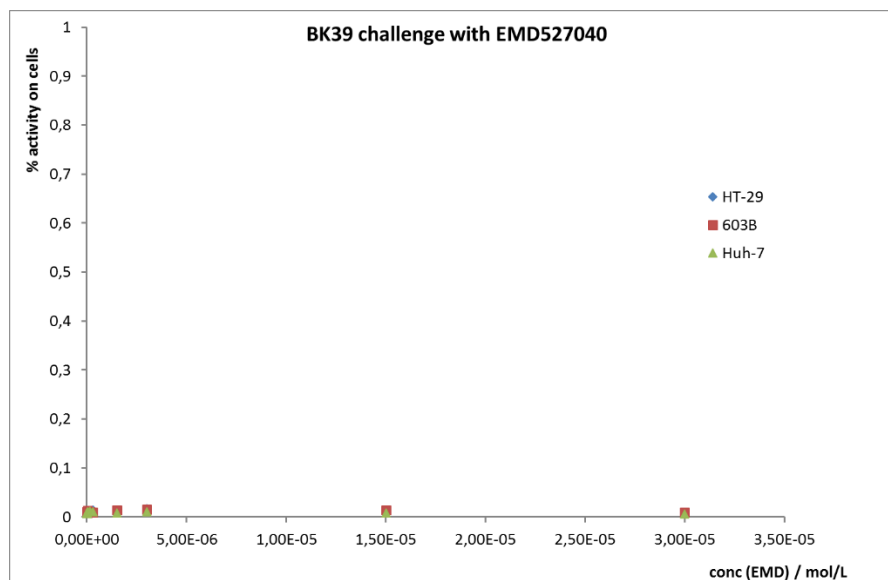


Figure 31: Challenge experiment with BK39 and varying concentrations of EMD527040.

Figure 31 shows the challenge experiment with constant radiotracer concentration of 770 nM (2.9 MBq/mL) and varying EMD527040 concentrations. Again, basically no retention on the cells

could be observed and the curve did not allow to perform a fitting in order to calculate an affinity value.

Subsequently, affinities were meant to be determined in a different way. Increasing radiotracer concentration yields a curve representing the sum of specific and unspecific binding. If the same radiotracer concentrations are applied together with an excess of blocking agent (EMD527040), solely the unspecific binding is determined. Subtracting those curves should give the Michaelis-Menten-function of the specific binding.

This was performed for **BK23** as well as **BK39**. A concentration of 3 μM EMD527040 was used for blocking and radiotracer concentrations of 5 pM till 1 μM were applied.

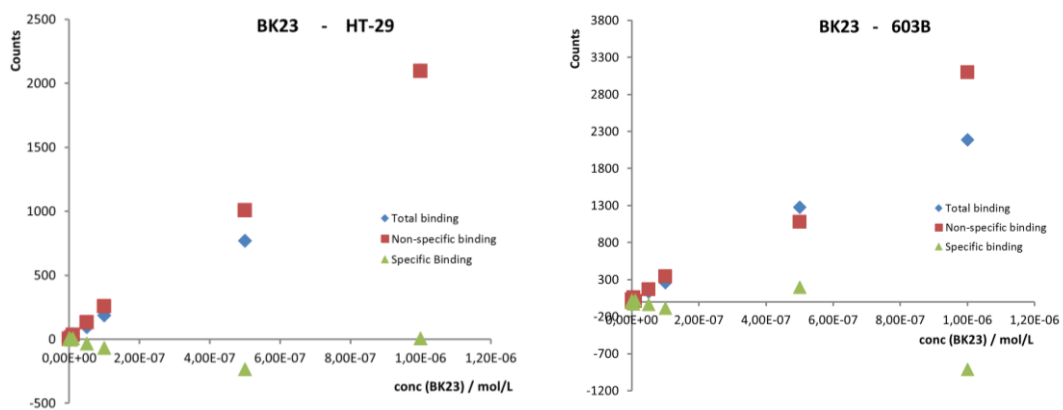


Figure 32: Affinity assay for BK23 on HT-29 and 603B cells. Total binding and Non-specific binding were measured to calculate Specific binding by subtraction.

Figure 32 shows the typically obtained diagrams for **BK23**. While both binding curves increase with higher concentrations, it is of note that for the lower concentrations the count rates were extremely low. If a reliable count statistic is given for those cases is questionable. Besides, the values for non-specific binding and total binding were very similar. In some cases this even lead to negative values for the calculated specific binding values. The fitting of a Michaelis-Menten-curve to such data did not seem reasonable and was therefore not performed. Hence, the calculation of an affinity value was not possible neither.

The results for **BK39** can be seen in Figure 33. They did not notably differ from those of **BK23**. The main characteristics of the curves were again, low count rates and very similar curves for total and non-specific binding. An affinity value was neither calculated in this case.

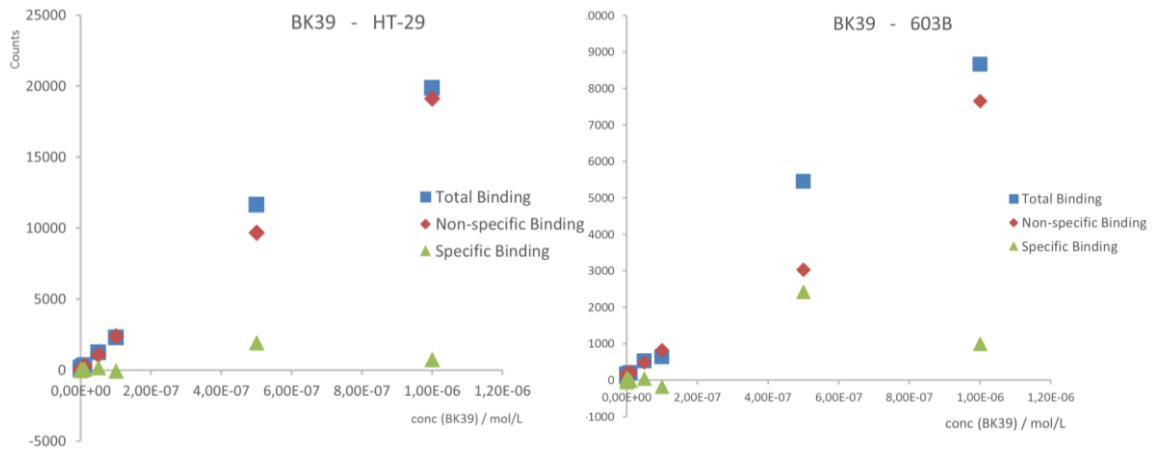


Figure 33: Affinity assay for BK39 on HT-29 and 603B cells. Total binding and Non-specific binding were measured to calculate Specific binding by subtraction.

If the affinities of **BK23** and **BK39** had been in the region of the lead substance (6 nM for EMD527040), a different behaviour in these assays would have been expected. Affinity values in the higher micromolar or even millimolar range are theoretically possible, as those concentrations were not investigated.

These results were finally underpinned by uptake assays with all three cell types. They were performed for both **BK23** as well as **BK39** on ice as well as at 37 °C. No differences were observed with respect to temperature, cell type, and radiotracer as in all cases 99 % of the tracer were found in the supernatant. Incubating the cells with an acidic stripping buffer did not show any difference between tracer attached outside to the cell wall and tracer taken up into the cell, since there was basically no tracer retained on the cells in the first place.

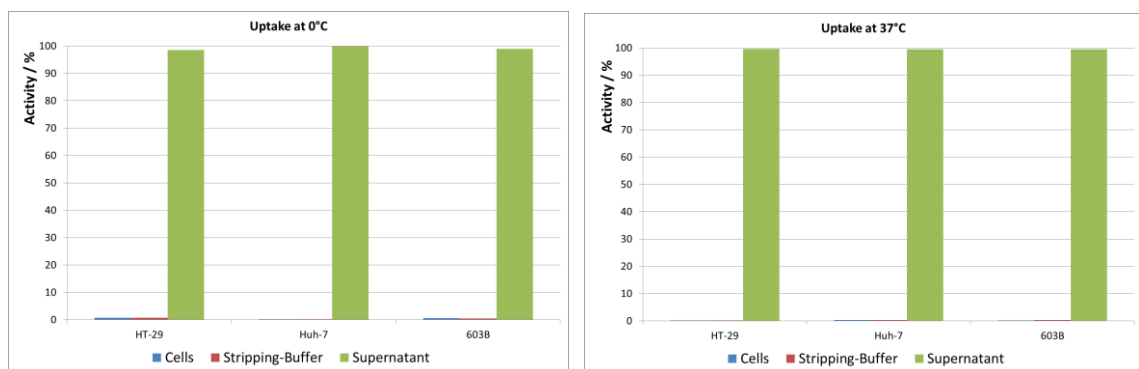


Figure 34: Uptake assay with BK23 on HT-29, 603B and Huh-7 cells at 0°C (left) and 37°C (right), respectively. In all cases, 99% of the activity were found in the supernatant and no retention on the cells could be observed.

The results are depicted in Figure 34 and Figure 35 for **BK23** and **BK39**.

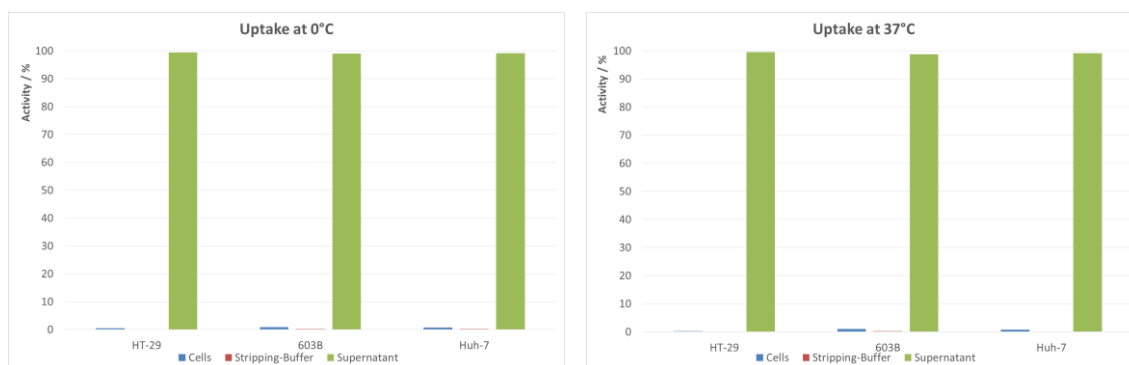


Figure 35: Uptake assay with BK39 on HT-29, 603B and Huh-7 cells at 0°C (left) and 37°C (right), respectively. In all cases, 99% of the activity were found in the supernatant and no retention on the cells could be observed.

In conclusion, all this data suggests that the ligands **BK23** and **BK39** do not show binding with the expected high affinity for the integrin $\alpha_v\beta_6$. This was unexpected, since the ligands **TC1**, **TC2** and **TC3** showed affinities in the nanomolar range, similar to the lead structure EMD527040.

In the case of **BK23** and **BK39**, the same position in EMD527040 was used for derivatization as for **TC1**, **TC2** and **TC3**, namely the carboxy function. Therefore, no drastic drop in affinity was expected – at least not for **BK39**, bearing a longer spacer than the ^{99m}Tc -compounds.

It is of note, that for this kind of affinity assay – by using the radioactive substance itself – we did not have access to a positive control. As outlined above, many parameters (incubation time, cell number, temperature) were systematically investigated without significant success. It was therefore not possible to further optimize assay conditions and actually prove the feasibility of the applied conditions.

Hence, the simplification of the system from complex cell surroundings to the isolated integrin was conducted in the following.

III.III.II ELISA Assays

In this chapter, two different aspects will be discussed. In the first place, this setup was meant as a replacement of the cell assays. In their case, the number of integrins present on the cells was not known – and therefore it could not be excluded that the lack of any binding observations was due to a reduced integrin expression and not due to low affinities. The purified integrin $\alpha_v\beta_6$ is commercially available from R & D Systems and can be coated on ELISA plates.

In order to prove the presence of integrins on the well surfaces, ELISA tests were performed. Subsequently, the affinity tests with the radiotracer were repeated on this system.

As a second part, the trial to establish a non-radioactive assay for affinity determination was undertaken. It is purely based on ELISA methods and the interaction of $\alpha_v\beta_6$ with the latency-associated-peptide (LAP), an endogenous ligand.

The first trial to prove successful integrin coating was performed with a commercial ELISA kit designed for human α_v . The kit is meant to measure α_v in solution and contains a plate, coated with an α_v -recognizing first antibody as well as a standard in order to obtain a calibration curve. This can be seen in Figure 36 (left) and shows a good linearity up to concentrations of 5 ng/mL. The error bar for the 10 ng/mL sample is rather large, which allows the assumption that with careful repetition a linearity up to 10 ng/mL could be achieved. On the right of Figure 36 the results for the self-coated plates can be seen. Three different buffers (carbonate pH 9.6, TBS and PBS) at two different concentrations (1 $\mu\text{g/mL}$ and 0.1 $\mu\text{g/mL}$) were investigated. Also incubation time and temperature (19 h, 4 °C vs. 1 h, 37 °C) were varied. Afterwards, all samples were treated for 1 h at 37 °C with 5 % BSA in PBS in order to minimize unspecific binding to the ELISA plates. Notably, all these samples do not show very high variation – and most importantly almost no increase above the BSA and blank samples. The $\alpha_v\beta_6$, which was used for coating, has also been investigated on the kit plate (same procedure as included standard). The result is not depicted, but it shall be reported here that optical densities of 0.1 were obtained for both 1.0 $\mu\text{g/mL}$ and 0.1 $\mu\text{g/mL}$ samples. This is the same range as it was observed for the self-coated plates, but it is far lower than it would have been expected from the standard curve.

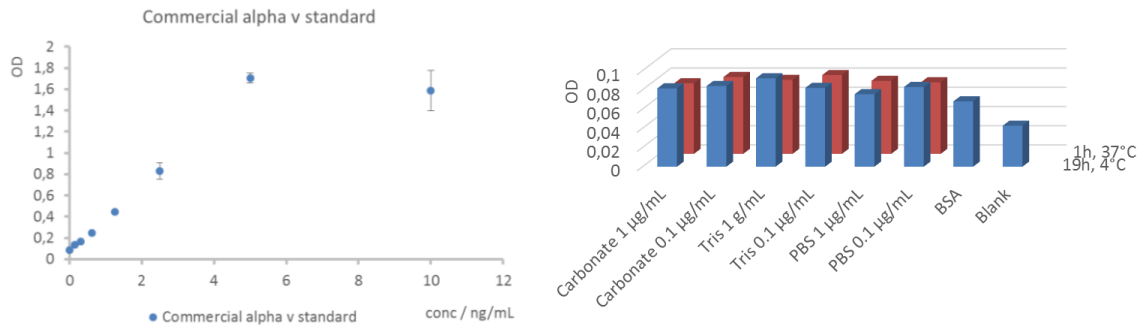


Figure 36: ELISA results from commercial alpha v kit. Left: standard curve obtained from included kit standard. Right: Results on self-coated plates with $\alpha_v\beta_6$.

The obtained values lie between the blank and the lowest standard sample (0.156 ng/mL). As the concentration was known to be 1000 – 10,000 times higher, it can only be concluded that the antibody-antigen reaction was not as specific as expected.

Since the epitope of the antibody is not known it can only be speculated about the reasons. A possible explanation is, that the epitope lies in a region of α_v , which is hidden by the β_6 chain and therefore does not allow a reaction with the antibody.

Hence, these results do not allow any assumptions about successful or unsuccessful coating of the integrin $\alpha_v\beta_6$ to the ELISA plates.

After this approach failed we decided to design our own detection assay. Two strategies were followed for this purpose. On the one hand, fibronectin – a native ligand – should be used for detection. On the other hand, an antibody specific for $\alpha_v\beta_6$ (STX-100) and not solely for α_v was planned to be employed.

For the first strategy, it was necessary to biotinylate the fibronectin, in order to make it detectable. For that purpose, it was reacted with biotinamidocaproate N-hydroxysuccinimide ester for one hour and subsequently dialysed overnight. The concentration of the resulting solution was determined with the BCA assay according to standard protocol (843 $\mu\text{g/mL}$).

In the following, it was used as a detection agent for the integrin $\alpha_v\beta_6$ on the ELISA plates. Together with anti-biotin-peroxidase, the integrin could be detected. As a control, the biotinylated fibronectin was coated directly on the plates (followed as well by blocking of free sites with 5 % BSA in PBS). This sample in fact resulted in the highest signal, which is not surprising as the coating of 1 $\mu\text{g/mL}$ fibronectin overnight was expected to give a higher total concentration than the incubation on integrins for only 3 hours.

The results can be seen in Figure 37 below. The BSA control lies with values of 0.26 far below the coated fibronectin at 0.63. The samples with an integrin surface show an interesting characteristic. The values for 0.1 $\mu\text{g}/\text{mL}$ coating concentration of integrin are found at 0.23 which is below the BSA control samples. But as they fall within their standard deviations, this is interpreted as no detection of integrin.

For the higher integrin concentration (1 $\mu\text{g}/\text{mL}$), a higher signal was obtained. The values of 0.32 are not very high above the BSA control, but since the errors do not overlap, this is interpreted as a hint for successful coating of $\alpha_v\beta_6$ at 1 $\mu\text{g}/\text{mL}$.

Note that for these experiments only the PBS buffer was used. The unspecific binding of anti-biotin-peroxidase to the residual compartments of the assay were also investigated (assay was performed without the biotinylated fibronectin) and found to be negligible.

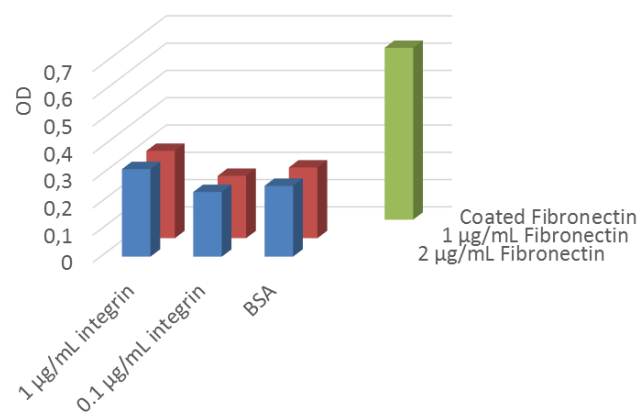


Figure 37: Detection of $\alpha_v\beta_6$ on ELISA plates with biotinylated fibronectin and following anti-biotin-peroxidase.

The approach using the $\alpha_v\beta_6$ antibody STX-100 for detection resulted to be the most successful. This antibody could be detected with a commercial anti-mouse-peroxidase. Figure 38 depicts the results. While in the case of the biotinylated fibronectin the different concentrations used did not show any effect – here an increasing signal could be observed with increasing STX-100 concentration. If STX-100 was left out in the procedure, no significant signal was obtained – the unspecific binding of the anti-mouse-peroxidase was therefore obviously neglectable. With this method even for the lower integrin concentration of only 0.1 $\mu\text{g}/\text{mL}$, a strong signal was observed. It was therefore concluded that both concentrations result in effective coating. This assay was of course not quantitative, but as expected the higher concentration is more effective in coating. Also, both concentrations seem to result in integrins, being accessible from the side of the solution.

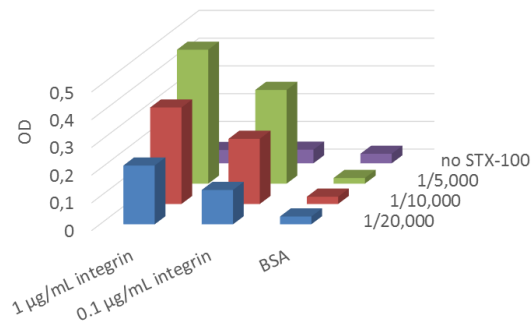


Figure 38: Detection of $\alpha_v\beta_6$ on ELISA plates with STX-100 and following anti-mouse-peroxidase.

With this prove of successful coating, we moved on to test the radiotracers **BK23** and **BK39** on the integrin-coated ELISA plates instead of a cell-based assay.

For this purpose, the higher coating concentration of 1 $\mu\text{g/mL}$ $\alpha_v\beta_6$ was used for coating overnight at 4 $^{\circ}\text{C}$ and as before, free sites were blocked with 5 % BSA in PBS for 1 h at 37 $^{\circ}\text{C}$.

The radiotracers were labelled with ^{68}Ga according to our optimized protocol and diluted to the respective concentrations from 5 pM to 1 μM . Additionally to that curve, also a blocked curve with 3 μM EMD527040 was measured, which should represent the non-specific binding – allowing the calculation of the specific binding. In this case a second way to determine the unspecific binding was chosen – samples bearing only the BSA for blocking free sites in the vial but lacking the integrin were prepared and incubated with the radiotracers.

The results are shown in Figure 39 and very similar to the ones which were obtained on cells. Total and unspecific binding curves are found almost exactly one on each other. Only for the highest concentrations, differences could be found – but for both tracers the unspecific binding values were higher than the respective ones for total binding. This resulted in negative values for specific binding, which does not make any sense and is probably due to the increasing size of errors. Again, similar to the cell tests, the count rates were very small which interferes with good and reliable counting statistics.

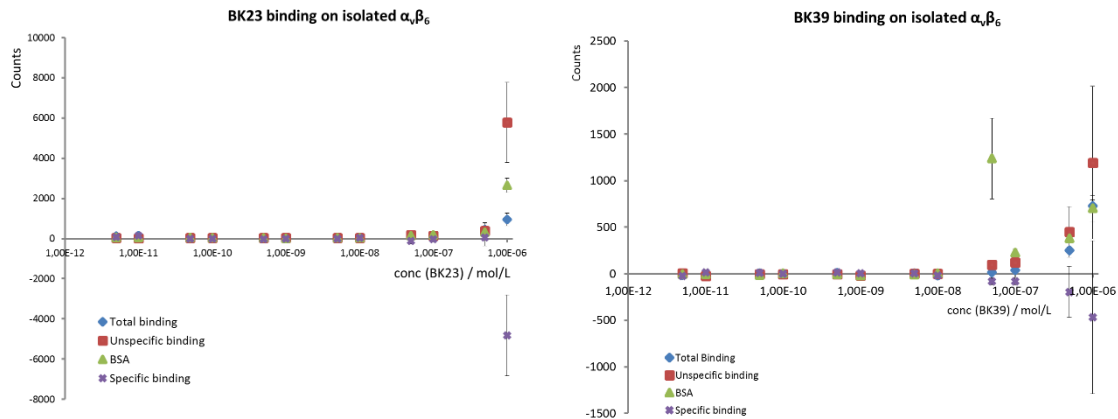


Figure 39: Binding curves for BK23 as well as BK39 on isolated integrin $\alpha_v\beta_6$. Note that the x-axis is logarithmic in this case.

At this point, it can be concluded that no binding could be detected for the new ^{68}Ga -labelled tracers **BK23** and **BK39** in any of the experimental conditions.

In the following, it shall therefore be described the attempt to establish a non-radioactive assay, which is capable of the determination of affinity values for the integrin $\alpha_v\beta_6$.

First of all, the fibronectin based assay was tested. In order to see whether a blocking of the bound fibronectin is possible, a challenge study with EMD527040 was performed. The plate was coated at $1\ \mu\text{g}/\text{mL}$ $\alpha_v\beta_6$. Concentrations of $500\ \text{pM}$ up to $5\ \mu\text{M}$ were tested, along with a blank sample. For the biotinylated fibronectin, a concentration of $1\ \mu\text{g}/\text{mL}$ was used. Incubation times for the ligand were $1\ \text{h}$ and $2\ \text{h}$, while the fibronectin was incubated constantly for three hours. The dilution of anti-biotin-peroxidase again was varied: $1/20,000$ as well as $1/30,000$ dilutions were applied.

Unfortunately, the result was not very promising. No correlation at all could be found for the resulting optical densities and the conditions applied. Large discrepancies within the triplicates could already be observed with human sight.

It was not possible therefore, to conclude whether any blockage effect had taken place – in any way the system was considered not stable enough in order to result in a reliable tool for affinity determination.

Also, the antibody STX-100 was tested in challenge experiments with EMD527040. Plates were again coated at $1\ \mu\text{g}/\text{mL}$ as well as at $0.1\ \mu\text{g}/\text{mL}$ of $\alpha_v\beta_6$. The same concentrations were used and

again incubation times of 1 h and 2 h were chosen. The antibody was diluted at 1/10.000 and the following anti-mouse-peroxidase at 1/20.000.

In this case – the results showed the same values over the whole concentration range. Lower signals were observed for the integrin coating at 0.1 µg/mL only and basically no signal was found on the control plates which lacked integrin.

This outcome suggests that the $\alpha_v\beta_6$ -antibody STX-100 recognizes an epitope which does not interfere with the binding of EMD527040 at the integrin. For that reason an assay system based on STX-100 cannot be useful for investigation on the interaction of EMD527040-like ligands with $\alpha_v\beta_6$.

A new ligand of $\alpha_v\beta_6$ was therefore searched. It should also be detectable by the immunological methods typically applied in ELISA assays. As $\alpha_v\beta_6$ plays a role in the activation of TGF- β 1, the latency-associated-peptide (LAP) was found as such. It binds with an RGD motif to the integrin¹¹¹ and an antibody is commercially available.

First of all, the incubation time as well as the concentration of Anti-LAP were investigated, as well as the unspecific binding. The obtained results are shown in Figure 40. For the incubation time of anti-LAP the manufacturer's recommendation of two hours at room temperature was followed. Since the anti-LAP did not bear a peroxidase itself, but instead was biotinylated – the aforementioned anti-biotin-peroxidase was used here again. With a dilution of 1/30,000 good results were expected.

It can be seen, that binding takes already place after only fifteen minutes. At about 45 minutes the highest value is achieved, the optical density remains on a plateau up to three hours. The lower concentration for anti-LAP of 100 ng/mL did not result in notably lower signal than 200 ng/mL.

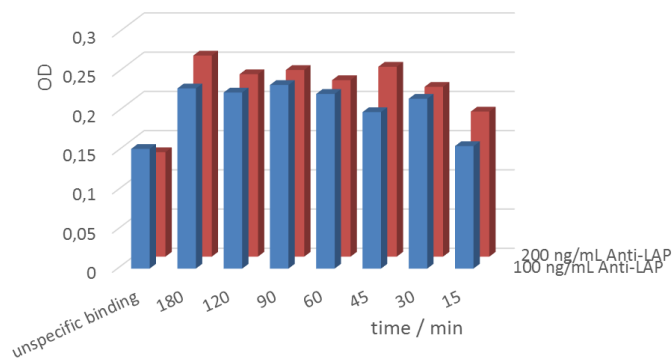


Figure 40: ELISA assay on integrin $\alpha v \beta 6$ coated plates with latency-associated-peptide. Incubation time for LAP as well as the concentration of the antibody were investigated.

A couple of controls were run to understand this system better: If the integrin-coated plates were treated with anti-LAP and anti-biotin-peroxidase or only with anti-biotin-peroxidase, optical densities as low as 0.06 were obtained. The signal is hence directly induced by the latency-associated-peptide. Also LAP and anti-LAP were coated to the plates and treated with anti-LAP + anti-biotin-peroxidase or only anti-biotin-peroxidase, respectively. As expected, high signals of 0.84 and 0.28 were obtained.

Since there is some evidence that for the case of $\alpha v \beta 3$ the activation is promoted at acidic pH values,¹¹² the pH-dependency in our situation was specifically determined.

As buffer was used, like before, a TBS + 10 μ M $MnCl_2$ + 1 mM $MgCl_2$ + 1 mM $CaCl_2$ + 0.1 % BSA. For this assay, it was acidified with HCl. Salts were added after pH equilibration in order to maintain the same concentration for all samples.

Unlike in the aforementioned example, a drop in binding of LAP was observed upon acidification of the buffer, which can be seen in Figure 41 below. No further changes were made to the buffer for the following experiments.

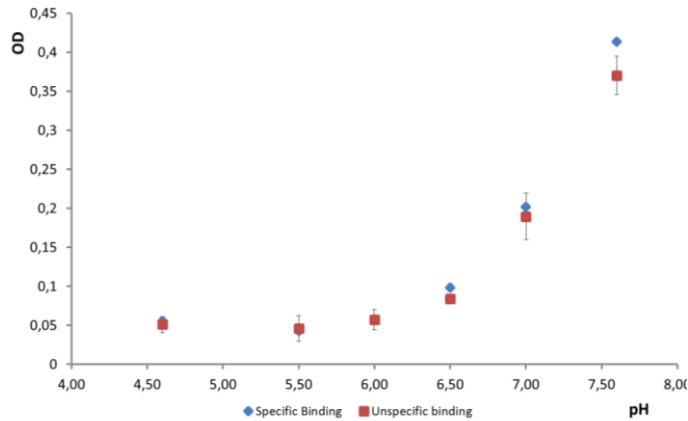


Figure 41: pH-dependency of the LAP-based ELISA system

Nevertheless, the unspecific binding increased alongside the specific binding. Hence, it was investigated whether this ratio is dependent on the LAP concentration. Therefore, it was varied from 0.01 $\mu\text{g}/\text{mL}$ up to 1 $\mu\text{g}/\text{mL}$, keeping other parameters constant. This was performed both for an anti-LAP dilution of 1/20,000 as well as 1/30,000. For the acquired results, both difference as well as ratio were plotted (cf. Figure 42).

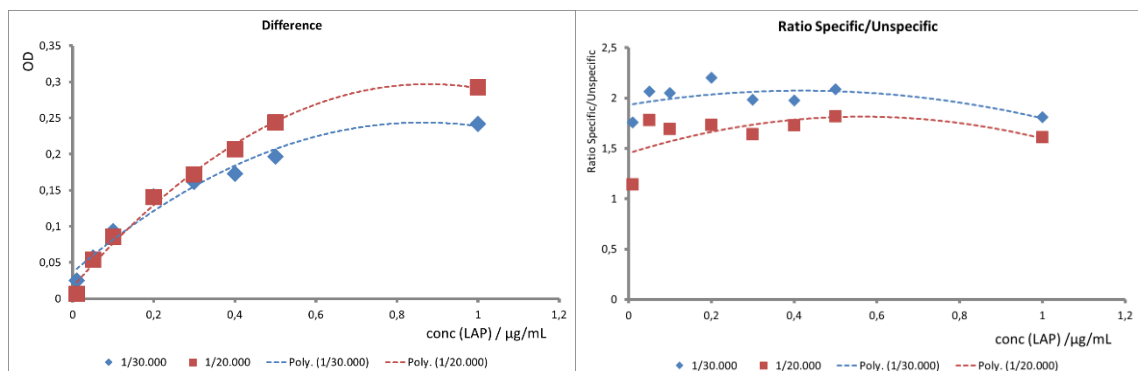


Figure 42: Investigation on the behaviour of specific and unspecific behaviour of LAP binding to $\alpha_v\beta_6$ -coated ELISA-plates with regard to the concentration of LAP. Coating concentration was 1 $\mu\text{g}/\text{mL}$. The respective two curves were obtained from different anti-LAP dilutions (1/20,000 and 1/30,000). Polynomial fits were obtained in Microsoft Excel.

It can be seen, that the use of very low LAP concentrations is not useful, as it does not result in measurable differences for the specific and unspecific case. At a concentration of 0.4 $\mu\text{g}/\text{mL}$ a difference becomes measurable and increases slightly towards 1 $\mu\text{g}/\text{mL}$. The ratio of specific to unspecific binding was found between 1.1 and 2.2. At low concentrations, this view on the data is not necessarily useful, as we do not have a difference anyway. But from 0.4 $\mu\text{g}/\text{mL}$ on, the ratio is increasing first, and drops later. The highest values were found for 0.5 $\mu\text{g}/\text{mL}$ LAP, both for anti-LAP dilutions of 1/20,000 as well as 1/30,000.

For the following blocking studies, a LAP concentration of 0.5 $\mu\text{g}/\text{mL}$ was used. The resulting increase in signal which can be gained from the higher anti-LAP concentration was considered too small to justify the additional use of material.

Blocking experiments were performed with EMD527040 as well as the fluorinated derivative **F2**, which was kindly provided by Dipl.-Chem. Sebastian Görres (for structure, cf. Figure 65). A very broad range of concentrations was used from 0.185 fM up to 6 μM .

In the first trials, quite unexpected results were found: The blank control without any integrin coated, yielded a signal of 0.22 optical density. The non-blocked integrin-surface yielded a signal of 0.40 – this would be expected to be the highest value. Interestingly, all samples with blockage resulted in signals between 0.61 and 0.67 – with no correlation to the concentration of the blocking agent. The values above are taken from the EMD527040 example, the same tendency was observed for the fluorinated ligand **F2**.

Our conclusion from this data was, that the concentration ratios were not yet optimal. The coating efficiency of $\alpha_v\beta_6$ was not known, but if 100% were assumed then the integrin would be present in a roughly 30 fold excess to LAP. Under such conditions, every LAP can still find a binding site, even if it is blocked in a high concentration – differences with regard to the concentration of the blocking agent are therefore not to be expected. These considerations do not explain why the signals were higher than for the non-blocked samples, but it does explain why they were all the same.

Therefore, the concentration for integrin coating was significantly lowered to only 0.05 $\mu\text{g}/\text{mL}$. On the other hand, the LAP concentration was increased to 3 $\mu\text{g}/\text{mL}$. For proof of principle and in order to save material, only four different concentrations were tested for **F2**, as well as EMD527040. Results are shown below in Figure 43.

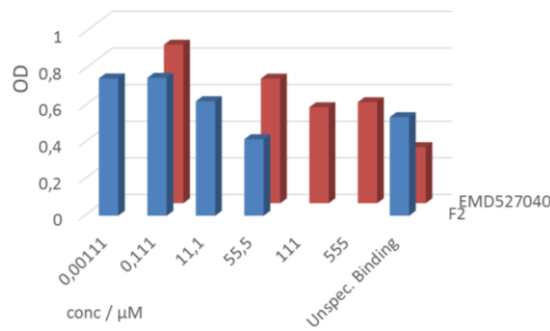


Figure 43: ELISA results for blocking LAP with the fluorinated ligand F2 and EMD527040, respectively.

It can be seen, that for **F2** as well as for EMD527040 a blocking effect is observed, for increasing concentrations. For the calculation of an affinity value, this data is not yet sufficient, as more concentration points are needed.

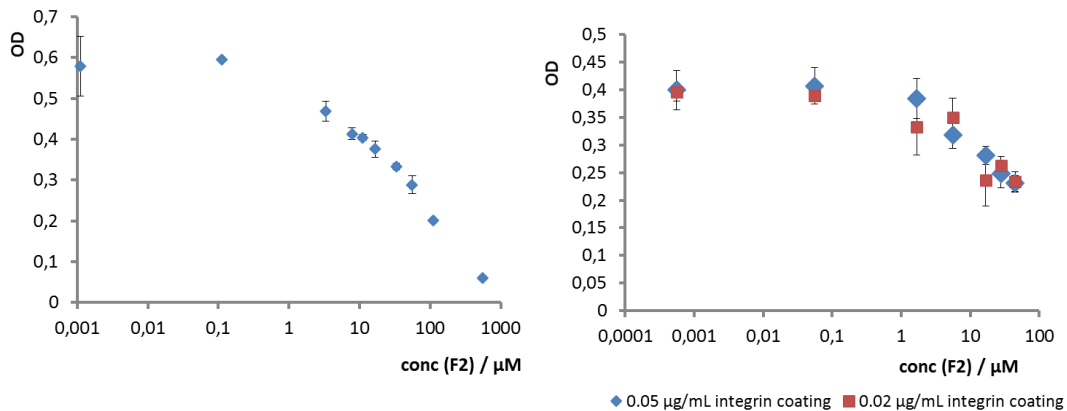


Figure 44: ELISA results for blocking LAP with the fluorinated ligand F2 - with a broader concentration range (left) and different integrin coating concentrations (right).

This was performed twice. In one approach it was tested if 0.02 μg/mL of integrin could also be sufficient for coating – as it can be seen on the right in Figure 44, the curve is not as consistent as it is for 0.05 μg/mL coating concentration. Also, the error bars are larger – therefore, the concentration of 0.05 μg/mL was kept for continuous experiments. The left diagram shows a quite promising result, but for high concentrations unfortunately no plateau was reached.

Also, the blank control without coated integrin and without any blocking agent, resulted in a value of 0.30. This is higher than the lowest value and was also observed for the experiments shown in Figure 43. If only the specific binding was blocked – the curve should theoretically converge at the value for unspecific binding.

It is therefore uncertain if the specific or the unspecific binding is being blocked by the addition of **F2** and EMD527040 – or both. In order to gain better understanding of the unspecific binding,

it was investigated if the addition of **F2** has an impact on the binding between LAP and its antibody. Coating of LAP at a concentration of 0.05 µg/mL and proceeding normally with the following steps, showed that addition of **F2** in concentrations between 55 nM and 388 µM resulted in signals of 0.16 for all samples. The interaction between LAP and its antibody is therefore specific and not affected by the addition of **F2**. Blank samples for anti-LAP and anti-biotin-peroxidase resulted in such low signals of 0.04, that any involvement of those assay parts in the unspecific signals was out ruled.

Since the unspecific binding is apparently achieved in the step of LAP addition, it was tested whether a better signal/noise ratio could be achieved by using a different blocking agent than BSA in the blocking step after integrin coating. Three other typical blocking agents have been tested: fish gelatine, milk powder and chicken serum.

Table 5: Influence of blocking agent on specific/unspecific signal.

	BSA (5%)	Fish gelatine (3%)	Milk powder (0.3%)	Chicken serum (10%)
Specific signal	0.63	1.04	0.24	0.19
Unspecific signal	0.54	0.86	0.27	0.17
Difference	0.09	0.18	-0.03	0.02
Ratio	1.2	1.2	0.9	1.1

The results are displayed in Table 5. The highest values for the specific signal were obtained with BSA and fish gelatine. The signal/noise ratio was equally low with 1.2. Though the difference was higher for fish gelatine, the actual signal was strongly exaggerated for the unspecific signal as well – this gives rise to the expectation of severer problems with the unspecific binding, which is why fish gelatine was not considered to be a better blocking agent than BSA.

For the determination of an affinity value for **F2** it was thus concluded that it would be necessary to measure the binding curve for total binding as well as unspecific binding simultaneously in order to obtain the curve for specific binding by subtraction of the former two.

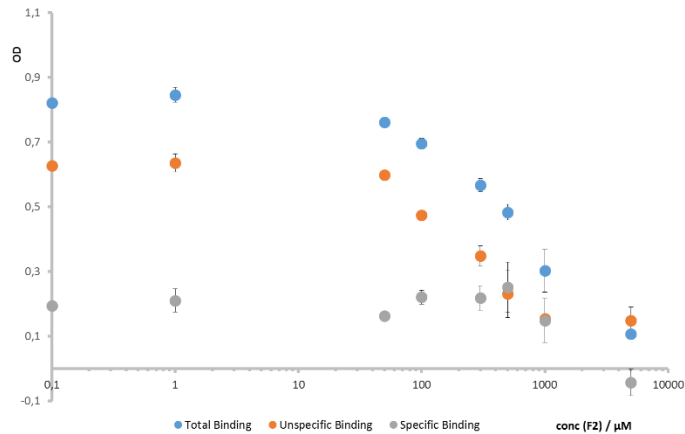


Figure 45: ELISA measurement for the fluorinated ligand **F2**. As the curve for total binding and unspecific binding converge, the ligand proves to be an $\alpha_v\beta_6$ ligand. Unfortunately, the method is not sensitive enough to calculate an affinity value.

The result is shown above in Figure 45. The two curves behave parallel for quite a wide range of concentrations until they finally converge. This means that the ligand **F2**, does interact with the integrin $\alpha_v\beta_6$.

On the other hand, the calculated curve for specific binding does again, not allow the calculation of an affinity value – the methods' sensitivity is not sufficient.

III.III.III Quartz Crystal Microbalance

In order to gain a better understanding of the binding characteristics of $\alpha_v\beta_6$ -ligands, QCM experiments were performed. Quartz crystals with a gold surface were incubated with a 4/94 solution of 1M HS-(CH₂)₁₁-EG₆-NH₂ in ethanol and 1M HS-(CH₂)₁₁-EG₃-OMe in ethanol in order to build a self-assembling-monolayer on the crystal. The amino groups were used for coupling with EMD527040 and fibronectin (via glutaraldehyde in two steps).

The integrin was injected at 20 $\mu\text{g}/\text{mL}$ in TBS + 1mM CaCl₂ + 1 mM MgCl₂ + 10 μM MnCl₂ at pH7.6. Also experiments with co-injected EMD527040 were performed in order to see whether any binding is blockable.

Unfortunately, the control sample on the non-modified SAM surface showed a very similar curve to the modified samples with a large frequency change of 30 – 33 Hz. The samples on an EMD527040 modified surface showed results from 29 – 38 Hz.

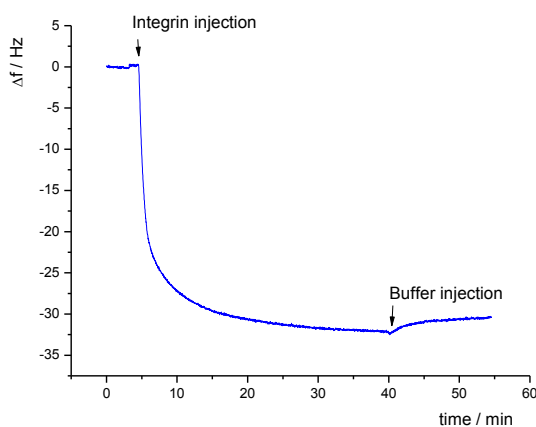


Figure 46: QCM measurement of unspecific binding - an unspecific deposition of $\alpha_v\beta_6$ to the SAM surface of -30 Hz is observed.

Unspecific binding again, like in the ELISA experiments interfered significantly with the obtainment of any quantitative data on the integrin $\alpha_v\beta_6$.

This was unexpected since the unspecific binding was only reported to be 10 Hz in a similar experiment by Wirkner et al.¹⁰⁸ In that case the integrin $\alpha_v\beta_3$ was used and the specific binding resulted in a frequency change of about 80 Hz. In their case, the monolayer was prepared with carboxy groups instead of amines for conjugation – this could be a reason for the great difference.

With the experience from the ELISA experiments, optimization of the experimental conditions is not expected to be promising and was therefore not performed.

III.III.IV Conclusion – *in vitro* experiments

The *in vitro* experiments can be concluded as such: Three different cell assays were performed for the two radiotracers **BK23** and **BK39**. Unfortunately, neither the classical Michaelis-Menten affinity assay, nor the challenge or the uptake experiments could show a binding for either one of them.

In order to prove these results, the purified integrin $\alpha_v\beta_6$ was coated onto ELISA plates, which could be proven successful in an STX-100 antibody based assay. On such modified plates, no retention of **BK23** or **BK39** could be observed neither. Therefore, it is concluded that those two compounds do not bind to the integrin $\alpha_v\beta_6$ with a suitable affinity for our approaches.

The attempts to develop a non-radioactive affinity assay based on the latency associated peptide of TGF- β 1 was not successful, in despite of thorough optimization of the experimental conditions. Finally, it was not possible to overcome the high unspecific binding of LAP to the $\alpha_v\beta_6$ /BSA surface. Only the hint, that **F2** does interact with $\alpha_v\beta_6$, can be concluded from the data – any quantification remained impossible so far.

Also, the intent to use the quartz crystal microbalance failed due to the same reason – the high unspecific binding of $\alpha_v\beta_6$ to the surface, in this case monolayers of HS-(CH₂)₁₁-EG₆-NH₂ and HS-(CH₂)₁₁-EG₃-OMe on gold.

For future development of new radiotracers for $\alpha_v\beta_6$, the test on immobilized integrin coated to ELISA plates, with measurement of the retained radioactivity, would be the most promising method, based on the experiences of this work.

III.IV Animal Studies

The two tracers **BK23** and **BK39** were tested in animals in order to investigate their properties and suitability for their application as tracers for the imaging of liver fibrogenesis. Two mouse strands were used for this purpose: Healthy wild-type animals of the FVB strand, female, between 7 and 9 weeks old and with weights ranging from 18.3 g to 20.5 g. Those were treated as the negative control. As a fibrosis positive model, a knock-out line was chosen: *Mdr2/Abcb4*^{-/-}. This strand bears a homozygous disruption of the multi-drug-resistance-2 gene¹¹³ and therefore lacks the canalicular phospholipid flippase – this is why their bile does not contain phospholipids and a spontaneous development of liver fibrosis is the consequence.¹¹⁴ The animals were also female, between 7 and 9 weeks old and weight ranges from 18.2 g to 22.8 g.

The radiotracers were freshly prepared according to our optimized protocol and taken up in saline. Between 4 and 8 MBq were injected (100 µL) as a bolus injection into the tail vein. It is of note, that the mice were not placed in the µPET scanner at the moment of injection but only transferred to the µPET scanner immediately after the injection. This means that the first 1 – 2 minutes after injection are not included in the dynamic scans over one hour.

Afterwards, the mice were allowed to wake up and sacrificed one hour later (two hours after injection) in order to harvest their organs for a quantitative impression of the tracers' distribution in tissues.

Table 6: Overview of performed animal experiments

<i>Tracer; Animal model</i>	<i>Total number of animals</i>	<i>Acquired PET images</i>	<i>Animals used for ex-vivo biodistribution</i>
<i>BK23; FVB</i>	4	2	4
<i>BK23; Mdr2^{-/-}</i>	3	3	3
<i>BK39; FVB</i>	4	2	4
<i>BK39; Mdr2^{-/-}</i>	3	2	3

The obtained results will be discussed with respect to the applied tracer.

III.IV.I BK23 – ethyl spacer

The *in vivo* behaviour of **BK23** has shown quite interesting features. First of all, the time-activity-curves (TACs) for liver, heart, bladder and muscle are displayed below. The averaged values for healthy and fibrotic animals are shown in Figure 47 as well as the single animals in Figure 48 and Figure 49. In the averaged values, one can see, that the SUV for the liver show a peak at about ten minutes, from where it is decreasing slowly. With their highest values at 1.08 and 0.79 for fibrotic and healthy mice, the ratio ranges over the whole time slope between 1.4 and 1.7. This signal-to-noise ratio is relatively low, especially if one considers the large error bars.

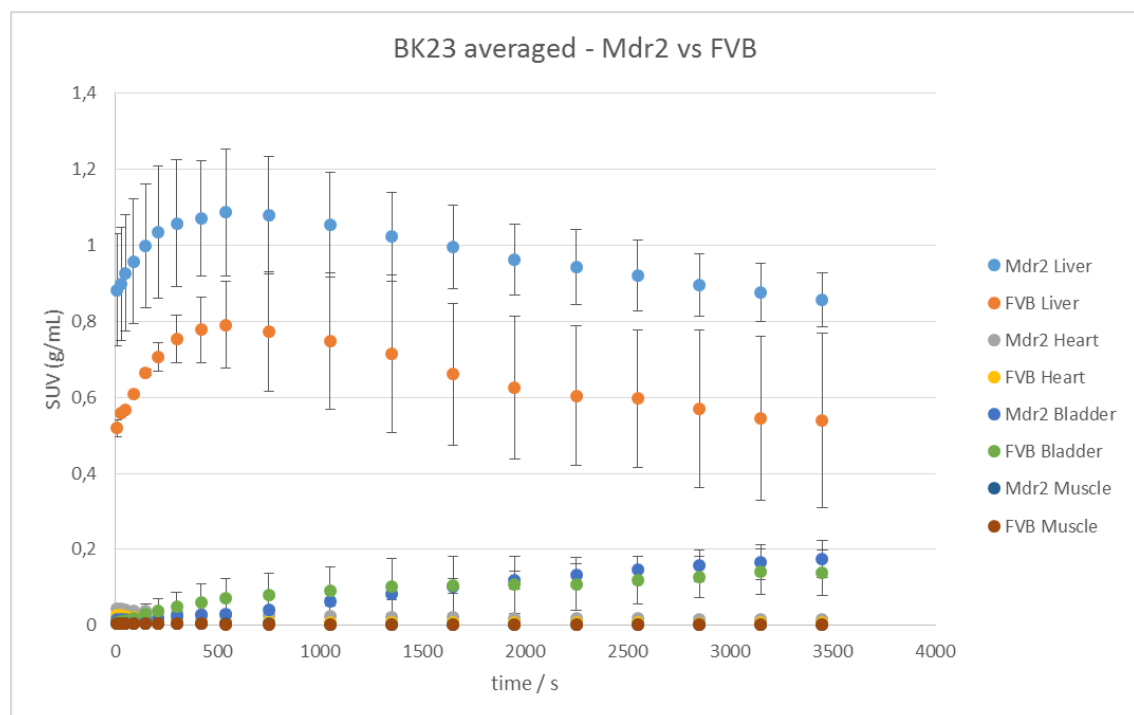


Figure 47: Averaged time-activity curves for BK23. Liver, Heart, Bladder and Muscle are displayed for both healthy as well as fibrotic mice. Values for heart and muscle are difficult to distinguish, as they overlay each other.

They are easily explained, if the TACs of the single animals are looked at. In both healthy animals the initial SUV of the liver is 0.5, while in one case (R0650) a maximum of 1 is reached, followed by a plateau at 0.8. In the second case (R0651), the reached maximum is only 0.7 which goes down to below 0.4. Interestingly, two of the fibrotic mice show the same course as R0650, a healthy sample – a maximum at 1 with a plateau of 0.8. The different starting value of 0.8 might be explained by a time difference between injection and measurement start in the two cases.

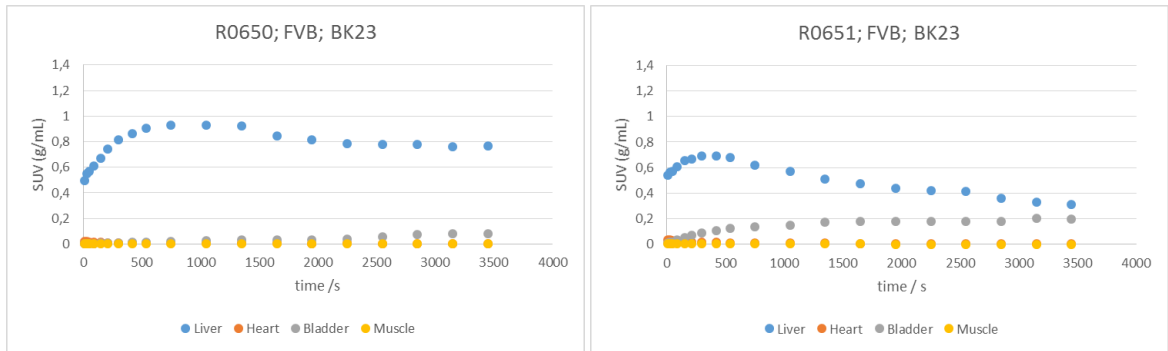


Figure 48: Time-activity-curves for healthy FVB mice. Liver, Heart, Bladder and Muscle are displayed. The values for heart (orange) can hardly be seen, as they are similarly low as the ones in muscle (yellow).

For the knockout mice, one exception was observed with sample R0648: A maximum of 1.3 was reached which decreased over time to 0.9, which is actually not very different from 0.8. It is therefore questionable, if a signal difference between healthy and fibrotic mice can be claimed at all.

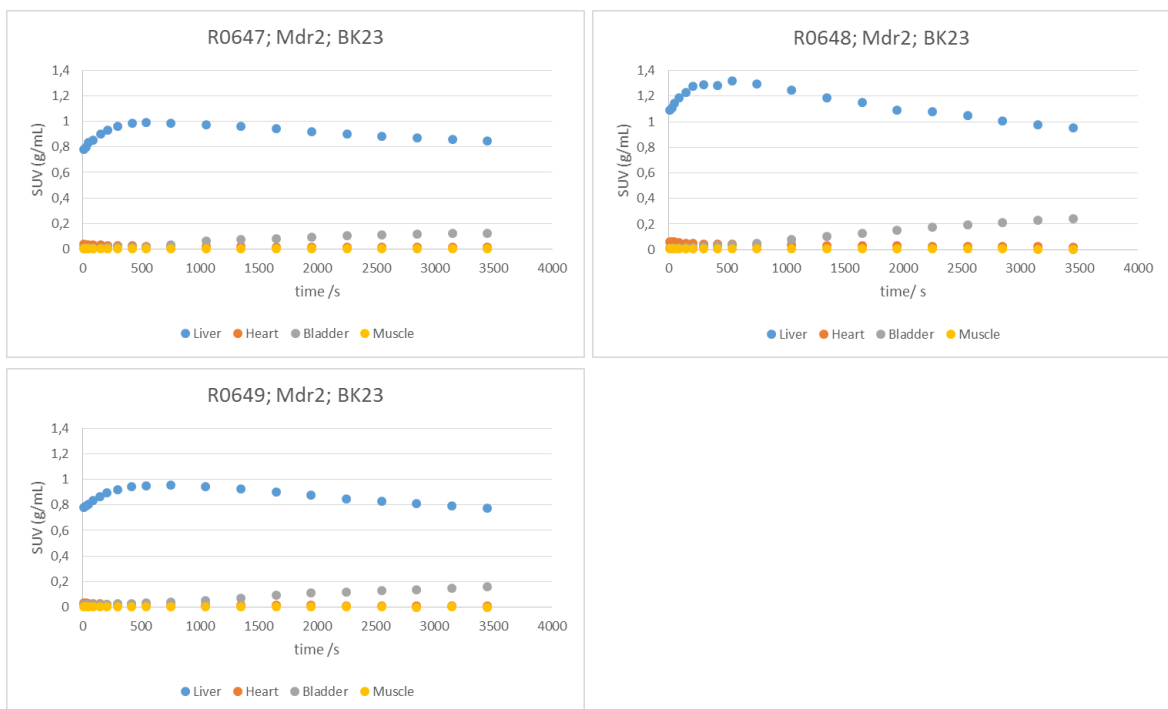


Figure 49: Time-activity-curves for fibrotic Mdr2^{-/-} mice. Liver, Heart, Bladder and Muscle are displayed. The values for heart (orange) can hardly be seen, as they are similarly low as the ones in muscle (yellow).

Apart from that, it could be observed that after one hour in both healthy as well as fibrotic mice, an SUV between 0.1 and 0.2 was present in the bladder. Heart and muscle did not show any uptake at all, apart from very low initial values.

If the obtained images are investigated optically, another important destination of the tracer BK23 could be observed. The tracer seems to accumulate in the intestines, moving through the whole abdomen. This is witnessed in both healthy as well as fibrotic animals. As it moves, the definition of volumes-of-interest (VOIs) seemed nearly impossible – which is why a quantitative analysis was omitted in this case. Below, this can be seen in representative images.

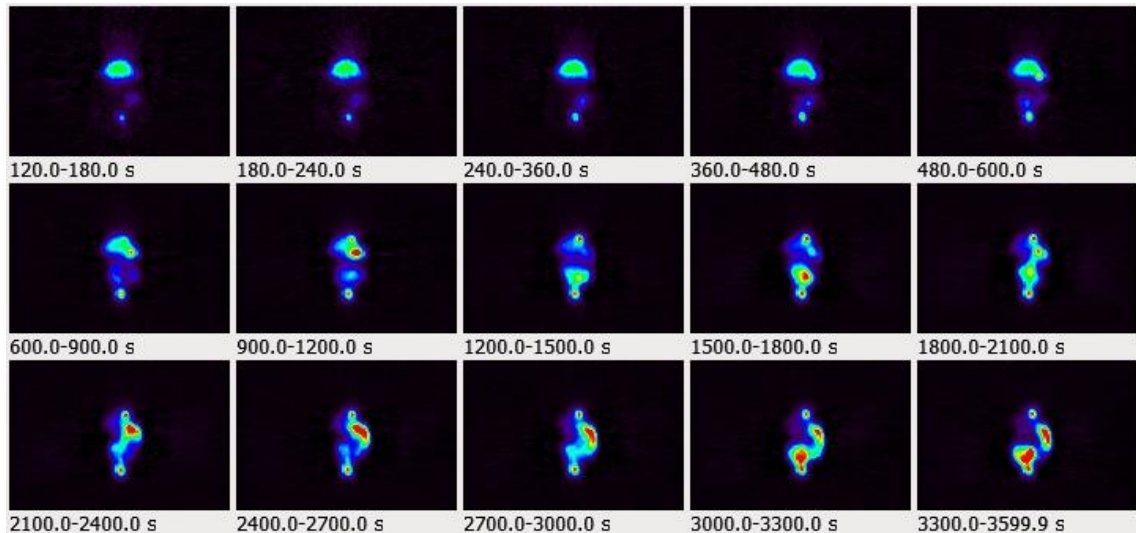


Figure 50: Dynamic μ PET scan. Tracer: BK23. Wild-type.

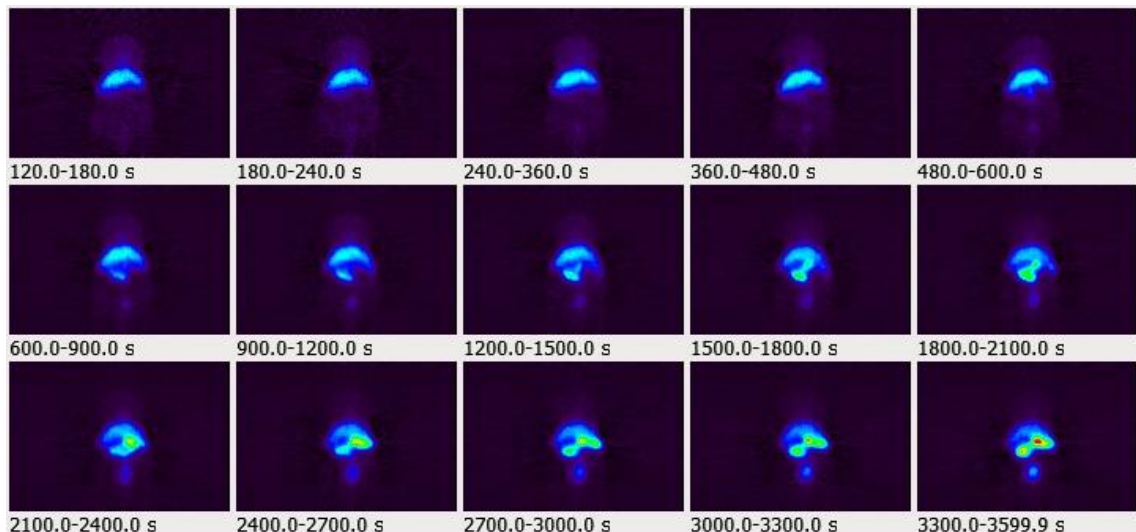


Figure 51: Dynamic μ PET scan. Tracer: BK23. *Mdr2*^{-/-} knockout mouse.

A possible hypothesis to explain this observation could be that the tracer is quickly metabolized in the liver – and subsequently excreted into the intestines. The images support such a hypothesis, as in the initial frames the intestinal accumulation is not observed.

For ex vivo biodistribution studies, values were obtained which fit relatively well to the obtained images. The livers were dissected into left, right and medium lobe, but no significant difference could be observed here. But apart from intestine and urine, they showed the highest uptake values of 1.5 % ID/g for fibrotic animals and 0.7 % ID/g for healthy controls. This signal-to-noise ratio of 2.1 displays significance, if subjected to a statistical student t-test. Also the differences for blood, kidney, intestines, heart, lungs, ovary and femoral bones displayed significance – but all of them were below 0.3 % ID/g, except the intestines with 4.8 % ID/g difference between knockout and wild-type mice.

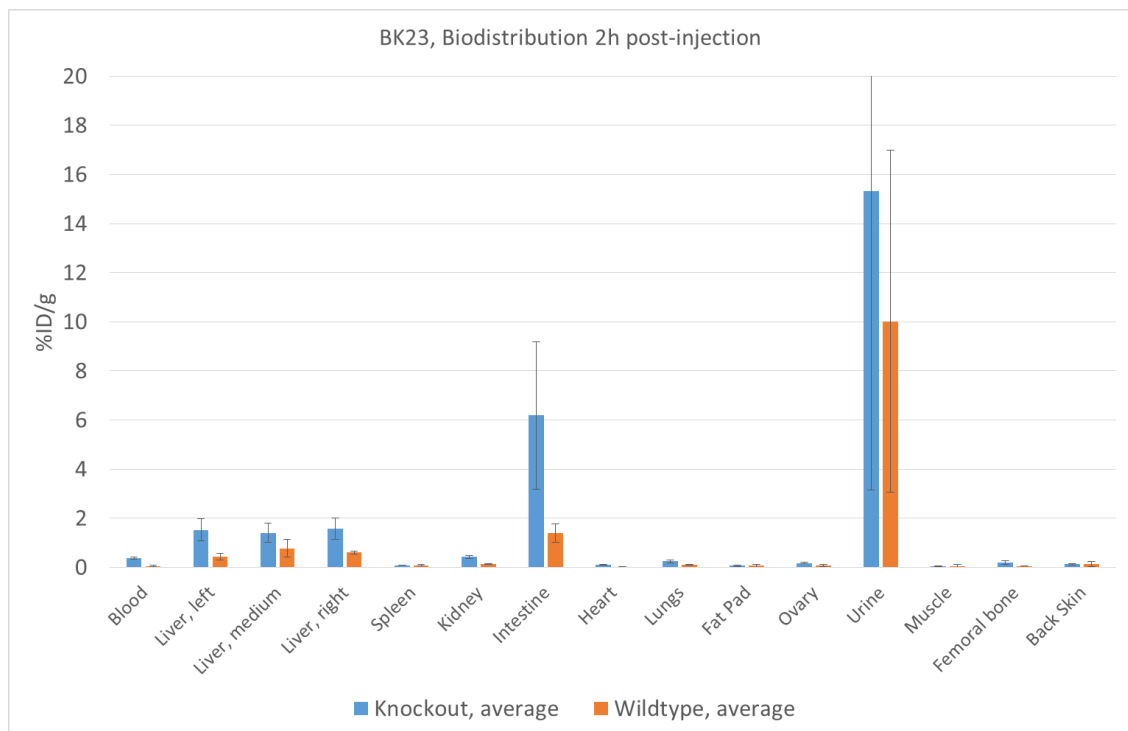


Figure 52: Averaged values of ex vivo biodistribution study, 2 hours post-injection.

The question remains, whether this difference is related to binding to $\alpha_v\beta_6$ or – getting back to the metabolism-hypothesis mentioned above – the kinetics of metabolomic pathways are different in wild-type and fibrotic animals. The higher retention in knockout animals could for example be related to a slower degradation.

The obtained values for the single animals can be seen below in Figure 53.

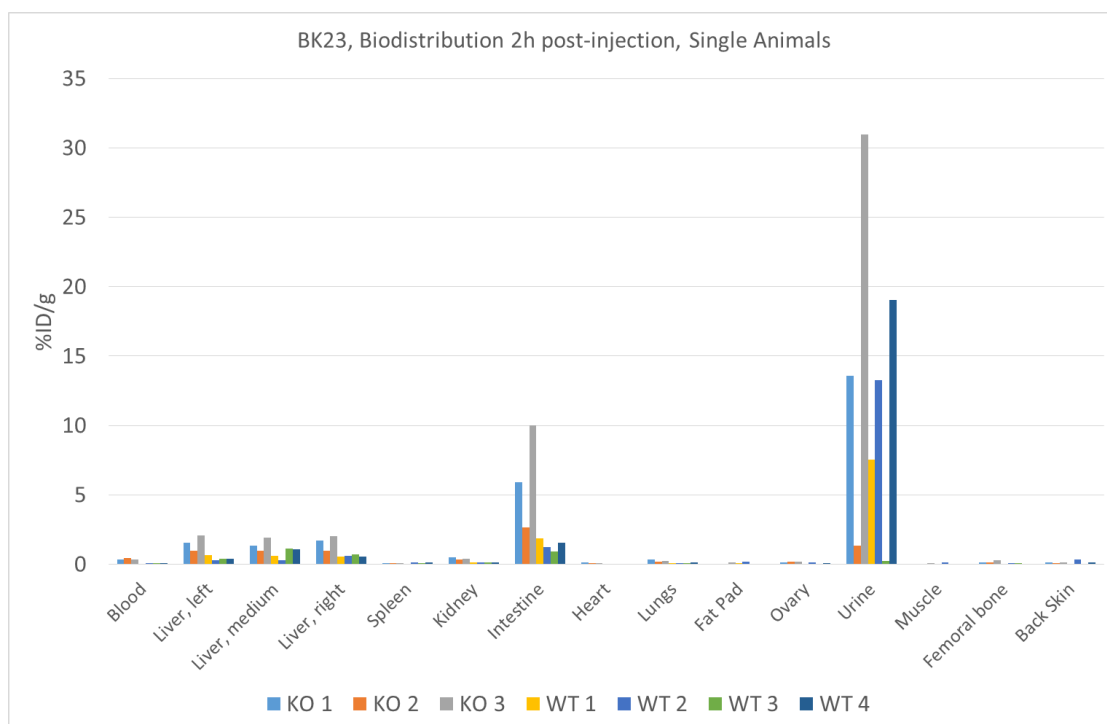


Figure 53: Single Animal results of the ex vivo biodistribution study; 2 hours post-injection. KO = Knockout; WT = Wildtype.

III.IV.II BK39 – oligo-ethylene-glycol-spacer

The larger tracer **BK39** has behaved rather differently from **BK23**. Upfront, it has to be mentioned that for one of the wild-type mice the PET measurement had to be disrupted and restarted due to unexpected movements of the mouse. Those two measurements had to be aligned manually for time, which may result in uncertainties of about one minute – which seems negligible at time points after 20 minutes. Nevertheless, certain cuts in the curves can be observed, but were not rated significant to exclude the obtained data from interpretation. Again, the TACs will be displayed first of all. In this case, unlike for **BK23**, it was possible to determine SUVs for the kidneys.

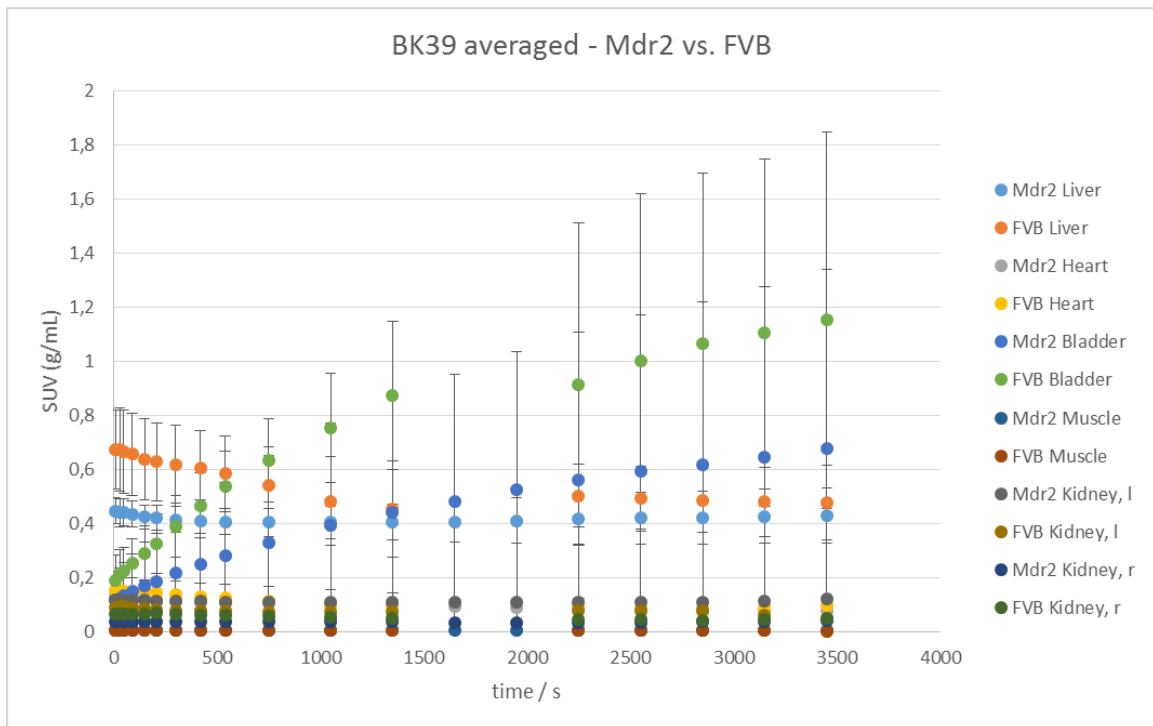


Figure 54: Averaged time-activity curves for BK39. Liver, Heart, Bladder, Muscle and the kidneys (left and right) are displayed for both healthy as well as fibrotic mice. Values for heart and muscle are difficult to distinguish, as they overlay each other.

As displayed in Figure 54, the highest SUV values are observed in the bladder for both FVB as well as Mdr2^{-/-} mice. Also, the uptake in the kidneys is not negligible anymore with initial values over 0.1. The decrease in the kidneys and increase in the bladder over time suggest an elimination pathway which is of (mainly) renal nature. For the liver – the organ of our interest – there is an initial slightly higher uptake for healthy animals compared to fibrotic Mdr2^{-/-} mice, while the two curves converge towards the end of the measurement.

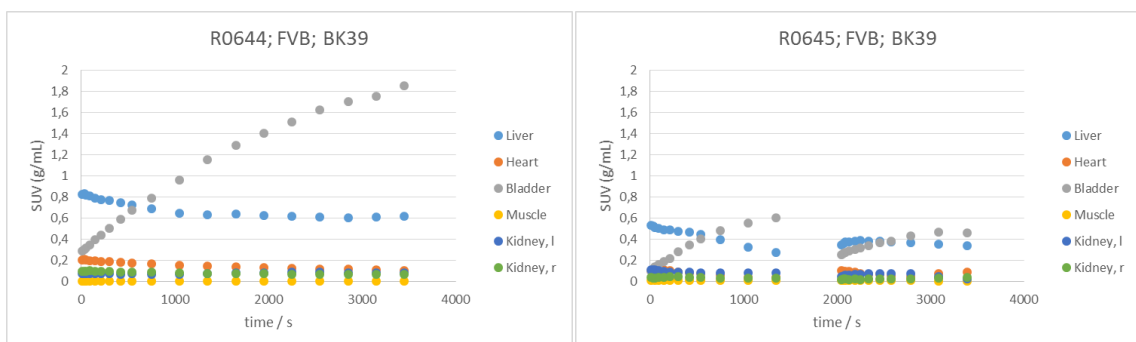


Figure 55: Time-activity-curves for healthy FVB mice. Liver, Heart, Bladder, Muscle and Kidneys are displayed. The R0645 measurement was interrupted and manually aligned for time.

Two of the cases stand out from the rest: In R0644 the liver value was higher than in all other individuals. Interestingly, R0644 is a healthy FVB mouse. For a tracer suitable for imaging liver

fibrogenesis, we would expect the higher values for the severely ill mice. Apparently, the variability observed already among wild-type animals is rather large and therefore unfortunately disqualifies the tracer for use in this purpose.

But, another interesting information can be obtained from the images – also, the elimination kinetics seem to vary for individual animals. All subjects suggest a renal pathway – three out of four show strongly increasing SUVs in the bladder over time up to 1.8. But one of them (R0642) does not display any bladder uptake – but then the kidneys display values of 0.1 and 0.2 which is about double as high as all the other animals examined in this study. Likely, the excretion of urine from kidneys into the bladder has apparently been halted in this case.

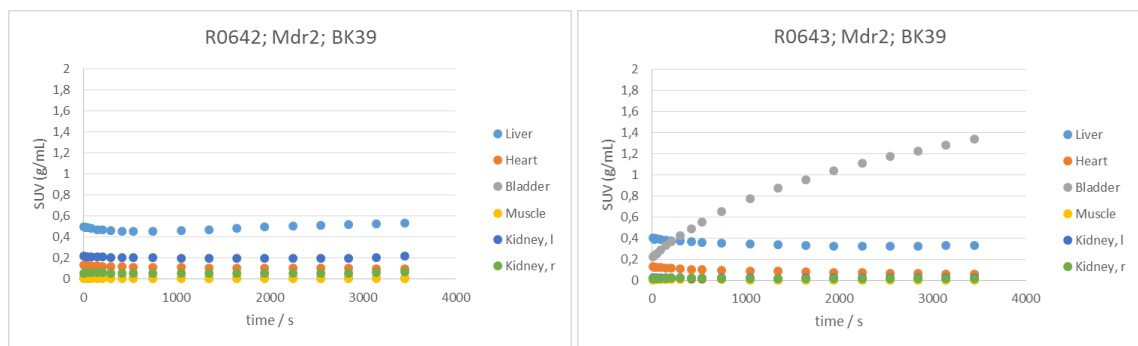


Figure 56: Time-activity-curves for fibrotic *Mdr2*^{-/-} mice. Liver, Heart, Bladder, Muscle and Kidneys are displayed. It is of note, that in one case (R0642) the kidney values were significantly higher but no uptake was observed in the bladder. Both kinetic profiles support the hypothesis of a renal elimination pathway.

Furthermore, in the case of **BK39**, SUVs for the heart are not close to zero (like for **BK23**) but ranging from 0.1 to 0.2. The uptake in this tissue is also shown clearly in the reconstructed images from the μ PET measurement.

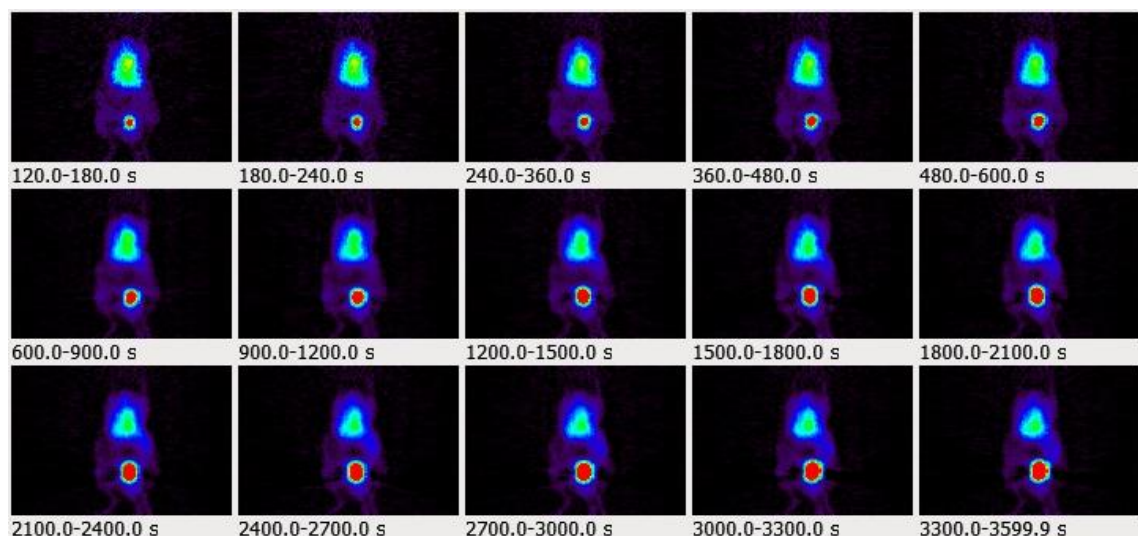


Figure 57: Dynamic μ PET scan. Tracer: BK39. Wild-type.

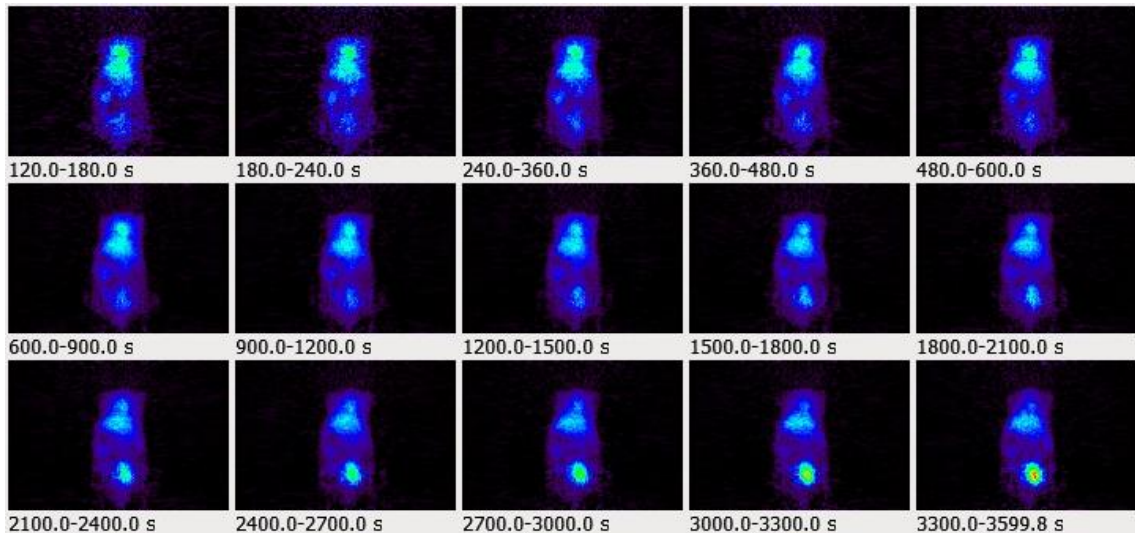


Figure 58: Dynamic μ PET scan. Tracer: BK39. *Mdr2*^{-/-} knockout mouse.

The frontier between liver and heart converges in the case of the wild-type in the coronal view and can be seen better in the knockout example above (Figure 58). Nevertheless, together with axial and transversal view an accurate delineation was possible.

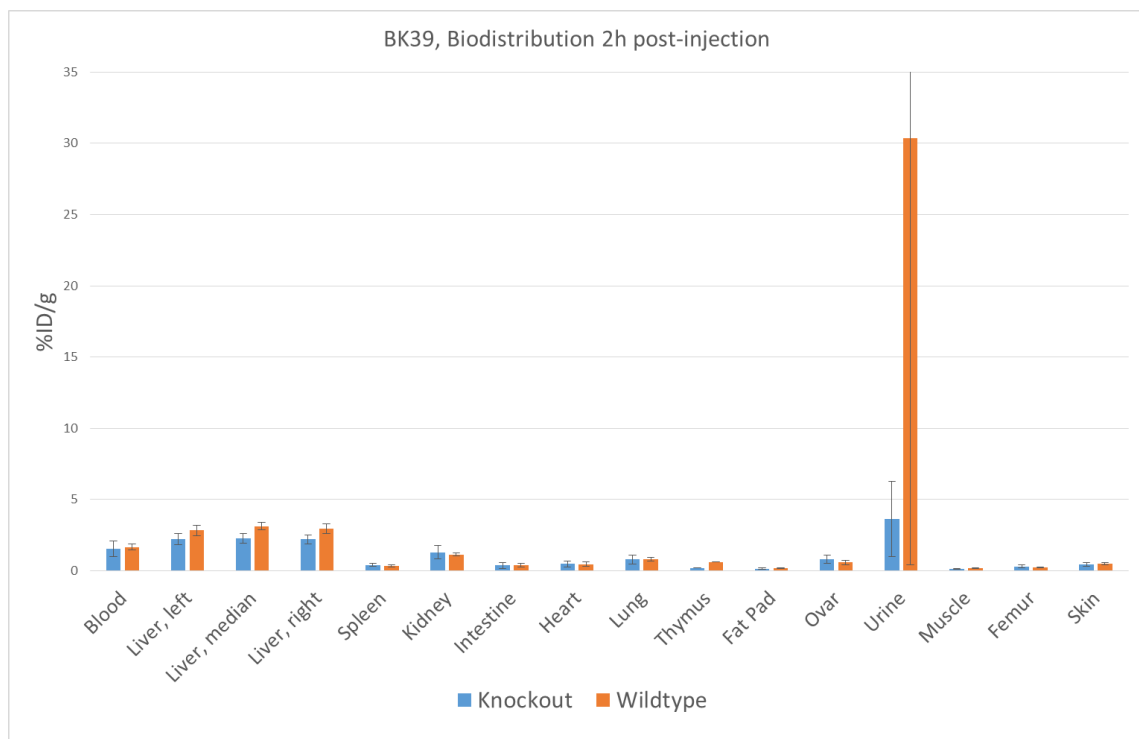


Figure 59: Averaged values of ex vivo biodistribution study, 2 hours post-injection.

Biodistribution studies two hours post-injection showed the liver as the organ of highest uptake apart from the urine. Values of 2.2 % ID/g were obtained for the knockout mice and 2.8-3.1 % ID/g for the wildtype strand. The kidney values (1.3 and 1.1 % ID/ g) also support the renal

elimination hypothesis. Generally, the pattern is in good agreement with the obtained image data. According to students' t-test, for none of the organs, the null hypothesis can be rejected – the differences are not statistically significant.

The obtained data of the single animals can be seen below in Figure 60.

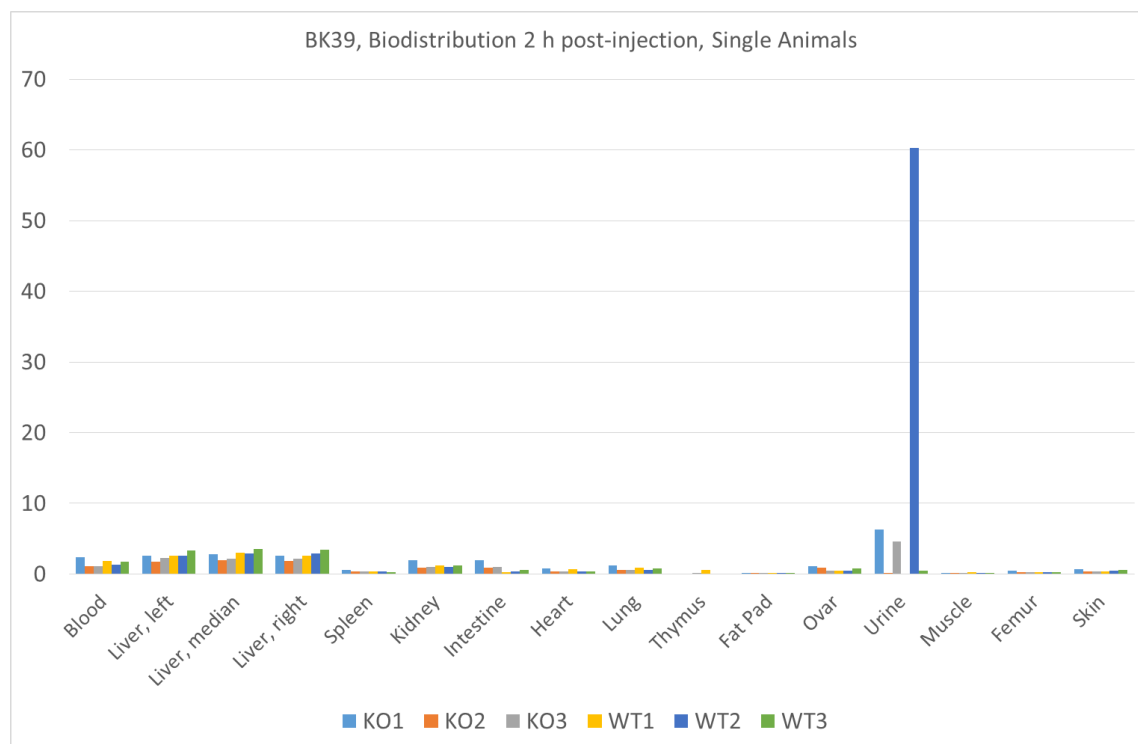


Figure 60: Single Animal results of the ex vivo biodistribution study; 2 hours post-injection. KO = Knockout; WT = Wildtype.

III.IV.III Summary

Unfortunately, it has to be concluded, that none of the two new radiotracers seems to be suitable as a liver fibrogenesis marker. Even though for both substances a liver uptake was observed both in μ PET as well as in biodistribution studies – no significant difference between healthy and fibrotic animals could be observed, which is essential for the successful application as a diagnostic tool.

Nevertheless, some useful insight for the design of future compounds could be drawn from these results. With molecular weights of 1014 and 1262 g/mol, both substances find themselves far from the renal filtration threshold of 70.000 g/mol. Therefore, for both of them, a renal elimination pathway was expected. It could be seen both in μ PET images as well as in the

biodistribution data (higher values for intestines) that the smaller tracer substance **BK23** has been metabolized – at least partly – via entero-hepatic mechanisms. This was unexpected, but is probably due to the higher lipophilicity of the compound. In order to obtain high quality images, with a specific signal due to receptor-mediated accumulation rather than unspecific metabolic processes, the renal excretion pathway should be a precondition to be fulfilled by a suitable compound. In order to achieve this, a logD value of below -0.19 therefore seems to be a requirement which future substances should fulfil.

III.V Computational Studies

In order to gain a better understanding of the molecular requirements, a suitable substance for our purposes needs to fulfil, the interaction of small molecules with the receptor $\alpha_v\beta_6$ was subjected to computational studies. First of all, ligands of known affinities were compared for structural similarities to derive such prerequisites and later compared to our own compounds. Additionally – as there is no crystal structure available in the literature – a model was constructed with homology modelling methods. Subsequently, docking studies of those were performed.

III.V.I Small Molecules / Ligands

In total, 17 structures have been investigated for their chemical characteristics and will be described in the following. Four of them are literature known ligands described by Goodman et al.¹⁰² in 2002, displaying a high affinity for $\alpha_v\beta_6$. The other 13 structures are either EMD527040 itself (in all four diastereomers, presented results will be based on the S,S-diastereomer), our own ⁶⁸Ga-labelled compounds **BK23** and **BK39** as well as other possible ⁶⁸Ga- or ¹⁸F-labelled derivatives of EMD527040. Also, the ^{99m}Tc-derivatives, described by Schuppan et al.⁹⁹ have been studied.

First of all, the structures have been drawn and energy minimized – this was not trivial, as first trials with software packages like for example VEGA ZZ¹¹⁵ did not support the metals Ga and Tc. Most Molecular Mechanics software focus on purely organic compounds, therefore, many commonly used force-fields do not contain any parameters for either metals at all – or only for

biologically more common metals like magnesium, calcium or iron. A way to overcome this problem was the use of the Universal Force Field (UFF).⁸⁸

This is implemented in the software Avogadro.¹¹⁶ Structures were drawn therein, and an energy minimization could be performed with a 500 step steepest descent algorithm by use of the AutoOpt tool with a convergence value of 10^{-7} . Afterwards, all hydrogens were removed and added again for pH7.4. By this way, initial structures were obtained to further work with.

All structures have three features in common: they consist of a basic part, an acidic part and a hydrophobic (aromatic) part in between them. This mimics the classical RGD binding motif – arginine being basic, glycine hydrophobic (or at least non-polar) and aspartate acidic. Most studies dealing with the binding mechanism of RGD-binding integrins, target $\alpha_v\beta_3$ as it is thoroughly studied for many applications and its crystal structure is available.¹¹⁷ The generally proposed binding mechanism claims that arginine builds two bidentate salt-bridges with two aspartate residues located in the β -propeller of the α -chain. On the other hand, the aspartate of the RGD ligand comes into contact with a divalent cation located at the “metal ion-dependent adhesion site” (MIDAS) of the β -chain.¹¹⁸

For the study of electronic characteristics, input files for MOPAC2012⁸³ were generated within Avogadro, reopened again with text editor and changed the keywords into the following:

```
AUX LARGE CHARGE=N SINGLET PM7 GRAPHF VECTORS MMOK EIGS
```

First of all, the keyword `AUX` allows the output of auxiliary information which is needed if the file should be readable for other programs – this is extended by `LARGE` from only 20 molecular orbitals (M.O.) around the HOMO-LUMO gap to all M.O.s. The charge of the overall system was set manually to the correct value `N` for each single molecule. The keyword `SINGLET` does not allow any other spin state than singlets during the calculation.

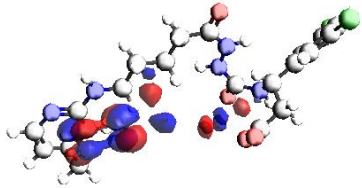
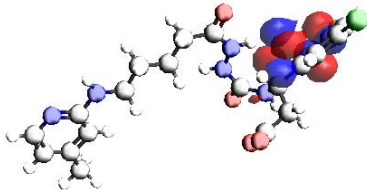
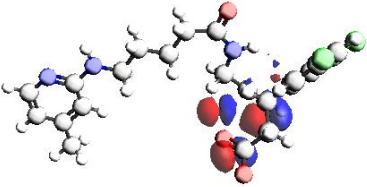
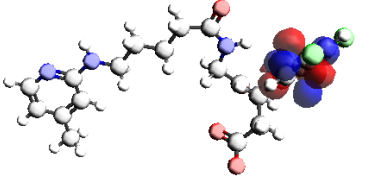
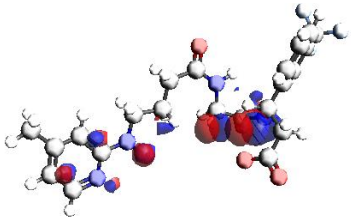
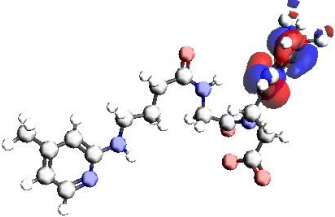
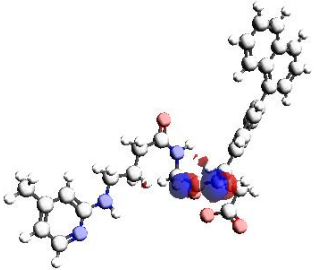
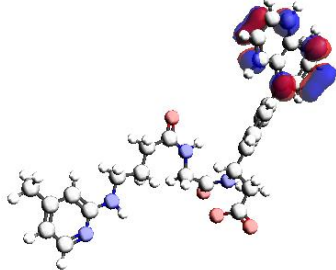
An important choice is the keyword `PM7` – as outlined in the theoretical chapter, `PM7` is a semi-empirical method, which uses not only mathematical methods to solve the Schrödinger equation, but contains set parameters which allow the exclusion of inner shell electrons for the calculations. `PM7`, compared to its predecessors, contains parameters for transition metals and was improved with regard to non-covalent bonds.⁸²

`GRAPHF` prints the results in a format suitable for graphics, while `VECTORS` includes all final eigenvectors. The keywords `MMOK` and `EIGS` stand for the use of molecular mechanics corrections

of CONH bonds and the printing of all eigenvalues of every iteration – which is important for the visualization of M.O.s.

First of all, the obtained structures and M.O.s for the literature ligands¹⁰² will be displayed and discussed below – the original numbering of the manuscript will be kept.

Table 7: Location of HOMOs and LUMOs of the $\alpha_v\beta_6$ binding literature ligands by Goodman et al.¹⁰²

Structure	HOMO	LUMO
8		
9		
10		
11		

The displayed structures in Table 7 show similar electronic characteristics: The HOMOs are located close to the acidic part of the molecule, whereas the LUMOs are found in the aromatic rings in the middle of the molecules.

If the next four orbitals with higher energies than the LUMO are considered – they are found in all cases at the basic guanidinium part of the molecules as well as the aromatic middle part.

For EMD527040, it was found that the situation is the other way around: the LUMO is found at the guanidinium position, whereas the higher LUMOs+1 up to LUMO+4, are found at the hydrophobic benzyl position (confer Figure 61).

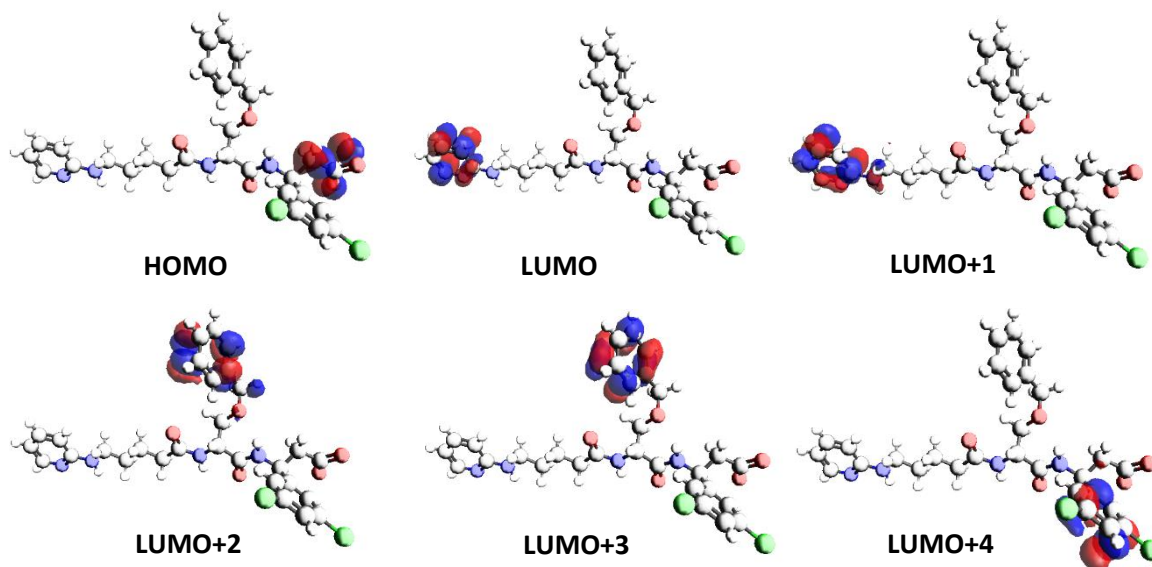


Figure 61: Orbital locations of EMD527040.

If these orbital locations are compared to those of cilengitide (a high affinity $\alpha_v\beta_3$ ligand), one can observe some differences (Figure 62). While the HOMO is found at the carboxy function as well, the LUMOs are found in this cyclic pentapeptide at the two residues that do not correspond to any of the three parts of the $\alpha_v\beta_6$ -ligands. Some are even found at the carbon backbone and not even in the side chains.

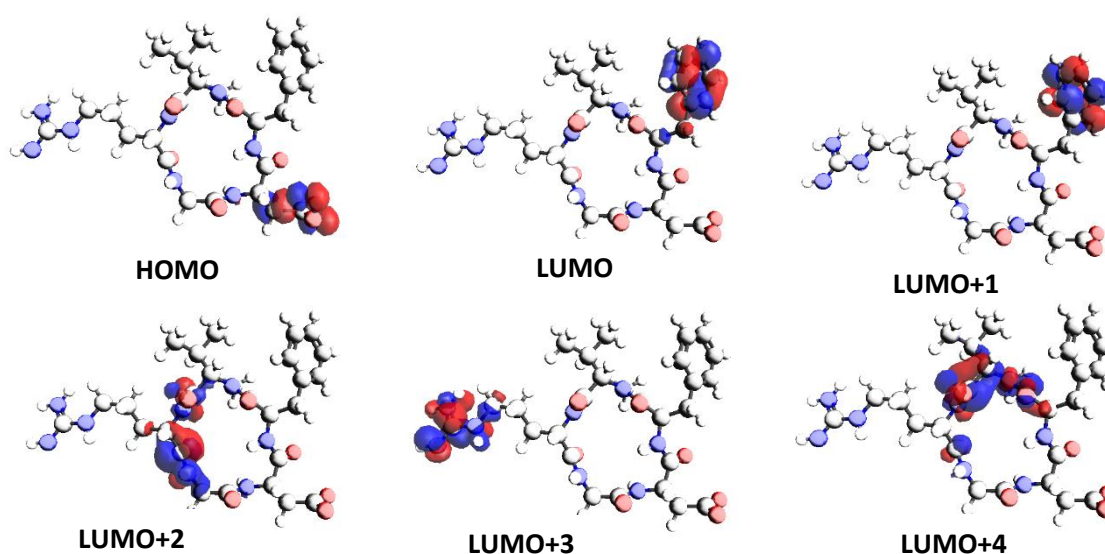


Figure 62: Orbital locations of cilengitide - a typical $\alpha_v\beta_3$ ligand.

Another feature which was compared for the ligands is the electrostatic potential map, which was generated for the literature compounds as well as the synthesized and hypothesized ligands.

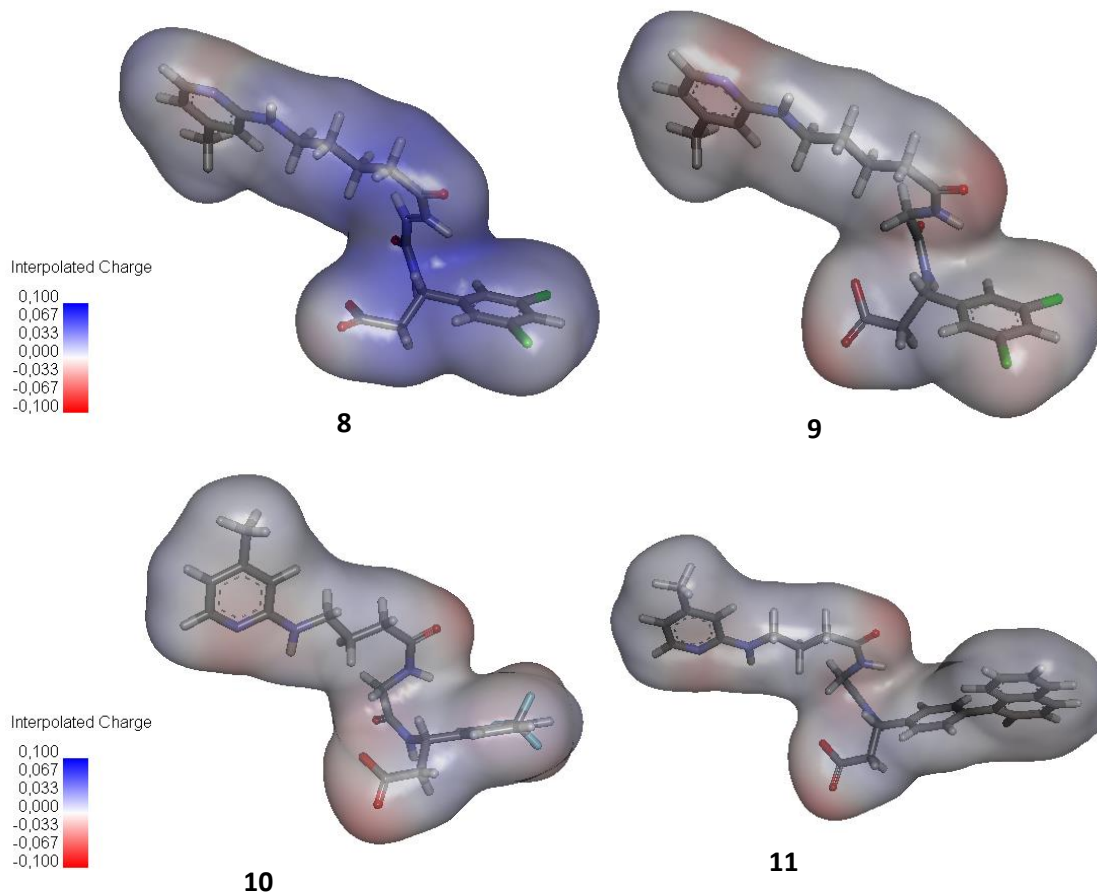


Figure 63: Interpolated Charges of α 66-binding ligands. Color code: Red = negative; blue = positive.

It can be seen in Figure 63 that ligands from literature are relatively neutral, showing negative parts at the carboxy function. Only compound **8** is rather positive in the middle part of the carbon backbone, which is due to its aza-moiety. Interestingly, compound **9**, **10** and **11** all show better affinities than compound **8** (even though 1.7 nM obviously is still a very good value).¹⁰² EMD527040, as depicted in Figure 64, is similarly neutral with negative parts at the carboxy group and slight positivity at the guanidine moiety.

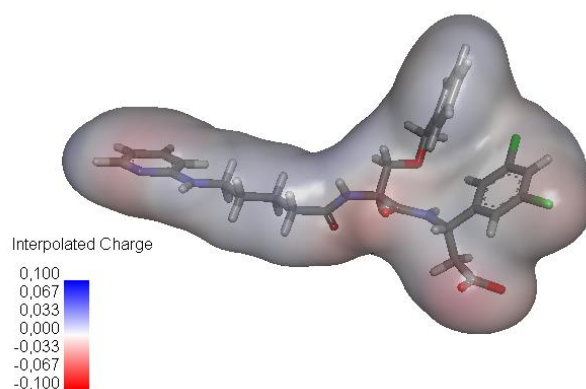


Figure 64: Interpolated Charge of EMD527040. Color Code: Red = negative; blue = positive.

Those characteristics were also investigated for EMD527040-derivatives with potential fibrogenetic tracer usage.

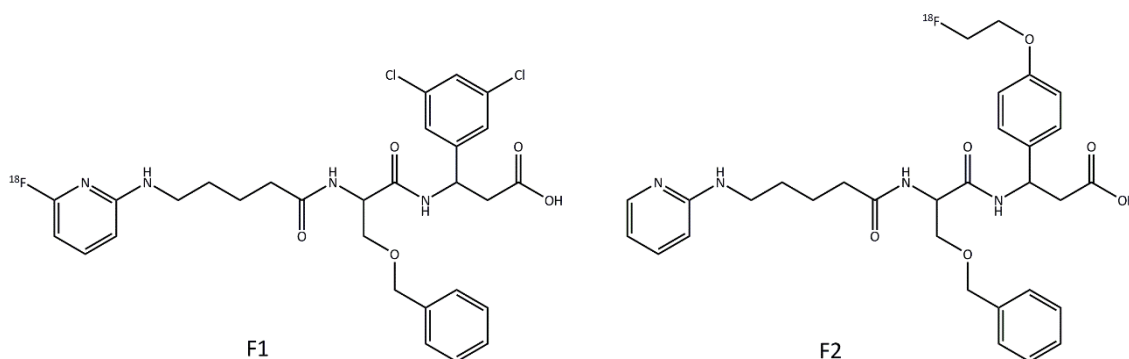


Figure 65: Possible ^{18}F -fluorinated derivatives of EMD527040.

In Figure 65 and Figure 66 the derivatives **F1** and **F2** which were further investigated are depicted. While Figure 65 shows two possible versions for ^{18}F -radiofluorination, Figure 66 shows the two tracers **BK23** and **BK39** as well as two further ligands, where the linkage with the chelator moiety would be performed via a phenolic or phenylpropanoic acid moiety. This is also the case for **F2**, the ^{18}F -ethyl-fluorinated ligand. **F1** displays the smallest structure variation in this case, as the radiofluorine would be introduced directly to the pyridine moiety.

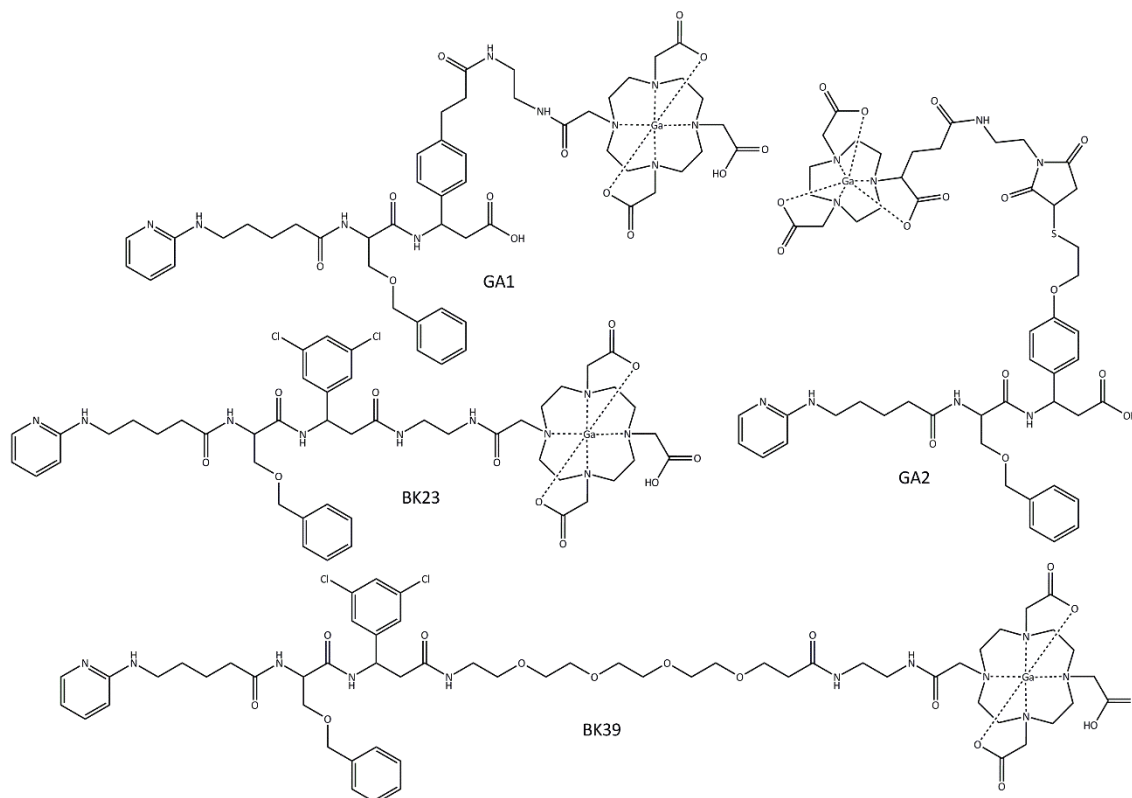


Figure 66: Potential ^{68}Ga -labelled derivatives of EMD527040

Furthermore, the $^{99\text{m}}\text{Tc}$ -labelled tracers described by Schuppan et al.⁹⁹ can be seen in Figure 67 below. The mono-, di- and trimeric EMD527040-derivatives on an adamantane scaffold, named **TC1**, **TC2** and **TC3** within this work.

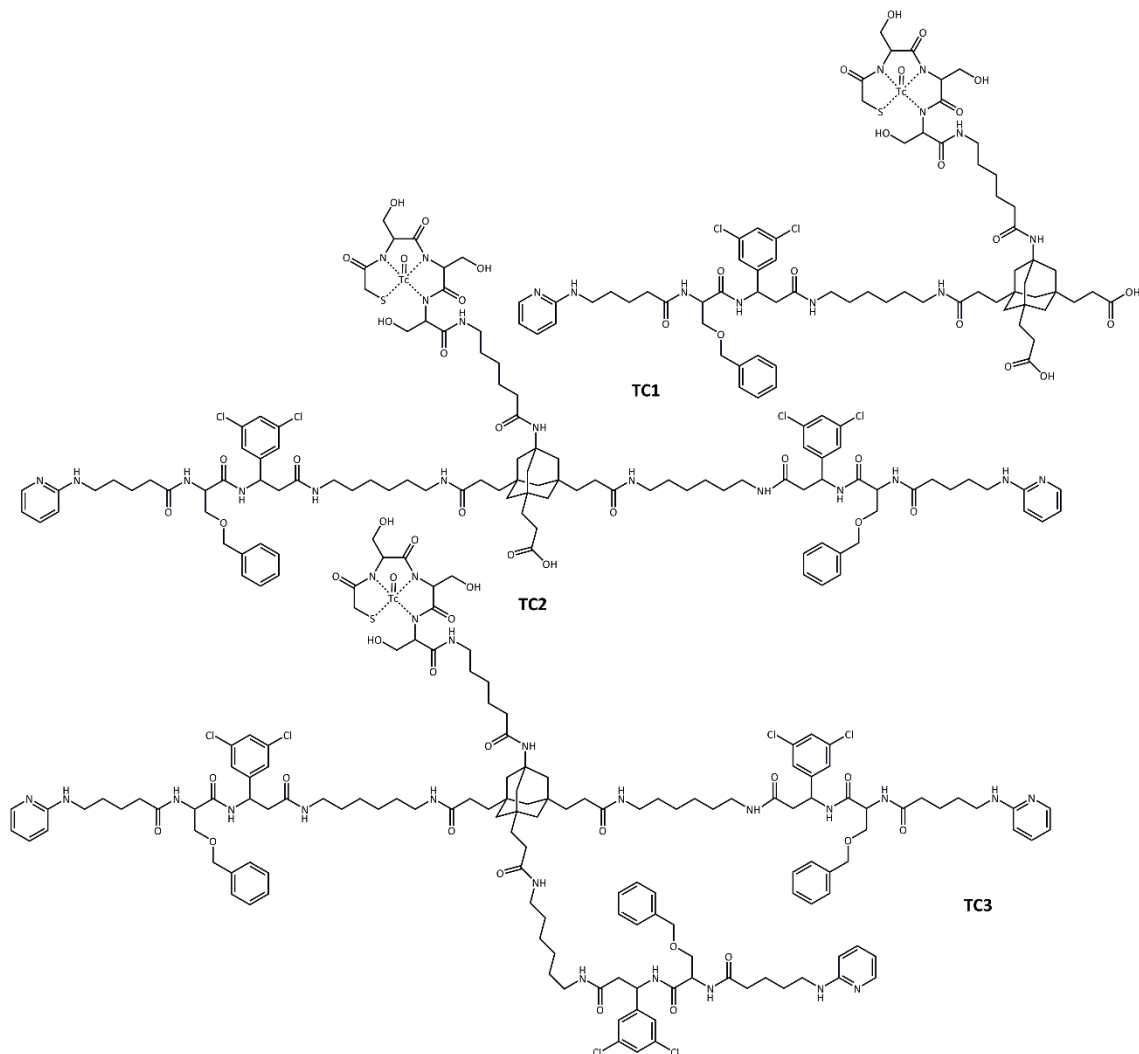


Figure 67: Structures of TC1, TC2 and TC3; mono-, di- and trimeric EMD527040-derivatives for ^{99m}Tc -labelling on an adamantane scaffold.

First of all, the electronic situation for the fluorinated derivatives **F1** and **F2** will be described. It is depicted in Figure 68 and shows clearly, that these small changes in the molecule do not have a great impact. The situation is very similar to EMD527040 with the HOMO located at the carboxy function and the LUMO located at the guanidine moiety. It is not depicted here, but also the higher LUMOs (1-4) are located similarly in the guanidine- and benzyl-moiety. This is the case for both **F1** and **F2** – the introduction of a fluorine into the pyridine or a fluoro-ethyl-group at the 3,5-dichloro-phenyle position do not seem to represent drastic changes.

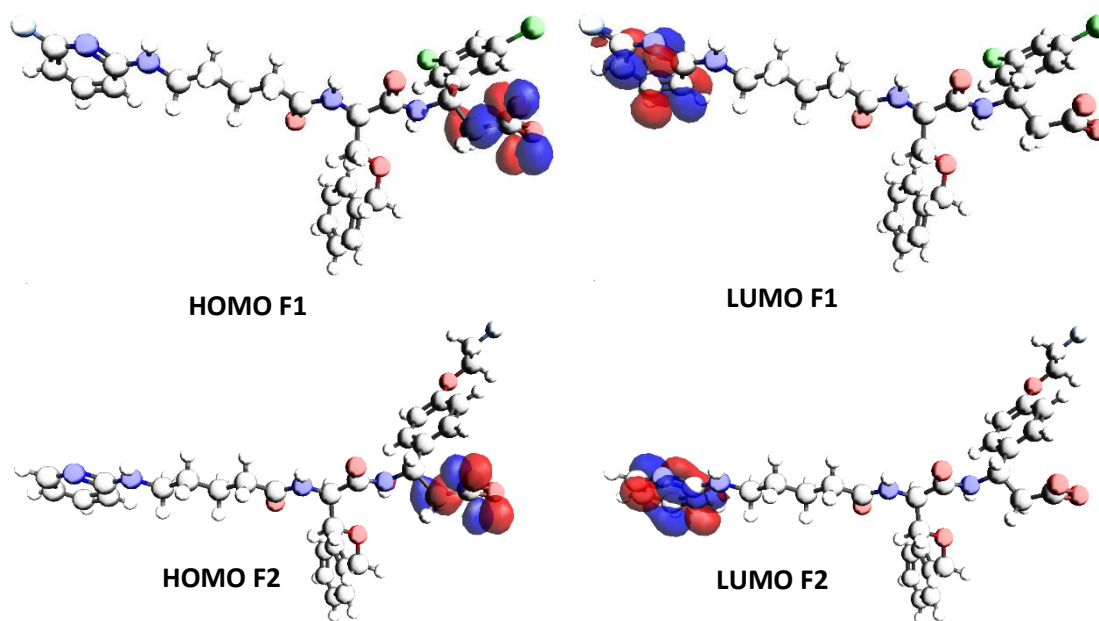


Figure 68: Localization of HOMO and LUMO for the fluorinated derivatives of EMD527040 F1 and F2.

The situation is very different for the tracers **BK23** and **BK39**. This situation is shown in Figure 69. For **BK23**, the HOMO as well as the LUMO are found within the metal complex and not near any part of the lead structure of EMD527040. Worth mentioning, the rather linear structure which could be observed for all ligands from literature discussed so far as well as for **F1** and **F2**, is not present anymore. Instead, a bent conformation is observed. The guanidine and the 3,4-dichloro-moiety bend towards the metal complex while the benzyl-group stretches away from it.

The same conformational observations can be made for **BK39**. The lead part of the molecule is bent towards the metal complex, while in this case the situation for benzyl- and 3,5-dichloro-phenyl-moiety is reversed. Benzyl- and guanidine-groups are bending to the metal complex. Furthermore, the flexibility of the tetra-ethylene-glycole linker allows it to form a 'loop' and hence shorten the intended distance between lead and metal complex to almost the same as in the case of **BK23**. This loop is surely not the only true conformation, but the tendency towards some form of 'knotting' resulting shorter distances can be assumed.

With regard to the orbitals, there is a difference to **BK23**. While both HOMO and LUMO are located within the metal complex in this case, for **BK39** only the LUMO is located there. The HOMO is found in the guanidine-moiety, which is contrary to the findings of the literature ligands as well as the lead structure EMD527040. In those examples, the guanidine-moiety bears the LUMO instead of the HOMO.

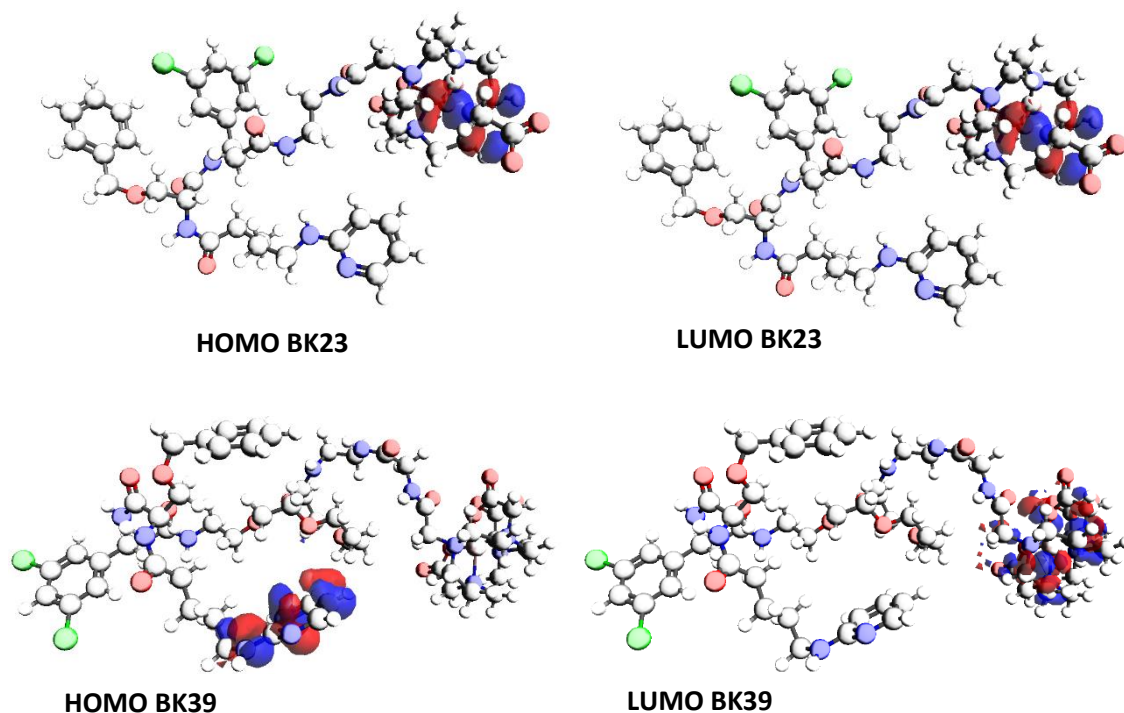


Figure 69: Localization of HOMO and LUMO for the Ga-labelled derivatives of EMD527040 BK23 and BK39.

The other two derivatives suitable for labelling with ^{68}Ga , show different characteristics again. The orbital location of **GA1** and **GA2** can be seen in Figure 70. Interestingly, the conformational form of those ligands is back to the rather linear form, which was observed for the literature ligands described by Goodman et al. and the lead structure EMD527040.

The metal complex does not seem to interfere that much with the residual molecule parts, if it is connected via the 3,5-dichloro-phenyl-moiety.

With regard to the orbitals – they show similarities to the other metal complex bearing compounds as well as to literature ligands and lead structure. The HOMO can be found at the acidic moiety just as for EMD527040, while the LUMO is located within the metal complex.

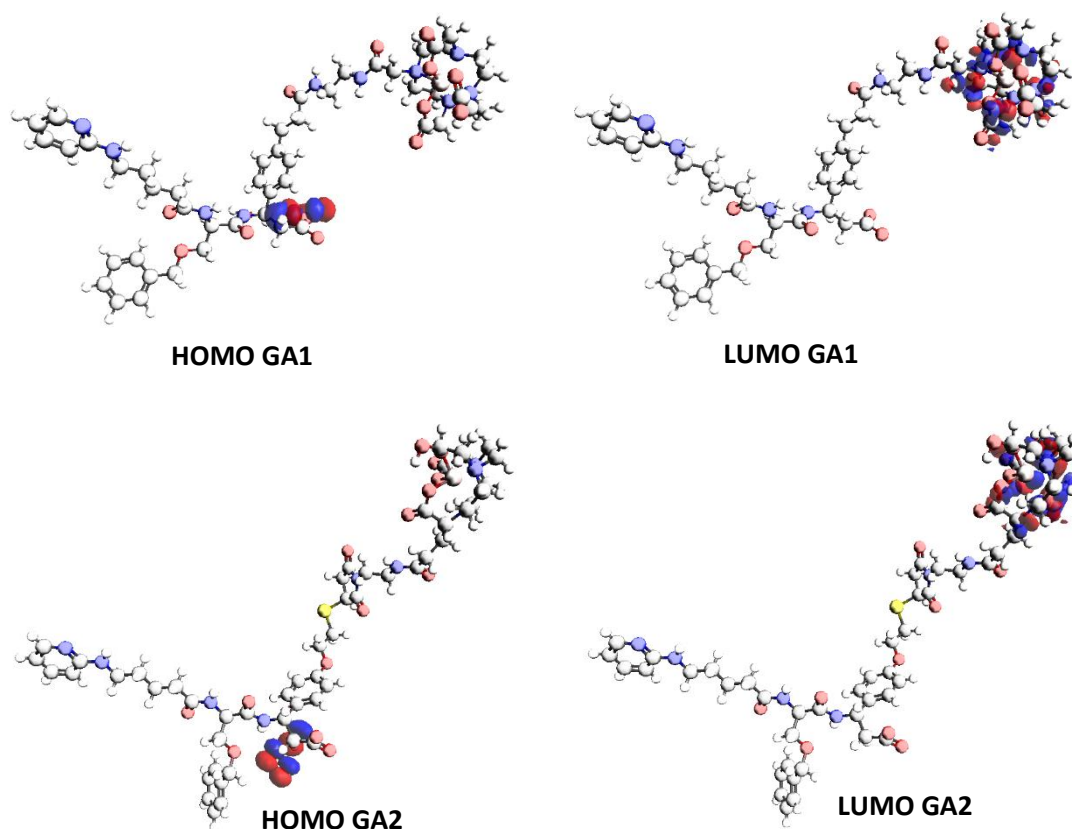


Figure 70: Localization of HOMO and LUMO for the Ga-labelled derivatives of EMD527040 GA 1 and GA 2.

The situation for ^{99m}Tc -labelled derivatives can be seen in Figure 71. Similar to **GA1** and **GA2**, the rather linear structure of the lead compound is kept for **TC1** and **TC2**, only slight bending can be observed. Both HOMOs are found near the adamantane core of the structures, while the LUMOs are placed within the targeting vector molecule part. For **TC1** it is located near the carbon backbone, while for **TC2** it is found near the pyridine-moiety.

The trimer **TC3** has displayed some technical problems. While the MOPAC calculation could be performed successfully, the output file could not be opened with Avogadro. The tendency to need long time for successful file opening was firstly observed for **TC1** and increased for **TC2**, finally failing totally for **TC3**.

Nevertheless, a similar tendency as for **TC1** and **TC2** is suspected, with a linear conformation for the lead moiety as well as for orbital locations.

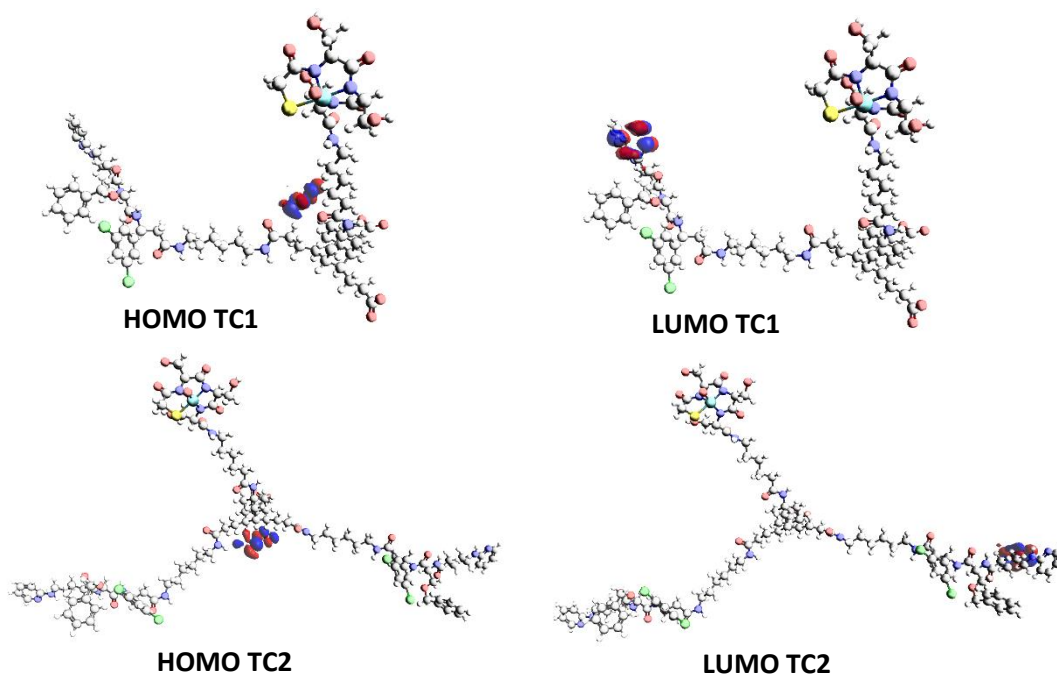


Figure 71: Localization of HOMO and LUMO for the Tc-labelled derivatives of EMD527040 TC 1 and TC 2.

In a next step, the electrostatic situations were also investigated for the substances described so far. The fluorinated versions **F1** and **F2** show a very similar profile to the lead structure EMD527040. Again, the main feature is the negative charge at the carboxy function, while only slight positivity is observed at the guanidine moiety (Figure 72).

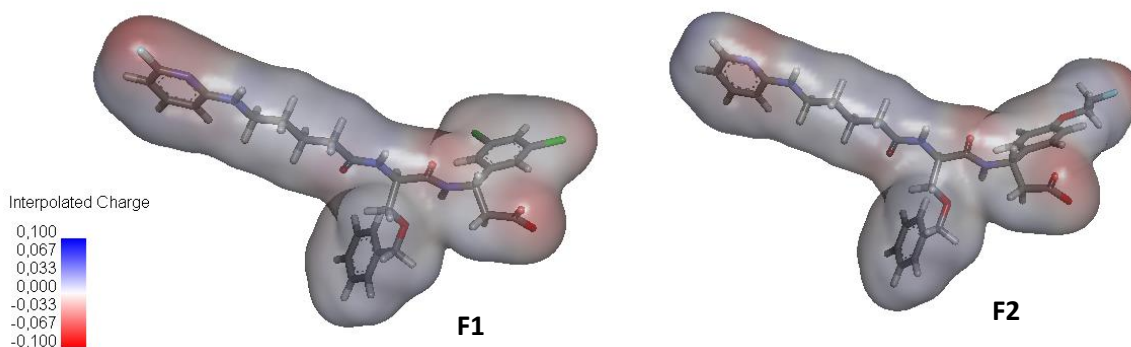


Figure 72: Interpolated Charge of the fluorinated derivatives of EMD527040 F1 and F2. Color Code: Red = negative; blue = positive.

An interesting difference is found upon changing to the Ga-chelating compounds. The metal complexes are depicted as positively charged with a dipolar direction. This effect is based on the positively charged gallium(+III)cation in the complex. In the cis-configuration of a Ga-DOTA complex, two carboxylates coordinate the Ga^{3+} and partly compensate the charge. The carbonyls remain for a negative partial charge. This can be seen in Figure 73 and Figure 76 for **BK23**, **BK39** as well as **GA1** and **GA2**.

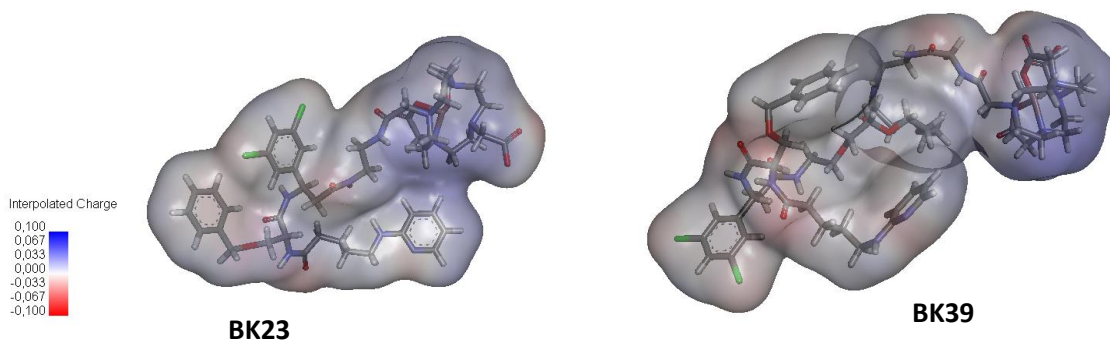


Figure 73: Interpolated Charge of the tracers BK23 and BK39. Obtained on basis of the MOPAC calculations. Color Code: Red = negative; blue = positive.

The electrostatic potential calculations had originally been performed on the basis of the minimized structures obtained from Avogadro. With this approach, the results shown in Figure 74 were obtained. The metal complexes were obviously depicted as far more positive as the interpolations which were based on the MOPAC results (Figure 73). This is probably caused by the difference, that Avogadro accounted the four N-Ga coordinating bonds as more covalent resulting in positive quaternary nitrogen cations, whereas the PM7 parameters used in the MOPAC calculations were better suited to represent the coordinate bonding type.

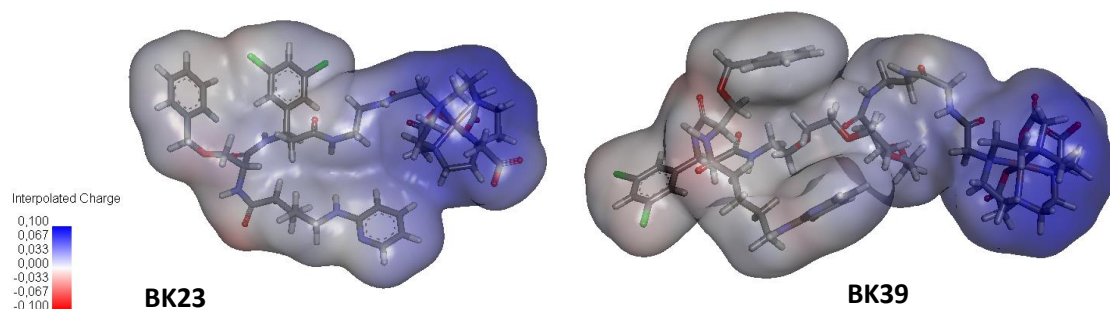


Figure 74: Interpolated Charge of the tracers BK23 and BK39. Obtained on basis of the minimized structures. Color Code: Red = negative; blue = positive.

López-Vidal et al. have published in 2012 an investigation about $[\text{Yb}(\text{DOTA})]^-$, which they used for NMR-studies on its complexation with cationic species like N-monoalkyl- and N,N'-dialkyl-4,4'-bipyridinium cations.¹¹⁹ Their obtained experimental results fitted well with the theoretical calculations regarding the electrostatic potential on MPWLYP/6-311G** level (*ab initio* method). Their results showed also a dipole for the $[\text{Yb}(\text{DOTA})]^-$ complex, which ranges from neutral on the side of the nitrogens to negative on the carboxy side of the complex:

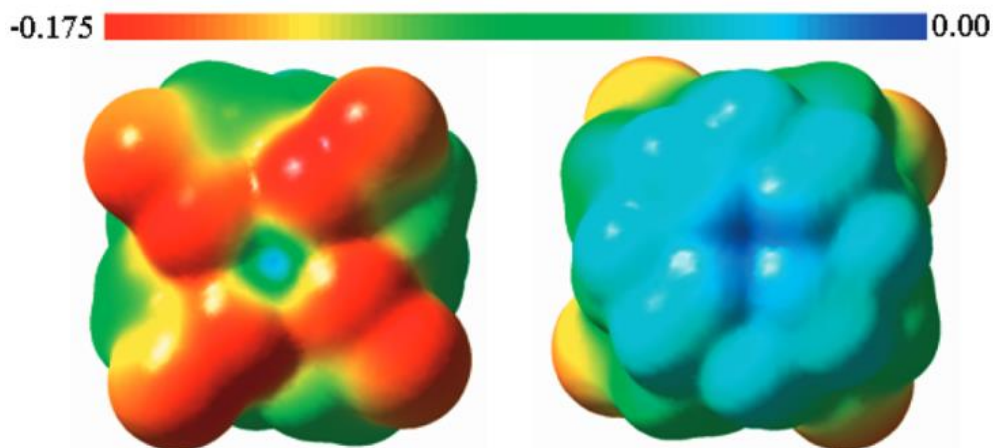


Figure 75: Computed MPWLYP/6-311G** electrostatic potential of $[\text{Yb}(\text{DOTA})]^-$ (hartree) on the molecular surface defined by the $0.001 \text{ electrons}\cdot\text{bohr}^{-3}$ contour of the electronic density. Views are along the molecule C_4 -symmetry axis.¹¹⁹

It can be assumed, that the dipolar nature of the metal complexes in **BK23** and **BK39** is realistic. Nevertheless, the obtained results straight after minimization, based solely on the UFF force field, resulted in an exaggerated depiction of the situation. Taking into account the higher electronegativity of Ga towards Yb, the slightly positive depiction rather than neutral (as in the Yb example) is understood as realistic.

All other electrostatic potential results presented in this work are based on the MOPAC calculations, if not noted otherwise.

Continuing with the potential tracers for usage in fibrogenetic diagnostics, the main difference to **BK23** and **BK39** is, as to be expected, the free carboxylic group for **GA1** and **GA2**. This shows, similar to all earlier structures, negative values as well as it is observed for the pyridine-nitrogen. The same dipolar situation is observed for the chelates in these compounds (Figure 76).

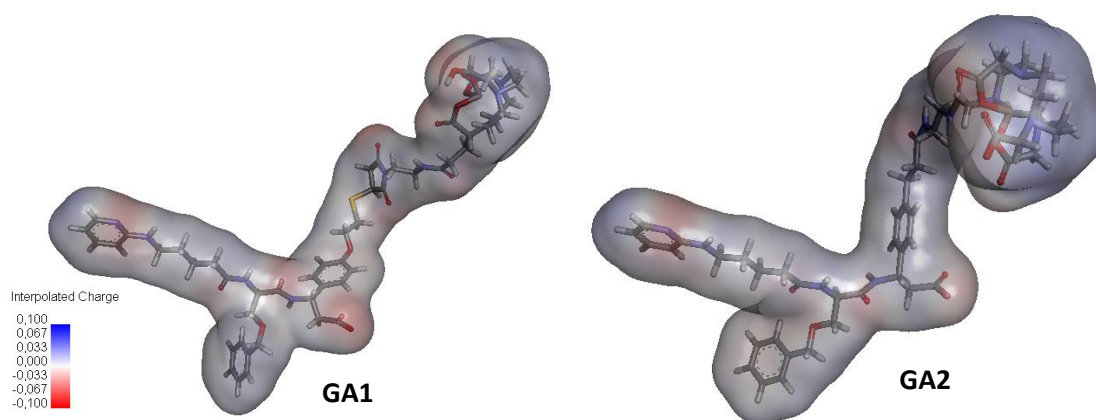


Figure 76: Interpolated Charge of potential Ga-labelled EMD527040-derivatives **GA1** and **GA2**. Color Code: Red = negative; blue = positive.

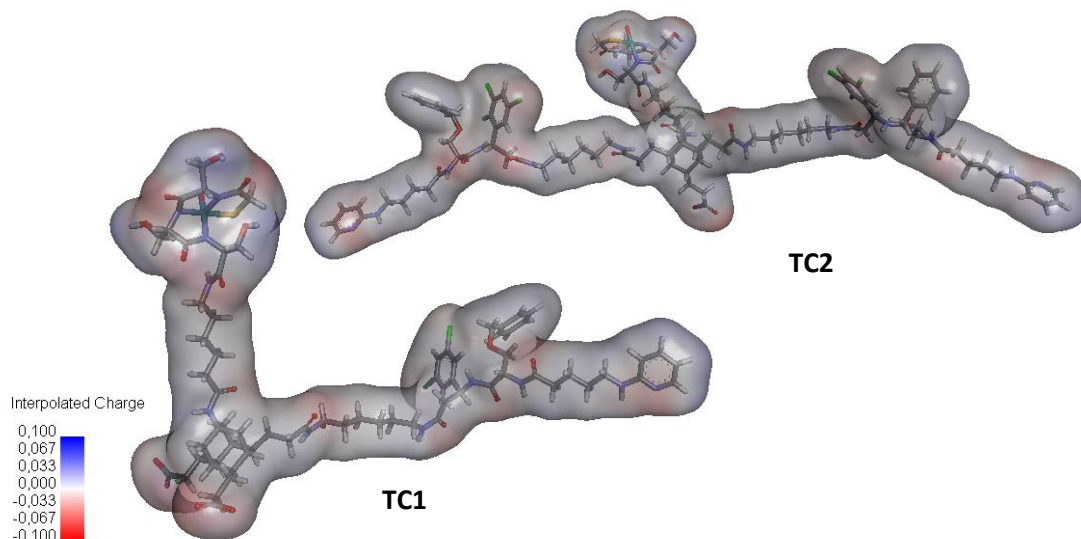


Figure 77: Interpolated Charge of potential Tc-labelled EMD527040-derivatives TC1 and TC2. Color Code: Red = negative; blue = positive.

For the Tc-derivatives, the situation presents itself similar to the one for **GA1** and **GA2**. The part derived from the lead structure does not show any differences to EMD527040. Only the negative carboxy function is obviously lacking, as it is coupled to the adamantane scaffold. Its free carboxylic acids for **TC1** and **TC2** are negative, though. Since the **TC3** compound was calculated with MOPAC, but could not be opened in Avogadro, the charge interpolation could not be performed on this one. Nevertheless, the metal complexes seem to be depicted in a reasonable fashion with partially negative and partially positive sites close to the oxygen and nitrogen atoms. The structural conformation in this case, however, does not allow the formation of a dipole.

It can be concluded from these studies that, while all included ligands from literature as well as the fluorinated derivatives, Tc-labelled and proposed Ga-labelled structures are in good agreement with the lead EMD527040, the two synthesized compounds **BK23** as well as **BK39** are quite outstanding due to their electronic as well as electrostatic characteristics. Also, large conformational differences were observed. Any of these features could be the reason for the negative binding results which were obtained experimentally. In order to decide if their combination is needed or if one out of the three characteristics is the crucial one, further experiments would have to be performed.

III.V.II Generation of Receptor Model for $\alpha_v\beta_6$

For the integrin $\alpha_v\beta_6$, to date, no crystal structure is available. This hampers the understanding of ligand – receptor interactions significantly. The structure of the homologue $\alpha_v\beta_3$, in contrast, has been investigated thoroughly and several x-ray structures under different experimental conditions are available.

The methods of homology modelling allow the prediction of a theoretical model, if homology between target and template sequence is high enough – therefore, it shall be applied to $\alpha_v\beta_6$.

The integrin $\alpha_v\beta_6$ is composed of the 1048 amino acid (aa) alpha chain (UniProt Code P06756) and the 788 amino acid beta chain (UniProt Code P18564). The alpha chain sequence starts with a 30 aa signalling peptide, followed by the large extracellular segment of 962 residues. The following 24 aa span across the membrane in a single helix and the final 32 residues represent the intracellular part.¹²⁰ These portions are similar in the beta chain: 21 aa for the signal peptide, 688 aa for the extracellular part, the transmembrane helix is made up of 21 aa and the intracellular part is short again – with 58 residues.¹²¹

The structural homology of the beta chains three and six has been investigated with Clustal Omega¹²² which is available on a server of The European Bioinformatics Institute (which is part of the European Molecular Biology Laboratory) via the website <http://www.ebi.ac.uk/Tools/msa/clustalo/>.

A homology of 49.94 % between the two chains was found – a promising value for a successful homology modelling.

III.V.II.I SWISS Model

The first trial was undertaken with a similar web-based approach. The swiss institute of bioinformatics (university of Basel) runs the SWISS-model server which offers homology modelling on their server. It is available via <http://swissmodel.expasy.org>.¹²³

The BLAST search which is incorporated in the SWISS-model interface resulted in several possible template structures. The pdb entry 1L5G was chosen, since it is the only one which represents a ligand-receptor complex and therefore closest to the desired binding form of the

receptor. It was also used as template for the homology modelling of the integrin $\alpha_v\beta_5$ by Marinelli et al.¹²⁴

The alignment obtained from Clustal Omega was uploaded to the SWISS model server and default parameters were used. The resulting structure for the beta 6 chain was merged manually with the alpha v chain from the template structure 1L5G. The result can be seen in Figure 78 – the pink chain being the newly calculated beta 6 chain.



Figure 78: Initial Model for $\alpha_v\beta_6$, obtained from the SWISS Model Server. The clashing chains can easily be seen in the lower part of the image.

It can be seen easily that the result was not satisfying – the ‘legs’ of the alpha and beta chains clash significantly into each other. Even though this is far away from the binding site, this approach was discarded and a different method was applied. The MODELLER software which was used for that purpose, has recently been implemented into SWISS-model¹²⁵ but was not yet available therein at the point of this study.

III.V.II.II MODELLER / Chimera

The approach towards model building which is applied in the MODELLER software is based on the satisfaction of spatial restraints.¹²⁶ For that purpose, a number of probability density functions are derived from the template structure with regard to for example C_α - C_α distances,

main chain N-O distances, dihedral angles or solvent accessibilities for side chains. These functions are being optimized in an iterative process until an optimal structure is found.¹²⁶

This scoring is therefore based on a probability value for this structure and not an energy minimization procedure. There is no relationship to physical properties present.¹²⁶

The software can be run independently on a personal workstation or used via the server of the developers. For that purpose, UCSF Chimera has been used as a graphical user interface in order to submit the calculation.¹²⁷

The beta 6 sequence (UniProt P18564) was loaded and the BLAST run was performed with the BLOSUM 62 matrix and an E-value of 1E-3. Again, the template structure from Xiong et al.¹¹⁷ was chosen, as it displays $\alpha_v\beta_3$ in its ligand binding conformation (pdb entry 1L5G). The alignment was improved again by running the Needleman-Wunsch algorithm⁹⁴ before submission to MODELLER.

Twenty models were calculated with MODELLER and scored with its objective function. The best model was subjected to further refinement in the SDL loop – according to Marinelli et al.¹²⁴ In this refinement, only five variations were build and again, the best score was chosen.

The model obtained by this method was again manually merged with the alpha v chain and ligand of the template structure 1L5G within VEGA ZZ.¹¹⁵ In this case, no clashing chains were observed and the model was subjected to energetic optimizations.

For this intermittent step, we worked with Dr. Xxxxxx Xxxxxx. The system was built in explicit water (SPC model) and a truncated octahedron box was established within Maestro. The system was neutralised by adding 50 Na atoms. Next, a steepest descent minimisation was performed with 3000 steps and a convergence threshold of 0.05 kcal/mol/Å. A force of 100 kcal/Å² was applied to the whole backbone in order to keep it constrained. After this minimization, the molecular dynamics were performed with a simulated annealing of 100 ps at 10 K, 300 ps heating to 300 K, followed by 100 ps at 300 K. This was performed at constant pressure and restricted backbone as before. The final production run was performed for 500 ps, also at 300 K and constant pressure.

The obtained model is displayed below in Figure 79. Already at a first glance, it can be seen that the former problem of clashing alpha and beta chains has been resolved.

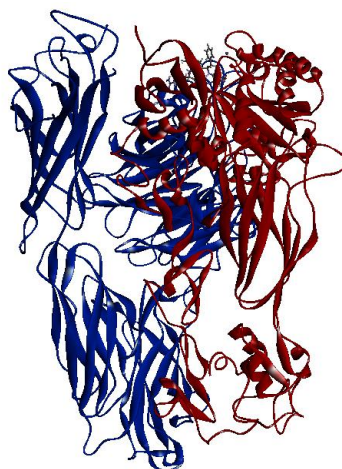


Figure 79: Model of $\alpha_v\beta_6$ obtained by homology modelling with MODELLER and subsequent molecular dynamics simulation.

For a further quality check, the Ramachandran plot¹²⁸ was obtained via VEGA ZZ. It is shown in Figure 80 on the left, while for comparison the plot of the experimental structure 1L5G is shown on the right. For $\alpha_v\beta_6$, 75.91 % of the residues are found within the allowed regions with 48.92 % of the residues in the preferred regions. Compared to the experimentally found structure of the integrin $\alpha_v\beta_3$, (with values of 71.79 % in the allowed and 43.98 % in the preferred region), our theoretical model shows similar, slightly better values. Also the chirality check implemented in VEGA ZZ was successful – no D amino acid was found.

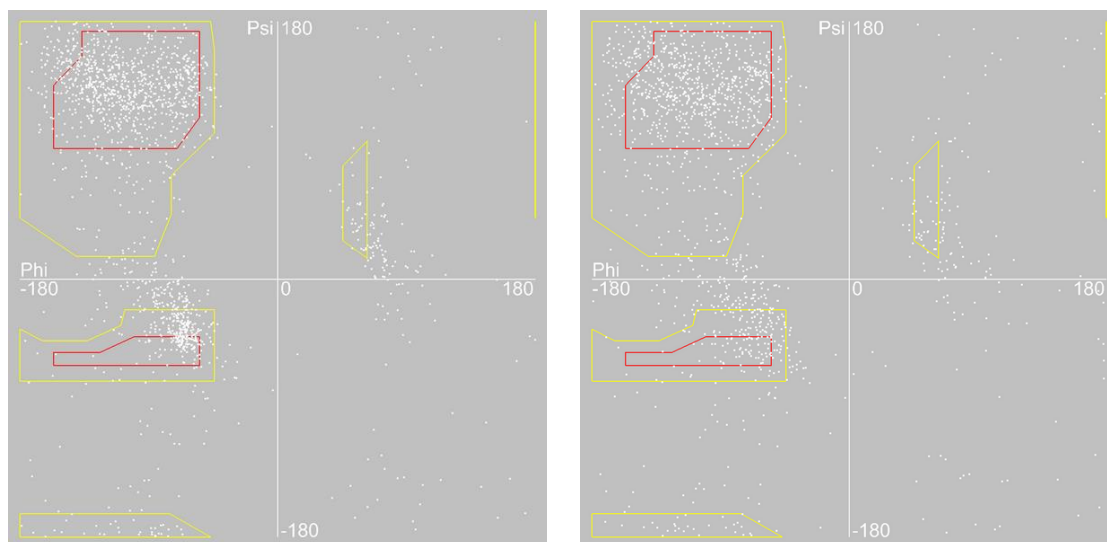


Figure 80: Ramachandran Plots of the calculated model for $\alpha_v\beta_6$ (left) and the x-ray structure of $\alpha_v\beta_3$ 1L5G (right).

With this successful checks on the obtained structure, the binding site was further investigated for its properties. In all cases a comparison with $\alpha_v\beta_3$ was performed. As for the small molecules, the surface characteristics were researched. In Figure 81, the electrostatic potential of the surface is shown. Notably, the strongly positive features at the edges of the $\alpha_v\beta_3$ binding site are less pronounced, but still present, in the case of $\alpha_v\beta_6$. Especially in the beta chain the difference can be observed.

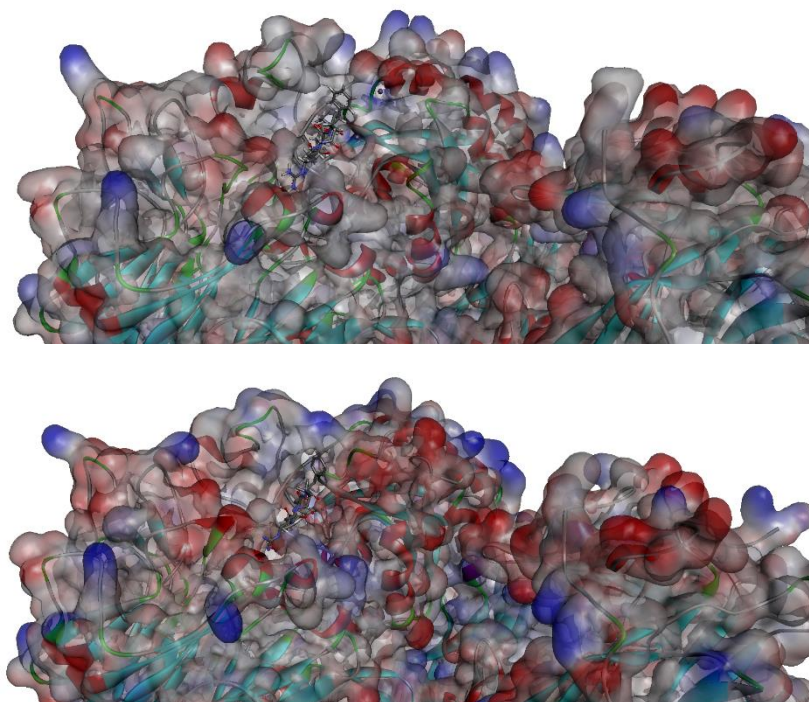


Figure 81: Inspection of the binding site with the 1L5G ligand for the surface charge (Interpolated Charge method in Discovery Studio). Top: $\alpha_v\beta_6$ model. Bottom: $\alpha_v\beta_3$ experimental structure 1L5G for comparison. Blue: positive charge. Red: negative charge.

As a second feature, the solvent accessibility was investigated. This is shown in Figure 82. Generally the binding site of $\alpha_v\beta_6$ is better accessible than the one of its more prominent homologue. Behind the ligand, a rather inaccessible pocket can be seen for $\alpha_v\beta_3$, which is better accessible for $\alpha_v\beta_6$. The remaining parts around the binding pocket are very similar in this regard. Overall, most of the surface is easily accessible.

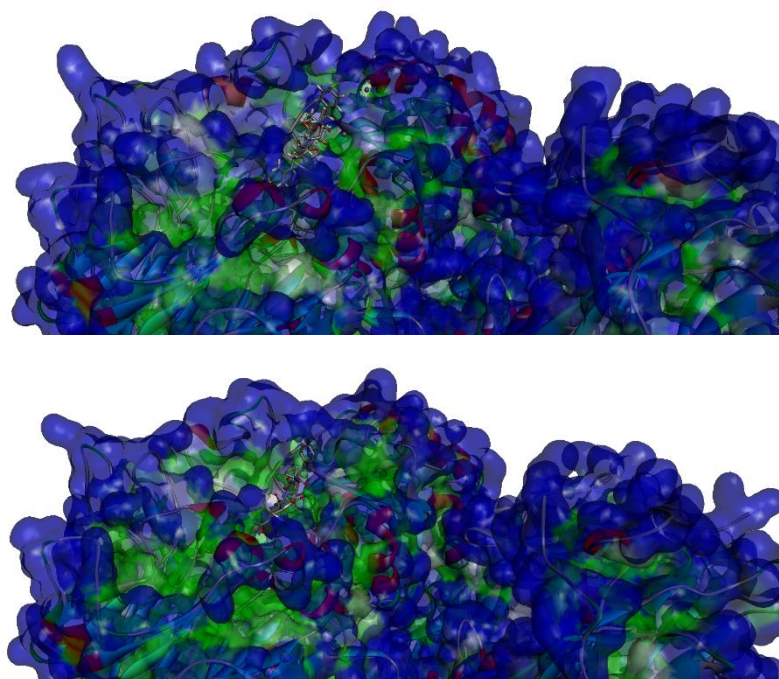


Figure 82: Inspection of the binding site with the 1L5G ligand for the solvent accessibility (Discovery Studio). Top: $\alpha_v\beta_6$ model. Bottom: $\alpha_v\beta_3$ experimental structure 1L5G for comparison. Blue: accessible. Green: badly accessible.

The third characteristic which was investigated is the lipophilicity of the proteins' surface. Here, an interesting difference can be observed. While the overall impression of the binding site is hydrophilic, a pocket before the binding site is rather neutral to hydrophobic. But this is found in both cases. It also overlaps with the inaccessible sites seen in Figure 82. The main difference is the so called 'specificity defining loop' (SDL).¹²⁴ This loop had already been treated with more care during model building with MODELLER.

In the case of $\alpha_v\beta_3$, it is strongly hydrophilic, while for $\alpha_v\beta_6$ an outstanding hydrophobic loop is observed. Also, the conformation of this loop is different compared to $\alpha_v\beta_3$. A magnification can be seen in Figure 84.

These differences which were observed agree with the finding of different specificities and selectivities of varying ligands to the different integrin isoforms. In which form this impacts the binding of our ligands, will be discussed in the next chapter.

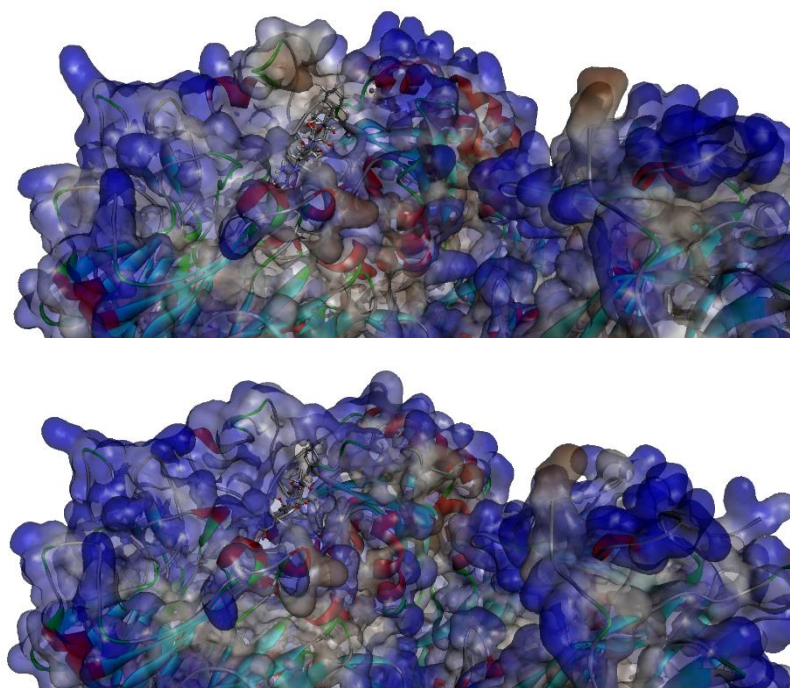


Figure 83: Inspection of the binding site with the 1L5G ligand for the surface hydrophobicity (Discovery Studio). Top: $\alpha_v\beta_6$ model. Bottom: $\alpha_v\beta_3$ experimental structure 1L5G for comparison. Blue: hydrophilic. Brown: Hydrophobic. The SDL structure is located in the upper part of the image – straight above the ligands.

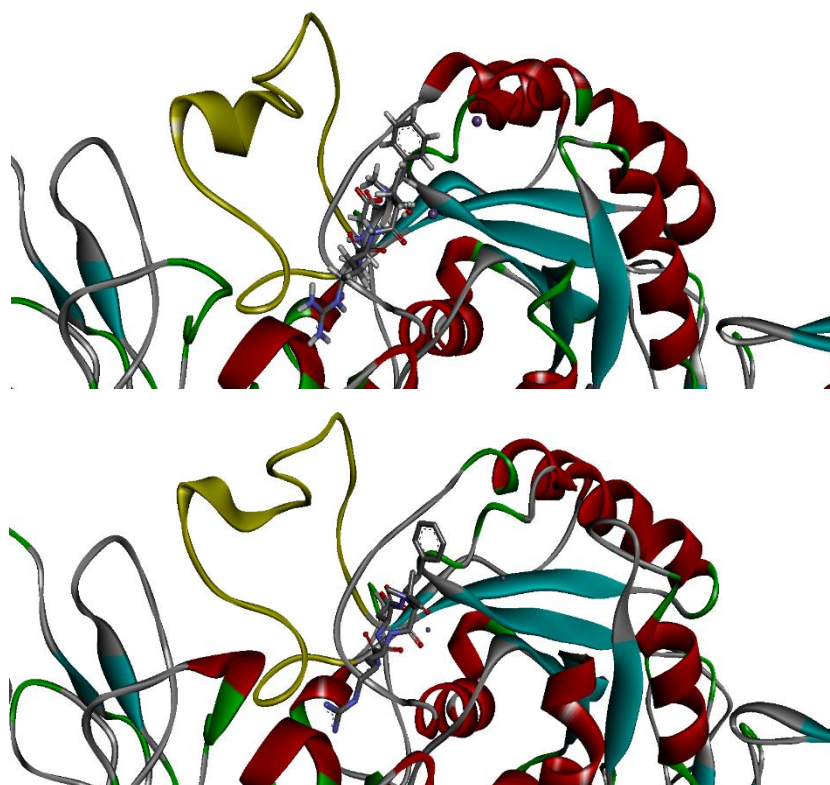


Figure 84: Specificity defining loop in $\alpha_v\beta_6$ (top) and $\alpha_v\beta_3$ (bottom). SDL labelled in yellow.

III.V.III Docking Experiments

The aim of these experiments was to gain an understanding about the binding modes of our ligands to the integrin $\alpha_v\beta_6$. For that purpose, the software AutoDock 4¹²⁹ was used which has been developed at The Scripps Research Institute. It is based on the calculation of grids across the receptor molecule for each atom type which is present in the ligand. The actual docking of the ligand with flexible torsions is then calculated on those grids in order to minimize computational demands.

This has been described before by Marinelli et al.¹²⁴ for the docking of small molecule ligands to their homology model of $\alpha_v\beta_5$. In our study, their protocol was followed in the main aspects, though the number of evaluations was raised up to 2.500.000 from 1.500.000.

A crucial problem which had to be overcome, where the metal ions of Ga and Tc, as they are not parameterized in AutoDock 4. But it allows the input of modified parameter files in order to add new atom types. The values necessary in order to define an atom type are the van der Waals radii, the energy well depth of two like atoms, the volume (which can be calculated from the van der Waals radii) and a desolvation parameter. Furthermore, for H-bonding atom types a couple of other parameters have to be set – in this case, the standard values for non-H-bonding atom types were used. The van der Waals radii and the energy well depth were taken from the UFF force field,⁸⁸ since the values for other atoms present in both the AutoDock default parameter file as well as the UFF force field did not differ too much. The desolvation parameter for all metals present in the default parameter file is the same and only differs for carbon, oxygen and other elements typically found in organic molecules. Therefore, this ‘metal standard value’ was also applied for Ga and Tc.

A validation of these parameters could not be performed any more, therefore the below presented results have to be interpreted with care.

The docking was performed for 5 molecules in total. First of all, the known ligand EMD527040 was docked to $\alpha_v\beta_6$. Furthermore, one example of the synthesized Ga-based as well as Tc-based ligands were investigated, namely **BK23** and **TC1**, in order to understand their observed

differences in binding. Finally, two of the compounds which have not yet experimentally been tested on their binding characteristics were chosen: **F2** and **GA1**.

For each compound, fifty independent dockings were run and the results were subsequently clustered for solutions with an rmsd of $< 1.5 \text{ \AA}$. Out of those, the five best solutions in terms of energy were looked at. The binding energies in kcal/mol are shown in Table 8.

Table 8: Obtained binding energies for the molecules EMD527040, BK23, TC1, F2 and GA1 with α, β_6 .

KCAL/MOL	EMD527040	BK23	TC1	F2	GA1
ENERGY 1	-7.1	-10.29	-6.42	-6.13	-9.3
ENERGY 2	-6.05	-9.95	-4.79	-5.49	-8.78
ENERGY 3	-6.04	-9.64	-4.34	-5.23	-8.74
ENERGY 4	-5.96	-9.33	-3.85	-5.08	-8.33
ENERGY 5	-5.75	-9.22	-3.77	-4.99	-8.27

Interestingly, the energy values of the Ga-containing compounds **BK23** and **GA1** are significantly lower than the ones of EMD527040 as well as **TC1** and **F2**. Since EMD527040 is the well-known reference substance – and we know from the experiments in chapter III.III that **BK23** is not a good binder. Therefore, this is a strong indicator that the parameters chosen for Ga were not in good agreement with the residual scoring functions implemented in the software. This also leaves the results for **GA1** questionable. For **TC1** on the other hand, values in the same range are found – this is in agreement with the experimental result of nanomolar affinities, which also falls in the same range with EMD527040. It is therefore concluded, that the parameters which were chosen for Tc were a better choice and the results are more reliable.

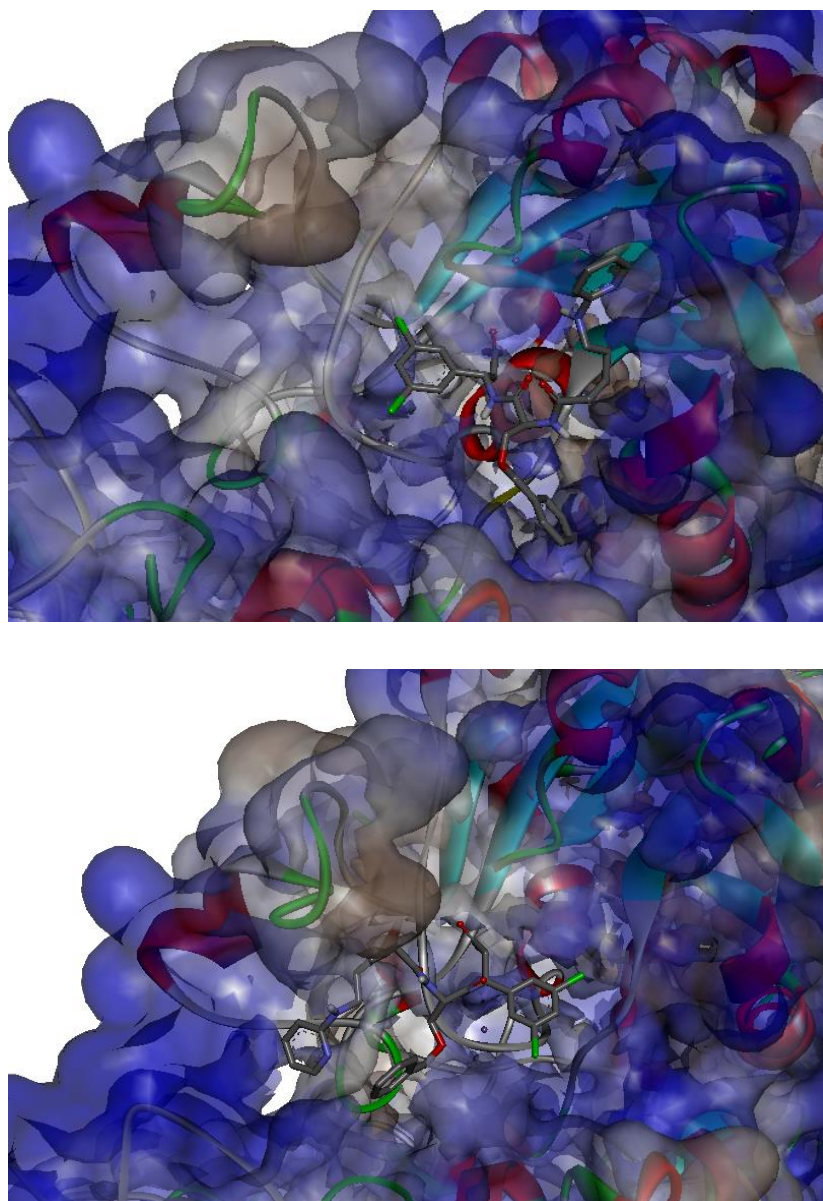


Figure 85: Docked conformations of EMD527040 with the integrin $\alpha_v\beta_6$. The upper image displays the lowest energy conformation, the lower one the solution with the second lowest binding energy, which is closer to the binding mode in the 1L5G pdb entry of $\alpha_v\beta_3$ and its ligand.

Above, in Figure 85, the two lowest energy conformations are depicted. The surface of $\alpha_v\beta_6$ is again coloured with the hydrophobicity index. Similar to the ligand in the crystal structure of $\alpha_v\beta_3$, the carboxy function is found in a pocket which allows coordination to a Mn^{2+} ion. This is the case for both conformations, while the lowest energy conformation sticks out from the receptor with the pyridine moiety but in the second lowest energy conformation the molecule lies itself in the pocket below the SDL loop. This is more similar to the binding mode which was observed for the cilengitide- $\alpha_v\beta_3$ complex in the 1L5G crystal structure.

Comparing this to the structurally most similar compound **F2**, the same two conformations are found for the lowest and second lowest energies. Interestingly, in this case they are found in reversed order (cf. Figure 86). Theoretically, the lowest energy conformation should be the most realistic one – but the risk of finding false-positive results can never be totally eliminated in such a theoretical model. Compared to the template crystal structure, the conformation buried by the SDL loop (second lowest energy for EMD527040 and lowest energy for **F2**) is considered to be the more realistic one.

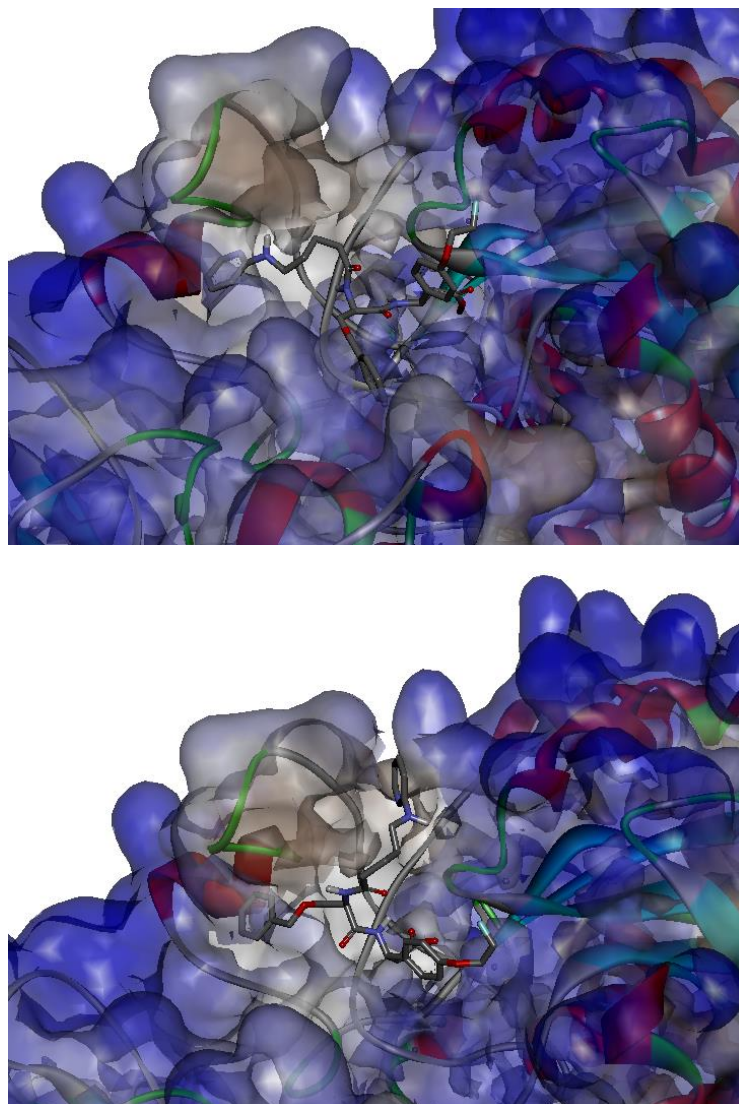


Figure 86: Docked conformations of F2 to the integrin $\alpha_v\beta_6$. The upper one displays the lowest energy conformation, while the lower image shows the second-lowest energy conformation. Notably, they are similar to the ones of EMD527040, but the other way around in their energy.

In order to affirm this, more thorough docking studies would have to be performed. A couple of possibilities are thinkable – increasing the number of evaluations within one docking, extending the number of dockings performed or including flexible residues within the receptor. In our

protocol only the ligands' bonds were acknowledged as flexible torsions while the receptor is kept rigid.

In any way – the similarity of the two ligands suggests that the fluorinated ligand F2 is a promising ligand for the integrin $\alpha_v\beta_6$ and should therefore be considered and further developed as a possible PET tracer for the imaging of liver fibrogenesis.

For the Ga-based tracers, it is difficult to draw a conclusion. As mentioned before, the binding energies which were obtained for the two compounds **BK23** and **GA1** were stronger than for the known ligand EMD527040, which makes the results unrealistic. As for the location, in both cases, the chelator was placed close to the SDL loop. Apart from the parameters which had to be set for AutoDock, one more feature was problematic here. For a calculation of the grids, not only the conformation of the ligands, but also their partial charges need to be known. Those are usually calculated by AutoDock according to Gasteiger¹³⁰ – again, Ga is not implemented here. Therefore, the charge was manually set to 3+. As this is the formal charge, this is overestimated with a high probability. Especially since the Ga ion is embraced by the chelator, its charge is probably shielded to a significant extent from the receptor. Hence, it plays such a significant – but overestimated – role in these docking calculations. For a successful docking experiment with these ligands, these two factors would have to be optimized: a more realistic estimation of the Ga charge as well as the parameters for the AutoDock parameter file (vdW radii and energy well depth). For successfully optimized parameters also the experimental proof of existing affinity to the receptor should be obtained for validation.

For the case of the Tc-based molecules **TC1** was examined as an example. The carboxy function is blocked in this case as it is used for the connection with the chelator, similar to **BK23** and **BK39**. The same problem with the charge assignment has appeared with **TC1** as mentioned before for the Ga compounds. Nevertheless, it seems not to have impacted it that strongly, as an interesting conformation was found at the second lowest energy (cf. Figure 87). The propionic acid residue of the adamantane backbone has taken the pocket which allows coordination with the metal bonds. Meanwhile, the carbon backbone of the EMD527040 moiety is strongly compressed and the guanidine moiety has contact to the same part of the integrin as the ligand in the template crystal structure 1L5G.

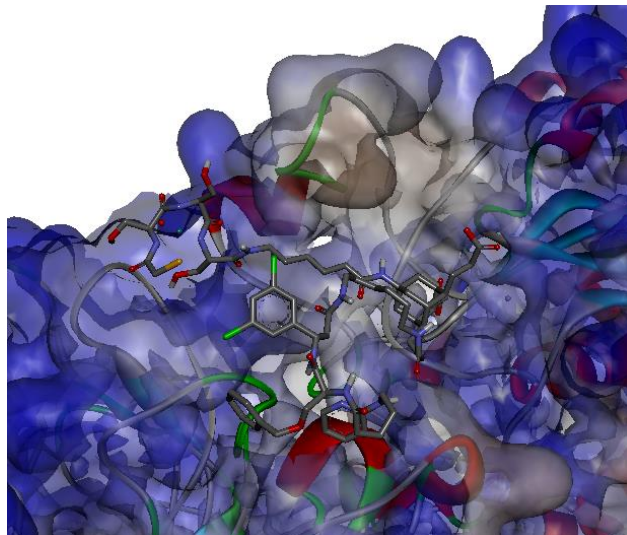


Figure 87: Docking of TC1 with the integrin $\alpha_v\beta_6$. Displayed is the second lowest energy conformation. The propionic acid residues on the adamantane backbone stick into the pocket with contact to the metal binding site. Interestingly, the EMD527040 moiety is compressed along its carbon chain – this could explain the binding of TC1 to $\alpha_v\beta_6$ in despite of the blocked carboxy function for coupling to the chelator.

This could be an explanation for the successful binding of **TC1** as well as **TC2** (also still bearing one propionic acid on the adamantane scaffold). Also, this is in accordance with the results from chapter III.V.I – the HOMOs of **TC1** and **TC2** were found on the propionic acids on the adamantane scaffold and therefore allows the binding. This explanation does of course not cover **TC3**, where all three propionic acids have been used for derivatization. The lack of the acidic moiety might in this case be compensated by the presence of three EMD527040 moieties instead of one or two.

In conclusion, these initial docking experiments were successful for the classical organic molecules, while there is room for improvement in the cases of the metal based ligands. Nevertheless, a hypothetical explanation for the different results in affinity for the Tc-based and Ga-based ligands can be derived from these dockings. The carboxy function of EMD527040 plays an important role in the binding to $\alpha_v\beta_6$. This is in good agreement with other RGD binding integrins. Therefore, **BK23** and **BK39** did not show good affinities to the integrin – the Tc-based compounds on the other hand are able to replace this carboxy function by the propionic acid on the adamantane scaffold and compensate this spatial expansion by a compression within the flexible backbone of the EMD527040 moiety.

IV. Conclusions and Outlook

In conclusion, five different aspects have been treated during this work. Starting from organic synthesis, via radiochemistry and in vitro assays this work was completed by animal experiments and structural studies on the receptor $\alpha_v\beta_6$.

First of all, the $\alpha_v\beta_6$ -binding lead structure EMD527040 was synthesized. This could successfully be achieved within 8 steps. An overall yield of 24 % was achieved. The lowest yield was obtained in the first step – the nucleophilic substitution of 5-bromo ethyl valerate with 2-amino pyridine did not result in yields beyond 27 %. The following steps of peptide coupling and protection group chemistry did not display any major problems.

Starting from EMD527040, the two labelling precursors **BK23** and **BK39** were obtained in two and four steps, respectively. Here, a peptide coupling method in a laboratory microwave was successfully applied. After HPLC purification, the precursors could be used for radiolabelling.

A labelling procedure could successfully be established in HEPES buffer at 95 °C for ten minutes. RCYs over 95 % could be reached by this method. The subsequent purification from remaining free $^{68}\text{Ga}^{3+}$ was achieved via the fixation of the tracer on a C-18 cartridge. Washing with water and the subsequent elution with ethanol yielded the pure tracers. Conveniently, the same procedure can be applied successfully to both tracers.

For both tracers stability studies over two hours were successfully performed as well as the logD values were determined. As expected, **BK39** (containing the longer and more hydrophilic spacer) showed more hydrophilic properties than **BK23**.

Further tests were performed in order to determine the compounds' affinity to the integrin $\alpha_v\beta_6$. Unfortunately, the different cell tests as well as the assay on isolated and immobilized integrin showed no binding whatsoever. The animal experiments in fibrogenic and healthy mice neither showed a difference between the two groups for both tracers. Nevertheless, it was concluded that the two substances were metabolized and eliminated via different pathway – while the more hydrophilic compound **BK39** was renally cleared, the smaller and more lipophilic substance

BK23 was found in the intestines – indicating an (at least partially) elimination via hepato biliary pathways. It was therefore concluded, that the aim for future substances should be a logD value of below -0.19 in order to ensure a renal elimination – which is important for image quality.

The attempts of establishing a non-radioactive assay for affinity determination were rather unsuccessful. ELISA methods based on biotinylated fibronectin as well as based on the latency associated peptide of TGF- β 1 could not be optimized to a sufficient sensitivity. The major obstacle was the high unspecific binding – which was also observed in a second method, the quartz crystal micro balance. Recently, it has been published by Elosegui-Artola et al.¹³¹ that $\alpha_v\beta_6$ shows increasing binding to the same substrate if the matrix in which it is embedded becomes more rigid. They have successfully measured binding rates with surface plasmon resonance experiments – this could be a promising alternative.

Finally, a computational chemistry project was performed in order to understand the discrepancies between the Tc-based compounds – showing good affinities – and our Ga-based compounds which did not show the expected characteristics. For that purpose, the characteristics of known literature ligands as well as our own ligands were compared for their molecular characteristics. The orbitals seem to play a major role – for all binding substances the HOMOs were found at the carboxy moiety and the LUMOs at the guanidine / basic moiety. In the case of the Tc-based compounds the HOMOs were found on the carboxy groups of the propionic acid on the adamantane scaffold.

By means of homology modelling, a theoretical model of $\alpha_v\beta_6$ was constructed. A major difference in the binding pocket was found to be at the specificity defining loop – being very hydrophobic in comparison to the template $\alpha_v\beta_3$.

Five ligands were docked to the homology model with AutoDock – for the metal-based ligands, the extension of the parameter file was necessary which was performed on the base of the UFF force field. Nevertheless, the results showed that at least the Ga parameters still need optimization. But still, first conclusions could be drawn from these docking experiments – the Tc-based derivatives probably show their good binding due to the replacement of the EMD527040-carboxy group by the propionic acids on the adamantane scaffold. This is not possible in the case of the Ga-based substances and therefore no binding was observed.

Getting back to the development of radiotracers for the imaging of liver fibrogenesis, these findings mean that the carboxy function of EMD527040 should be left free. The structures **F2** and possibly also **F1** and **GA1** and **GA2** should be promising candidates for further evaluation. In the case of the Ga-based structures this is not based on the theoretical calculations – but if their experimental data was available it could be used for the further development of docking methods for Ga-containing ligands. Since ^{68}Ga is of high importance in nuclear medicine due to its simple availability, this could also have an impact on the development and design of radiotracers for other diseases.

V. Experimental

V.I Organic Synthesis

The chemicals used in this work, were obtained from commercial suppliers (ABCR, Acros Organics, Alfa Aesar, Chematech, Fisher Scientific, Fluka, Merck and Sigma-Aldrich) and used without further purification. Dry solvents were obtained from Sigma-Aldrich and used for all reactions if not otherwise specified. Deuterated solvents for NMR spectroscopy were obtained from Deutero GmbH (Germany).

For radioactive labelling with ^{68}Ga , a $^{68}\text{Ge}/^{68}\text{Ga}$ generator was used from Cyclotron Obninsk Ltd. Co. (Russia) or an EZAG-IGG-100-Generator from Eckert & Ziegler AG, Berlin (Germany). Starting activities after elution ranged between 100 – 700 MBq.

For thin layer chromatography TLC plates from the company Merck, Darmstadt (Germany), Silica 60, F254 were used with the indicated running solvent (v/v). Detection of inactive compounds was performed with UV-light ($\lambda = 254 \text{ nm}$) or staining with KMnO_4 or Ninhydrine solutions, respectively. For radioactive compounds, the Instant Imager (cf. below) was used.

Column chromatography was performed at standard pressure with Silica 60 of particle size 0.04 – 0.063 mm by Acros, Fisher Scientific and Sigma Aldrich as stationary phase.

For solid phase extractions C-18 Strata-X-cartridges (30 mg) by Phenomenex, Torrance, CA (USA) were used.

Instruments:

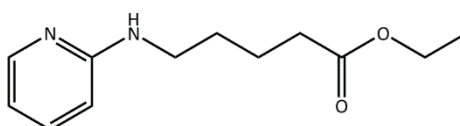
- Nuclear magnetic resonance:
All spectra were obtained on a Bruker 300 or 400 Ultrashield TM, as well as on a Bruker 300 Advance II HD (Bruker, Billerica, Ma, USA). Chemical shifts are reported relative to the reference tetramethylsilane ($\delta = 0$). Spectra were analysed with the software MestReNova 6.
- Mass spectrometry:
ESI spectra were obtained with a Thermo Quest Navigator Instrument (Thermo Electron). Additionally, a 6130 Single Quadrupole LC/MS in combination with 1220

Infinity LC (Agilent Technologies, Santa Clara, CA, USA) was used. For FD measurements, a MAT90-Spektrometer (Finnigan) was used.

- HPLC:
Purification of labelling precursors was performed on a semi-preparative HPLC with a Dionex ICS-Series 5000 (Dionex Corporation, Sunnyvale, CA, USA).
- Laboratory Microwave: CEM Discovery.
- Activity measurements:
Activities were measured with an Isomed 2000-Aktimeter (MED Nuklear-Medizintechnik Dresden GmbH, Dresden, Germany). Radio-thin-layer-chromatography (TLC) measurements were performed with an Instant Imager (Canberra Packard, Schwadorf, Austria). Tissue activities in biodistribution studies and activities determined in cell tests were measured with the Gamma-Counter Wizard²® (Perkin-Elmer, Rodgau, Germany).
- PET-measurements:
Images were obtained with a μ PET Focus 120 small animal PET scanner (Siemens/Concorde, Knoxville, USA).
- ELISA:
Optical densities were determined with a Tecan Infinite 200 Pro (Tecan Group Ltd., Männedorf, Switzerland).

V.1.1 Synthesis of EMD 527040

V.1.1.1 Ethyl 5-(pyridin-2-ylamino)pentanoate



4.49 g (0.048 mol, 1.00 eq.) 2-aminopyridine and 5.08 g (0.048 mol, 1.00 eq.) sodium carbonate were mixed and stirred before addition of 10 g (0.048 mol, 1.00 eq.) 5-bromo-ethylvalerate. The mixture was heated to 130 °C and stirred overnight. After cooling to room temperature, it was taken up in water and ethyl acetate (100 mL each). The aqueous phase was extracted three more

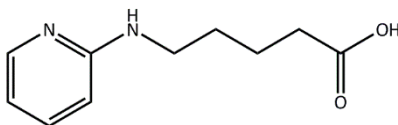
times with ethyl acetate, before the combined organic phases were dried over magnesium sulfate and evaporated. The residue was purified with a silica column (dichloromethane/methanol: 10/1).

2.378 g (0.0107 mol, 27%) ethyl 5-(pyridine-2-ylamino)pentanoate were obtained as a brown oil.

$^1\text{H-NMR}$ (d_4 -MeOH, 300 MHz), δ [ppm] = 1.58-1.71 (m, 6H, -NH-(CH₂)₆-), 2.38 (t, J = 6.7 Hz, 3H, -O-CH₂-CH₃), 4.69-4.87 (m, 4H, -CH₂-CO-O-CH₂-), 6.78 (t, J = 6.8 Hz, 1H, CH_{pyridin}), 6.93 (d, J = 9.2 Hz, 1H, CH_{pyridin}), 7.68 (d, J = 6.5 Hz, 1H, CH_{pyridin}), 7.78 (m, 1H, CH_{pyridin}).

MS (FD) m/z (% rel. Int.): 222.58 ([M+H]⁺, 100.00); 445.75 ([2M+H]⁺, 64.01), 667.86 ([3M+H]⁺, 68.41), calculated: 222.13.

V.I.I.II 5-(Pyridin-2-ylamino)pentanoic acid



2.378 g (0.011 mol, 1.00 eq.) ethyl 5-(pyridin-2-ylamino)pentanoate was dissolved in 10 mL dioxane and 40 mL 1N hydrochloric acid. The mixture was refluxed at 105°C for 18 h. The solvents were subsequently evaporated in vacuum. 2.554 g raw product of a brown solid were obtained as the hydrochloric salt. This was purified by taking it up in 1M sodium hydrogen carbonate solution, setting the pH to 7 with formic acid and several extraction steps with ethyl acetate.

2.084 g (0.011 mol, quantitative) 5-(pyridin-2-ylamino)pentanoic acid were obtained as a light yellow solid.

$^1\text{H-NMR}$ (D₂O, 300 MHz), δ [ppm] = 1.67-1.87 (m, 4H, -CH₂-(CH₂)₂-CH₂-), 2.38 (t, J = 6.5 Hz, 2H, -NH-CH₂-), 3.22 (t, J = 5.8 Hz, 2H, -CH₂-COOH), 6.46-6.60 (m, 2H, CH_{pyridin}), 7.56 (t, J = 8 Hz, 1H, CH_{pyridin}), 7.82 (d, J = 5.6 Hz, 1H, CH_{pyridin}).

MS (ESI) m/z (% rel. Int.): 239.09 ([M+HCO₂H]⁺, 44.24); 455.18 ([2M+Na+HCO₂H]⁺, 57.85), 671.28 ([3M+2Na+HCO₂H]⁺, 100.00), calculated: 194.11.

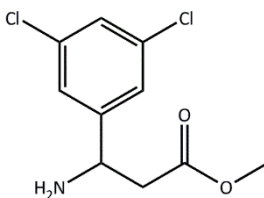
V.I.I.III 3-Amino-3-(3,5-dichlorophenyl)propanoic acid

12.5 g (0.071 mol, 1.00 eq.) 3,5-dichlorobenzaldehyde and 14.91 g (0.143 mol, 2.00 eq.) malonic acid were suspended in 25 mL methanol. 11.01 g (0.143 mol, 2.00 eq.) ammonium acetate were added slowly under formation of a colourless precipitate. The mixture was stirred and heated to reflux for 15 h and subsequently cooled down to room temperature. The colourless precipitate was filtered, washed with little methanol and dried in vacuum.

10.63 g (0.046 mol, 64 %) 3-Amino-3-(3,5-dichlorophenyl)-propanoic acid were obtained as a colourless solid.

$^1\text{H-NMR}$ (CD_3COOD , 300 MHz), δ [ppm] = 3.35-3.65 (m, 2H, CH_2), 7.79 (m, 1H, CH), 7.84 (m, 2H, $\text{C}_{\text{ring}}\text{H}$), 7.92 (s, 1H, $\text{C}_{\text{ring}}\text{H}$).

MS (ESI) m/z (% rel. Int.): 234.03 ($[\text{M}]^+$, 72.08); calculated: 234.08.

V.I.I.IV Methyl 3-amino-3-(3,5-dichlorophenyl)propanoate

A solution of 90 mL methanol and 420 μL dimethylformamide was cooled down to -78 $^\circ\text{C}$. Subsequently, 3.64 mL (50.2 mmol, 1.1 eq.) thionylchloride were added under stirring within five minutes. After ten minutes, to this mixture 10.63 g (45.4 mmol, 1.00 eq.) 3-amino-3-(3,5-dichlorophenyl)-propionic acid were slowly added and subsequently stirred for two days at

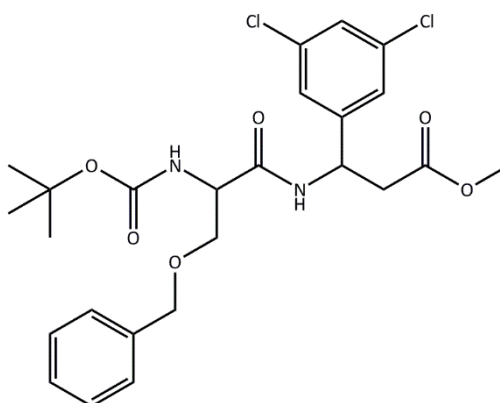
room temperature. The colourless precipitate was filtered and the yellow filtrate was co-evaporated four times with 50 mL of methanol. The remaining white solid was crystallized from chilly diethylether and filtered over a Büchner funnel.

7.62 g (30.7 mmol, 68 %) of methyl 3-amino-3-(3,5-dichlorophenyl)propanoate were obtained as a colourless solid.

$^1\text{H-NMR}$ (CD_3OD , 300 MHz), δ [ppm] = 1.49-1.65 (m, 2H, CH_2), 2.20 (s, 3H, CH_3), 3.25 (t, 1H, CH , $J = 7.5$ Hz), 5.98-6.01 (m, 2H, $\text{C}_{\text{ring}}\text{H}$), 6.04-6.05 (m, 1H, $\text{C}_{\text{ring}}\text{H}$).

MS (ESI) m/z (% rel. Int.): 248.0 ($[\text{M}]^+$, 100); 287.0 ($[\text{M}+\text{K}]^+$, 17.9); calculated: 247.02.

V.I.I.V Methyl 3-(3-(benzyloxy)-2-(tert-butoxycarbonylamino)propanamido)-3-(3,5-dichlorophenyl)propanoate



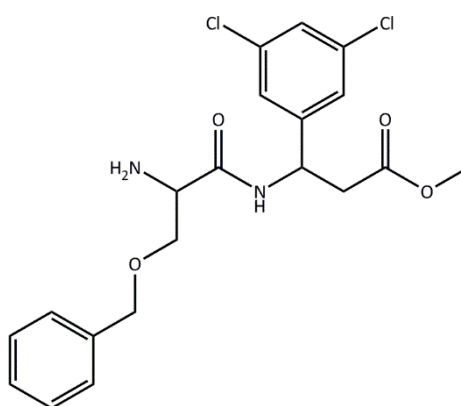
6.60 g (26.6 mmol, 1.00 eq.) 3-amino-3-(3,5-dichlorophenyl)-propionatemethylester, 9.5 g (32.1 mmol, 1.2 eq.) Boc-L-Ser(Bz)OH, 3.8 mL (29.2 mmol, 1.1 eq.) N,N-diisopropyl-ethylamine and 4.7 g (34.7 mmol, 1.3 eq.) 1-hydroxybenzotriazole were dissolved in dimethylformamide. After ten minutes, 6.2 g (32.1 mmol, 1.2 eq.) 1-ethyl-3-(3-dimethylamino-propyl)carbodiimide hydrochloride were added slowly to the reaction mixture and stirred for 18 h at room temperature. The yellow solution was poured onto ice water under formation of a white viscous second phase. The aqueous phase was decanted from the viscous phase and extracted with 300 mL dichloromethane. The viscous phase was dissolved in 200 mL dichloromethane. The combined organic phases were extracted with water, dried over sodium sulfate and the solvent was removed in vacuum.

10.80 g (20.6 mmol, 77 %) of methyl 3-(3-(benzyloxy)-2-(tert-butoxycarbonylamino)-propanamido)-3-(3,5-dichlorophenyl)propanoate were obtained as a yellow oil.

$^1\text{H-NMR}$ (CD_3OD , 300 MHz), δ [ppm] = 1.42 (s, 9H, C- CH_3), 2.77-2.82 (m, 2H, CH_2), 2.86 (m, 1H, CH), 2.95 (m, 1H, CH), 3.03 (m, 1H, CH), 3.57 (m, 3H, CH_3), 3.84-3.94 (m, 1H, CH), 4.45-4.61 (m, 2H, CH_2), 5.28-5.44 (m, 2H, CH_2), 7.22-7.37 (m, 8H, $\text{C}_{\text{ring}}\text{H}$).

MS (ESI) m/z (% rel. Int.): 525.19 ($[\text{M}]^+$, 25.52), 526.19 ($[\text{M}+\text{H}]^+$, 7.52), 547.17 ($[\text{M}+\text{Na}]^+$, 64.28), 563.14 ($[\text{M}+\text{K}]^+$, 100.00), 1073.35 ($[\text{2M}+\text{Na}]^+$, 89.16); calculated: 525.42.

V.I.I.VI Methyl 3-(2-amino-3-(benzyloxy)propanamido)-3-(3,5-dichlorophenyl)propanoate



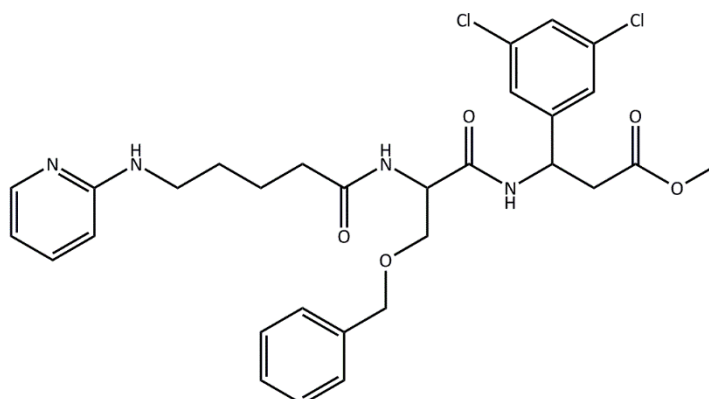
10.8 g (20.6 mmol, 1.00 eq.) methyl 3-(3-(benzyloxy)-2-(tert-butoxycarbonylamino)propanamido)-3-(3,5-dichlorophenyl)propanoate were dissolved in 130 mL 4N hydrogen chloride in dioxane and stirred at room temperature for 20 h. The solvent was removed in vacuum.

8.49 g (19.6 mmol, 97%) of methyl 3-(2-amino-3-(benzyloxy)propanamido)-3-(3,5-dichlorophenyl)propanoate were obtained as a yellow oil.

$^1\text{H-NMR}$ (CDCl_3 , 300 MHz), δ [ppm] = 2.51-2.94 (m, 2H, CH_2), 3.44 (m, 3H, CH_3), 3.78-4.04 (m, 2H, CH_2), 4.32-4.63 (m, 1H, CH), 4.32-4.63 (m, 2H, CH_2), 5.25 (s, 1H, CH), 7.03-7.41 (m, 5H, CH), 7.93-8.45 (m, 3H, CH).

MS (ESI) m/z (% rel. Int.): 425.05 ($[\text{M}]^+$, 100); calculated: 424.10.

V.I.I.VII Methyl 3-(3-(benzyloxy)-2-(5-(pyridin-2-ylamino)pentanamido)propanamido)-3-(3,5-dichlorophenyl)propanoate



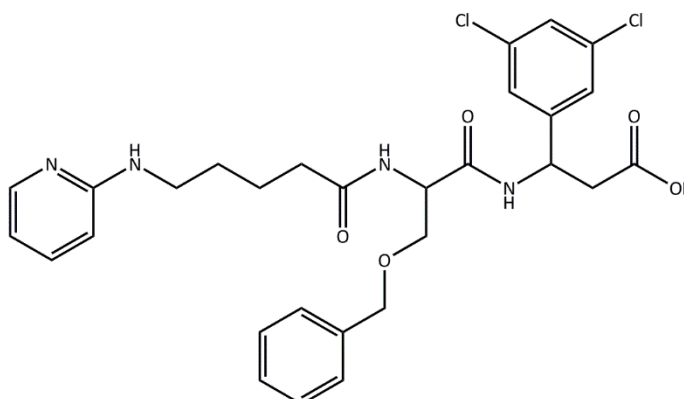
3.52 g (8.28 mmol, 0.90 eq.) of methyl 3-(2-amino-3-(benzyloxy)propanamido)-3-(3,5-dichlorophenyl)propanoate, 1.79 g (9.22 mmol, 1.00 eq.) of 5-(pyridin-2-ylamino)pentanoic acid, 1.72 mL (10.14 mmol, 1.10 eq.) N,N-diisopropyl-ethylamine and 1.49 g (11.03 mmol, 1.20 eq.) 1-Hydroxybenzotriazole were dissolved in 18 mL dimethylformamide. The mixture was stirred for ten minutes, followed by the addition of 2.12 g (11.06 mmol, 1.20 eq.) 1-Ethyl-3-(3-dimethylamino-propyl)carbodiimide hydrochloride. The reaction was stirred overnight at room temperature. 100 mL dichloromethane were added to the colourless solution, which was extracted with 0.5 M potassium hydrogen sulfate solution, 0.5 M sodium hydrogen carbonate solution and 0.1 M hydrochloric acid. The organic phase was dried over sodium sulfate before the solvent was removed in vacuum.

3.16 g (5.25 mmol, 63 %) of methyl 3-(3-(benzyloxy)-2-(5-(pyridin-2-ylamino)pentanamido)-propanamido)-3-(3,5-dichlorophenyl)propanoate were obtained as a light brown oil.

$^1\text{H-NMR}$ (CDCl_3 , 300 MHz), δ [ppm] = 2.67-2.80 (m, 4H, CH_2), 3.42-3.59 (m, 3H, CH), 3.57 (m, 3H, CH_3), 3.82-3.90 (m, 1H, CH), 4.37-4.71 (m, 4H, CH_2), 4.37-4.71 (m, 2H, CH_2), 5.28-5.37 (m, 2H, CH_2), 7.12-7.39 (m, 12H, CH).

MS (ESI) m/z (% rel. Int.): 601.2 ($[\text{M}]^+$, 100); calculated: 600.19.

V.I.I.VIII 3-(3-(benzyloxy)-2-(5-(pyridin-2-ylamino)pentanamido)propanamido)-3-(3,5-dichlorophenyl)propanoic acid (EMD 527040)



1.7 g (0.0028 mol, 1.00 eq.) methyl 3-(3-(benzyloxy)-2-(5-(pyridin-2-ylamino)pentanamido)propanamido)-3-(3,5-dichlorophenyl)propanoate was dissolved in 50 mL methanol and 20 mL water. The pH is adjusted to 11 with 1 N sodium hydroxide solution. The mixture is stirred for four days at room temperature, before the solvents are removed in vacuum.

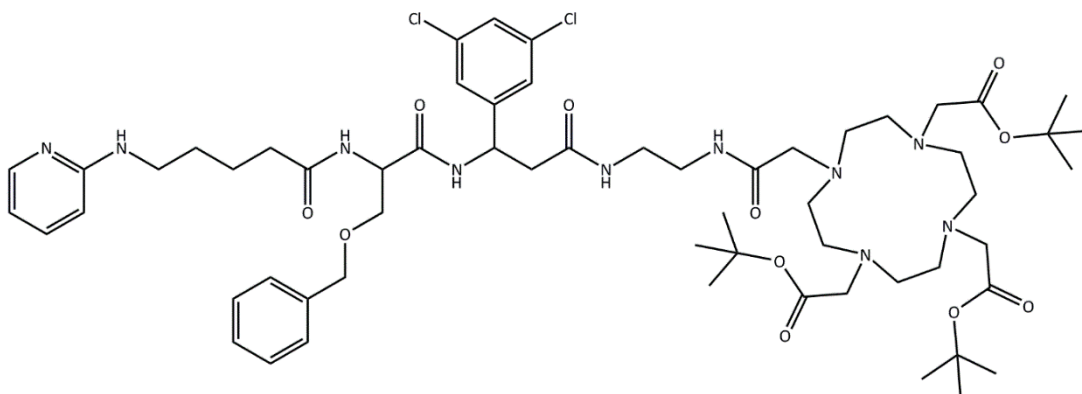
1.598 g (0.0027 mol, 97%) 3-(3-(benzyloxy)-2-(5-(pyridin-2-ylamino)pentanamido)propanamido)-3-(3,5-dichlorophenyl)propanoic acid (EMD 527040) were obtained as a yellow solid.

$^1\text{H-NMR}$ (D_2O , 300 MHz), δ [ppm] = 1.38-1.62 (m, 4H, $-\text{CH}_2-(\text{CH}_2)_2-\text{CH}_2-$), 2.03-2.25 (m, 2H, Pyridin-NH- CH_2-), 2.42-2.56 (m, 2H, Pyridin-NH- $(\text{CH}_2)_3-\text{CH}_2-$), 3.03-3.12 (m, 2H, CONH-CH- $\text{CH}_2-\text{O}-\text{CH}_2$ -Phenyle), 3.18 (s, 2H, $-\text{O}-\text{CH}_2$ -Phenyle), 3.53-3.67 (m, 1H, $-\text{CONH}-\text{CH}-\text{CONH}-$), 4.30-4.47 (m, 2H, $-\text{CH}_2-\text{COOH}$), 4.96-5.09 (m, 1H, $-\text{CH}-\text{CH}_2-\text{COOH}$), 6.28-6.38 (m, 2H, $\text{CH}_{\text{aromat.}}$), 7.02-7.31 (m, 9H, $\text{CH}_{\text{aromat.}}$), 7.67-7.82 (m, 1H, $\text{CH}_{\text{aromat.}}$).

MS (ESI) m/z (% rel. Int.): 587.2 ($[\text{M}]^+$, 100); calculated: 586.17.

V.I.II Synthesis of labelling precursors

V.I.II.1 *tert-butyl 2,2',2''-(10-(12-(benzyloxymethyl)-9-(3,5-dichlorophenyl)-2,7,11,14-tetraoxo-18-(pyridin-2-ylamino)-3,6,10,13-tetraazaoctadecyl)-1,4,7,10-tetraazacyclododecane-1,4,7-triyl)triacetate*



10.4 mg (17 μmol , 1.00 eq.) tris(*tert*-Bu)DOTA-ethylamine was dissolved in 400 μL of dimethylformamide to which 3.5 μL 2,2,6,6-tetramethyl piperidine were added. Separately, 7.3 mg (17 μmol , 1.00 eq.) COMU ((1-Cyano-2-ethoxy-2-oxoethylideneaminoxy)dimethylamino-morpholino-carbenium hexafluorophosphate) were dissolved in 200 μL dimethylformamide and mixed with a solution of 10 mg (17 μmol , 1.00 eq.) of 3-(3-(benzyloxy)-2-(5-(pyridin-2-ylamino)pentanamido)propanamido)-3-(3,5-dichlorophenyl)propanoic acid (EMD 527040) in 500 μL . To this mixture, also 3.5 μL 2,2,6,6-tetramethyl piperidine are added. After ten minutes of activation, the two solutions were combined and subjected to a microwave procedure: 20 times for 10 seconds at 55W. Between microwave treatments the mixture was cooled down to room temperature with ice. Subsequently, the solvent was removed in vacuum and the residue was purified by column chromatography (SiO_2 , dichloromethane/methanol: 13/1 + 1% NH_3).

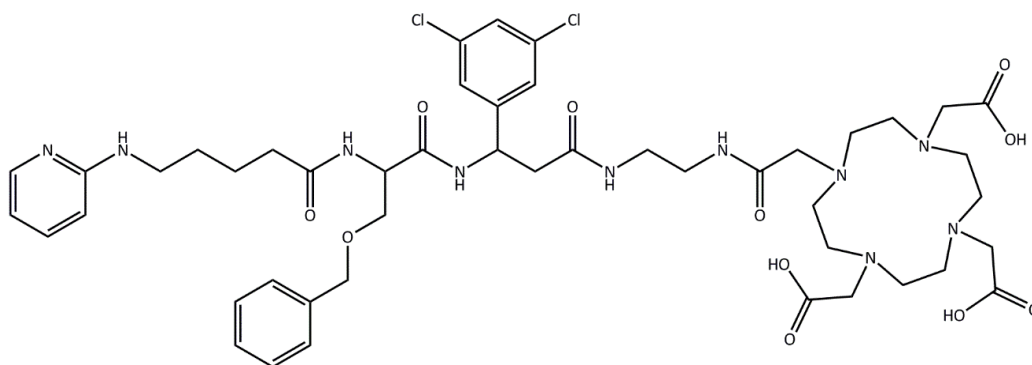
12 mg (10 μmol , 60 %) of *tert-butyl 2,2',2''-(10-(12-(benzyloxymethyl)-9-(3,5-dichlorophenyl)-2,7,11,14-tetraoxo-18-(pyridin-2-ylamino)-3,6,10,13-tetraazaoctadecyl)-1,4,7,10-tetraazacyclododecane-1,4,7-triyl)triacetate* were obtained as a light yellow oil.

$^1\text{H-NMR}$ (CDCl_3 , 300 MHz), δ [ppm] = 1.42 (s, 18H, *tert*-Bu *H* (ring position 4,10)), 1.45 (s, 9H, *tert*-Bu *H* (ring position 7)), 1.57-1.79 (m, 4H, $\text{CH}_{\text{aliph.}}$), 1.98-3.69 (very broad, m, 34H, $\text{CH}_{\text{aliph.}}$), 3.84-3.93 (m, 1H, $\text{CH}_{\text{aliph.}}$), 4.38-4.58 (m, 2H, $\text{CH}_{\text{aliph.}}$), 4.61-4.71 (m, 1H, $\text{CH}_{\text{aliph.}}$), 5.29-5.47 (m, 2H, $\text{CH}_{\text{aliph.}}$), 6.45-6.58 (m, 2H, $\text{CH}_{\text{aromat.}}$), 6.67-6.74 (m, 1H, $\text{CH}_{\text{aromat.}}$), 6.86-6.99 (m, 1H, $\text{CH}_{\text{aromat.}}$),

7.12-7.18 (m, 1H, $CH_{\text{aromat.}}$), 7.18-7.33 (m, 4H, $CH_{\text{aromat.}}$), 7.39-7.47 (m, 2H, $CH_{\text{aromat.}}$), 7.89-7.96 (1H, $CH_{\text{aromat.}}$).

MS (ESI) m/z (% rel. Int.): 1183.65 ($[M+H]^+$, 8.75); 1205.64 ($[M+Na]^+$, 99.99); calculated: 1182.60.

V.I.II.II 2,2',2''-(10-(12-(benzyloxymethyl)-9-(3,5-dichlorophenyl)-2,7,11,14-tetraoxo-18-(pyridin-2-ylamino)-3,6,10,13-tetraazaoctadecyl)-1,4,7,10-tetraazacyclododecane-1,4,7-triyl)triacetic acid



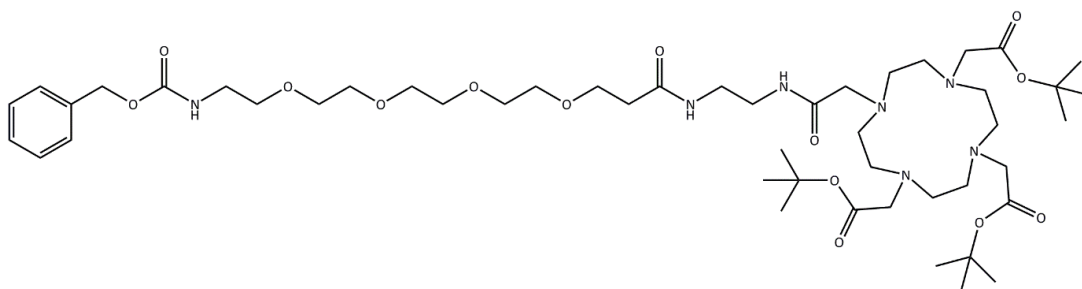
12 mg (10 μmol , 1.00 eq.) tert-butyl 2,2',2''-(10-(12-(benzyloxymethyl)-9-(3,5-dichlorophenyl)-2,7,11,14-tetraoxo-18-(pyridin-2-ylamino)-3,6,10,13-tetraazaoctadecyl)-1,4,7,10-tetraazacyclododecane-1,4,7-triyl)triacetate were dissolved in 6 mL of a trifluoro acetate / dichloromethane (1:1) mixture and stirred at room temperature for 36 h. The solvent was removed in vacuum and the raw product was purified by HPLC. Column: Onyx Monolythic C18, 100 x 4.6 mm (Phenomenex); Water + 0.05 % TFA / Acetonitrile; Gradient: 0 min: 98 % aqueous \rightarrow 20 min: 60 % aqueous \rightarrow 25 min: 60 % aqueous \rightarrow 27 min: 98 % aqueous. R_t = 12.6 min.

3.4 mg (3.4 μmol , 33%) of 2,2',2''-(10-(12-(benzyloxymethyl)-9-(3,5-dichlorophenyl)-2,7,11,14-tetraoxo-18-(pyridin-2-ylamino)-3,6,10,13-tetraazaoctadecyl)-1,4,7,10-tetraazacyclododecane-1,4,7-triyl)triacetic acid were obtained as a colourless oil.

$^1\text{H-NMR}$ (d_4 -MeOH, 400 MHz), δ [ppm] = 0.83-0.98 (m, 1H, $CH_{\text{aliph.}}$), 1.12-1.22 (m, 1H, $CH_{\text{aliph.}}$), 1.27-1.47 (m, 7H, $CH_{\text{aliph.}}$), 1.62-1.84 (m, 4H, $CH_{\text{aliph.}}$), 2.22 – 3.95 (very broad, m, 28H, $CH_{\text{aliph.}}$), 4.23-4.71 (m, 3H, $CH_{\text{aliph.}}$), 6.70-6.82 (m, 1H, $CH_{\text{aromat.}}$), 6.86-6.95 (m, 1H, $CH_{\text{aromat.}}$), 7.18-7.35 (m, 5H, $CH_{\text{aromat.}}$), 7.39-7.49 (m, 2H, $CH_{\text{aromat.}}$), 7.61-8.11 (br, m, 3H, $CH_{\text{aromat.}}$).

MS (ESI) m/z (% rel. Int.): 508.22 ($[(M/2)+H]^+$, 48.84), 1015.44 ($[M+H]^+$, 30.23); 1039.43 ($[M+Na]^+$, 52.91); calculated: 1014.41.

V.I.II.III tert-butyl 2,2',2''-(10-(3,19,24-trioxo-1-phenyl-2,7,10,13,16-pentaoxa-4,20,23-triazapentacosan-25-yl)-1,4,7,10-tetraazacyclododecane-1,4,7-triyl)triacetate



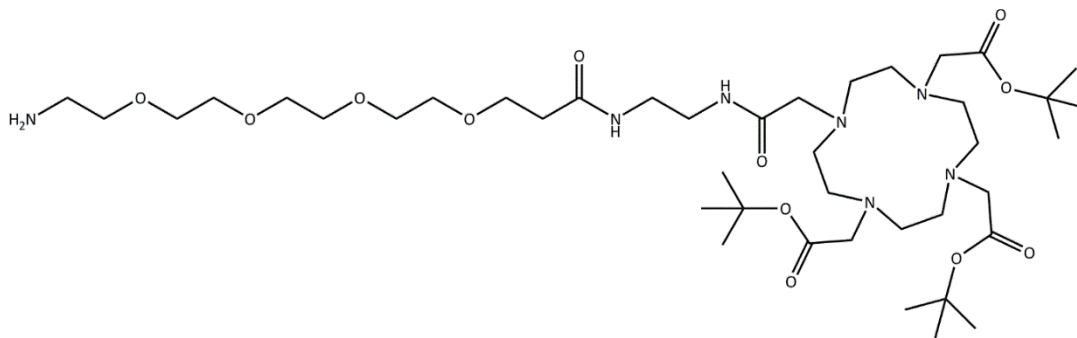
23.1 mg (37.5 μmol , 1.00 eq.) tris(tert.-Bu)DOTA-ethylamine was dissolved in 500 μL of dimethylformamide to which 7.6 μL 2,2,6,6-tetramethyl piperidine were added. Separately, 16.1 mg (17 μmol , 1.00 eq.) COMU ((1-Cyano-2-ethoxy-2-oxoethylideneaminoxy)dimethylamino-morpholino-carbenium hexafluorophosphate) were dissolved in 500 μL DMF and mixed with a solution of 15 mg (37.5 μmol , 1.00 eq.) of Cbz-N-amido-dPEG4-acid in 1 mL. To this mixture, also 7.6 μL 2,2,6,6-tetramethyl piperidine are added. After ten minutes of activation, the two solutions were combined and subjected to a microwave procedure: 20 times for 10 seconds at 55W. Between microwave treatments the mixture was cooled down to room temperature with ice. Subsequently, the solvent was removed in vacuum and the residue was purified by column chromatography (SiO_2 , dichloromethane/methanol: 15/1).

18 mg (18 μmol , 48%) of tert-butyl 2,2',2''-(10-(3,19,24-trioxo-1-phenyl-2,7,10,13,16-pentaoxa-4,20,23-triazapentacosan-25-yl)-1,4,7,10-tetraazacyclododecane-1,4,7-triyl)triacetate were obtained as a colourless oil.

$^1\text{H-NMR}$ (CDCl_3 , 300 MHz), δ [ppm] = 1.43 (s, 18H, tert-Bu H (ring position 4,10)), 1.44 (s, 9H, tert-Bu H (ring position 7)), 1.98-3.78 (very broad, m, 48H, $\text{CH}_{\text{aliphatic}}$), 5.08 (s, 2H, Phenyle- $\text{CH}_2\text{-O}$), 7.30-7.41 (m, 5H, $\text{CH}_{\text{aromatic}}$).

MS (ESI) m/z (% rel. Int.): 996.64 ($[\text{M}+\text{H}]^+$, 16.36); 1018.60 ($[\text{M}+\text{Na}]^+$, 100.00); 509.80 ($[(\text{M}+\text{Na})/2]^+$, 2.38); calculated: 995.62.

V.I.II.IV *tert*-butyl 2,2',2''-(10-(1-amino-15,20-dioxo-3,6,9,12-tetraoxa-16,19-diazahenicosan-21-yl)-1,4,7,10-tetraazacyclododecane-1,4,7-triyl)triacetate

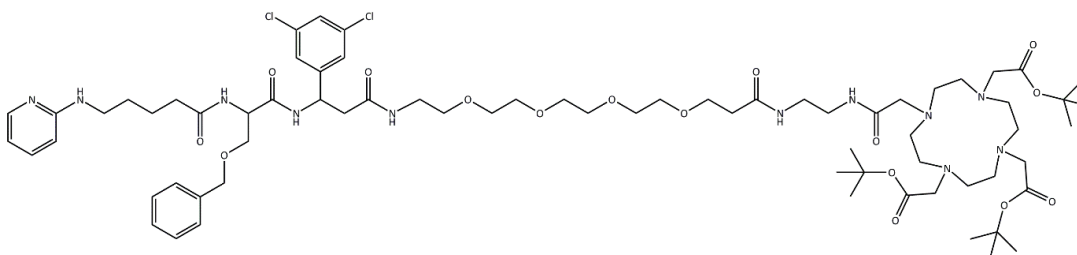


12 mg (12 μmol , 1.00 eq.) *tert*-butyl 2,2',2''-(10-(3,19,24-trioxo-1-phenyl-2,7,10,13,16-pentaoxa-4,20,23-triazapentacosan-25-yl)-1,4,7,10-tetraazacyclododecane-1,4,7-triyl)triacetate were dissolved in 8 mL of a methanol/triethyl amine mixture (3/1) and 0.5 mg of Pd/C (10%) were added. This mixture was hydrated at room temperature and atmospheric pressure for 10 h. The catalyst was filtered over celite and the remaining filtrate was concentrated in vacuum. Subsequently, the residue was purified via column chromatography (SiO_2 , DCM/MeOH/ NH_3 : 10/1/1 \rightarrow 10/2/1 \rightarrow 10/3/1).

4.2 mg (4.8 μmol , 40%) of *tert*-butyl 2,2',2''-(10-(1-amino-15,20-dioxo-3,6,9,12-tetraoxa-16,19-diazahenicosan-21-yl)-1,4,7,10-tetraazacyclododecane-1,4,7-triyl)triacetate as light yellow oil were obtained.

$^1\text{H-NMR}$ (CDCl_3 , 300 MHz), δ [ppm] = 1.43 (s, 18H, *tert*-Bu *H* (ring position 4,10)), 1.44 (s, 9H, *tert*-Bu *H* (ring position 7)), 2.07-3.76 (very broad, m, $\text{CH}_{\text{aliphatic}}$).

V.I.II.V *tert*-butyl 2,2',2''-(10-(28-(benzyloxymethyl)-25-(3,5-dichlorophenyl)-2,7,23,27,30-pentaoxa-34-(pyridin-2-ylamino)-10,13,16,19-tetraoxa-3,6,22,26,29-pentaazatetraatriacontyl)-1,4,7,10-tetraazacyclododecane-1,4,7-triyl)triacetate



20 mg (23 μmol , 1.00 eq.) *tert*-butyl 2,2',2''-(10-(1-amino-15,20-dioxo-3,6,9,12-tetraoxa-16,19-diazahenicosan-21-yl)-1,4,7,10-tetraazacyclododecane-1,4,7-triyl)triacetate was dissolved in

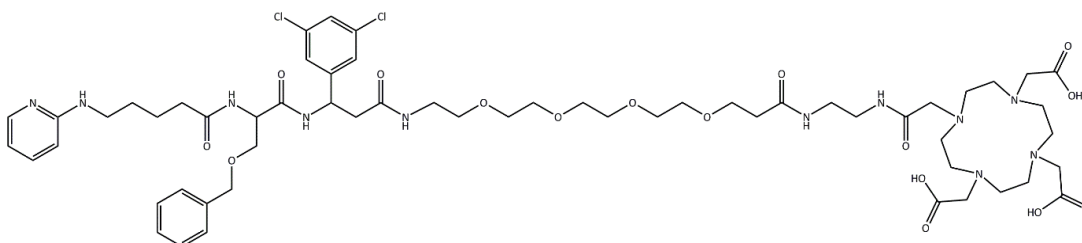
250 μL of DMF to which 4.7 μL 2,2,6,6-tetramethyl piperidine were added. Separately, 9.9 mg (23 μmol , 1.00 eq.) COMU ((1-Cyano-2-ethoxy-2-oxoethylideneaminoxy)dimethylamino-morpholino-carbenium hexafluorophosphate) were dissolved in 500 μL dimethylformamide and mixed with a solution of 13 mg (23 μmol , 1.00 eq.) of 3-(3-(benzyloxy)-2-(5-(pyridin-2-ylamino)pentanamido)propanamido)-3-(3,5-dichlorophenyl)propanoic acid (EMD 527040) in 100 μL . To this mixture, also 4.7 μL TMP are added. After ten minutes of activation, the two solutions were combined and subjected to a microwave procedure: 20 times for 10 seconds at 55W. Between microwave treatments the mixture was cooled down to room temperature with ice. Subsequently, the solvent was removed in vacuum and the residue was purified by column chromatography (SiO_2 , dichloromethane/methanol: 20/1 + 3% NH_3).

15 mg (10 μmol , 45%) of tert-butyl 2,2',2''-(10-(28-(benzyloxymethyl)-25-(3,5-dichlorophenyl)-2,7,23,27,30-pentaoxo-34-(pyridin-2-ylamino)-10,13,16,19-tetraoxa-3,6,22,26,29-pentaazatetraatriacontyl)-1,4,7,10-tetraazacyclododecane-1,4,7-triyl)triacetate were obtained as a light yellow oil.

$^1\text{H-NMR}$ (CDCl_3 , 300 MHz), δ [ppm] = 1.41 (s, 18H, tert-Bu H (ring position 4,10)), 1.43 (s, 9H, tert-Bu H (ring position 7)), 1.97-3.72 (very broad, m, 64H, $\text{CH}_{\text{aliph.}}$), 4.46-4.64 (m, 4H, $\text{CH}_{\text{aliph.}}$), 5.22-5.36 (m, 3H, $\text{CH}_{\text{aliph.}}$), 6.51-6.59 (m, 1H, $\text{CH}_{\text{aromat.}}$), 7.01-7.09 (m, 1H, $\text{CH}_{\text{aromat.}}$), 7.12-7.18 (m, 1H, $\text{CH}_{\text{aromat.}}$), 7.19-7.34 (m, 8H, $\text{CH}_{\text{aromat.}}$), 7.41-7.54 (m, 1H, $\text{CH}_{\text{aromat.}}$).

MS (ESI) m/z (% rel. Int.): 1430.93 ($[\text{M}+\text{H}]^+$, 5.47); 1452.90 ($[\text{M}+\text{Na}]^+$, 28.46); 1480.93 ($[\text{M}+2\text{Na}]^+$, 57.83); calculated: 1429.74.

V.I.II.VI 2,2',2''-(10-(28-(benzyloxymethyl)-25-(3,5-dichlorophenyl)-2,7,23,27,30-pentaoxo-34-(pyridin-2-ylamino)-10,13,16,19-tetraoxa-3,6,22,26,29-pentaazatetraatriacontyl)-1,4,7,10-tetraazacyclododecane-1,4,7-triyl)triacetic acid



15 mg (10 μmol , 1.00 eq.) tert-butyl 2,2',2''-(10-(28-(benzyloxymethyl)-25-(3,5-dichlorophenyl)-2,7,23,27,30-pentaoxo-34-(pyridin-2-ylamino)-10,13,16,19-tetraoxa-3,6,22,26,29-pentaazatetraatriacontyl)-1,4,7,10-tetraazacyclododecane-1,4,7-triyl)triacetate were dissolved

in a mixture of 3 mL dichloromethane and 1 mL trifluoro acetate. It was stirred overnight at room temperature before the solvents were removed in vacuum. 18 mg raw product were obtained, which were subjected to HPLC purification. Column: Onyx Monolythic C18, 100 x 10 mm (Phenomenex); Water + 0.05 % TFA / Acetonitrile; Gradient: 0 min: 90 % aqueous → 35 min: 50 % aqueous → 37 min: 50 % aqueous → 40 min: 90 % aqueous → 45 min: 90 % aqueous. R_t = 21.7 min.

7.2 mg (6 μ mol, 60 %) 2,2',2''-(10-(28-(benzyloxymethyl)-25-(3,5-dichlorophenyl)-2,7,23,27,30-penta-oxo-34-(pyridin-2-ylamino)-10,13,16,19-tetra-oxa-3,6,22,26,29-penta-azatetra-riacontyl)-1,4,7,10-tetra-azacyclododecane-1,4,7-triyl)tri-acetic acid were obtained as a colourless oil.

$^1\text{H-NMR}$ (d_4 -MeOH, 400 MHz), δ [ppm] = 0.99-1.10 (m, 2H, $\text{CH}_{\text{aliph.}}$), 1.28-1.39 (m, 4H, $\text{CH}_{\text{aliph.}}$), 1.66-1.81 (m, 5H, $\text{CH}_{\text{aliph.}}$), 2.31-2.50 (m, 5H, $\text{CH}_{\text{aliph.}}$), 2.64-4.02 (very broad, m, 40H, $\text{CH}_{\text{aliph.}}$), 4.51-4.63 (m, 4H, $\text{CH}_{\text{aliph.}}$), 5.23-5.37 (m, 4H, $\text{CH}_{\text{aliph.}}$), 6.86 (t, J = 6.5 Hz, 1H, $\text{CH}_{\text{aromat.}}$), 7.01 (t, J = 8.6 Hz, 1H, $\text{CH}_{\text{aromat.}}$), 7.21-7.39 (m, 7H, $\text{CH}_{\text{aromat.}}$), 7.77-7.92 (m, 3H, $\text{CH}_{\text{aromat.}}$).

MS (ESI) m/z (% rel. Int.): 1262.65 ($[\text{M}+\text{H}]^+$, 21.74); 631.82 ($[(\text{M}+\text{H})/2]^+$), 25.65) calculated: 1261.56.

V.II Radiochemistry

V.II.I Labelling procedure

For labellings with ^{68}Ga , the $^{68}\text{Ge}/^{68}\text{Ga}$ generator was eluted according to standard procedure and the cation exchange resin-based post-processing by Zhernosekov et al. was applied.⁴³ Therefore, the generator was eluted with 5-7 mL 0.1 M HCl – this was directly loaded onto the cation exchanger. In order to remove other metals, the resin was washed with 1 mL N1 (80 % acetone / 0.15 M HCl). Elution of ^{68}Ga from the resin was achieved with 400 μL N2 (97.6 % acetone / 0.05 M HCl).

The labelling reaction was performed by mixing X μL of the stock solution (1 mg/mL) of precursor with 400 μL HEPES-buffer (238 mg Na-HEPES dissolved in 0.1 M HCl). 200 μL of ethanol were added to the mixture before addition of the ^{68}Ga -eluate (400 μL). Then, it was incubated (95 °C) and shaken (400 rpm) for 10 minutes in the thermomixer.

Precursor amounts were varied from 10 to 30 nmol.

For purification, a solid phase extraction method was used. The reaction mixture was taken up in 8 mL of water and applied to a pre-conditioned Strata X cartridge. (Conditioning: 1 mL ethanol followed by 3 mL of water). The free ^{68}Ga was eluted with 3 mL water before the product could be eluted with 0.5 mL of ethanol. Evaporation of the solvent allowed the use for further experiments.

V.II.II Kinetic studies

For the determination of the kinetic behaviour of the labelling reactions, the labelling was performed according to standard procedure. During the reaction aliquots were taken at 0, 1, 3, 5, 7 and 10 minutes and analysed with radio – TLC (SiO_2 , 0.1 M citrate buffer pH 4).

V.II.III Stability studies

The determination of *in vitro* stabilities was performed according to Fellner et al.¹³² 20 µL of the purified radiotracer were added to 400 µL isotonic saline (0.9%), 400 µL PBS, 400 µL Apo-Transferrine (3 mg/mL in PBS) or 400 µL human serum (Sigma Aldrich GmbH, Taufkirchen, Germany). This was incubated at 37°C in a thermoshaker.

Aliquots were taken at 0, 10, 20, 30, 45, 60, 90, 120 and 180 minutes and analysed with radio-TLC (SiO₂, 0.1 M citrate buffer pH 4) – they were analysed with the Instant Imager.

All tests were performed in triplicates.

V.II.IV Log D

In order to evaluate the complexes' polarity, the distribution coefficient between PBS buffer and octanol logD was evaluated according to the 'shake flask method'.¹³² The radiotracers were synthesized according to standard procedure and the purified compounds were taken up in 1 mL PBS buffer. This was partitioned to 4 eppendorf vials (2 mL). Each vial was adjusted to a content of 700 µL of octanol and 700 µL of PBS buffer. The vials were then mixed for two minutes at 1500 rpm in a HLC Biotech HeatingThermoMixer MHR 13. Afterwards they were centrifuged at 12000 rpm to separate the phases.

3 µL of the octanol as well as the PBS phase were taken and spotted on absorbent paper – the activity was measured with the Instant Imager and used for calculation of $\log D =$

$$\log_{10} \left(\frac{A_{\text{Octanol}}}{A_{\text{Water}}} \right).$$

400 µL of the octanol phase were taken and added to a vial containing 300 µL octanol and 700 µL PBS buffer – therefore a reextraction could be performed. This was done twice and only the second and third extractions were included in the calculation.

V.III Cell Assays

V.III.I Affinity

Cell lines used for the experiments were HT-29 (human colorectal adenocarcinoma, $\alpha_v\beta_6$ positive), 603B (mouse biliary epithelial, $\alpha_v\beta_6$ positive), and Huh-7 (hepatic carcinoma, $\alpha_v\beta_6$ negative). Cells were seeded in single-breakable and high binding ELISA plates (Greiner BioOne) and grown to 80 % confluence. The respective radiotracer was labelled according to the general protocol and 100 μL were added in different concentrations to the cells. All tests were performed in triplicates. In a second series of triplicates, the same amounts of radiotracer were added to cells pre-treated with 10 μL of EMD527040 solution – yielding a final concentration of 3 μM . It was incubated for 45 minutes on ice before aspiration and a double washing step with 250 μL of PBS. The plates were broken into the single wells and radioactivity was measured for 1 minute each (2470 WIZARD² Automatic Gamma Counter).

V.III.II Uptake

Cell lines used for the experiments were HT-29 (human colorectal adenocarcinoma, $\alpha_v\beta_6$ positive), 603B (mouse biliary epithelial, $\alpha_v\beta_6$ positive), and Huh-7 (hepatic carcinoma, $\alpha_v\beta_6$ negative). Cells were seeded in single-breakable and high binding ELISA plates (Greiner BioOne) and grown to 80 % confluence. The respective radiotracer was labelled according to the general protocol and 100 μL were added to the cells. All tests were performed in triplicates. Incubation time was 30 minutes at 0 °C and at 37 °C. The supernatant was removed and the wells were washed with 250 μL PBS, which was added to the supernatant fraction. Afterwards, 100 μL of stripping buffer (diluted acetic acid, pH 3) were added for two minutes and collected separately. Fractions of supernatant, stripping buffer and cells were measured for radioactivity for 1 minute with the 2470 WIZARD² Automatic Gamma Counter.

V.III.III Challenge

As above, cell lines used for the experiments were HT-29 (human colorectal adenocarcinoma, $\alpha_v\beta_6$ positive), 603B (mouse biliary epithelial, $\alpha_v\beta_6$ positive), and Huh-7 (hepatic carcinoma, $\alpha_v\beta_6$ negative). Cells were seeded in single-breakable and high binding ELISA plates (Greiner BioOne) and grown to 80 % confluence. 20 μL of different concentrations of EMD527040 in PBS were added before the addition of 100 μL radiotracer (yielding final concentrations of EMD527040 of 30 μM , 15 μM , 3 μM , 1.5 μM , 300 nM, 150 nM, 30 nM, 15 nM, 3 nM, 1.5 nM, 300 pM and 150 pM). All tests were performed in triplicates. It was incubated for 45 minutes before a washing step with 250 μL PBS was performed. The plates were broken into single wells and measured for 1 minute with the 2470 WIZARD² Automatic Gamma Counter.

V.IV ELISA – Protocols

V.IV.I Alpha_v – Sandwich-Assay

The assay was performed in single-breakable and high binding ELISA plates (Greiner BioOne). 100 µL of the integrin $\alpha_v\beta_6$ (1µg/mL and 0.1 µg/mL) were coated over night at 4 °C and for 1 hour at 37 °C. Three different buffers were tested: PBS, TBS + 1 mM CaCl₂ + 1 mM MgCl₂ + 40 µM MnCl₂ and a carbonate buffer of pH 9.6. Subsequently, a commercial ELISA Kit for the detection of human alpha V was used according to the instructions. (www.antikoerper-online.de; Product number ABIN417609). It was started at the third step 'addition of the Detection Reagent A', as the coated plate corresponds to the sample. Additionally, the pre-coated plates from the kit were used for a dilution series of α_v sample, provided by the manufacturer: 10, 5, 2.5, 1.25, 0.625, 0.312 and 0.156 ng/mL were tested together with samples of the integrin $\alpha_v\beta_6$ (1µg/mL and 0.1 µg/mL in PBS and the TBS buffer mentioned above) fully according to the instructions. The optical density was measured at 450 nm

V.IV.II Anti- $\alpha_v\beta_6$ -based Assay

The assays were performed in single-breakable and high binding ELISA plates (Greiner BioOne). 100 µL of the integrin $\alpha_v\beta_6$ (1µg/mL and 0.1 µg/mL) were coated in PBS at 4 °C over night. Subsequently, the supernatant was removed and incubated for 1 h with 150 µL of 5 % BSA in PBS at 37 °C. This was followed by a double washing step with 200 µL of PBS + 0.05 % TWEEN 20. Subsequently, 100 µL of Anti- $\alpha_v\beta_6$ (STX-100) were added at different dilutions (in integrin binding buffer – TBS + 1 mM CaCl₂ + 1 mM MgCl₂ + 10 µM MnCl₂ + 0.1 % BSA): 1/5.000, 1/10.000 and 1/20.000; the stock solution's concentration was 1.1111mg/mL. The incubation was performed for 3 hours at 37 °C. The aforementioned double washing step was repeated with integrin binding buffer replacing PBS. The next step was the addition of 100µL Anti-Mouse-Peroxidase (diluted to 1/20.000 in integrin binding buffer) for 1 hour at 37 °C. The double washing step with integrin binding buffer + 0.05 % TWEEN 20 was repeated before the addition of 100 µL ortho-phenylenediamine at 0.4 mg/mL in 0.05M phosphate-citrate-buffer with 0.03 %

sodium perborate. This was incubated for 30 minutes at room temperature. The optical density was measured at 450 nm.

For blocking experiments with EMD527040, it was diluted in integrin binding buffer to various concentrations: 5 μ M, 1 μ M, 100 nM, 50 nM, 10 nM, 5 nM and 500 pM. 100 μ L of the ligands were added after BSA was incubated and washed off. They were incubated for 1 or 2 hours at 37 °C. Afterwards, the supernatant was removed but no washing step followed before addition of 100 μ L of Anti- $\alpha_v\beta_6$ (1/10.000). This was again incubated for 3 h at 37 °C. From this point on, the protocol was followed as outlined above.

V.IV.III Fibronectin Biotinylation

1 mg fibronectin was reconstituted in 1 mL sterile filtered water at 37°C for 30 min. 5 mg biotinamidocaproate N-hydroxysuccinimide ester were dissolved in 100 μ L of dry dimethylformamide. 0.5 M sodium carbonate solution and 0.5 M sodium hydrogen carbonate solution were combined to yield a carbonate buffer of pH 9.03. 900 μ L fibronectin stock solution were mixed with 100 μ L carbonate buffer, finally 1.5 μ L of the biotinylation agent were added. The mixture was stirred for one hour at room temperature and was stopped by addition of 110 μ L of a 1M ammonium chloride solution.

A dialysis tube (Spectrapor 12000 – 14000) was pre-incubated with 1% BSA in PBS for 1h and washed several times with water before filling in the reaction mixture. It was dialysed at 4 °C against 1 L PBS buffer, which was exchanged after 4 h before dialysis was continued overnight.

The solution was not worked up any further, only its concentration was determined with a BCA assay (Thermo Scientific Pierce) according to standard protocol. The peak maximum was identified at 561 nm, which was used for analysis. The concentration was determined to be 843 μ g/mL.

V.IV.IV Fibronectin-based Assay

The assays were performed in single-breakable and high binding ELISA plates (Greiner BioOne). 100 μL of the integrin $\alpha_v\beta_6$ (1 $\mu\text{g}/\text{mL}$ and 0.1 $\mu\text{g}/\text{mL}$) were coated in PBS at 4 $^\circ\text{C}$ over night. Subsequently, the supernatant was removed and incubated for 1 h with 200 μL of 5 % BSA in PBS at 37 $^\circ\text{C}$. This was followed by a double washing step with 250 μL of PBS + 0.05 % TWEEN 20. Subsequently, 100 μL of the biotinylated fibronectin were incubated for 3 hours at 37 $^\circ\text{C}$ at concentrations of 1 $\mu\text{g}/\text{mL}$ and 2 $\mu\text{g}/\text{mL}$. An integrin binding buffer (TBS + 1mM CaCl_2 + 1 mM MgCl_2 + 10 μM MnCl_2 at pH 7.6) was used for dilution. Subsequently, the aforementioned double washing step was repeated, replacing PBS by the binding buffer. Fibronectin was detected by addition of 100 μL of Anti-Biotin-Peroxidase (diluted to 1/30.000) for 1 hour at 37 $^\circ\text{C}$, followed by the double washing step with integrin binding buffer and 0.05 % TWEEN 20, and the subsequent addition of 100 μL ortho-phenylenediamine at 0.4 mg/mL in 0.05M phosphate-citrate-buffer with 0.03 % sodium perborate. This was incubated for 30 minutes at room temperature. The optical density was measured at 450 nm.

For blocking experiments with EMD527040, it was diluted in integrin binding buffer to various concentrations: 5 μM , 1 μM , 100 nM, 50 nM, 10 nM, 5 nM and 500 pM. 100 μL of the ligands were added after BSA was incubated and washed off. They were incubated for 1 or 2 hours at 37 $^\circ\text{C}$. Afterwards, the supernatant was removed but no washing step followed before addition of 100 μL of the biotinylated fibronectin (1 $\mu\text{g}/\text{mL}$). This was again incubated for 3 h at 37 $^\circ\text{C}$. From this point on, the protocol was followed as outlined above (with dilutions for Anti-Biotin-Peroxidase of 1/20.000 and 1/30.000).

V.IV.V Radioassay on $\alpha_v\beta_6$ –coated ELISA plates

The assays were performed in single-breakable and high binding ELISA plates (Greiner BioOne) and all tests were performed in triplicates. 100 μL of the integrin $\alpha_v\beta_6$ (1 $\mu\text{g}/\text{mL}$) were coated in PBS at 4 $^\circ\text{C}$ over night. Subsequently, the supernatant was removed and incubated for 1 h with 200 μL of 5 % BSA in PBS at 37 $^\circ\text{C}$. This was followed by a double washing step with 250 μL of PBS + 0.05 % TWEEN 20. The samples were pre-treated with 50 μL of EMD527040 solution (yielding a final concentration of 5 μM). 50 μL of the radiotracer were added in a dilution series in integrin binding buffer (TBS + 1mM CaCl_2 + 1 mM MgCl_2 + 10 μM MnCl_2 + 0.1 % BSA at pH7.6) or PBS and

incubated for 2 hours at room temperature. Dilutions yielded final concentrations of 1 μM , 500 nM, 100nM, 50 nM, 10 nM, 5 nM, 1 nM, 500 pM, 100 pM, 50 pM, 10 pM and 5 pM for the radiotracer. After incubation, the supernatant was removed and plates were washed twice with 250 μL of the respective buffer. The plates were broken into single wells and measured for 1 minute with the 2470 WIZARD² Automatic Gamma Counter.

V.IV.VI General Procedure – LAP Assay

The assays were performed in single-breakable and high binding ELISA plates (Greiner BioOne). Generally, 100 μL of the integrin $\alpha_v\beta_6$ were coated in PBS at 4 °C over night. Subsequently, the supernatant was removed and incubated for 1 h with 200 μL of 5 % BSA in PBS at 37°C. This was followed by a double washing step with 250 μL of PBS + 0.05 % TWEEN 20. Then the respective ligands were incubated together with LAP (total volume 100 μL) at 37 °C for usually 90 minutes (unless noted otherwise). For this step an integrin binding buffer was used, consisting of TBS + 1mM CaCl_2 + 1 mM MgCl_2 + 10 μM MnCl_2 + 0.1 % BSA at pH7.6. This was followed by another double washing step of 250 μL , with the above mentioned binding buffer containing additional 0.05 % TWEEN 20. This was followed by the incubation of 100 μL Anti-LAP for 2 h at room temperature. Again, afterwards followed a double washing step with binding buffer containing 0.05 % TWEEN 20. 100 μL Anti-Biotin-Peroxidase were added for 1 h at 37 °C in binding buffer and finally the wells were washed again doubly with the binding buffer including 0.05 % TWEEN 20. For detection, 100 μL ortho-phenylenediamine at 0.4 mg/mL in 0.05M phosphate-citrate-buffer with 0.03 % sodium perborate were added and incubated for 30 minutes at room temperature. The optical density was measured at 450 nm.

V.V Quartz Crystal Microbalance

For QCMD measurements, clean gold sensors (Biolin Scientific / Q-Sense; Sweden) were incubated overnight at 4°C in a 4/94 solution of 1M HS-(CH₂)₁₁-EG₆-NH₂ in EtOH and 1M HS-(CH₂)₁₁-EG₃-OMe in EtOH. For this purpose, 50 µL of the solution are placed on parafilm and covered with the sensor. Afterwards, the sensors are washed with ethanol and modified by a 2h incubation at room temperature with 0.5 mg/mL EMD527040 in MES-buffer (0.1 M 2-(N-morpholino)ethanesulfonic acid + 0.5 M NaCl), containing 100 mg EDC (1-Ethyl-3-(3-dimethylaminopropyl)carbodiimide) and 30 mg NHS (N-Hydroxysuccinimide) per mL. After this coupling step, the sensors were washed with water and EtOH before keeping them at 4°C in EtOH for measurements the next day.

Integrin $\alpha_v\beta_6$ was reconstituted to 100 µg/mL with PBS and further diluted to 20 µg/mL with binding buffer (TBS + 1mM CaCl₂ + 1 mM MgCl₂ + 10 µM MnCl₂ at pH7.6). The Q-Sense E1 (Biolin Scientific / Q-Sense; Sweden) was equilibrated with binding buffer before 0.5 mL of integrin solution were injected. The binding was observed in real time until a steady plateau was reached and subsequently flushed with binding buffer.

V.VI Animal studies

For the animal studies 7-9 week old female mice (18.3 – 20.5 g) of the FVB strand (negative control) and Mdr-2- knockout mice (positive control) were used. They were anaesthetized with 2% gaseous isoflurane/oxygen mixture and injected with 4-8 MBq of the respective radiotracer, prepared according to general procedure. For dilution to about 100 μ L, isotonic brine was used. Then, they were placed onto the bed of the μ PET (Focus 120, Siemens) in head-first-prone position and a dynamic scan was performed for one hour. The animals were allowed to wake up and after another hour (two hours after injection) they were sacrificed and organs (blood, liver, spleen, kidney, intestine, heart, lungs, fat pad, ovary, urine, muscle, femoral bone and back skin) were harvested. The liver was sectioned into three parts (left, right and medium lobe). The organ samples were weighed and measured for 1 minute with the 2470 WIZARD² Automatic Gamma Counter. The obtained activities were time-corrected and related to sample weight and total injected dose, to allow an expression in % ID/g.

The obtained images were reconstructed using the 'filtered back projection' method. Volumes of interest (VOIs) were drawn manually and analysed for SUV values with Pmod 3.1 (PMOD Technologies LTD) according to the following equation:

$$SUV = Activity\ VOI \left(\frac{Bq}{mL} \right) * body\ weight\ (g) * injected\ dose\ (Bq)$$

Results were exported and processed with Microsoft Excel to calculate averages and obtain graphs.

V.VII Computational Methods

V.VII.I Obtaining Ligand structures

The small molecules were drawn with Avogadro 1.1.0. After drawing, all hydrogens were removed and automatically added again for pH 7.4. This was followed by a geometry optimization step which used the default parameters, i.e. steepest descent algorithm, the UFF force field, 500 steps and a convergence of 10^{-7} . Finally, an energy minimization was run by use of the AutoOpt tool. Again, the UFF force field was chosen as well as the steepest descent algorithm. When $dE=0$, the files were saved in pdb as well as mol2 format.

V.VII.II Ligand characteristics – orbitals and electrostatic potential

For the determination of electronic characteristics, mol2 files of the minimized structures were opened with Avogadro 1.1.0, wherein the MOPAC extension was used to generate the input file. The obtained .mop files were opened with text editor to change the keywords into the following:

```
AUX LARGE CHARGE=n SINGULET PM7 GRAPHF VECTORS MMOK EIGS
```

The charge was set manually, according to the respective substance. Those files were run in MOPAC 2012. The output files were again opened in text editor to extract values of area, volume and HOMO/LUMO energies, whereas it was opened with Avogadro 1.1.0 in order to display the calculated orbitals.

For the electrostatic potential, MOPAC output files were opened in Avogadro and saved as pdb file. Those files were opened with Discovery Studio v3.5.0.12158. A surface is added with the following settings: Display Style “soft”; Surface rendering “solid”; Probe radius 1.4; Type “Closed”; Color by “Interpolated Charge”; Transparency level: 0.5. For coloring, the settings “Red-White-Blue; 100 Bands; Min: -0,100 to Max: +0,100” were chosen.

In case of the Tc-derivatives, the hybridization was changed to “Square Pyramid” in the Atom Property list.

V.VIII Homology Modelling

V.VIII.I Production of $\alpha\beta_6$ – model with SWISS-Model

The SWISS-Model server was reached via the following URL: <http://swissmodel.expasy.org/>. Subsequently, the UniProt Code P18564 was entered and a search for templates was conducted. The pdb database structure 1L5G was selected as the template structure to build the model on.

V.VIII.II Production of $\alpha_v\beta_6$ –model with MODELLER

Chimera 1.8.1 was used as interface to submit input to MODELLER 9.11. The sequence of beta 6 was loaded into Chimera via the UniProt Code P18564. The BLAST run with BLOSUM 62 matrix and an E-value of 1E-3 yielded several structures of $\alpha\beta_3$, out of which pdb entry 1L5G was chosen. The alignment was improved by running the Needleman-Wunsch algorithm with default parameters. The comparative modelling task was send to the web server - requiring 20 models and including non-water hetero atoms.

The SDL loop was refined within MODELLER based on the best model obtained before. The sequence **KPVSPFVKTTPEEIANPCSSIPYFCLPTF** (K being residue #180) was subjected to refinement with bold residues kept restricted. For this refinement five models were produced, out of which the best one was chosen.

The obtained model for beta 6 was merged with the alpha v chain and the ligand of 1L5G with VEGA ZZ.

V.VIII.III Protein-Model refinement

Within Maestro, the system was built in explicit water (SPC model) and a truncated octahedron box was established. The system was neutralised by adding 50 Na⁺ ions. Next, a steepest descent minimization was performed with 3000 steps and a convergence threshold of 0.05 kcal/mol/Å.

A force of 100 kcal/Å⁻² was applied to the whole backbone in order to keep it constrained. After this minimization, the molecular dynamics were performed with a simulated annealing of 100 ps at 10 K, 300 ps heating to 300 K, followed by 100 ps at 300 K. This was performed at constant pressure and restricted backbone as before. The final production run was performed for 500 ps, also at 300 K and constant pressure.

V.IX Docking studies

In order to perform the docking studies AutoDock 4.2 was used together with AutoDock Tools. The averaged structure of $\alpha_v\beta_6$ was prepared as follows: The ligand was removed as well as all hydrogens. Polar hydrogens were added within AutoDock Tools. Gasteiger charges were added, the charge of Mn²⁺ ions was manually changed in the pdbqt file. The ligands were also set up with AutoDock Tools – for EMD527040 and F2 all possible torsions were allowed, while for BK23 and TC1 the rotatable bonds were manually located at the EMD527040 moiety and the linker towards the chelate.

Grids were calculated with AutoGrid. Parameters for Ga and Tc were manually added to the parameter file. For that purpose, vdW radii and the energy well depth were taken from the UFF force field.⁸⁸ The atomic volume was calculated from the vdW radius according to $\frac{4}{3}\pi (R_{vdw}/2)^3$. The atomic solvation parameter value was set to -0.00110, equal to all other metals already present in the parameter file. The remaining parameters were set to the default values for non-hydrogen bonding atom types.

In order to set the grid box' position, the 1L5G complex was opened for comparison and the box (80 x 80 x 80) was positioned around the binding site. A Lamarckian genetic algorithm, as implemented in AutoDock, was applied with a protocol of a maximum number of 2.500.000 energy evaluations, a mutation rate of 0.01, a crossover rate of 0.80 and an elitism value of 1. For each ligand, fifty docking runs were performed and the results were clustered for results differing by 1.5 Å in positional root-mean-square deviation (rmsd).

VI. Literature

1. DSO: Zahlen zur Organspende und -transplantation. at <<http://www.dso.de/servicecenter/fachpublikum/zahlen-zur-organspende-und-transplantation.html>>
2. WHO | World Health Organization. at <http://gamapserver.who.int/gho/interactive_charts/gisah/death_rates_cirrhosis/atlas.html>
3. Rosenbloom, J., Mendoza, F. A. & Jimenez, S. A. Strategies for anti-fibrotic therapies. *Biochim. Biophys. Acta BBA - Mol. Basis Dis.* **1832**, 1088–1103 (2013).
4. Walter de Gruyter & Co. *Pschyrembel klinisches Wörterbuch 2012*. (Boston : De Gruyter, 2011).
5. Mutschler, E., Thews, G., Schaible, H.-G. & Vaupel, P. *Anatomie, Physiologie, Pathophysiologie des Menschen: 140 Tabellen*. (Wiss. Verl.-Ges., 2007).
6. The Human Body. *Encycl. Br.* at <<http://www.britannica.com/EBchecked/media/68633/Anterior-and-posterior-views-of-the-liver>>
7. Bataller, R. & Brenner, D. A. Liver fibrosis. *J. Clin. Invest.* **115**, 209–218 (2005).
8. The Human Body. *Encycl. Br.* at <<http://www.britannica.com/EBchecked/media/60419/Microscopic-structure-of-the-liver-Liver-cells-or-hepatocytes-have>>
9. Schuppan, D. & Afdhal, N. H. Liver cirrhosis. *The Lancet* **371**, 838–851 (2008).
10. Friedman, S. L. Liver fibrosis – from bench to bedside. *J. Hepatol.* **38**, Supplement 1, 38–53 (2003).
11. Friedman, S. L. Molecular Regulation of Hepatic Fibrosis, an Integrated Cellular Response to Tissue Injury. *J. Biol. Chem.* **275**, 2247–2250 (2000).
12. Munger, J. S. *et al.* A Mechanism for Regulating Pulmonary Inflammation and Fibrosis: The Integrin $\alpha\beta 6$ Binds and Activates Latent TGF $\beta 1$. *Cell* **96**, 319–328 (1999).
13. Popov, Y. & Schuppan, D. Targeting liver fibrosis: Strategies for development and validation of antifibrotic therapies. *Hepatology* **50**, 1294–1306 (2009).
14. Di Sario, A., Feliciangeli, G., Bendia, E. & Benedetti, A. Diagnosis of liver fibrosis. *Eur. Rev. Med. Pharmacol. Sci.* 11–18 (2004).
15. Castera, L. Hepatitis B: are non-invasive markers of liver fibrosis reliable? *Liver Int.* **34**, 91–96 (2014).
16. Biologist — BioPredictive. at <<http://www.biopredictive.com/intl/biologist/>>
17. Castera, L. & Pinzani, M. Biopsy and non-invasive methods for the diagnosis of liver fibrosis: does it take two to tango? *Gut* **59**, 861–866 (2010).

18. Bedossa, P. & Carrat, F. Liver biopsy: The best, not the gold standard. *J. Hepatol.* **50**, 1–3 (2009).
19. Bravo, A. A., Sheth, S. G. & Chopra, S. Liver Biopsy. *N. Engl. J. Med.* **344**, 495–500 (2001).
20. MENGHINI, G. One-second needle biopsy of the liver. *Gastroenterology* **35**, 190–199 (1958).
21. Bedossa, P. Intraobserver and Interobserver Variations in Liver Biopsy Interpretation in Patients with Chronic Hepatitis C. *Hepatology* **20**, 15–20 (1994).
22. Regev, A. *et al.* Sampling error and intraobserver variation in liver biopsy in patients with chronic HCV infection. *Am. J. Gastroenterol.* **97**, 2614–2618 (2002).
23. Ratziu, V. *et al.* Sampling Variability of Liver Biopsy in Nonalcoholic Fatty Liver Disease. *Gastroenterology* **128**, 1898–1906 (2005).
24. Garrido, M. C. & Hubscher, S. G. Accuracy of staging in primary biliary cirrhosis. *J. Clin. Pathol.* **49**, 556–559 (1996).
25. Berson, S. A. & Yalow, R. S. General principles of radioimmunoassay. *Clin. Chim. Acta* **22**, 51–69 (1968).
26. Haberkorn, U. in *Morphol. Imaging Mol. Target.* (eds. Schwaiger, M., Dinkelborg, L. & Schweinfurth, H.) 111–134 (Springer Berlin Heidelberg, 2004). at <http://link.springer.com/chapter/10.1007/978-3-662-07310-0_6>
27. Karavida, N. & Notopoulos, A. Radiation Synovectomy: an effective alternative treatment for inflamed small joints. *Hippokratia* **14**, 22–27 (2010).
28. The Nobel Prize in Chemistry 1943. at <http://www.nobelprize.org/nobel_prizes/chemistry/laureates/1943/>
29. Hevesy, G. The Absorption and Translocation of Lead by Plants. *Biochem. J.* **17**, 439–445 (1923).
30. *Positron emission tomography: basic sciences.* (Springer, 2005).
31. Becquerel, H. Sur les radiations émises par phosphorescence. *Comptes Rendus Hebd. Séances Académie Sci.* **122**, 420–421 (1896).
32. Lieser, K. H. *Einführung in die Kernchemie.* (VCH, 1991).
33. Ache, H. J. Chemie des Positrons und Positroniums. *Angew. Chem.* **84**, 234–255 (1972).
34. Anicin, I. V. The Neutrino - Its Past, Present and Future. *arXiv:physics/0503172* (2005). at <<http://arxiv.org/abs/physics/0503172>>
35. Herzog, H. & Rösch, F. PET- und SPECT-Technik: Chemie und Physik der Bildgebung. *Pharm. Unserer Zeit* **34**, 468–473 (2005).
36. West, C. M. L., Jones, T. & Price, P. The potential of positron-emission tomography to study anticancer-drug resistance. *Nat. Rev. Cancer* **4**, 457–469 (2004).
37. Torigian, D. A. *et al.* PET/MR Imaging: Technical Aspects and Potential Clinical Applications. *Radiology* **267**, 26–44 (2013).
38. Machulla, H.-J. PET-Diagnostika in der Onkologie: Beispiele aus der Praxis. *Pharm. Unserer Zeit* **34**, 490–497 (2005).

39. Haug, A. *et al.* Intraindividual comparison of ⁶⁸Ga-DOTA-TATE and ¹⁸F-DOPA PET in patients with well-differentiated metastatic neuroendocrine tumours. *Eur. J. Nucl. Med. Mol. Imaging* **36**, 765–770 (2009).
40. Gomes, C. M., Abrunhosa, A. J., Ramos, P. & Pauwels, E. K. J. Molecular imaging with SPECT as a tool for drug development. *Adv. Drug Deliv. Rev.* **63**, 547–554 (2011).
41. Chatziioannou, A. F. Instrumentation for Molecular Imaging in Preclinical Research: Micro-PET and Micro-SPECT. *Proc. Am. Thorac. Soc.* **2**, 533–536 (2005).
42. Cattin, P. C. parallel_hole_collimator.png (PNG-Grafik, 1235 × 1131 Pixel) - Skaliert (30%). at <http://miac.unibas.ch/PMI/07-NuclearMedicineImaging-media/figs/parallel_hole_collimator.png>
43. Zhernosekov, K. P. *et al.* Processing of Generator-Produced ⁶⁸Ga for Medical Application. *J. Nucl. Med.* **48**, 1741–1748 (2007).
44. Wadas, T. J., Wong, E. H., Weisman, G. R. & Anderson, C. J. Coordinating Radiometals of Copper, Gallium, Indium, Yttrium, and Zirconium for PET and SPECT Imaging of Disease. *Chem. Rev.* **110**, 2858–2902 (2010).
45. International Atomic Energy Agency. *Manual for reactor produced radioisotopes*. (IAEA, 2003).
46. Hermanne, A. *et al.* Limitation of the long-lived ¹²¹Te contaminant in production of ¹²³I through the ¹²⁴Xe(p,x) route. *Appl. Radiat. Isot.* **69**, 358–368 (2011).
47. Čomor, J. J. *et al.* Solid targetry at the TESLA Accelerator Installation. *Nucl. Instrum. Methods Phys. Res. Sect. Accel. Spectrometers Detect. Assoc. Equip.* **480**, 7–15 (2002).
48. Green, M. A. & Welch, M. J. Gallium radiopharmaceutical chemistry. *Int. J. Rad. Appl. Instrum. B* **16**, 435–448 (1989).
49. Holleman, A. F. & Wiberg, E., Wiberg, Nils. *Lehrbuch der anorganischen Chemie*. (de Gruyter, 2007).
50. Bartholomä, M. D., Louie, A. S., Valliant, J. F. & Zubieta, J. Technetium and Gallium Derived Radiopharmaceuticals: Comparing and Contrasting the Chemistry of Two Important Radiometals for the Molecular Imaging Era. *Chem. Rev.* **110**, 2903–2920 (2010).
51. Steinhilber, D., Schubert-Zsilavec, M. & Roth, H. J. *Medizinische Chemie: Targets, Arzneistoffe, Chemische Biologie*. (Deutscher Apotheker Verlag, 2010).
52. Derendorf, H. *Pharmakokinetik: Einführung in die Theorie und Relevanz für die Arzneimitteltherapie*. (WVG, Wissenschaftliche Verlagsgesellschaft, 2002).
53. Barczyk, M., Carracedo, S. & Gullberg, D. Integrins. *Cell Tissue Res.* **339**, 269–280 (2010).
54. Campbell, I. D. & Humphries, M. J. Integrin Structure, Activation, and Interactions. *Cold Spring Harb. Perspect. Biol.* **3**, a004994 (2011).
55. Krauss, G. *Biochemistry of signal transduction and regulation*. (Wiley-VCH Verlag GmbH & Co. KGaA, 2008).
56. Goodman, S. L. & Picard, M. Integrins as therapeutic targets. *Trends Pharmacol. Sci.* **33**, 405–412 (2012).

57. Hausner, S. H. *et al.* Targeted In vivo Imaging of Integrin $\alpha\beta_6$ with an Improved Radiotracer and Its Relevance in a Pancreatic Tumor Model. *Cancer Res.* **69**, 5843–5850 (2009).
58. Popov, Y. *et al.* Integrin $\alpha\beta_6$ is a marker of the progression of biliary and portal liver fibrosis and a novel target for antifibrotic therapies. *J. Hepatol.* **48**, 453–464 (2008).
59. Thomas, G. J., Nyström, M. L. & Marshall, J. F. $\alpha\beta_6$ integrin in wound healing and cancer of the oral cavity. *J. Oral Pathol. Med.* **35**, 1–10 (2006).
60. Page, M. J. & Di Cera, E. Evolution of Peptidase Diversity. *J. Biol. Chem.* **283**, 30010–30014 (2008).
61. Berg, J. M., Tymoczko, J. L. & Stryer, L. *Biochemie.* (Spektrum Akad. Verl., 2003).
62. Rawlings, N. D., Barrett, A. J. & Bateman, A. MEROPS: the peptidase database. *Nucleic Acids Res.* **38**, D227–D233 (2010).
63. MEROPS - the Peptidase Database. at <http://merops.sanger.ac.uk/cgi-bin/clan_index?type=P>
64. Page, M. J. & Cera, E. D. Serine peptidases: Classification, structure and function. *Cell. Mol. Life Sci.* **65**, 1220–1236 (2008).
65. Blow, D. M., Birktoft, J. J. & Hartley, B. S. Role of a Buried Acid Group in the Mechanism of Action of Chymotrypsin. *Nature* **221**, 337–340 (1969).
66. Lee, K. N. *et al.* Antiplasmin-cleaving enzyme is a soluble form of fibroblast activation protein. *Blood* **107**, 1397–1404 (2006).
67. O'Brien, P. & O'Connor, B. F. Seprase: An overview of an important matrix serine protease. *Biochim. Biophys. Acta BBA - Proteins Proteomics* **1784**, 1130–1145 (2008).
68. Aertgeerts, K. *et al.* Structural and kinetic analysis of the substrate specificity of human fibroblast activation protein alpha. *J. Biol. Chem.* **280**, 19441–19444 (2005).
69. Acharya, P. S., Zukas, A., Chandan, V., Katzenstein, A.-L. A. & Puré, E. Fibroblast activation protein: a serine protease expressed at the remodeling interface in idiopathic pulmonary fibrosis. *Hum. Pathol.* **37**, 352–360 (2006).
70. Levy, M. T. *et al.* Fibroblast activation protein: A cell surface dipeptidyl peptidase and gelatinase expressed by stellate cells at the tissue remodelling interface in human cirrhosis. *Hepatology* **29**, 1768–1778 (1999).
71. Pollard, T. D. A Guide to Simple and Informative Binding Assays. *Mol. Biol. Cell* **21**, 4061–4067 (2010).
72. Hulme, E. C. & Trevethick, M. A. Ligand binding assays at equilibrium: validation and interpretation. *Br. J. Pharmacol.* **161**, 1219–1237 (2010).
73. Cheng, Y.-C. & Prusoff, W. H. Relationship between the inhibition constant (KI) and the concentration of inhibitor which causes 50 per cent inhibition (I50) of an enzymatic reaction. *Biochem. Pharmacol.* **22**, 3099–3108 (1973).
74. Porstmann, T. & Kiessig, S. T. Enzyme immunoassay techniques an overview. *J. Immunol. Methods* **150**, 5–21 (1992).
75. Hornbeck, P. in *Curr. Protoc. Immunol.* (John Wiley & Sons, Inc., 2001). at <<http://onlinelibrary.wiley.com/doi/10.1002/0471142735.im0201s01/abstract>>
76. Atkins, P. W., Höpfner, A. & Schleitzer, A. *Physikalische Chemie.* (Wiley-VCH, 2001).

77. Leach, A. R. *Molecular modelling: principles and applications*. (Prentice Hall, 2001).
78. Born, M. & Oppenheimer, R. Zur Quantentheorie der Molekeln. *Ann. Phys.* **389**, 457–484 (1927).
79. Bingham, R. C., Dewar, M. J. S. & Lo, D. H. Ground states of molecules. XXV. MINDO/3. Improved version of the MINDO semiempirical SCF-MO method. *J. Am. Chem. Soc.* **97**, 1285–1293 (1975).
80. Dewar, M. J. S. & Thiel, W. Ground states of molecules. 38. The MNDO method. Approximations and parameters. *J. Am. Chem. Soc.* **99**, 4899–4907 (1977).
81. Dewar, M. J. S., Zoebisch, E. G., Healy, E. F. & Stewart, J. J. P. Development and use of quantum mechanical molecular models. 76. AM1: a new general purpose quantum mechanical molecular model. *J. Am. Chem. Soc.* **107**, 3902–3909 (1985).
82. Stewart, J. J. P. Optimization of parameters for semiempirical methods VI: more modifications to the NDDO approximations and re-optimization of parameters. *J. Mol. Model.* **19**, 1–32 (2013).
83. Stewart, J. P. *MOPAC*. (Stewart Computational Chemistry, Colorado Springs, CO, USA, 2012). at <[HTTP://OpenMOPAC.net](http://OpenMOPAC.net)>
84. Allinger, N. L. Conformational analysis. 130. MM2. A hydrocarbon force field utilizing V1 and V2 torsional terms. *J. Am. Chem. Soc.* **99**, 8127–8134 (1977).
85. Lii, J. H. & Allinger, N. L. Molecular mechanics. The MM3 force field for hydrocarbons. 2. Vibrational frequencies and thermodynamics. *J. Am. Chem. Soc.* **111**, 8566–8575 (1989).
86. Allinger, N. L., Chen, K. & Lii, J.-H. An improved force field (MM4) for saturated hydrocarbons. *J. Comput. Chem.* **17**, 642–668 (1996).
87. Weiner, S. J. *et al.* A new force field for molecular mechanical simulation of nucleic acids and proteins. *J. Am. Chem. Soc.* **106**, 765–784 (1984).
88. Rappe, A. K., Casewit, C. J., Colwell, K. S., Goddard, W. A. & Skiff, W. M. UFF, a full periodic table force field for molecular mechanics and molecular dynamics simulations. *J. Am. Chem. Soc.* **114**, 10024–10035 (1992).
89. González, M. A. Force fields and molecular dynamics simulations. *Éc. Thématique Société Fr. Neutron.* **12**, 169–200 (2011).
90. Cheatham, T. E. I., Miller, J. L., Fox, T., Darden, T. A. & Kollman, P. A. Molecular Dynamics Simulations on Solvated Biomolecular Systems: The Particle Mesh Ewald Method Leads to Stable Trajectories of DNA, RNA, and Proteins. *J. Am. Chem. Soc.* **117**, 4193–4194 (1995).
91. Lesk, A. M., Vogel, S. & Mewes, H. W. *Bioinformatik: eine Einführung*. (Spektrum, Akad. Verl., 2003).
92. Dayhoff, M. O. & Schwartz, R. M. Chapter 22: A model of evolutionary change in proteins. in *Atlas Protein Seq. Struct.* (1978).
93. Henikoff, S. & Henikoff, J. G. Amino acid substitution matrices from protein blocks. *Proc. Natl. Acad. Sci.* **89**, 10915–10919 (1992).
94. Needleman, S. B. & Wunsch, C. D. A general method applicable to the search for similarities in the amino acid sequence of two proteins. *J. Mol. Biol.* **48**, 443–453 (1970).

95. Krieger, E., Nabuurs, S. B. & Vriend, G. in *Struct. Bioinforma.* (eds. Bourne, P. E. & Weissig, H.) (Wiley-Liss, 2003). at <http://www.cmbi.ru.nl/edu/bioinf4/articles/homologymodeling.pdf>
96. Jonczyk, A. *et al.* Alfvbeta3 and Alfvbeta6 Integrin Antagonists as Antifibrotic Agents. (2008).
97. Popov, Y. Alfvbeta3 and Alfvbeta6 Integrin Antagonists as Antifibrotic Agents. (2006).
98. Patsenker, E. *et al.* Inhibition of Integrin $\alpha\beta 6$ on Cholangiocytes Blocks Transforming Growth Factor- β Activation and Retards Biliary Fibrosis Progression. *Gastroenterology* **135**, 660–670 (2008).
99. AASLD Abstracts 1–219. *Hepatology* **48**, 354A (2008).
100. Hu, Y. *et al.* Synthesis and structure–activity relationship of N-alkyl Gly-boro-Pro inhibitors of DPP4, FAP, and DPP7. *Bioorg. Med. Chem. Lett.* **15**, 4239–4242 (2005).
101. Sulyok, G. A. G. *et al.* Solid-Phase Synthesis of a Nonpeptide RGD Mimetic Library: New Selective $\alpha\beta 3$ Integrin Antagonists. *J. Med. Chem.* **44**, 1938–1950 (2001).
102. Goodman, S. L., Hölzemann, G., Sulyok, G. A. G. & Kessler, H. Nanomolar Small Molecule Inhibitors for $\alpha\beta 6$, $\alpha\beta 5$, and $\alpha\beta 3$ Integrins. *J. Med. Chem.* **45**, 1045–1051 (2002).
103. Patriciu, O.-I., Pillard, C., Fînaru, A.-L., Săndulescu, I. & Guillaumet, G. Synthesis of Nitro N, N'-Dipyridinylamines via Oxidative Nucleophilic Substitution of Hydrogen. *Synthesis* **2007**, 3868–3876 (2007).
104. El-Faham, A., Funosas, R. S., Prohens, R. & Albericio, F. COMU: A Safer and More Effective Replacement for Benzotriazole-Based Uronium Coupling Reagents. – *Eur. J.* **15**, 9404–9416 (2009).
105. Kühle, B. Synthese und Entwicklung von ^{68}Ga -markierten Pteroinsäure-basierten PET-Tracern. (2010).
106. Cheng, C. I., Chang, Y.-P. & Chu, Y.-H. Biomolecular interactions and tools for their recognition: focus on the quartz crystal microbalance and its diverse surface chemistries and applications. *Chem. Soc. Rev.* **41**, 1947–1971 (2012).
107. Sauerbrey, G. Verwendung von Schwingquarzen zur Wägung dünner Schichten und zur Mikrowägung. *Z. Für Phys.* **155**, 206–222 (1959).
108. Wirkner, M. *et al.* Photoactivatable Caged Cyclic RGD Peptide for Triggering Integrin Binding and Cell Adhesion to Surfaces. *ChemBioChem* **12**, 2623–2629 (2011).
109. Cui, J. *et al.* Phototunable Response in Caged Polymer Brushes. *Macromolecules* **45**, 3213–3220 (2012).
110. Cui, J., Wang, D., Koynov, K. & del Campo, A. 2-Ureido-4-Pyrimidone-Based Hydrogels with Multiple Responses. *ChemPhysChem* **14**, 2932–2938 (2013).
111. Shi, M. *et al.* Latent TGF- β structure and activation. *Nature* **474**, 343–349 (2011).
112. Paradise, R. K., Lauffenburger, D. A. & Van Vliet, K. J. Acidic Extracellular pH Promotes Activation of Integrin $\alpha\beta 3$. *PLoS ONE* **6**, e15746 (2011).
113. Smit, J. J. M. *et al.* Homozygous disruption of the murine MDR2 P-glycoprotein gene leads to a complete absence of phospholipid from bile and to liver disease. *Cell* **75**, 451–462 (1993).

114. Popov, Y., Patsenker, E., Fickert, P., Trauner, M. & Schuppan, D. Mdr2 (Abcb4)^{-/-} mice spontaneously develop severe biliary fibrosis via massive dysregulation of pro- and antifibrogenic genes. *J. Hepatol.* **43**, 1045–1054 (2005).
115. Pedretti, A. & Vistoli, G. VEGA ZZ. (Dipartimento di Scienze Farmaceutiche; Università degli Studi di Milano). at <<http://www.vegazz.net>>
116. Hanwell, M. D. *et al.* Avogadro: an advanced semantic chemical editor, visualization, and analysis platform. *J. Cheminformatics* **4**, 17 (2012).
117. Xiong, J.-P. *et al.* Crystal Structure of the Extracellular Segment of Integrin $\alpha\text{V}\beta\text{3}$ in Complex with an Arg-Gly-Asp Ligand. *Science* **296**, 151–155 (2002).
118. Yu, Y.-P., Wang, Q., Liu, Y.-C. & Xie, Y. Molecular basis for the targeted binding of RGD-containing peptide to integrin $\alpha\text{V}\beta\text{3}$. *Biomaterials* **35**, 1667–1675 (2014).
119. López-Vidal, E. M. *et al.* Probing Electrostatic Potential by NMR with the Use of a Paramagnetic Lanthanide(III) Chelate. *Inorg. Chem.* **51**, 4429–4431 (2012).
120. Integrin alpha-V precursor - ITGAV - Homo sapiens (Human). at <<http://www.uniprot.org/uniprot/P06756>>
121. Integrin beta-6 precursor - ITGB6 - Homo sapiens (Human). at <<http://www.uniprot.org/uniprot/P18564>>
122. Sievers, F. *et al.* Fast, scalable generation of high-quality protein multiple sequence alignments using Clustal Omega. *Mol. Syst. Biol.* **7**, 539–539 (2014).
123. Arnold, K., Bordoli, L., Kopp, J. & Schwede, T. The SWISS-MODEL workspace: a web-based environment for protein structure homology modelling. *Bioinformatics* **22**, 195–201 (2006).
124. Marinelli, L., Gottschalk, K.-E., Meyer, A., Novellino, E. & Kessler, H. Human Integrin $\alpha\text{v}\beta\text{5}$: Homology Modeling and Ligand Binding. *J. Med. Chem.* **47**, 4166–4177 (2004).
125. Biasini, M. *et al.* SWISS-MODEL: modelling protein tertiary and quaternary structure using evolutionary information. *Nucleic Acids Res.* (2014). doi:10.1093/nar/gku340
126. Šali, A. & Blundell, T. L. Comparative Protein Modelling by Satisfaction of Spatial Restraints. *J. Mol. Biol.* **234**, 779–815 (1993).
127. Pettersen, E. F. *et al.* UCSF Chimera—A visualization system for exploratory research and analysis. *J. Comput. Chem.* **25**, 1605–1612 (2004).
128. Ramachandran, G. N., Ramakrishnan, C. & Sasisekharan, V. Stereochemistry of polypeptide chain configurations. *J. Mol. Biol.* **7**, 95–99 (1963).
129. Morris, G. M. *et al.* AutoDock4 and AutoDockTools4: Automated Docking with Selective Receptor Flexibility. *J. Comput. Chem.* **30**, 2785–2791 (2009).
130. Gasteiger, J. & Marsili, M. Iterative partial equalization of orbital electronegativity—a rapid access to atomic charges. *Tetrahedron* **36**, 3219–3228 (1980).
131. Elosegui-Artola, A. *et al.* Rigidity sensing and adaptation through regulation of integrin types. *Nat. Mater.* **13**, 631–637 (2014).
132. Fellner, M. *et al.* Assessing p-Glycoprotein (Pgp) Activity In Vivo Utilizing ⁶⁸Ga–Schiff Base Complexes. *Mol. Imaging Biol.* **13**, 985–994 (2010).

VII. List of Abbreviations

I

[¹⁸F]FDG.....2-[¹⁸F]fluoro-2-desoxy-*D*-glucose

[¹⁸F]FDOPA.....2-[¹⁸F]fluoro-3,4-dihydroxy-*L*-phenylalanine

[⁶⁸Ga]DOTA-TATE.....[⁶⁸Ga]DOTA-(Tyr³)-octreotate, Somatostatin-receptor ligand

μ

μPET.....mikro-Positron-Emission-Tomography. The device is geometrically
..... optimized for small animals, especially rodents.

A

aa.....amino acid

ADME.....absorption, distribution, metabolism, excretion

ALT.....Alanine Aminotransferase

AM1.....Austin Model 1

APCE.....antiplasmin cleaving-enzyme

AST.....Aspartate Aminotransferase

B

BLOSUM.....BLOCKS substitution matrix; BLOCKS is a database for protein sequences

C

CAV-9.....Coxsackie virus 9

D

DFO.....deferoxamine

DNA.....Deoxyribonucleic Acid

DOTA.....1,4,7,10-tetra-acetic acid – 1,4,7,10-tetra-aza-cyclo-dodecane

DSO.....Deutsche Stiftung Organtransplantation; German Organ Transplantation Foundation

E

EC.....Electron Capture

ECM.....Extracellular Matrix

EDC.....1-Ethyl-3-(3-dimethylaminopropyl)carbodiimide

EDTA.....Diaminoethane-tetra-acetic acid

ELISA	Enzyme Linked Immuno Sorbent Assay
ET-1	Endothelin-1
EtOH	Ethanol
F	
FAP	Fibroblast Activating Protein
FMDV	Foot-and-mouth-disease virus
G	
GGT	Gamma Glutamyl Transpeptidase
H	
HOMO	Highest occupied molecular orbital
HSAB	Hard and Soft Acids and Bases
HSC	Hepatic stellate cells
Hz	Hertz; unit for frequency: 1/s
L	
LAP	latency-associated-peptide
LOR	Line of Response
LUMO	Lowest unoccupied molecular orbital
M	
M.O.	molecular orbital
Mdr2	multi-drug-resistance-2 gene
MES	2-(N-morpholino)ethanesulfonic acid
MIDAS	metal ion-dependent adhesion site
MMP	Matrix-Metallo-Protease
MRI	Magnetic resonance imaging
N	
NASH	Non-alcoholic-steato-hepatitis
NHS	N-Hydroxysuccinimide
NOTA	1,4,7-tri-acetic acid – 1,4,7-tri-aza-cyclo-nonane
P	
PAM	Percent Accepted Mutation
PBC	Primary biliary cirrhosis
PDGF	Platelet-derived Growth Factor
PET	Positron Emission Tomography

PET/CT..... Positron Emission Tomography - Computer Tomography
 PET/MRI Positron Emission Tomography - Magnetic Resonance Imaging
 pH..... *potentia hydrogenii*; $\text{pH} = -\log_{10}([\text{H}^+])$

Q

QCM Quartz Crystal Microbalance

R

RCY radiochemical yield
 RGD Arginine-Glycine-Aspartic Acid
 RIA Radio Immuno Assay
 RNA Ribonucleic Acid
 ROI Reactive Oxygen Intermediates
 rt room temperature

S

SDL specificity defining loop
 SMAD An intracellular signalling-protein, effector of TGF-beta1.
 Name stems from a combination of the homologous proteins SMA and MAD.
 SPECT Single Photon Emission Computed Tomography

T

TAC..... time-activity-curve
 TE Transient Elastography
 TGF- β 1..... Transforming Growth Factor- β 1
 TGF- β 3..... Transforming growth factor beta 3
 TIMP Tissue Inhibitor of Metalloproteinases
 TV Targeting Vector

U

UFF universal force field
 US..... Ultrasound

V

vdW.....van der Waals
 VOI volume-of-interest

W

WHO..... World Health Organization

VIII. List of Figures

Figure 1:	Macroscopic structure of the human liver. ⁶	2
Figure 2:	Microscopic structure of the human liver, detailing some liver sinusoids. ⁸	3
Figure 3:	Activated hepatic stellate cells and their role in fibrogenesis. Whether they reverse into a quiescent state or undergo apoptosis upon resolution of liver injury remains unsure. ¹¹	5
Figure 4:	Different cell types with the capability of converting into activated myofibroblasts. It is shown as well how they contribute to the establishment of fibrosis. ¹³	6
Figure 5:	Decay of the Positronium into 2 vs. 3 gamma-quants. Left: para, Right: ortho. ³³	11
Figure 6:	Principle of PET examination (left) ³⁶ and site uncertainty (right).	12
Figure 7:	PET image examples. The primary pancreas tumour of the patient is well delineated on the CT image (d) and shows inhomogeneous increased uptake of both [¹⁸ F]-DOPA (a,c SUVmax 3.9) and [⁶⁸ Ga]-DOTA-TATE (b,e SUVmax 7.2) while the hepatic metastases were visualized only by [⁶⁸ Ga]-DOTA-TATE PET but not by [¹⁸ F]-DOPA PET indicating a different tumour biology of the primary tumour and the metastases. ³⁹	13
Figure 8:	Principle of SPECT Detectors. The Collimator only allows entry of gamma rays from a distinct direction. ⁴²	15
Figure 9:	Chemical structures of the chelates DOTA, NOTA and derivatives thereof.	20
Figure 10:	Structures of typical Tc-chelates. A) Tc(V)oxo; b) Tc(V)-nitrido; c) Tc(V)imido; d) Tc(III)tricarbonyl; e) Tc(V)hydrazido. ⁵⁰	20
Figure 11:	Left: Combinations of α - and β -chains, sorted by ligand specificity. ⁵³ Right: Bent (rather inactive) and upright (presumably inactive) conformation of integrins. ⁵⁴	22
Figure 12:	Structure of the extracellular part of FAP. PDB entry 1Z68. ⁶⁸	25
Figure 13:	Typical curve of a ligand binding assay. The ligand concentration at the 50% value of B_{max} is equivalent to the K_d value. ⁷²	26
Figure 14:	Structure of EM527040, a highly specific and selective ligand of $\alpha_v\beta_6$.	37
Figure 15:	Structures of TC1, TC2 and TC3 - ^{99m} Tc-labelled mono-, di- and trimers of EMD527040. ⁹⁹	38

Figure 16:	Proposed synthesis route to EMD527040. Based on methods of Goodman and Sulyok. ^{101,102}	40
Figure 17:	DOTA based chelators to be coupled to EMD527040.	41
Figure 18:	a) Na ₂ CO ₃ , 130°C, overnight (27 %); b) dioxane, HCl (1N), 105 °C, reflux, overnight (quantitative).	42
Figure 19:	a) MeOH, reflux → rt (53 – 64 %); b) MeOH, SOCl ₂ , DMF, -78°C → rt (56-84%).	42
Figure 20:	a) DIPEA, HOBt, EDCI*HCl, DMF, 18-25 h, rt (64 – 77 %); b) HCl in dioxane (4M), rt, 20 h, (97 %).	43
Figure 21:	DIPEA, HOBt, EDCI*HCl, DMF, overnight, rt (63%); b) NaOH, pH 11, 4 days (97%).	43
Figure 22:	a) DMF, COMU, TMP, 20 x 10 s microwave 55W, (60%); b) DCM/TFA (1/1), 36 h, rt (33% after HPLC purification).	45
Figure 23:	a) DMF, COMU, TMP, 20 x 10 s microwave 55W, (48 %); b) MeOH/TEA (3/1), Pd/C (10%), H ₂ , rt, 10 h (40%).	46
Figure 24:	a) DMF, COMU, TMP, 20 x 10 s microwave 55W, (45 %); b) DCM/TFA (3/1), overnight, rt (60 % after HPLC purification).	47
Figure 25:	Intended reaction for talabostat derivatization.	48
Figure 26:	Possible cyclisation products during the course of talabostat coupling.	49
Figure 27:	Kinetic studies for radio labelling of BK23 and BK39 with 10, 20 and 30 nmol precursor, respectively (blue, red, green). RCY determined by radio-TLC.	50
Figure 28:	Stability investigation on the ⁶⁸ Ga-labelled tracers BK23 and BK39. Determined by radioTLC.	52
Figure 29:	Typical experimental setup of QCM measurements. ¹⁰⁶	53
Figure 30:	Incubation of αvβ6 positive (HT-29 and 603B) and negative (Huh-7) cells with BK39.	55
Figure 31:	Challenge experiment with BK39 and varying concentrations of EMD527040.	55
Figure 32:	Affinity assay for BK23 on HT-29 and 603B cells. Total binding and Non-specific binding were measured to calculate Specific binding by subtraction.	56
Figure 33:	Affinity assay for BK39 on HT-29 and 603B cells. Total binding and Non-specific binding were measured to calculate Specific binding by subtraction.	57
Figure 34:	Uptake assay with BK23 on HT-29, 603B and Huh-7 cells at 0°C (left) and 37°C (right), respectively. In all cases, 99% of the activity were found in the supernatant and no retention on the cells could be observed.	57

- Figure 35: Uptake assay with BK39 on HT-29, 603B and Huh-7 cells at 0°C (left) and 37°C (right), respectively. In all cases, 99% of the activity were found in the supernatant and no retention on the cells could be observed. 58
- Figure 36: ELISA results from commercial alpha v kit. Left: standard curve obtained from included kit standard. Right: Results on self-coated plates with $\alpha_v\beta_6$. 60
- Figure 37: Detection of $\alpha_v\beta_6$ on ELISA plates with biotinylated fibronectin and following anti-biotin-peroxidase. 61
- Figure 38: Detection of $\alpha_v\beta_6$ on ELISA plates with STX-100 and following anti-mouse-peroxidase. 62
- Figure 39: Binding curves for BK23 as well as BK39 on isolated integrin $\alpha_v\beta_6$. Note that the x-axis is logarithmic in this case. 63
- Figure 40: ELISA assay on integrin $\alpha_v\beta_6$ coated plates with latency-associated-peptide. Incubation time for LAP as well as the concentration of the antibody were investigated. 65
- Figure 41: pH-dependency of the LAP-based ELISA system 66
- Figure 42: Investigation on the behaviour of specific and unspecific behaviour of LAP binding to $\alpha_v\beta_6$ -coated ELISA-plates with regard to the concentration of LAP. Coating concentration was 1 $\mu\text{g}/\text{mL}$. The respective two curves were obtained from different anti-LAP dilutions (1/20,000 and 1/30,000). Polynomial fits were obtained in Microsoft Excel. 66
- Figure 43: ELISA results for blocking LAP with the fluorinated ligand F2 and EMD527040, respectively. 68
- Figure 44: ELISA results for blocking LAP with the fluorinated ligand F2 - with a broader concentration range (left) and different integrin coating concentrations (right). 68
- Figure 45: ELISA measurement for the fluorinated ligand **F2**. As the curve for total binding and unspecific binding converge, the ligand proves to be an $\alpha_v\beta_6$ ligand. Unfortunately, the method is not sensitive enough to calculate an affinity value.70
- Figure 46: QCM measurement of unspecific binding - an unspecific deposition of $\alpha_v\beta_6$ to the SAM surface of -30 Hz is observed. 71
- Figure 47: Averaged time-activity curves for BK23. Liver, Heart, Bladder and Muscle are displayed for both healthy as well as fibrotic mice. Values for heart and muscle are difficult to distinguish, as they overlay each other. 74

Figure 48:	Time-activity-curves for healthy FVB mice. Liver, Heart, Bladder and Muscle are displayed. The values for heart (orange) can hardly be seen, as they are similarly low as the ones in muscle (yellow).	75
Figure 49:	Time-activity-curves for fibrotic Mdr2 ^{-/-} mice. Liver, Heart, Bladder and Muscle are displayed. The values for heart (orange) can hardly be seen, as they are similarly low as the ones in muscle (yellow).	75
Figure 50:	Dynamic μ PET scan. Tracer: BK23. Wild-type.	76
Figure 51:	Dynamic μ PET scan. Tracer: BK23. Mdr2 ^{-/-} knockout mouse.	76
Figure 52:	Averaged values of ex vivo biodistribution study, 2 hours post-injection.	77
Figure 53:	Single Animal results of the ex vivo biodistribution study; 2 hours post-injection. KO = Knockout; WT = Wildtype.	78
Figure 54:	Averaged time-activity curves for BK39. Liver, Heart, Bladder, Muscle and the kidneys (left and right) are displayed for both healthy as well as fibrotic mice. Values for heart and muscle are difficult to distinguish, as they overlay each other.	79
Figure 55:	Time-activity-curves for healthy FVB mice. Liver, Heart, Bladder, Muscle and Kidneys are displayed. The R0645 measurement was interrupted and manually aligned for time.	79
Figure 56:	Time-activity-curves for fibrotic Mdr2 ^{-/-} mice. Liver, Heart, Bladder, Muscle and Kidneys are displayed. It is of note, that in one case (R0642) the kidney values were significantly higher but no uptake was observed in the bladder. Both kinetic profiles support the hypothesis of a renal elimination pathway.	80
Figure 57:	Dynamic μ PET scan. Tracer: BK39. Wild-type.	80
Figure 58:	Dynamic μ PET scan. Tracer: BK39. Mdr2 ^{-/-} knockout mouse.	81
Figure 59:	Averaged values of ex vivo biodistribution study, 2 hours post-injection.	81
Figure 60:	Single Animal results of the ex vivo biodistribution study; 2 hours post-injection. KO = Knockout; WT = Wildtype.	82
Figure 61:	Orbital locations of EMD527040.	86
Figure 62:	Orbital locations of cilengitide - a typical $\alpha_v\beta_3$ ligand.	86
Figure 63:	Interpolated Charges of $\alpha_v\beta_6$ -binding ligands. Color code: Red = negative; blue = positive.	87
Figure 64:	Interpolated Charge of EMD527040. Color Code: Red = negative; blue = positive.	88
Figure 65:	Possible ¹⁸ F-fluorinated derivatives of EMD527040.	88

Figure 66:	Potential ^{68}Ga -labelled derivatives of EMD527040	89
Figure 67:	Structures of TC1, TC2 and TC3; mono-, di- and trimeric EMD527040-derivatives for $^{99\text{m}}\text{Tc}$ -labelling on an adamantane scaffold.	90
Figure 68:	Localization of HOMO and LUMO for the fluorinated derivatives of EMD527040 F1 and F2.	91
Figure 69:	Localization of HOMO and LUMO for the Ga-labelled derivatives of EMD527040 BK23 and BK39.	92
Figure 70:	Localization of HOMO and LUMO for the Ga-labelled derivatives of EMD527040 GA 1 and GA 2.	93
Figure 71:	Localization of HOMO and LUMO for the Tc-labelled derivatives of EMD527040 TC 1 and TC 2.	94
Figure 72:	Interpolated Charge of the fluorinated derivatives of EMD527040 F1 and F2. Color Code: Red = negative; blue = positive.	94
Figure 73:	Interpolated Charge of the tracers BK23 and BK39. Obtained on basis of the MOPAC calculations. Color Code: Red = negative; blue = positive.	95
Figure 74:	Interpolated Charge of the tracers BK23 and BK39. Obtained on basis of the minimized structures. Color Code: Red = negative; blue = positive.	95
Figure 75:	Computed MPWLYP/6-311G** electrostatic potential of $[\text{Yb}(\text{DOTA})]^-$ (hartree) on the molecular surface defined by the 0.001 electrons·bohr ⁻³ contour of the electronic density. Views are along the molecule C4-symmetry axis. ¹¹⁹	96
Figure 76:	Interpolated Charge of potential Ga-labelled EMD527040-derivatives GA1 and GA2. Color Code: Red = negative; blue = positive.	96
Figure 77:	Interpolated Charge of potential Tc-labelled EMD527040-derivatives TC1 and TC2. Color Code: Red = negative; blue = positive.	97
Figure 78:	Initial Model for $\alpha_v\beta_6$, obtained from the SWISS Model Server. The clashing chains can easily be seen in the lower part of the image.	99
Figure 79:	Model of $\alpha_v\beta_6$ obtained by homology modelling with MODELLER and subsequent molecular dynamics simulation.	101
Figure 80:	Ramachandran Plots of the calculated model for $\alpha_v\beta_6$ (left) and the x-ray structure of $\alpha_v\beta_3$ 1L5G (right).	101
Figure 81:	Inspection of the binding site with the 1L5G ligand for the surface charge (Interpolated Charge method in Discovery Studio). Top: $\alpha_v\beta_6$ model. Bottom: $\alpha_v\beta_3$ experimental structure 1L5G for comparison. Blue: positive charge. Red: negative charge.	102

- Figure 82: Inspection of the binding site with the 1L5G ligand for the solvent accessibility (Discovery Studio). Top: $\alpha_v\beta_6$ model. Bottom: $\alpha_v\beta_3$ experimental structure 1L5G for comparison. Blue: accessible. Green: badly accessible. 103
- Figure 83: Inspection of the binding site with the 1L5G ligand for the surface hydrophobicity (Discovery Studio). Top: $\alpha_v\beta_6$ model. Bottom: $\alpha_v\beta_3$ experimental structure 1L5G for comparison. Blue: hydrophilic. Brown: Hydrophobic. The SDL structure is located in the upper part of the image – straight above the ligands. 104
- Figure 84: Specificity defining loop in $\alpha_v\beta_6$ (top) and $\alpha_v\beta_3$ (bottom). SDL labelled in yellow. 104
- Figure 85: Docked conformations of EMD527040 with the integrin $\alpha_v\beta_6$. The upper image displays the lowest energy conformation, the lower one the solution with the second lowest binding energy, which is closer to the binding mode in the 1L5G pdb entry of $\alpha_v\beta_3$ and its ligand. 107
- Figure 86: Docked conformations of F2 to the integrin $\alpha_v\beta_6$. The upper one displays the lowest energy conformation, while the lower image shows the second-lowest energy conformation. Notably, they are similar to the ones of EMD527040, but the other way around in their energy. 108
- Figure 87: Docking of TC1 with the integrin $\alpha_v\beta_6$. Displayed is the second lowest energy conformation. The propionic acid residues on the adamantane backbone stick into the pocket with contact to the metal binding site. Interestingly, the EMD527040 moiety is compressed along its carbon chain – this could explain the binding of TC1 to $\alpha_v\beta_6$ in despite of the blocked carboxy function for coupling to the chelator. 110

IX. List of Tables

Table 1:	The METAVIR score scheme with the respective histological characteristics. ²¹	8
Table 2:	Occurrence of 1 stage difference in the METAVIR scheme, which is due to sampling error. PBC = Primary biliary cirrhosis.	8
Table 3:	A choice of typical nuclides for PET and SPECT. ^{35,43,44,45,46,47}	16
Table 4:	Activity balance for BK23 purification via Strata-X cartridge. Non decay-corrected values.	50
Table 5:	Influence of blocking agent on specific/unspecific signal.	69
Table 6:	Overview of performed animal experiments	73
Table 7:	Location of HOMOs and LUMOs of the $\alpha_v\beta_6$ binding literature ligands by Goodman et al. ¹⁰²	85
Table 8:	Obtained binding energies for the molecules EMD527040, BK23, TC1, F2 and GA1 with $\alpha_v\beta_6$.	106

X. Danksagung / Acknowledgements

Only available in printed version.

XI. Eidesstattliche Erklärung

Die vorliegende Arbeit wurde in der Zeit vom 01.04.2011 bis zum 30.06.2014 unter Anleitung von Herrn Univ.-Prof. Dr. Xxxxxx X. Xxxx am Institut für Kernchemie der Johannes Gutenberg-Universität, Mainz durchgeführt. Ich versichere, dass ich die Arbeit selbst durchgeführt und keine anderen als die in der Arbeit angegebenen Quellen und Hilfsmittel verwendet habe.

I hereby declare that I wrote the dissertation submitted without any unauthorized external assistance and used only sources acknowledged in the work. All textual passages which are appropriated verbatim or paraphrased from published and unpublished texts as well as all information obtained from oral sources are duly indicated and listed in accordance with bibliographical rules. In carrying out this research, I complied with the rules of standard scientific practice as formulated in the statutes of Johannes Gutenberg-University Mainz to ensure standard scientific practice.

Berit Kühle

XII. Curriculum Vitae - only available in printed version

XII. Curriculum Vitae - only available in printed version

XII. Curriculum Vitae - only available in printed version